SCUOLA DI DOTTORATO

UNIVERSITÀ DEGLI STUDI DI MILANO-BICOCCA

Department of

Biotechnologies and Biosciences

Ph. D program in Biology and Biotechnologies

Cycle XXXII

Role of SERCA stimulation and voltage-dependent Ca^{2+} channels in improving Ca^{2+} handling and sustaining heart automaticity

Surname	Torre
Name	Eleonora
Registration number	735333

Tutor:	Prof. Marcella Rocchetti
Coordinator:	Prof. Paola Branduardi

Academic Year 2018-2019

To myself, a gift for this heard experience.

To changes, so much in three years.

To my first supporter, since five years.

To my family, since I was born.

To my friends, since I met them.

To my colleagues, since I started working with.

To the future, 'cause I want to grow and learn more.

Contents

Introduction

From the first part (Chapter 1 and 2): the sarcoplasmic reticulum (SR) Ca^{2+} pump (SERCA2a) results fundamental for the Ca^{2+} re-uptake into the SR to guarantee the cardiac relaxation. In the heart failure, one of the major alterations that causes the contractile dysfunction is the reduction of the SR Ca^{2+} content which is due to a reduced SERCA2a function. Therefore, in the first part of the thesis I will focus on the role of SERCA2a and the possibility to use SERCA2a as a target to improve Ca^{2+} handling in a model of HF.

In the second part (Chapter 3 and 4), the aim of the thesis was to define the role of the voltage-gated L-type $Ca_v1.3$ and T-type $Ca_v3.1$ Ca^{2+} (Ca_v) channels essential for the generation of heart automaticity by using mutant mice carrying individual or concomitant genetic ablation of $Ca_v1.3$ and $Ca_v3.1$.

Chapter 1

Role of SERCA and its inhibitor phospholamban in Ca^{2+} handling

1.1. Cardiac excitation-contraction (EC) coupling

Myocardial mechanical activity is strictly dependent on electrical activity in a process called excitation-contraction coupling (ECC). Several factors are involved to generate the specific firing of the cardiac cells as a delicate balance between action potential (AP), Ca^{2+} transient and contraction. The excitation process starts with an AP followed by several phenomenon that lead to the single myocyte contraction[1].

Myocardial APs reflect the sequential activation and inactivation of inward (Na^+ and Ca^{2+}) and outward (K^+) current carrying ion channels[2]. Cardiomyocytes exhibit an AP morphology with 4 phases (Fig. 1). Phase 0 is the rapid depolarizing phase that results when Na^+ channels activate and an influx of Na^+ (I_{Na}) causes the membrane potential depolarization. Phase 1 corresponds to the inactivation of Na^+ channels and outward movement of K^+ ions through outward current (I_{to}). In phase 2, a low conductance plateau phase, inward and outward ion movements are balanced mainly by L-type calcium current (I_{CaL}) and delayed rectifier K^+ channels (rapid I_{Kr} and slow I_{Ks}), respectively. Phase 3 marks the final repolarization phase of the AP, which returns to the resting potential at about -80 mV (phase 4) where the non-voltage-gated inwardly rectifying K^+ current (I_{K1}) represents an important player.

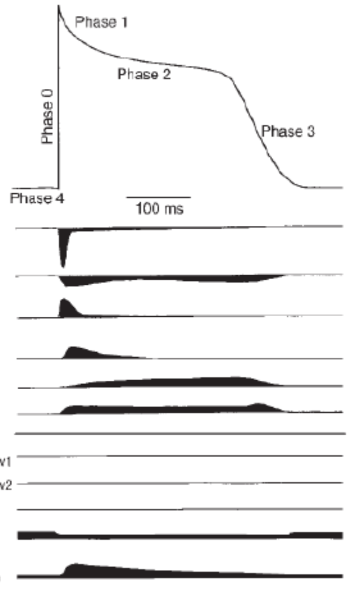

Figure 1: Contribution of ion channels to ventricular AP. The ventricular AP is generated by transmembrane inwardly and outwardly directed ion currents in adult human ventricular myocytes [According to Nerbonne and Kass, 2005].

During the cardiac AP, Ca^{2+} entry through I_{CaL} (situated in the surface membrane and transverse tubules) is the trigger for the Ca^{2+} release from the sarcoplasmic reticulum (SR) through the cardiac ryanodine receptors (RyR2) in a system defined as Ca^{2+}- induced Ca^{2+} release (CICR) (Fig. 2). The combination of Ca^{2+} influx and release raises the free intracellular Ca^{2+} concentration ($[Ca^{2+}]_i$). The N-terminus domain of the myofilament protein troponin C contains low affinity sites that are specific for Ca^{2+}. When the $[Ca^{2+}]_i$ reaches ~ $1\mu M$, Ca^{2+} binding to the troponin C sites switches on the contractile machinery which is an ATP-consuming process.

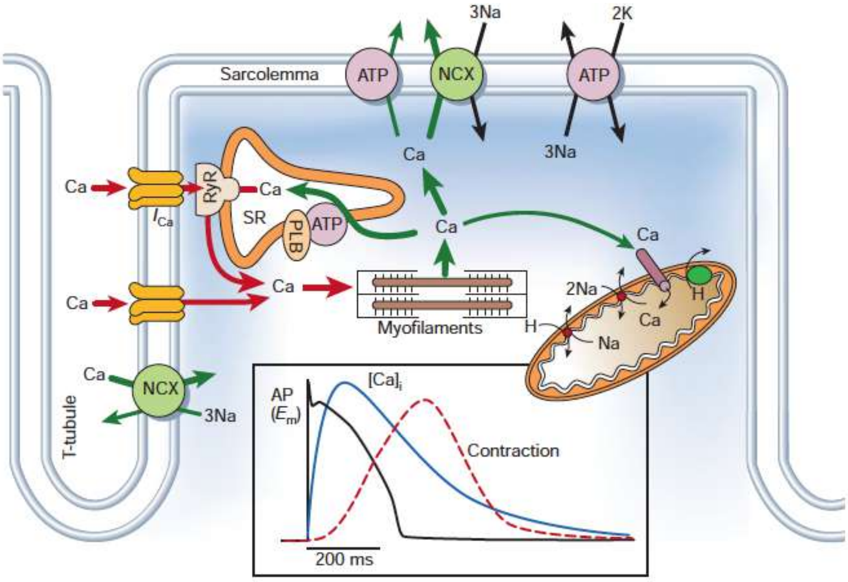

Figure 2: Ca^{2+} transport in ventricular myocytes. Inset shows the time course of an AP, Ca^{2+} transient and contraction measured in a rabbit ventricular myocyte at 37°C [According to Bers, 2002].

To occur cardiac relaxation, Ca^{2+} must be removed from the cytoplasm (i.e. to $[Ca^{2+}]_i$ ~ 100nM), allowing Ca^{2+} to dissociate from troponin. These events require that the RyRs close and then that Ca^{2+} is pumped (1) back into the SR, by the SERCA2a (cardiac isoform of the sarco/endoplasmic reticulum Ca^{2+}- ATPase) and (2) out of the cell, largely by the sodium–calcium exchanger (NCX). Other mechanisms (known collectively as "slow" Ca^{2+} extrusion pathways) are involved in the Ca^{2+} transport out of the cytosol, i.e. the sarcolemmal Ca^{2+}-ATPase (PMCA), the mitochondrial Na^+/Ca^{2+} exchanger (mitNCX) or the mitochondrial Ca^{2+} uniport (MCU)[1].

The Na^+-Ca^{2+} exchanger is a secondary active membrane transport mechanism that depends on the Na^+ trans-membrane gradient. NCX is reversible, with a stoichiometry of three Na^+ ions to one Ca^{2+} ion that produces an ionic current (I_{NCX}). Na^+-Ca^{2+} exchanger can extrude Ca^{2+} (as an inward I_{NCX}) or bring Ca^{2+} into the cell (as outward I_{NCX}). In normal myocytes, under physiological conditions NCX works almost exclusively in the Ca^{2+} extrusion mode, driven mostly by the high subsarcolemmal Ca^{2+} transient (forward mode). However, in pathological conditions, when the intracellular Na^+ concentration ($[Na^+]_i$) is elevated, NCX can increase greatly the amount of Ca^{2+} influx by working in reverse mode[3].

SERCA2a is a Ca^{2+}-ATPase (1ATP:2Ca^{2+}) that serves a dual function: 1) to cause muscle relaxation by lowering $[Ca^{2+}]_i$ and 2) to restore SR Ca^{2+} load necessary for muscle contraction.

1.2. Phospholamban-SERCA2a interaction

SERCA2a enzymatic activity is controlled by the inhibitory peptide phospholamban (PLN). In its dephosphorylated form, PLN inhibits SERCA2a activity by lowering its affinity for Ca^{2+}. Phosphorylation of PLN alters the PLN-SERCA2a interaction, relieving Ca^{2+}-pump inhibition and enhancing cardiac relaxation (lusitropic effect) and contractility (inotropic effect)[4].

Ca^{2+} and ATP bind independently, forming $E_1.2Ca^{2+}$ and $E_1.ATP.2Ca^{2+}$ conformations in the Ca^{2+}-binding stage; $E_1P.(Ca^{2+})_2$, the high-energy phosphoenzyme conformation, is formed in the phosphorylation (occlusion) stage; E_2P, the low-energy phosphoenzyme, is formed during the stage of Ca^{2+} release to the lumen; and E_2 is formed after hydrolysis of the acyl phosphate and release of inorganic phosphate (Fig. 3).

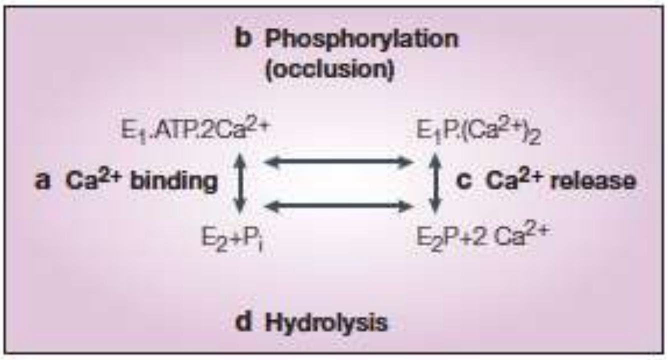

Figure 3: **Cycle of Ca^{2+} transport catalyzed by SERCA2a**. [According to MacLennan and Kranias, 2003].

PLN asserts its inhibitory effect by binding to SERCA2a in its E_2 conformation and prolonging the time that SERCA2a spends in this conformation. The phosphorylation of PLN and the Ca^{2+} binding to SERCA2a are driving forces for the progression from the E_2 to the $E_1.2Ca^{2+}$ state thereby dissociating the PLN–SERCA2a heterodimer[5].

PLN has been proposed to contain 2 major domains: a cytosolic domain, containing the phosphorylable sites (Ser^{10}, Ser^{16} and Thr^{17}), and a hydrophobic C-terminal domain, anchored in the SR membrane[6].

The current modeling of PLN indicates a dynamic equilibrium between monomeric and oligomeric states. In the dephosphorylated form, a substantial fraction of PLN monomers exists, and this has been proposed to be the active species of PLN that binds SERCA2a and inhibits it. On phosphorylation, PLN appears to form mainly pentamers, which are inactive or at least less active than the monomeric unit[7] (Fig. 4).

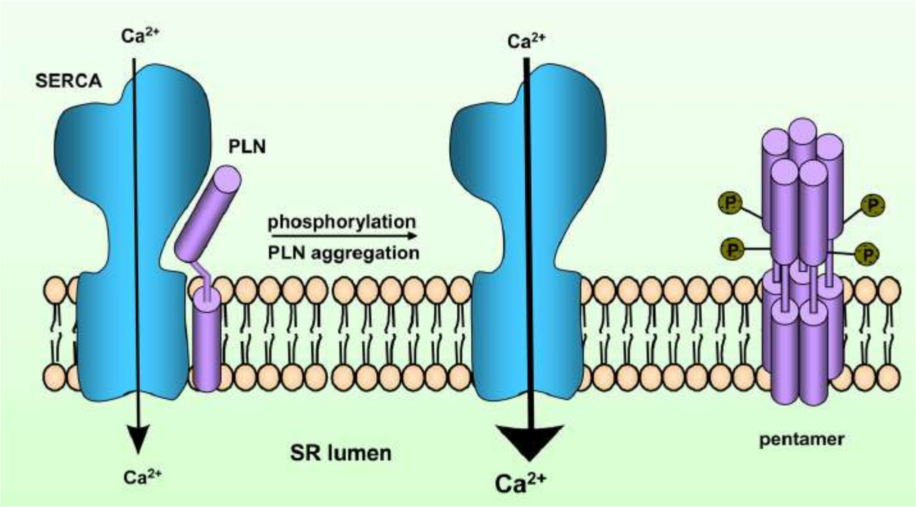

Figure 4: **Regulatory features of the PLN-SERCA2a interaction.** [According to Kranias and Hajjar, 2012].

1.3. Distribution of SERCA isoforms in mammalian tissues

The SERCA pump is a 110-kDa transmembrane protein that has been identified both in prokaryotes and eukaryotes. In vertebrates there are three distinct homologous genes (ATP2A1, ATP2A2, ATP2A3) encoding SERCA 1, 2, and 3 that are known to produce more than 10 isoforms, mainly through alternative splicing[8]. SERCA1 is expressed in fast-twitch skeletal muscle and is alternatively spliced to encode SERCA1a (adult) and 1b (fetal)[9]. SERCA2 encodes SERCA2a which is expressed predominantly in cardiac and slow-twitch skeletal muscle[10]. SERCA2b is expressed in all tissues at low levels including muscle and non-muscle cells[11]. Recently, a third isoform, SERCA2c, has been reported in cardiac muscle[12]. SERCA3 isoforms are expressed in several non-muscle tissues but appear to be a minor form in muscle. In humans, SERCA3 is known to encode for six isoforms, 3a–3f at the mRNA level expressed in multiple tissues and cell types. At the protein level there are data only for the 3a, b, and c isoforms. SERCA3 isoforms are expressed at high levels in the hematopoietic cell lineages, platelets, epithelial cells, fibroblasts, and endothelial cells[13].

The different isoforms of SERCA are inhibited by the binding of different small transmembrane micropeptides, which in general lower the affinity of SERCA for Ca^{2+} and decrease the rate of Ca^{2+} reuptake into the sarcoplasmic reticulum (SR)[14]. In the heart, PLN primarily and sarcolipin (SLN) inhibit the activity of SERCA2a and function as important regulators of cardiac contractility and disease[4]. Moreover, other two micropeptides are identified that directly bind SERCA in muscle, myoregulin (MLN) and dwarf open reading frame (DWORF)[15,16]. Finally, endoregulin (ELN) and another-regulin (ALN), function as direct inhibitors of SERCA pump activity in non-muscle cell types[14] (Fig. 5). Despite the conserved mechanism for the control of intracellular Ca^{2+} dynamics in both muscle and non-muscle cell types, the specific coupling between the several SERCA isoforms and their inhibitors provides a potential therapeutic approach to design drugs that would disrupt this interaction selectively.

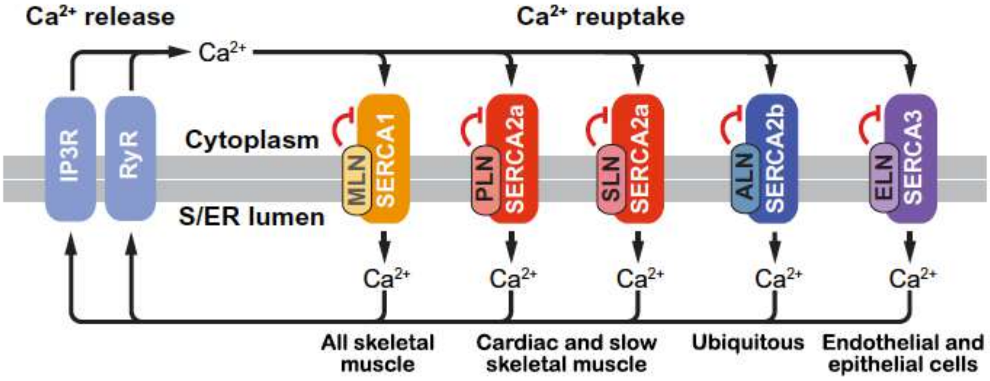

Figure 5: A family of SERCA-inhibiting micropeptides. Model depicting the expression patterns of the predominant SERCA and micropeptide inhibitors across different muscle and non-muscle tissues in vertebrates. [According to Anderson et al., 2016].

1.4. Physiological role of SERCA2a-PLN heterodimer in β-adrenergic stimulation

Cardiac function is regulated on a beat-to-beat basis through the sympathetic nervous system. When the demand arises, the heart can respond to stress and increase blood flow to peripheral tissues within seconds. Adrenaline and other β-agonist initiate an important signal-transduction pathway in the heart by binding to and activating β-adrenergic receptors in the cell membrane. PLN is a key regulator of cardiac function and a prominent mediator of the β-adrenergic effects in the myocardium.

In vitro studies have shown that PLN can be phosphorylated at Ser^{16} by cAMP-dependent protein kinase (PKA), and at Thr^{17} by Ca^{2+}-calmodulin-dependent protein kinase (CaMKII) in cardiac myocytes and perfused hearts[17].

The effect of β-agonist stimulation on PLN phosphorylation is mainly associated with activation of the cAMP-dependent signaling pathway. Stimulation of adenylate cyclase and the consequent increase of cAMP lead to phosphorylation of Ser^{16} in PLN via PKA[17]. Stimulation of β-receptors also elevates intracellular Ca^{2+}, which is expected to contribute to phosphorylation of Thr^{17} in PLN via CaMKII[17]. Thus, PKA-dependent phosphorylation of Ser^{16} in PLN plays a dominant role in mediating the cardiac contractile responses to β-agonists. In particular, by PLN phosphorylation, PKA mediates a lusitropic effect, speeding up SR Ca^{2+} re-uptake.

1.5. SERCA2a binding partners

Although PLN has proven to be a major regulator of SERCA2a activity, SERCA2a has been found to interact with several proteins of the SR lumen, i.e. the histidine-rich Ca-binding (HRC) protein, the small ubiquitin-like modifier type 1 (SUMO1) and S100A1. In addition, PLN activity is regulated by the HS-1 associated protein X-1 (HAX-1), the inhibitor-1 (I-1) of protein phosphatase 1 (PP1) and the small heat shock protein 20 (HSP20), which affect the overall SERCA-mediated Ca-transport[18] (Fig. 6).

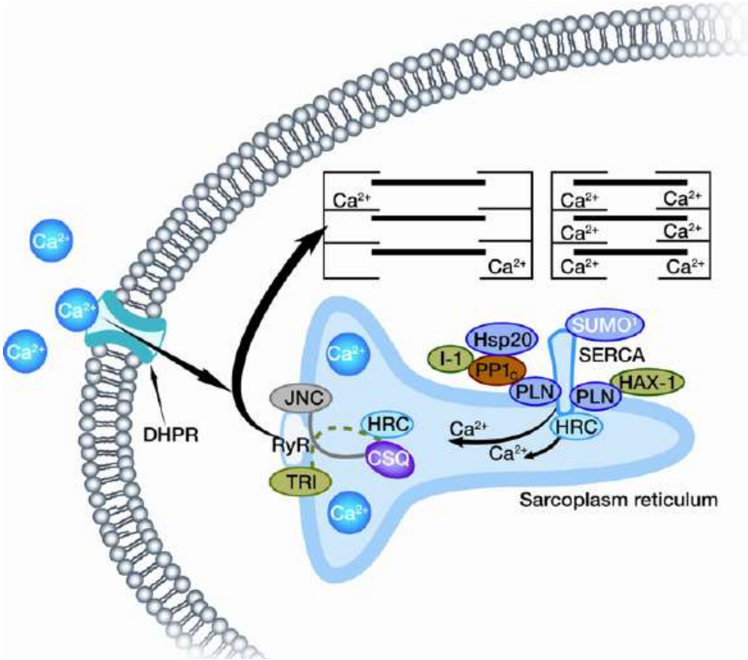

Figure 6: Regulation of SR Ca-transport by a multimeric protein complex. SERCA2a activity is regulated by its reversible inhibitor PLN, SUMO, and the histidine rich Ca-binding protein (HRC). Phosphorylation of PLN is mediated by cAMP-dependent or Ca-CAM–dependent PKs and dephosphorylation occurs by protein phosphatase 1 (PP1). The activity of PP1 is regulated by inhibitor-1 (I-1). [According to Kranias and Hajjar, 2012].

1.5.1. Histidine-rich Ca-binding (HRC) protein

HRC is a cardiac SR component that binds to triadin. Triadin together with the junctin is required to physically link the RyR2 and calsequestrin (CASQ2) proteins. HRC binds directly to SERCA2a and triadin through different domains and it may regulate both SR Ca^{2+}-sequestration and Ca^{2+}-release. In particular, the amount of HCR binding to triadin or SERCA2a depends on the SR Ca^{2+} concentration. Thus, HRC may serve as a nodal point bridging these two key Ca^{2+}-processes in the SR[19]. However, the functional significance of these interactions under physiological and pathophysiological conditions remains to be determined.

1.5.2. Small ubiquitin-like modifier type 1 (SUMO1) protein

SUMO1 is a peptide that alter the levels and the activity of SERCA2a in cardiomyocytes through a posttranslational modification described as SUMOylation. SUMOylation is a process where SUMO peptides can be conjugated to lysine residues of target proteins and is involved in many cellular processes. SERCA2a is SUMOylated at lysines 480 and 585 and that this SUMOylation is essential for preserving SERCA2a ATPase activity and stability in mouse and human cells. The reduction in SUMOylation correlates with reduced ATPase activity and decreased SERCA2a stability[20].

1.5.3. S100A1 protein

S100A1 is a small protein that contains two distinct EF-hands, responsible for Ca^{2+}-binding. S100A1 represents a potent molecular chaperone that protect the client proteins against irreversible damage during heat shock[21]. However, it is reported that S100A1 interacts with SERCA2a and PLN by the C-terminal part[22]. The central hinge region of S100A1 exhibits a conformational change upon Ca^{2+}-binding allowing the S100A1 interaction with SERCA2a-PLN heterodimer resulting in a regulation of cytosolic Ca^{2+} sequestration into the SR[22].

1.5.4. HS-1 associated protein X-1 (HAX1)

The HAX-1 is a ubiquitously expressed protein that was originally identified as an intracellular anti-apoptotic factor. In cardiomyocytes, HAX-1 binds independently to monomeric PLN and to SERCA. Binding of HAX-1 to PLN monomers induces depolymerization of PLN, while simultaneous binding of HAX-1 to PLN and SERCA in a ternary complex stabilizes the PLN-SERCA interaction. On the contrary, PKA phosphorylation of PLN abolishes the inhibition of HAX-1[23].

1.5.5. The inhibitor-1 (I-1) of protein phosphatase 1 (PP1)

PP1 is the major phosphatase dephosphorylating PLN and, at the level of the cardiac SR, is endogenous inhibitor is I-1. On stimulation of the β-adrenergic axis, PKA phosphorylates I-1, resulting in PP1 inhibition and allowing an increase in the SERCA2a activity. On the contrary, inactivation of I-1 occurs by dephosphorylation of Thr^{35} by PP2A and PP2B, leading to relief of PP1 inhibition and to decrease SR Ca^{2+} cycling[24,25].

1.5.6. Heat shock protein 20 (Hsp20)

Hsp20 is a small heat shock protein expressed in the heart that has the consensus motif (RRAS) for PKA-dependent phosphorylation at its Ser^{16} site. The Hsp20 expression and phosphorylation is increased on sustained β-adrenergic signaling in cardiomyocytes. The small Hsp20 is able to inhibit the PP1 leading to augmented PLN phosphorilation and consequently to amplified SR Ca^{2+} cycling by SERCA2a increased activity[26].

1.6. SERCA2a in heart failure

Heart failure (HF), the leading cause of human morbidity and mortality with estimated 550,000 new cases annually, is an inotropic abnormality, resulting in diminished systolic emptying (systolic dysfunction), and a compliance abnormality in which the ability of the ventricles to suck blood from the venous system is impaired (diastolic dysfunction). This, in turn, causes a reduction in the amount of blood available for systolic contraction (impairment of left ventricle (LV) filling)[27].

Common causes of HF include myocardial infarction, hypertension, atrial fibrillation, valvular diseases, alcohol abuse, diabetes, obesity, infection and cardiomyopathy. The main consequences arising from HF are the electrophysiological alterations, which increase the propensity for cardiac arrhythmias, and ECG abnormalities, associated with severe contractile dysfunctions[27]. Current long-term therapy of HF is aimed at prevention of "myocardial remodeling" (e.g., beta-blockers, ACE inhibitors, and aldosterone antagonists), which is a chronic maladaptive response to reduced contractility that amplifies the initial damage and underlies disease evolution[27].

The major alteration that causes the contractile dysfunction is the reduction of Ca^{2+} transient amplitude, which is due to lower SR Ca^{2+} content. Three factors lower SR Ca^{2+} content (CaSR) in HF: 1) reduced SERCA2a function; 2) increased expression and function of NCX and 3) enhanced diastolic SR Ca^{2+} leak[3] (Fig. 7).

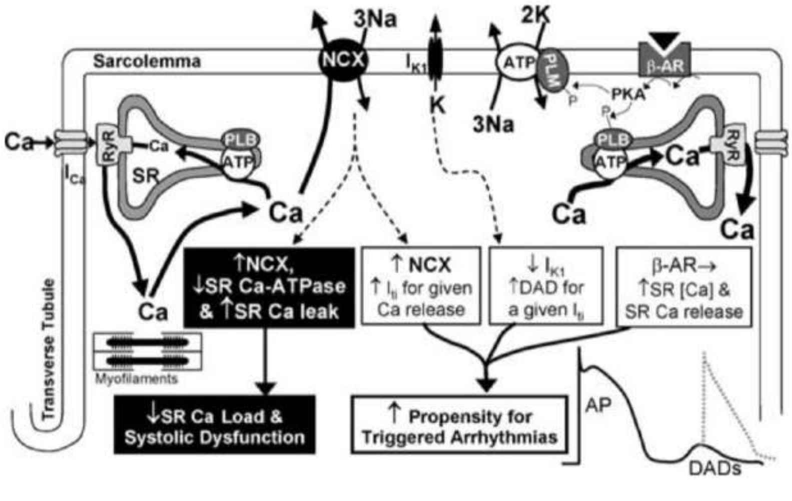

Figure 7: Heart Failure. Ca^{2+} entry via Ca^{2+} channel (I_{Ca}) activates SR Ca^{2+} release via RyRs, which activates the myofilaments and Ca^{2+} is cleared from the cytoplasm by SERCA2a and NCX. Three factors contribute to reduced SR Ca^{2+} load in HF (left in black), while enhanced NCX function, reduced I_{K1}, and residual adrenergic receptor (β-AR) responsiveness contribute

to arrhythmogenesis via induction of delayed afterdepolarizations (DADs). [According to Bers and Despa, 2006].

Most findings now indicate that the levels of PLN protein remain unchanged, whereas the levels of SERCA2a protein decrease in human HF[28,29]. A decrease in the level of SERCA2a relative to PLN would be expected to lead to an increased functional stoichiometry of PLN to SERCA2a, increased inhibition of the Ca^{2+} affinity of SERCA2a and prolonged relaxation time. In addition, the phosphorylation status of PLN at Ser^{16} and Thr^{17} is decreased[30], indicating that there is an increased inhibitory function by PLN. Indeed, alterations in the PLN:SERCA2a ratio and the degree of PLN phosphorylation might contribute to depressed SR Ca^{2+} uptake, leading to increased diastolic Ca^{2+} levels. Consequently, the SR Ca^{2+} store decreases and less Ca^{2+} is available for subsequent contractions. Reduced SERCA2a function also increases the energy cost of contraction because it requires a compensatory increase in Ca^{2+} extrusion through NCX, which is less energy efficient[31].

Substantial evidence indicates that normalization of SERCA2a function restores intracellular Ca^{2+} homeostasis and improves contractility and relaxation of cardiomyocytes and of the heart *in situ*[32,33]. Moreover, SERCA2a activation, because of improved Ca^{2+} sequestration, can also elevate the intra-SR threshold for the generation of pro-arrhythmic Ca^{2+} waves exerting a negative feedback on the Ca^{2+}-induced-Ca^{2+} release sustaining the waves[34].

To summarize, recovery of SERCA2a function in HF may improve cardiac relaxation and, possibly, contractility while minimizing arrhythmias, myocardial oxygen consumption, and myocyte death[31]. This highlights a need for “pure” or predominantly pure SERCA2a activators.

1.7. SERCA2a-PLN machinery as a therapeutic target for heart failure

Various therapeutic approaches that altering SERCA2a and/or PLN levels or activity to restore perturbed Ca^{2+} uptake into the SR have been recently investigated. Potential therapeutic strategies are to increase SERCA2a levels or to attenuate the PLN inhibitory effect on SERCA2a.

1.7.1. SERCA2a overexpression

A large number of experimental models of HF have demonstrated improved cardiac contractility after SERCA2a gene transfer[32,35]. Beyond their effects on enhancing contractility, SERCA2a gene transfer has been shown to restore the energetic state of the heart both in terms of energy supply and utilization, decrease ventricular arrhythmias, and enhance coronary flow through activation of the endothelial nitric oxide synthase (eNOS) in endothelial cells.

One of the most promising gene delivery platforms for cardiac gene therapy is based on adeno-associated virus (AAV) vectors that are small, non-pathogenic, non-enveloped, single-stranded DNA viruses[36]. AAV vectors effectively transfect dividing and non-dividing cells providing stable long term (up to a year) expression in most systems. One of the main advantages of AAV vectors for cardiac gene therapy is that a number of AAV serotypes display natural tropism for cardiomyocytes[37]. Moreover, AAV vectors evoke minimal immune response in humans and are not known to cause human disease[38]. In contrast to the near absence of a cellular immune response against AAVs, pre-existing neutralizing antibodies against the naturally occurring serotypes (presumably, a result of a prior infection with wild-type AAVs) rapidly emerged as a significant obstacle to the broad application of AAV gene therapy. In fact, more than half the patients (and up to 80% in certain regions such as Eastern Europe) present with high title of neutralizing antibodies, limiting uniform application of this vectors[39].

Nonetheless, these constraints and the comparably small DNA packaging capacity (≤5 kb) notwithstanding, AAVs are arguably the most promising vectors currently available for cardiac gene therapy and there are several ongoing clinical trials targeting HF (i.e. Calcium Upregulation by Percutaneous Administration of Gene Therapy in Cardiac Disease -CUPID- trial)[40].

In particular, Greenberg and collaborators designed the randomized, multinational, placebo-controlled, phase IIb CUPID 2 trial to assess the benefits and safety of gene therapy with AAV1/SERCA2a in patients with moderate-to-severe HF and reduced ejection fraction[39]. Unfortunately, in the CUPID 2 trial, infusion of AAV1/SERCA2a did not reduce recurrent HF events (primary end point) or terminal events (secondary end point) compared with placebo.

1.7.2. PLN inactivation

Other potential approaches to influence the PLN–SERCA2a complex might use techniques that decrease PLN levels or activity.

Primarily, Minamisawa team addressed the question of whether PLN alternations defect SR Ca^{2+} cycling in HF, by proposing a genetic complementation study[41]. In particular, double knockout mice, which harbor the muscle lim-protein (MLP) cardiomyopathic mutation, but also lack the PLN, were generated and subsequently examined to determine whether removing PLN inhibition alone would have a measurable effect on the progression of HF. Remarkably, PLN ablation prevented the appearance of HF phenotypes found in MLP-KO mice. Fifty-percent reduction of PLN is effective to significantly suppress the progression of HF in MLP-deficient mice, which validates this as a potential therapeutic target for HF. Nevertheless, it remained unclear whether PLN inhibition would prove therapeutically efficient after the onset of cardiomyopathy and whether this effect would carry a long-term benefit over several months of inhibition.

Overexpression of the PLN dominant-negative (DN) mutants was considered an approach to increase the SERCA2a activity and to rescue HF in animal models with a long-term efficiency. In particular, Hoshijima et al. used a newly developed long-term cardiac gene transfer system with AAV vectors and a pseudo phosphorylated (S16E) mutant of PLN carried by an AAV vector[42]. The Ser^{16} amino acid residue of PLN peptide was substituted with Glu (S16E mutation) to mimic the conformational change in PLN after phosphorylation of this amino acid residue by PKA, obtaining a DN mutation. S16EPLN was delivered via a transcoronary *in vivo* system into BIO14.6 cardiomyopathic hamsters (well-characterized model of progressive HF), providing evidence that chronic enhancement of SR Ca^{2+} cycling promotes the improvement of progressive cardiac contractile dysfunction and providing a histological demonstration that cytopathic changes are suppressed by this treatment. Cardiac contractility and relaxation were augmented in the absence of adrenergic stimuli, which is analogous to the null phenotype of the PLN mutant mice. The chronic efficacy of S16EPLN treatment was further confirmed in post infarction rats[43].

Despite these promising results, there is no doubt that further long-term validation is required before clinical application could be considered. In particular safety and efficiency studies in large animals, including primates, may be necessary.

RNA interference (RNAi) has been investigated as a new treatment option of HF by locally induced RNAi. RNAi is a technique of sequence-specific, post-transcriptional gene silencing that utilizes double-stranded RNA that is homologous to the target gene[44]. Specifically, duplexes of 21-nucleotide small interfering RNAs (siRNAs) with a short 3ʿ-overhang modulate gene expression, even when used at very low concentrations (low nanomolar range) in cultured mammalian cells.

Watanabe and collaborators proposed a study where a PLN siRNA was used to suppress PLN gene expression[45]. Specifically, siRNA was introduced into cardiomyocytes through the use of the hemagglutinating virus of Japan (HVJ) envelope vector, an inactivated viral envelope protein in which the viral genome was completely excluded. Unfortunately, RNAi-mediated PLN suppression showed very low efficacy and stability even in vitro. Fundamental limitations of synthetic small interfering RNAs are their rapid degradation in plasma and target cells and the unsolved problem of achieving adequate transfer and targeting *in vivo*.

To overcome these limitations, Suckau et al. developed a method for gene delivery by AAV-based RNAi[46]. They combined the AAV9 vectors to a short hairpin RNA (shRNA) to obtain an AAV-based shRNA able to silence PLN in primary neonatal rat cardiomyocytes (NRCMs). The data provided the evidence that cardiac rAAV9-based shRNA production remains stable for a period of time sufficient for long-term improvement of cardiac function and possibly also survival in HF.

The possible side effect of RNAi therapy is related to the fact that shRNAs mediate therapeutic effects by mimicking the endogenous process, thus they may disturb cellular miRNA pathways and thereby cause hepatotoxicity[47]. However, by using a cardiotropic AAV9 serotype with low affinity for the liver, no histological evidences of acute or chronic liver damage are observed[46]. Moreover, because malignant arrhythmias and hypertrophy are important complications in HF, respectively deregulation of miRNA-1[48] or miRNA-133[49], by a novel treatment should be considered as a possibly serious adverse effect. Therefore, clarification of the mechanism by which shPLN-RNAi is linked to miRNA-1/133 requires future studies.

An alternative approach to modify PLN–SERCA interaction used antibodies directed against PLN[50]. These antibodies bind to the cytoplasmic portion of PLN and thereby enhance SERCA function in vitro. However, these antibodies can only be used in isolated SR vesicles and are impracticable for in vivo therapeutic use. One way to overcome this limitation is to express an antibody or an antibody-derived protein targeting PLN in the cardiac myocyte.

In 2005, Dieterle and collaborators generated a recombinant single chain antibody, developed from avian heavy and light chain IgY chains, that specifically targets the cytoplasmic portion of PLN named PLN-antibody derived protein (PLADP)[51]. It was shown that protein–protein interactions alteration induced a beneficial effect in cardiomyocytes of the BIO14.6 hamster. However longer-term studies will be needed to assess the potential of this approach as a future therapy to improve cardiac function in HF.

More recently, a small molecule (pyridone derivative) inhibiting PLN has been also described[52]. Although further improvement of the in vitro activity and pharmacokinetic properties are required to obtain a compound with clinical benefits.

1.8. PLN mutations

The excitement generated by these studies has been tempered by the discovery in human mutations on PLN, leading to PLN-null genotype in homozygous individuals with a phenotype of dilated cardiomyopathy[31,53–55].

Several mutations have been identified in the PLN gene in HF patients.

The first mutation was V49G (valine to glycine), which resulted in potent inhibition of the Ca^{2+} affinity of SERCA2a. Cardiac overexpression of the V49G mutant PLN in mouse led to super-inhibition of cardiac contractility and remodeling, which progressed to dilated cardiomyopathy (DCM) and early mortality[56].

The second mutation identified in the PLN gene was an arginine to cysteine missense mutation at codon 9 (R9C). PLN^{R9C} is constitutively active and produces chronic SERCA2a inhibition, leading to autosomal dominant DCM in a large American family[53].

Another mutation involved the conversion of leucine at position 39 to a premature stop codon (L39stop). This PLN mutation was identified in two large Greek families with hereditary HF[54]. The heterozygous individuals exhibited hypertrophy without diminished contractile performance. Individuals homozygous for L39stop developed DCM and HF, requiring cardiac transplantation at ages 16 and 27. Thus, in contrast to reported benefits of PLN ablation in different animal models of HF, humans lacking PLN develop lethal DCM. These findings describe a naturally occurring loss-of-function human PLN mutation (PLN null).

The fourth PLN mutation was a deletion of amino acid 14 (R14del) and was first described in a large Greek family with hereditary HF[55]. No homozygous individuals were identified. By middle age, heterozygous individuals developed left ventricular dilation, contractile dysfunction, and episodic ventricular arrhythmias, with overt HF in some cases. Interestingly, a larger cohort has been identified in the Netherlands, where R14del carriers are at high risk for malignant ventricular arrhythmias and end-stage HF[57]. The R14del mutation results in super-inhibition of SERCA2a, which is irreversible. Inhibition of calcium transport and, consequently, cardiac function over years may lead to DCM and premature death in humans.

Recently, a new mutation (R25C) in the coding region of the human PLN gene has also been identified, in a pedigree with DCM that also showed prominent ventricular arrhythmia and need for implantable cardiac defibrillators (ICDs)[58]. The mutation enhanced interaction of R25C-PLN mutant with SERCA2a, leading to super-inhibition of SERCA2a activity.

Thus, these latter developments (i.e. the discovering of PLN-null lethal mutations) raise doubts about using PLN ablation as a universal approach to treat all forms of HF.

1.9. Istaroxime affecting directly SERCA2a function

Istaroxime [(*E*,*Z*)-3-((2-aminoethoxy)imino) androstane-6,17-dione hydrochloride)] or PST2744 (Fig. 8) is a new small-molecule drug under clinical development for the treatment of HF. Istaroxime is characterized by a double mechanism of action inhibiting Na^+-K^+ ATPase[59] while stimulating SERCA2a[60].

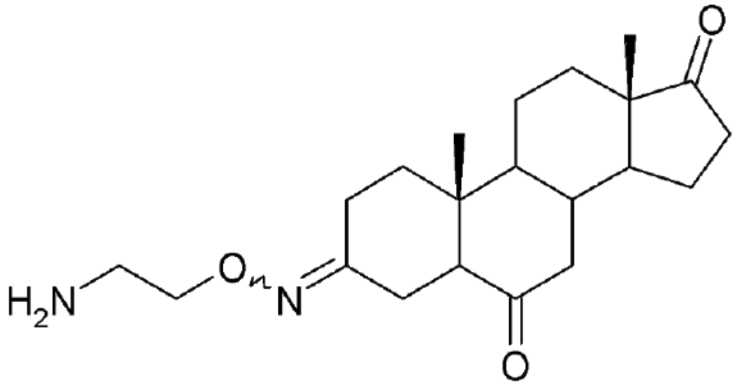

Figure 8: Chemical structure of istaroxime

At the same level of inotropy, the proarrhythmic effect of istaroxime is considerably lower than that of Digoxin, which is a pure Na^+/K^+ pump inhibitor[61]. This suggests that by improving Ca^{2+} clearance from the cytosol[62], SERCA2a stimulation may also minimize the proarrhythmic effect of Na^+/K^+ pump blockade[61] while preserving its inotropic effect. The reduction of the proarrhythmic effect by istaroxime has been confirmed in clinical studies[63].

Istaroxime mechanism has been investigated in cardiac SERCA2a-enriched preparations or in dog kidney purified Na^+-K^+ ATPase[59] and in isolated cardiac myocytes[64]. Istaroxime efficacy in stimulating SERCA2a activity has been demonstrated in healthy and failing guinea pig and human SR heart preparations. Notably, in failing preparations, where the SERCA2a activity is reduced compared with healthy hearts, istaroxime reactivates SERCA2a approaching normal levels[65]. In isolated guinea pig[60] and mouse cardiac myocytes[62], istaroxime stimulates twitch amplitude and relaxation by increasing Ca^{2+} transients and accelerating Ca^{2+} re-uptake into SR through SERCA2a. istaroxime accelerates Ca^{2+} re-uptake into SR through SERCA2a by displacing the interaction between SERCA2a and PLN[66] (Fig. 9).

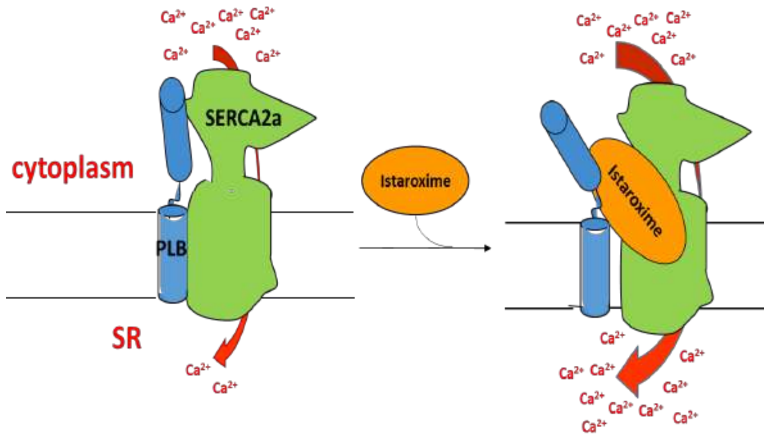

Figure 9: Molecular mechanism of SERCA2a stimulation by istaroxime. [According to Ferrandi et al., 2013].

Despite its favorable activity in the treatment of heart failure, istaroxime is not completely devoid of drawbacks. The aminoethoxyimino moiety of the molecule undergoes to metabolic transformation which can lead to possible genotoxicity. Further, istaroxime is active only by intravenous administration, therefore, it can be administered only in hospitals and related environments. Istaroxime administration requires well-trained medical personnel and is not suitable for chronic therapy. Moreover, Na^+/K^+ ATPase inhibition increases the risk of arrhythmias.

Accordingly, there is a long-felt need for a compound with the ability to activate SERCA2a (lusitropic effect) without significantly inhibiting the Na^+/K^+ ATPase to improve heart function without increasing the risk of arrhythmias and to administer preferably by oral route.

1.10. Aim of the study

Diabetes affects globally more than 300 million people and type 1 diabetes (T1D) accounts for up to 10% of cases[67]. HF is the predominant cardiovascular complication of diabetes and represents the leading cause of morbidity and mortality[68]. Diabetic cardiomyopathy (DCM) is a complex and multifactorial disease characterized by an early onset of diastolic dysfunction, which precedes the development of systolic impairment[69]. The molecular and pathophysiological mechanisms underlying diabetes include abnormalities in the regulation of Ca^{2+} homeostasis in cardiomyocytes and the consequent alteration of ventricular EC- coupling[1]. In the diabetic heart, a dysregulation of Ca^{2+} cycling includes a reduction of SERCA2a activity, which may be accompanied by a decreased SERCA2a protein expression[70]. In most diabetic models, PLN expression level appears increased while its phosphorylation state is impaired, thus contributing to the inhibition of SERCA2a function[71]. This defect generates an impairment of SR Ca^{2+} refilling that results in slow diastolic relaxation, reduction of Ca^{2+} sequestered into the SR after each contraction and decreased amplitude of the subsequent systolic contraction[1].

Hence, the defect of SR Ca^{2+} loading through SERCA2a represents a molecular target for a pharmacological intervention aimed at increasing the mechanical function and the energetic efficiency of the diabetic heart. In this contest, istaroxime is the first-in-class original luso-inotropic agent targeting SERCA2a, shown to be highly effective and safe in patients[72].

The aim of the study is to characterize istaroxime effects in a rat model of T1D (streptozotocin-induced) with diastolic dysfunction and preserved global systolic function. SERCA-dependent istaroxime effects will be evaluated by testing istaroxime at concentrations marginally affecting Na^+/K^+ ATPase. In this contest, istaroxime 'acting like a pure SERCA2a stimulator' might afford a lusitropic effect with reduced arrhythmogenic risk, elevating the intra-SR threshold for the generation of Ca^{2+} waves.

1.11 References

1. Bers DM. Cardiac excitation contraction coupling. *Nature* 2002;**415**:198–215.

2. Nerbonne JM, Kass RS. Molecular physiology of cardiac repolarization. *Physiol Rev* 2005;**85**:1205–1253.

3. Bers DM, Despa S, Bossuyt J. Regulation of Ca2+ and Na+ in normal and failing cardiac myocytes. *Ann N Y Acad Sci* 2006;**1080**:165–177.

4. MacLennan DH, Kranias EG. Phospholamban: A crucial regulator of cardiac contractility. *Nat Rev Mol Cell Biol* 2003;**4**:566–577.

5. Toyoshima C, Asahi M, Sugita Y, Khanna R, Tsuda T, MacLennan DH. Modeling of the inhibitory interaction of phospholamban with the Ca2+ ATPase. *Proc Natl Acad Sci U S A* 2003;**100**:467–472.

6. MaClennan DH, Kimura Y, Toyofuku T. Sites of regulatory interaction between calcium ATPases and phospholamban. *Ann N Y Acad Sci* 1998;**853**:31–42.

7. Simmerman HKB, Jones LR. Phospholamban: Protein structure, mechanism of action, and role in cardiac function. *Physiol Rev* 1998;**78**:921–947.

8. Periasamy M, Kalyanasundaram A. SERCA pump isoforms: Their role in calcium transport and disease. *Muscle and Nerve* 2007;**35**:430–442.

9. Brandl CJ, DeLeon S, Martin DR, MacLennan DH. Adult forms of the Ca2+ATPase of sarcoplasmic reticulum. Expression in developing skeletal muscle. *J Biol Chem* 1987;**262**:3768–3774.

10. MacLennan DH, Brandl CJ, Korczak B, Green NM. Amino-acid sequence of a Ca2+ + Mg2+ -dependent ATPase from rabbit muscle sarcoplasmic reticulum, deduced from its complementary DNA sequence. *Nature* 1985;**316**:696–700.

11. Gunteski-Hamblin AM, Greeb J, Shull GE. A novel Ca2+ pump expressed in brain, kidney, and stomach is encoded by an alternative transcript of the slow-twitch muscle sarcoplasmic reticulum Ca-ATPase gene. *J Biol Chem* 1988;**263**:15032–15040.

12. Dally S, Bredoux R, Corvazier E, Andersen JP, Clausen JD, Dode L, Fanchaouy M, Gelebart P, Monceau V, Monte F Del, Gwathmey JK, Hajjar R, Chaabane C,

Bobe R, Raies A, Enouf J. Ca2+-ATPases in non-failing and failing heart: Evidence for a novel cardiac sarco/endoplasmic reticulum Ca2+-ATPase 2 isoform (SERCA2c). *Biochem J* 2006;**395**:249–258.

13. Anger M, Samuel JL, Marotte F, Wuytack F, Rappaport L, Lompré AM. The sarco(endo)plasmic reticulum Ca 2+ -ATPase mRNA isoform, SERCA 3, is expressed in endothelial and epithelial cells in various organs. *FEBS Lett* 1993;**334**:45–48.

14. Anderson DM, Makarewich CA, Anderson KM, Shelton JM, Bezprozvannaya S, Bassel-Duby R, Olson EN. Widespread control of calcium signaling by a family of SERCA-inhibiting micropeptides. *Sci Signal* 2016;**9**.

15. Anderson DM, Anderson KM, Chang CL, Makarewich CA, Nelson BR, McAnally JR, Kasaragod P, Shelton JM, Liou J, Bassel-Duby R, Olson EN. A micropeptide encoded by a putative long noncoding RNA regulates muscle performance. *Cell* 2015;**160**:595–606.

16. Nelson BR, Catherine A. Makarewich, Douglas M. Anderson, Benjamin R. Winders, Constantine D. Troupes FW, Reese AL, McAnally JR, Chen X, Kavalali ET, Cannon SC, Houser SR, Bassel-Duby R, Olson EN. A peptide encoded by a transcript annotated as long noncoding RNA enhances SERCA activity in muscle. *Science (80-)* 2016;**351**:271–275.

17. Chu G, Lester JW, Young KB, Luo W, Zhai J, Kranias EG. A single site (Ser16) phosphorylation in phospholamban is sufficient in mediating its maximal cardiac responses to β-agonists. *J Biol Chem* 2000;**275**:38938–38943.

18. Kranias EG, Hajjar RJ. Modulation of cardiac contractility by the phopholamban/SERCA2a regulatome. *Circ Res* 2012;**110**:1646–1660.

19. Arvanitis DA, Vafiadaki E, Sanoudou D, Kranias EG. Histidine-rich calcium binding protein: The new regulator of sarcoplasmic reticulum calcium cycling. *J Mol Cell Cardiol* 2011;**50**:43–49.

20. Kho C, Lee A, Jeong D, Oh JG, Chaanine AH, Kizana E, Park WJ, Hajjar RJ. SUMO1-dependent modulation of SERCA2a in heart failure. *Nature* Nature Publishing Group; 2011;**477**:601–606.

21. Heizmann CW, Fritz G, Schäfer BW. S100 proteins: structure, functions and pathology. *Front Biosci* 2002;**7**:1356–1368.

22. Kiewitz R, Acklin C, Schäfer BW, Maco B, Uhrík B, Wuytack F, Erne P, Heizmann CW. Ca2+-dependent interaction of S100A1 with the sarcoplasmic reticulum Ca2+-ATPase2a and phospholamban in the human heart. *Biochem Biophys Res Commun* 2003;**306**:550–557.

23. Zhao W, Waggoner JR, Zhang ZG, Lam CK, Han P, Qian J, Schroder PM, Mitton B, Kontrogianni-Konstantopoulos A, Robia SL, Kranias EG. The anti-apoptotic protein HAX-1 is a regulator of cardiac function. *Proc Natl Acad Sci U S A* 2009;**106**:20776–20781.

24. Pathak A, Monte F Del, Zhao W, Schultz J El, Lorenz JN, Bodi I, Weiser D, Hahn H, Carr AN, Syed F, Mavila N, Jha L, Qian J, Marreez Y, Chen G, McGraw DW, Heist EK, Guerrero JL, DePaoli-Roach AA, Hajjar RJ, Kranias EG. Enhancement of cardiac function and suppression of heart failure progression by inhibition of protein phosphatase. *Circ Res* 2005;**96**:756–766.

25. Nicolaou P, Rodriguez P, Ren X, Zhou X, Qian J, Sadayappan S, Mitton B, Pathak A, Robbins J, Hajjar RJ, Jones K, Kranias EG. Inducible Expression of Active Protein Phosphatase-1 Inhibitor-1 Enhances Basal Cardiac Function and Protects Against Ischemia/Reperfusion Injury. *Circ Res* 2009;**104**:1012–1020.

26. Qian J, Vafiadaki E, Florea SM, Singh VP, Song W, Lam CK, Wang Y, Yuan Q, Pritchard TJ, Cai W, Haghighi K, Rodriguez P, Wang HS, Sanoudou D, Fan GC, Kranias EG. Small heat shock protein 20 interacts with protein phosphatase-1 and enhances sarcoplasmic reticulum calcium cycling. *Circ Res* 2011;**108**:1429–1438.

27. Heineke J, Molkentin JD. Regulation of cardiac hypertrophy by intracellular signalling pathways. *Nat Rev Mol Cell Biol* 2006;**7**:589–600.

28. Meyer M, Schillinger W, Pieske B, Holubarsch C, Heilmann C, Posival H, Kuwajima G, Mikoshiba K, Just H, Hasenfuss G. Alterations of sarcoplasmic reticulum proteins in failing human dilated cardiomyopathy. *Circulation* 1995;**92**:778–784.

29. Hasenfuss G. Alterations of calcium-regulatory proteins in heart failure. *Cardiovasc Res* 1998;**37**:279–289.

30. Schwinger RHG, Münch G, Bölck B, Karczewski P, Krause EG, Erdmann E. Reduced Ca2+-sensitivity of SERCA 2a in failing human myocardium due to reduced serin-16 phospholamban phoshorylation. *J Mol Cell Cardiol* 1999;**31**:479–491.

31. Larissa Lipskaia, PhD, Elie R. Chemaly, MD, Lahouaria Hadri, PhD, Anne-Marie Lompre, PhD, and Roger J. Hajjar M. Sarcoplasmic reticulum Ca2+ ATPase as a therapeutic target for heart failure. *Expert Opin Biol Ther* 2010;**10**:29–41.

32. Byrne MJ, Power JM, Preovolos A, Mariani JA, Hajjar RJ, Kaye DM. Recirculating cardiac delivery of AAV2/1SERCA2a improves myocardial function in an experimental model of heart failure in large animals. *Gene Ther* 2008;**15**:1550–1557.

33. Sato Y, Kiriazis H, Yatani A, Schmidt AG, Hahn H, Ferguson DG, Sako H, Mitarai S, Honda R, Mesnard-Rouiller L, Frank KF, Beyermann B, Wu G, Fujimori K, Dorn GW, Kranias EG. Rescue of Contractile Parameters and Myocyte Hypertrophy in Calsequestrin Overexpressing Myocardium by Phospholamban Ablation. *J Biol Chem* 2001;**276**:9392–9399.

34. Fernandez-Tenorio M, Niggli E. Stabilization of Ca2+ signaling in cardiac muscle by stimulation of SERCA. *J Mol Cell Cardiol* Elsevier; 2018;**119**:87–95.

35. Sakata S, Lebeche D, Sakata Y, Sakata N, Chemaly ER, Liang LF, Nakajima-Takenaka C, Tsuji T, Konishi N, Monte F Del, Hajjar RJ, Takaki M. Transcoronary gene transfer of SERCA2a increases coronary blood flow and decreases cardiomyocyte size in a Type 2 diabetic rat model. *Am J Physiol - Hear Circ Physiol* 2007;**292**:1204–1207.

36. Gray SJ, Samulski RJ. Optimizing gene delivery vectors for the treatment of heart disease. Expert Opin. Biol. Ther. 2008.

37. Zincarelli C, Soltys S, Rengo G, Rabinowitz JE. Analysis of AAV serotypes 1-9 mediated gene expression and tropism in mice after systemic injection. *Mol Ther* The American Society of Gene Therapy; 2008;**16**:1073–1080.

38. Jessup M, Greenberg B, Mancini D, Cappola T, Pauly DF, Jaski B, Yaroshinsky A, Zsebo KM, Dittrich H, Hajjar RJ. Calcium upregulation by percutaneous

administration of gene therapy in cardiac disease (CUPID): A phase 2 trial of intracoronary gene therapy of sarcoplasmic reticulum Ca2+-ATPase in patients with advanced heart failure. *Circulation* 2011;**124**:304–313.

39. Greenberg B, Butler J, Felker GM, Ponikowski P, Voors AA, Desai AS, Barnard D, Bouchard A, Jaski B, Lyon AR, Pogoda JM, Rudy JJ, Zsebo KM. Calcium upregulation by percutaneous administration of gene therapy in patients with cardiac disease (CUPID 2): A randomised, multinational, double-blind, placebo-controlled, phase 2b trial. *Lancet* 2016;**387**:1178–1186.

40. Jaski BE, Jessup ML, Mancini DM, Cappola TP, Pauly DF, Greenberg B, Borow K, Dittrich H, Zsebo KM, Hajjar RJ. Calcium Upregulation by Percutaneous Administration of Gene Therapy in Cardiac Disease (CUPID Trial), a First-in-Human Phase 1/2 Clinical Trial. *J Card Fail* Elsevier Inc; 2009;**15**:171–181.

41. Minamisawa S, Hoshijima M, Chu G, Ward CA, Frank K, Gu Y, Martone ME, Wang Y, Ross J, Kranias EG, Giles WR, Chien KR. Chronic phospholamban-sarcoplasmic reticulum calcium atpase interaction is the critical calcium cycling defect in dilated cardiomyopathy. *Cell* 1999;**99**:313–322.

42. Hoshijima M, Ikeda Y, Iwanaga Y, Minamisawa S, Date MO, Gu Y, Iwatate M, Li M, Wang L, Wilson JM, Wang Y, Ross J, Chien KR. Chronic suppression of heart-failure progression by a pseudophosphorylated mutant of phospholamban via in vivo cardiac rAAV gene delivery. *Nat Med* 2002;**8**:864–871.

43. Iwanaga Y, Hoshijima M, Gu Y, Iwatate M, Dieterle T, Ikeda Y, Date MO, Chrast J, Matsuzaki M, Peterson KL, Chien KR, Ross J. Chronic phospholamban inhibition prevents progressive cardiac dysfunction and pathological remodeling after infarction in rats. *J Clin Invest* 2004;**113**:727–736.

44. Fire A, Xu S, Montgomery MK, Kostas SA, Driver SE, Mello CC. 35888. *Nature* 1998;**391**:806–811.

45. Watanabe A, Arai M, Yamazaki M, Koitabashi N, Wuytack F, Kurabayashi M. Phospholamban ablation by RNA interference increases Ca2+uptake into rat cardiac myocyte sarcoplasmic reticulum. *J Mol Cell Cardiol* 2004;**37**:691–698.

46. Suckau L, Fechner H, Chemaly E, Krohn S, Hadri L, Kockskamper J, Westermann D, Bisping E, Ly H, Wang X, Kawase Y, Chen J, Liang L, Sipo I,

Vetter R, Weger S, Kurreck J, Erdmann V, Tschope C, Pieske B, Lebeche D, Schultheiss HP, Hajjar RJ, Poller WC. Long-term cardiac-targeted RNA interference for the treatment of heart failure restores cardiac function and reduces pathological hypertrophy. *Circulation* 2009;**119**:1241–1252.

47. Grimm D, Streetz KL, Jopling CL, Storm TA, Pandey K, Davis CR, Marion P, Salazar F, Kay MA. Fatality in mice due to oversaturation of cellular microRNA/short hairpin RNA pathways. *Nature* 2006;**441**:537–541.

48. Yang B, Lin H, Xiao J, Lu Y, Luo X, Li B, Zhang Y, Xu C, Bai Y, Wang H, Chen G, Wang Z. The muscle-specific microRNA miR-1 regulates cardiac arrhythmogenic potential by targeting GJA1 and KCNJ2. *Nat Med* 2007;**13**:486–491.

49. Carè A, Catalucci D, Felicetti F, Bonci D, Addario A, Gallo P, Bang ML, Segnalini P, Gu Y, Dalton ND, Elia L, Latronico MVG, Høydal M, Autore C, Russo MA, Dorn GW, Ellingsen Ø, Ruiz-Lozano P, Peterson KL, Croce CM, Peschle C, Condorelli G. MicroRNA-133 controls cardiac hypertrophy. *Nat Med* 2007;**13**:613–618.

50. Suzuki T, Wang JH. Stimulation of bovine cardiac sarcoplasmic reticulum Ca2+ pump and blocking of phospholamban phosphorylation and dephosphorylation by a phospholamban monoclonal antibody. *J Biol Chem* 1986;**261**:7018–7023.

51. Dieterle T, Meyer M, Gu Y, Belke DD, Swanson E, Iwatate M, Hollander J, Peterson KL, Ross J, Dillmann WH. Gene transfer of a phospholamban-targeted antibody improves calcium handling and cardiac function in heart failure. *Cardiovasc Res* 2005;**67**:678–688.

52. Kaneko M, Yamamoto H, Sakai H, Kamada Y, Tanaka T, Fujiwara S, Yamamoto S, Takahagi H, Igawa H, Kasai S, Noda M, Inui M, Nishimoto T. A pyridone derivative activates SERCA2a by attenuating the inhibitory effect of phospholamban. *Eur J Pharmacol* 2017;**814**:1–8.

53. Schmitt JP, Kamisago M, Asahi M, Hua Li G, Ahmad F, Mende U, Kranias EG, MacLennan DH, Seidman JG, Seidman CE. Dilated cardiomyopathy and heart failure caused by a mutation in phospholamban. *Science (80-)* 2003;**299**:1410–1413.

54. Haghighi K, Kolokathis F, Pater L, Lynch RA, Asahi M, Gramolini AO, Fan GC, Tsiapras D, Hahn HS, Adamopoulos S, Liggett SB, Dorn GW, MacLennan DH, Kremastinos DT, Kranias EG. Human phospholamban null results in lethal dilated cardiomyopathy revealing a critical difference between mouse and human. *J Clin Invest* 2003;**111**:869–876.

55. Haghighi K, Kolokathis F, Gramolini AO, Waggoner JR, Pater L, Lynch RA, Fan GC, Tsiapras D, Parekh RR, Dorn GW, MacLennan DH, Kremastinos DT, Kranias EG. A mutation in the human phospholamban gene, deleting arginine 14, results in lethal, hereditary cardiomyopathy. *Proc Natl Acad Sci U S A* 2006;**103**:1388–1393.

56. Haghighi K, Schmidt AG, Hoit BD, Brittsan AG, Yatani A, Lester JW, Zhai J, Kimura Y, Dorn GW, MacLennan DH, Kranias EG. Superinhibition of Sarcoplasmic Reticulum Function by Phospholamban Induces Cardiac Contractile Failure. *J Biol Chem* 2001;**276**:24145–24152.

57. Hof IE, Heijden JF van der, Kranias EG, Sanoudou D, Boer RA de, Tintelen JP van, Zwaag PA van der, Doevendans PA. Prevalence and cardiac phenotype of patients with a phospholamban mutation. *Netherlands Hear J* 2019;**27**:64–69.

58. Liu GS, Morales A, Vafiadaki E, Lam CK, Cai WF, Haghighi K, Adly G, Hershberger RE, Kranias EG. A novel human R25C-phospholamban mutation is associated with super-inhibition of calcium cycling and ventricular arrhythmia. *Cardiovasc Res* 2015;**107**:164–174.

59. Micheletti R, Mattera GG, Rocchetti M, Schiavone A, Loi MF, Zaza A, Gagnol RJ, Munari S De, Melloni P, Carminati P, Bianchi G, Ferrari P. Pharmacological profile of the novel inotropic agent (E,Z)-3-((2-aminoethoxy)imino)androstane-6,17-dione hydrochloride (PST2744). *J Pharmacol Exp Ther* 2002;**303**:592–600.

60. Rocchetti M, Besana A, Mostacciuolo G, Micheletti R, Ferrari P, Sarkozi S, Szegedi C, Jona I, Zaza A. Modulation of sarcoplasmic reticulum function by Na+/K+ pump inhibitors with different toxicity: digoxin and PST2744 [(E,Z)-3-((2-aminoethoxy)imino)androstane-6,17-dione hydrochloride]. *J Pharmacol Exp Ther* 2005;**313**:207–215.

61. Rocchetti M, Besana A, Mostacciuolo G, Ferrari P, Micheletti R, Zaza A. Diverse

toxicity associated with cardiac Na+/K+ pump inhibition: evaluation of electrophysiological mechanisms. *J Pharmacol Exp Ther* 2003;**305**:765–771.

62. Alemanni M, Rocchetti M, Re D, Zaza A. Role and mechanism of subcellular Ca 2+ distribution in the action of two inotropic agents with different toxicity. *J Mol Cell Cardiol* Elsevier Ltd; 2011;**50**:910–918.

63. Gheorghiade M, Blair JEA, Filippatos GS, Macarie C, Ruzyllo W, Korewicki J, Bubenek-Turconi SI, Ceracchi M, Bianchetti M, Carminati P, Kremastinos D, Valentini G, Sabbah HN. Hemodynamic, Echocardiographic, and Neurohormonal Effects of Istaroxime, a Novel Intravenous Inotropic and Lusitropic Agent. A Randomized Controlled Trial in Patients Hospitalized With Heart Failure. *J Am Coll Cardiol* 2008;

64. Micheletti R, Palazzo F, Barassi P, Giacalone G, Ferrandi M, Schiavone A, Moro B, Parodi O, Ferrari P, Bianchi G. Istaroxime, a Stimulator of Sarcoplasmic Reticulum Calcium Adenosine Triphosphatase Isoform 2a Activity, as a Novel Therapeutic Approach to Heart Failure. *Am J Cardiol* 2007;**99**:24–32.

65. Rocchetti M, Alemanni M. sarcoplasmic reticulum function by PST2744 in a pressure-overload heart failure. *J Pharmacol Exp Ther* 2008;**326**:957–965.

66. Ferrandi M, Barassi P, Tadini-Buoninsegni F, Bartolommei G, Molinari I, Tripodi MG, Reina C, Moncelli MR, Bianchi G, Ferrari P. Istaroxime stimulates SERCA2a and accelerates calcium cycling in heart failure by relieving phospholamban inhibition. *Br J Pharmacol* 2013;**169**:1849–1861.

67. Silvio Inzucchi, MD; Richard Bergenstal MD; Vivian Fonseca, MD; Edward Gregg, PhD; Beth Mayer-Davis, MSPH, PhD RD; Geralyn Spollett, MSN, CDE, ANP; and Richard Wender M. Diagnosis and classification of diabetes mellitus. *Diabetes Care* 2009;**33**:S62–S69.

68. Jeong EM, Chung J, Liu H, Go Y, Gladstein S, Farzaneh-Far A, Lewandowski ED, Dudley SC. Role of Mitochondrial Oxidative Stress in Glucose Tolerance, Insulin Resistance, and Cardiac Diastolic Dysfunction. *J Am Heart Assoc* 2016;**5**:1–17.

69. Schannwell C.M. · Schneppenheim M. · Perings S. · Plehn G. · Strauer. Left Ventricular Diastolic Dysfunction as an Early Manifestation of Diabetic

Cardiomyopathy. *Cardiology* 2002;**98**:33–39.

70. Choi KM, Zhong Y, Hoit BD, Grupp IL, Hahn H, Dilly KW, Guatimosim S, Jonathan Lederer W, Matlib MA. Defective intracellular Ca2+ signaling contributes to cardiomyopathy in type 1 diabetic rats. *Am J Physiol - Hear Circ Physiol* 2002;

71. Vasanji Z, Dhalla NS, Netticadan T. Increased inhibition of SERCA2 by phospholamban in the type I diabetic heart. *Mol Cell Biochem* 2004;**261**:245–249.

72. Shah SJ, Blair JEA, Filippatos GS, MacArie C, Ruzyllo W, Korewicki J, Bubenek-Turconi SI, Ceracchi M, Bianchetti M, Carminati P, Kremastinos D, Grzybowski J, Valentini G, Sabbah HN, Gheorghiade M. Effects of istaroxime on diastolic stiffness in acute heart failure syndromes: Results from the Hemodynamic, Echocardiographic, and Neurohormonal Effects of Istaroxime, a Novel Intravenous Inotropic and Lusitropic Agent: A Randomized Controlled Trial in P. *Am Heart J* Mosby, Inc.; 2009;**157**:1035–1041.

Chapter 2

SERCA2a stimulation by istaroxime improves Ca^{2+} handling in a model of diabetic diastolic dysfunction

Eleonora Torre[1], Martina Arici[1], Alessandra Maria Lodrini[1], Mara Ferrandi[2], Paolo Barassi[2], Elisabetta Boz[3], Emanuela Sala[1], Sara Vagni[1], Claudia Altomare[4], Gaspare Mostacciuolo[1], Claudio Bussadori[3], Patrizia Ferrari[2], Giuseppe Bianchi[2], Marcella Rocchetti[1*].

[1]Department of Biotechnology and Biosciences, Università degli Studi di Milano-Bicocca, Milan, Italy.

[2]Windtree Therapeutics Inc., Warrington, Pennsylvania, USA.

[3]Clinica Veterinaria Gran Sasso, Milano, Italy.

[4]Fondazione Cardiocentro Ticino, Lugano, Switzerland.

*Corresponding Author

[Submitted, 6 Jen 2020, Cod: CARDIOVASCRES-S-20-00023]

2.1. Abstract

Aims

Diabetic cardiomyopathy is a multifactorial disease characterized by an early onset of diastolic dysfunction (DD), that precedes the development of systolic impairment. Mechanisms that can restore cardiac relaxation improving intracellular Ca^{2+} dynamics, represent a promising therapeutic approach for cardiovascular diseases associated to DD. Istaroxime is a Na^+/K^+ ATPase (NKA) inhibitor with the property of accelerating Ca^{2+} re-uptake into sarcoplasmic reticulum (SR) through the SR Ca^{2+} pump (SERCA2a) stimulation. The project aims to characterize istaroxime activity at a concentration mostly unaffecting NKA, in order to highlight its effects dependent on the stimulation of SERCA2a in a model of mild diabetes.

Methods and Results

Streptozotocin (STZ) treated diabetic rats were studied at 9 weeks after STZ injection in comparison to controls (CTR). SERCA2a-dependent istaroxime effects were evaluated in cell-free system and in isolated left ventricular myocytes. STZ animals showed marked DD, reduced SERCA2 protein level and activity and increased monomeric phospholamban (PLN)/SERCA2 ratio, implying that SERCA2 (mostly 2a isoform) was not only reduced but also much more inhibited in comparison to CTR. In STZ myocytes, SERCA2a downregulation caused 1) increased diastolic Ca^{2+}, 2) reduction in SR Ca^{2+} content and Ca^{2+} transient amplitude following control of membrane potential, 3) slower SR reloading process under Na^+/Ca^{2+} exchanger inhibition, 4) unchanged Ca^{2+} sparks rate. Action potentials (AP) were significantly prolonged, resulting in increased short-term variability (STV) of AP duration. Istaroxime (100 nM) significantly stimulated SERCA2a activity and reverted STZ-induced effects by 1) reducing diastolic Ca^{2+}, 2) increasing Ca^{2+} transient amplitude and SR Ca^{2+} content, and 3) accelerating SR Ca^{2+} reuptake in STZ group. Moreover, istaroxime, by stimulating SERCA2a, partially restored Ca^{2+} sparks characteristics and significantly accelerated Ca^{2+} sparks decay.

Conclusions

SERCA2a stimulation by istaroxime restores STZ-induced intracellular Ca^{2+} handling anomalies. Thus, SERCA2a stimulation can be considered a promising therapeutic approach for DD treatment.

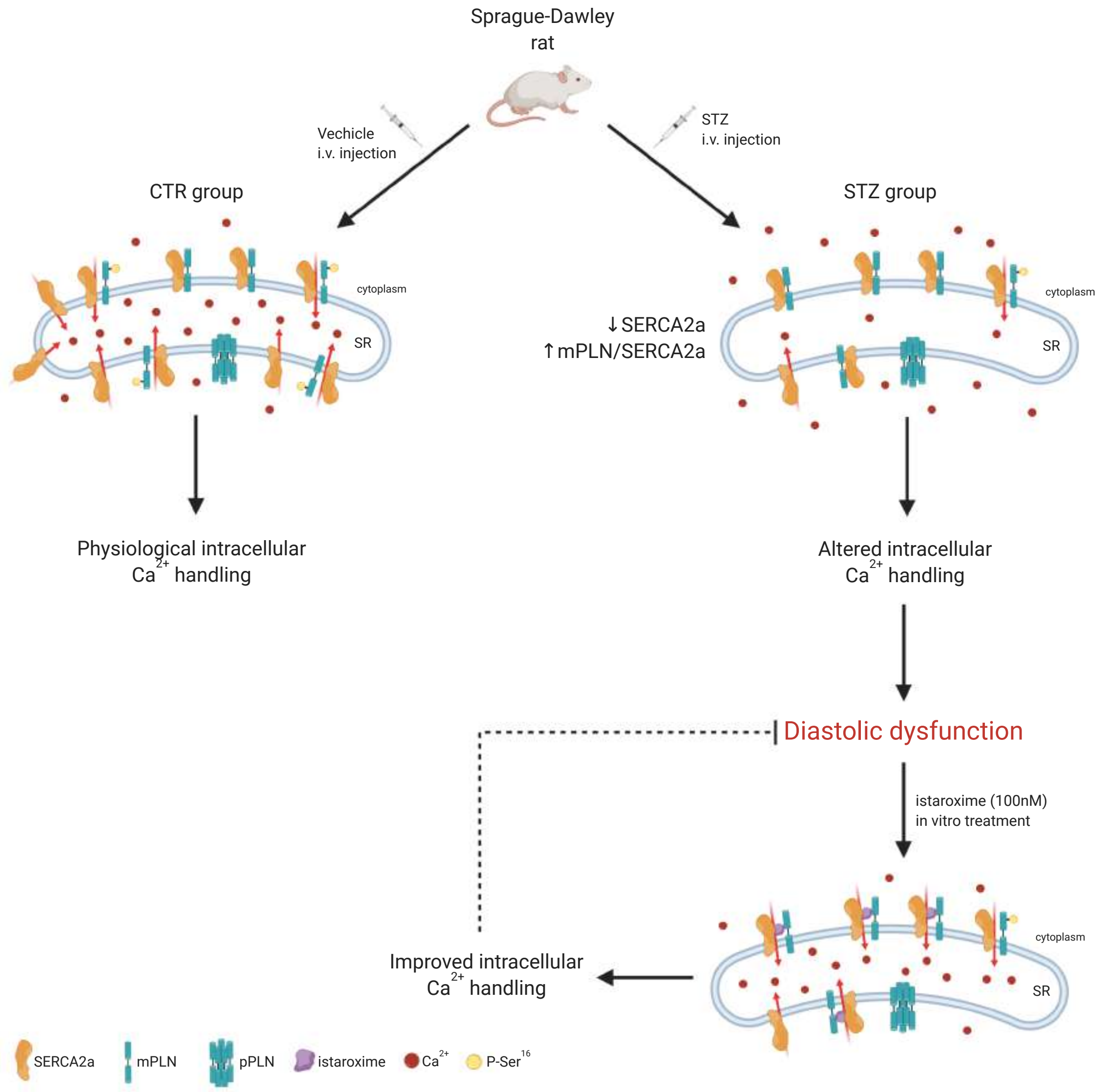

Translational perspective

Deficient sarcoplasmic reticulum (SR) Ca^{2+} uptake has been identified in cardiomyocytes from failing human hearts with impaired diastolic relaxation (e.g. diabetic hearts) and has been associated with a decrease in the expression and activity of SERCA2a and/or with a higher SERCA2a inhibition by phospholamban. Thus, SERCA2a may represent a pharmacological target for interventions aimed at improving cytosolic Ca^{2+} compartmentalization into the SR to limit diastolic dysfunction pathologies. In this contest, istaroxime is the first-in-class luso-inotropic agent targeting SERCA2a that has already demonstrated its efficacy in clinical trials and may clarify the relevance of SERCA2a stimulation in controlling cytosolic Ca^{2+} level.

2.2. Introduction

Diabetes affects globally more than 300 million people and type 1 diabetes (T1D) accounts for up to 10% of cases[1]. Heart failure (HF) is the predominant cardiovascular complication of diabetes and represents the leading cause of morbidity and mortality. Diabetic cardiomyopathy (DCM) is a complex and multifactorial disease characterized by an early onset of diastolic dysfunction (DD), which precedes the development of systolic impairment[2–5].

The molecular and pathophysiological mechanisms underlying diabetes include abnormalities in the regulation of Ca^{2+} homeostasis in cardiomyocytes and the consequent alteration of ventricular excitation-contraction coupling (ECC)[6]. In the diabetic heart, a dysregulation of Ca^{2+} cycling includes a reduction of SERCA2 activity, which may be accompanied by a decreased SERCA2 protein expression (mostly SERCA2a isoform)[7,8]. A key role in the regulation of SERCA2a activity is played by phospholamban (PLN), a protein that behaves like its endogenous inhibitor, when it is in its non-phosphorylated state[9]. In most diabetic models, PLN expression level appears increased while its phosphorylation state is reduced, thus contributing to the inhibition of SERCA2a function[7–9]. This defect generates an impairment of sarcoplasmic reticulum (SR) Ca^{2+} refilling that results in slow diastolic relaxation, reduction of Ca^{2+} sequestered into the SR after each contraction and decreased amplitude of the subsequent systolic contraction. An abnormal Ca^{2+} distribution may facilitate cardiac arrhythmias appearance and myocyte apoptosis[10,11].

Therefore, SERCA2a may represent a molecular target for a pharmacological intervention aimed at increasing the mechanical function and the energetic efficiency of the diabetic heart characterized by a defective SR Ca^{2+} loading. To date, the current medications have shown a limited efficacy in preventing the progression to HF in patients with DCM and diabetic complications[11–13]. New hypotheses have been recently proposed in HF aimed at improving cardiac contractility[14–20], however, all these attempts are still far from being considered as beneficial treatment options available for clinicians and the treatment of HF and DCM remains an open field of research. The development of a small-molecule as SERCA2a activator represents a promising strategy for HF and DCM treatment. Along this line, istaroxime is the first-in-class original luso-inotropic agent, shown to be highly effective and safe in patients[21]. Istaroxime is endowed of a double mechanism of action that consists in the ability to inhibit Na^+-K^+ ATPase (NKA) and enhance SERCA2a ATPase activity[22], this last obtained though the relief of PLN inhibitory effect on SERCA2a[23], without inducing spontaneous Ca^{2+} release from SR[22,24]. In healthy and failing animal models and in patients with acute HF syndrome, istaroxime improves systolic and diastolic performance[21,25–28] and efficiency of contraction with a low oxygen consumption[27], minimizing the risk of arrhythmias or ischemia, without affecting other cardiovascular functions[29–32].

In the present study, we test whether SERCA2a stimulation by a small molecule can improve the altered intracellular Ca^{2+} handling responsible for the DD in streptozotocin (STZ) treated rats. To this end, istaroxime was tested in cell-free system and left ventricular myocytes isolated from STZ rats at a concentration marginally affecting NKA, in order to highlight its effects mostly dependent on SERCA2a activation. We characterized the STZ model on different levels of biological organization, such as: (i) *in vivo*, to evaluate STZ-induced DD, (ii) in the cell-free system, to assess SERCA2a activity and protein level, (iii) in isolated ventricular cardiomyocytes, to evaluate intracellular Ca^{2+} dynamics and electrical activity.

2.3. Materials and methods

All experiments involving animals (methods detailed in the on line Supplementary Material) conformed to the guidelines for Animal Care endorsed by the University of Milano-Bicocca and to the Directive 2010/63/EU of the European Parliament on the protection of animals used for scientific purposes. Male Sprague Dawley rats (150-175 gr) were used to generate a STZ-induced T1D cardiomyopathy model according to the Health Minister of Italy permission.

2.3.1. STZ model

T1D was induced through a single STZ (Sigma-Aldrich, 50 mg/kg) injection into rat tail vein. STZ was freshly dissolved in 0.1 M citric acid-trisodium citrate buffer (pH 4,5); littermate control rats received only citrate buffer (vehicle). Overnight fasting or non-fasting glycaemia was measured after 1 week by Contour XT system (Bayer). Animals were considered diabetic with fasting glycaemia values > 290 mg/dL.

2.3.2. Echocardiography

Eight weeks after vehicle/STZ injection, rats were submitted to a transthoracic echocardiographic and Doppler evaluation, performed under ketamine-xylazine (130-7.5 mg/kg i.p.) anesthesia, (CX50 Echographer, Philips, equipped with a 12 MHz probe, S12-4 Transducer, Philips, Italy). Systolic and diastolic parameters were measured in CTR and STZ animals by a blinded investigator. Details are shown in the on line Supplementary Material.

2.3.3. Body parameters

Rats were euthanized by cervical dislocation under anesthesia with ketamine-xylazine (130-7.5 mg/kg i.p) 9 weeks after STZ injection. Body weight (BW), heart weight (HW), LV weight (LVW) and kidney weight (KW) were measured. Body weight gain (BW gain) was obtained by subtracting the initial BW from the BW at sacrifice. HW and KW were normalized to tibia length (TL) to assess respectively cardiac and kidney hypertrophy indexes in control (CTR) and diabetic (STZ) groups.

2.3.4. SERCA2a and Na^+/K^+ pump (NKA) activity measurement

SERCA2a activity was measured *in vitro* as ^{32}P-ATP hydrolysis at different Ca^{2+} concentrations (100-3000 nM) in heart homogenates as previously described[26] (see on line

Supplementary Material). Ca^{2+} concentration-response curves were fitted by using a logistic function to estimate SERCA2a Ca^{2+} affinity (K_d Ca^{2+}) and V_{max}.

NKA activity was assayed *in vitro* by measuring the release of ^{32}P-ATP, as previously described[33]. The activity of the tested compound on NKA was expressed as percent of the activity of control samples processed in the absence of ouabain or tested compound. The concentration of compound causing 50% inhibition of the NKA activity (IC_{50}) was calculated by using a logistic function.

2.3.5. Intracellular Ca^{2+} dynamics

Left ventricular myocytes were incubated in Tyrode solution for 30 min with the membrane-permeant form of the dye Fluo4-AM (10 μmol/L). Intracellular Ca^{2+} dynamics were measured in field stimulated (2 Hz) and in patch-clamped myocytes. In field stimulated cells, caffeine (10 mM) was superfused at steady-state to evaluate SR Ca^{2+} content (Ca_{SR}); then, cells were de novo paced to evaluate diastolic Ca^{2+} (Ca_D) increment during the reloading process. Protocol outline is shown in Fig S1. A quantification of the kinetic of Ca_D enhancement was obtained by mono-exponential fit of Ca_D values normalized to the 1st value recorded after SR depletion ($Ca_{D,n}/Ca_{D,1}$). Moreover, spontaneous Ca^{2+} release (SCR) events were evaluated in each group at resting and during diastole.

To better highlight changes in Ca^{2+} handling not affected by modifications on electrical activity, intracellular Ca^{2+} dynamic was also evaluated in voltage-clamped cells. Transmembrane current and cytosolic Ca^{2+} were simultaneously measured during a train of depolarizing (100 ms) pulses to 0 mV (0.25 Hz) applied from a holding of -40 mV. At steady state condition, an electronically timed 10 mM caffeine pulse was applied at the same cycle length to estimate Ca_{SR}. The slope of the Na^+-Ca^{2+} exchanger (NCX) current (I_{NCX})/Ca_{SR} relationship during the final third of the caffeine-induced transient was used to estimate NCX ‘conductance’. Fluorescence signal was converted to Ca_f by measuring maximal fluorescence (F_{max}) in each cell (see on line Supplementary Material).

Finally, to estimate changes in SR function only, the NCX was blocked by removing Na^+ from both sides of the sarcolemma. The protocol consisted in emptying the SR by a caffeine pulse (with 154 mM Na^+ to allow Ca^{2+} extrusion through NCX) and then progressively refilling it by voltage steps to 0 mV activating Ca^{2+} influx through I_{CaL} in the presence of 1 mM Ca^{2+} (Fig S2)[22]. Kinetics of SR Ca^{2+} reloading was evaluated; in particular, the time constant of Ca^{2+} transient (Ca_T) decay (τ_{decay}) reflecting Ca^{2+} transport rate across the SR membrane, can be considered a functional index of SERCA2a activity.

2.3.6. Ca^{2+} sparks rate and characteristics

Spontaneous unitary Ca^{2+} release events (Ca^{2+} sparks) were recorded at room temperature in Fluo 4-AM (10μM) loaded myocytes at resting condition. Tyrode's bath solution contained 1 mM $CaCl_2$. Images were acquired at x60 magnification in line-scan mode (*xt*) at 0.5 kHz by confocal Nikon A1R microscope. Confocal setting parameters were kept constant throughout all experimental groups to permit group comparison analysis.

2.3.7. Action potential rate-dependency and variability

Action potentials (APs) were recorded in I-clamp condition by pacing myocytes at 1, 2, 4 and 7 Hz during Tyrode's superfusion. Rate-dependency of AP duration (APD) at 50% (APD_{50}) and 90% (APD_{90}) of repolarization and diastolic potential (E_{diast}) were evaluated at steady state. Moreover, at each rate a minimum of 30 APs were recorded at steady state to evaluate the short-term variability (STV) of APD_{90}, a well-known proarrhythmic index[34], according to Eq. 1:

$$STV=\sum(|APD_{(n+1)}-APD_n|)/[n_{beats}*\sqrt{2}] \qquad \text{(Eq. 1)}$$

Incidence of delayed afterdepolarizations (DADs) was evaluated; a depolarization during diastole having a minimum amplitude of 1 mV was considered a DAD.

2.3.8. Statistical analysis

Unpaired Student's t-test, one-way or two-way ANOVA were applied as appropriate to test for significance between means. Post-hoc comparison between individual means was performed by Tukey's multiple comparison tests. Chi2-test was used for comparison of categorical variables. Results are expressed as mean ± SEM. Sample size is reported in the figure legends. A value of $P<0.05$ was considered significant.

Istaroxime effects were analyzed by incubating cells with the drug for at least 30 min, thus group comparison analysis was performed. Experimental groups were CTR, STZ and STZ + ista. Number of animals (N) and cells (n) are shown in each figure legend.

2.4. Results

2.4.1. STZ induces diastolic dysfunction

Diabetic rats were obtained by a single injection of STZ (50 mg/kg) into the tail vein and were compared to controls receiving only vehicle. Fasting and non-fasting glycaemia increased significantly 1 week after STZ administration (Table 1).

At the time of STZ administration body weight (BW) was comparable among CTR and STZ groups (data not shown), while 9 weeks after STZ infusion, BW was significantly lower in STZ than in CTR (Table 1). Heart weight (HW) and kidney weight (KW) were thus normalized to tibia length (TL) as index of cardiac and renal hypertrophy. STZ rats showed a significant reduction of HW/TL and a significant increase of KW/TL (Table 1), suggesting STZ-induced heart hypotrophy and kidney hypertrophy. Accordingly, left ventricular (LV) weight (LVW/HW, Table 1) and cell membrane capacitance (C_m), an index of cell dimension, were significantly reduced in STZ in comparison to CTR myocytes (136±4 pF N=13/n=8 vs 179±6 pF N=12/n=75, $p<0.05$), thus suggesting STZ-induced LV hypotrophy at the cellular level.

The echocardiographic parameters were measured in CTR and STZ rats 8 weeks after STZ injection (Table 2). Wall thickness for the interventricular septum (IVSTd) and posterior wall (PWTd) in diastole were significantly lower in STZ rats, while the left ventricle diastolic diameter (LVEDD) remained unchanged. The corresponding parameters for interventricular septum and posterior wall thickness measured in systole (IVSTs, PWTs) were unchanged between the two groups while the left ventricle diameter in systole (LVESD) was lower in STZ rats.

The calculated fractional shortening (FS) was significantly increased while the TDI contraction velocity (s') was reduced in STZ animals when compared to CTR, thus suggesting an overall systolic function only partially compromised in STZ rats at this stage.

The transmitral Doppler parameters were significantly altered in STZ rats, indicating an impairment of diastolic function with reduced early peak diastolic velocity (E) and prolonged E wave deceleration time (DT), increased mitral deceleration index (DT/E) and reduced deceleration slope (E/DT). Conversely, late peak diastolic velocity (A) was almost unchanged. As a consequence, STZ rats showed a significantly lower E/A ratio.

Moreover, Tissue Doppler examination showed a significant reduction of early diastolic myocardial velocity (e'), paralleling the change in mitral E wave, while the late diastolic myocardial velocity (a') was unchanged in STZ rats, similarly to A wave. STZ rats showed a significantly reduced e'/a' ratio, conversely the E/e' ratio was significantly increased in STZ rats.

The overall cardiac function indicated a comparable stroke volume (SV), a reduced heart rate (HR), leading to a significant reduction of cardiac output (CO) in STZ versus CTR. The calculated EF% was significantly higher in STZ rats than CTR.

Overall, echocardiographic data mostly indicate that at this time point STZ induced a diabetic cardiomyopathy characterized by DD and mostly preserved systolic function.

2.4.2. STZ induces SERCA2a downregulation

Cardiomyocytes from LV tissues of CTR and STZ rats were used to measure SERCA2a and PLN protein level by Western blot analysis. A representative Western blot from CTR and STZ myocytes and the relative densitometric analysis is shown in Fig 1A-B. Protein levels were normalized to the corresponding actin content. SERCA2a protein expression resulted significantly reduced in STZ versus CTR samples (-52%, $p<0.001$), while monomeric (m) and pentameric (p) PLN levels were unchanged. As a consequence, mPLN/SERCA2a ratio was significantly increased (+85%, $p<0.002$), suggesting higher SERCA2a inhibitory activity by PLN in STZ group. These measurements were also performed in heart homogenates showing comparable results (Fig S3). Moreover, in heart homogenates, the fraction of phosphorylated Ser^{16}-mPLN ($pSer^{16}$-mPLN/mPLN) was also evaluated, resulting reduced in STZ (-42%, $p<0.05$), thus highlighting SERCA2a function inhibition in STZ model (Fig S3B).

SERCA2a activity was measured in heart SR homogenates from CTR and STZ rats as ^{32}P-ATP hydrolysis assay (Fig 1C-D). In comparison to CTR preparations, SERCA2a V_{max} was significantly decreased (-25%, $p<0.05$) in STZ, while the K_d Ca^{2+} did not differ (Fig S4).

Overall, SERCA2a protein level and activity were reduced in STZ preparations, a result in line with echocardiographic parameters showing STZ-induced DD.

2.4.3. Istaroxime affinity for NKA in rat

To identify the istaroxime concentration suitable to limit its effects dependent on NKA inhibition, I_{NaK} was isolated in rat ventricular myocytes and the concentration-response curve for istaroxime was evaluated as previously shown for guinea-pig[30] and mouse myocytes[24]. A saturating concentration of ouabain (1 mM) was used (Fig S5A) to evaluate the I_{NaK} inhibition by istaroxime as percentage of the ouabain-induced change. In CTR rat ventricular myocytes the estimated IC_{50} was 32 ± 4 μM (Fig S5B); a similar value was detected in cell-free system on purified rat NKA (55 ± 19 μM).

Consistently with the aim of the study, istaroxime effects on STZ-induced changes were evaluated by testing the compound at concentrations mostly unaffecting NKA (from 100 nM in isolated myocytes up to 500 nM in the cell free system).

2.4.4. Istaroxime stimulates SERCA2a and reduces STZ-induced Ca_D enhancement

Istaroxime (500 nM) stimulated SERCA2a activity in heart SR homogenates from STZ diabetic rats by increasing SERCA2a V_{max} (+25%, $p<0.01$) to a value similar to CTR rats (Fig 1C-D) without affecting Ca^{2+} affinity (0.587 ± 0.09 μM vs 0.463 ± 0.063 μM, ns). Conversely, in CTR rat preparations, V_{max} (Fig 1C-D) and K_d (Fig S4) parameters were unchanged in the presence of istaroxime.

STZ-induced changes in intracellular Ca^{2+} handling were firstly evaluated in field stimulated cells (Fig 2). STZ induced a significant increase in Ca_D leaving unchanged all the other Ca_T parameters, including Ca_T amplitude and Ca_{SR} (Fig 2A-B). Following caffeine-induced SR depletion, Ca_D increased during the reloading process reaching a higher steady state value ($ssCa_D$) (Fig 2C) as expected, while the rate of Ca_D raising was similar between groups (Fig 2C). Istaroxime treatment (100 nM, Fig 2C) completely reverted STZ-induced $ssCa_D$ enhancement. Overall, STZ-induced SERCA2a down-regulation resulted in cytosolic Ca_D enhancement mainly due to a reduced SR Ca^{2+} compartmentalization. In parallel, istaroxime by stimulating SERCA2a reverted STZ-induced Ca_D enhancement.

SCR events were evaluated in CTR and STZ cells. SCR events were absent in CTR and a low number of events occurred in STZ myocytes (STZ 14%, STZ + ista 7%, ns).

2.4.5. STZ induces changes in electrical activity and short term variability of APD. Analysis of istaroxime effects

Simultaneous changes in ion channels and electrical activity in STZ myocytes might mask expected effects resulting from SERCA2a downregulation (e.g. changes in Ca_{SR}). Thus, to verify potential STZ-induced changes in electrical activity, AP rate dependency was evaluated in STZ myocytes in comparison to CTR. STZ induced a significant APD prolongation at all stimulation rates, accordingly to voltage-dependent K^+ channels downregulation[35,36] (Fig 3A). Moreover, rate dependency of E_{diast} observed in CTR myocytes was absent in STZ myocytes, probably due to STZ-induced NKA downregulation[37]. Istaroxime at 100 nM leaved unaltered STZ-induced APD_{50} prolongation, partially affected APD_{90} prolongation, while further depolarized E_{diast} at all stimulation rates (Fig 3A). E_{diast} depolarization induced by istaroxime was also observed in CTR myocytes (Fig S6), suggesting the presence of a marginal NKA blockade at this drug concentration.

Overall, as expected, STZ treatment largely affects ion channels and pumps resulting in AP shape changes. In particular, to what we concern, STZ-induced APD prolongation might explain why STZ-induced SERCA2a downregulation was not associated to a reduced SR Ca^{2+} content in field stimulated cells.

The short-term variability (STV) of APD was evaluated in all groups as well-known pro-arrhythmic index. In STZ myocytes STV was significantly higher at all pacing rates and partially reduced in the presence of istaroxime (Fig 3B). As expected, STV was directly correlated to APD_{90} in all groups; this dependency tended to increase in STZ groups without reaching statistical significance (Fig 3B), thus suggesting the absence of major mechanisms other than APD prolongation significantly affecting STV in all groups[35].

Likewise, to SCR incidence, delayed afterdepolarizations (DADs) incidence was completely absent in CTR myocytes and DADs were present only in few cells in STZ groups (STZ 17%, STZ + ista 15%, ns).

2.4.6. SERCA2a stimulation by istaroxime reverts STZ-induced Ca^{2+} handling changes in voltage clamped myocytes

To clarify direct effects of SERCA2a down-regulation and its stimulation by istaroxime on intracellular Ca^{2+} handling, analysis on voltage clamped myocytes was performed (Fig

4). Cells were superfused with Tyrode's solution to allow evaluation of both SR and NCX function. Ca_T and membrane current were simultaneously recorded and Fluo4 fluorescence was calibrated in nmol/L of free Ca^{2+} (see on line Supplementary Material for details) to quantify changes on intracellular Ca^{2+} dynamics. As shown in Fig 4A-B, STZ induced Ca_T and Ca_{SR} amplitude reduction, leaving unchanged FR. Influx through L-type Ca^{2+} channels (Ca_L influx) was not affected in STZ group, leading to an excitation-release (ER) gain that tended to be reduced in comparison to CTR. Moreover, the slope of the linear correlation between NCX current (I_{NCX}) and the Ca_{SR} ($\Delta I_{NCX}/\Delta Ca_{SR}$) was similar in CTR and STZ myocytes, suggesting that SERCA2a down-regulation was not associated to changes in NCX activity in STZ myocytes. Differences between CTR and STZ were abolished by istaroxime through SERCA2a stimulation.

SR Ca^{2+} uptake was further investigated by removing the contribution of NCX in controlling cytosolic Ca^{2+}. To this end, cells were incubated in a Na^+/Ca^{2+}-free solution and dialyzed with a Na^+-free pipette solution. As shown in Fig 4C, after SR depletion, SR reloaded with a slower kinetic in STZ myocytes, clearly confirming that SERCA2a function was reduced. In particular, in STZ myocytes, during the SR reloading process, the rate of Ca_T increment was reduced and this was associated with a slower enhancement of the ER gain. Moreover, the decay time constant, mostly representing SR uptake function, increased at each pulse, accordingly to a reduced SERCA2a function in STZ myocytes. Stimulation of SERCA2a by istaroxime caused faster SR reloading and all parameters were restored to control condition.

2.4.7. Ca^{2+} sparks rate and characteristics

As shown before, both DADs and SCR events were detected only in few STZ myocytes, suggesting that SR stability is mostly preserved in this DCM model. To further analyze this point, Ca^{2+} sparks rate and characteristics were evaluated in all groups (Fig 5). In STZ myocytes in comparison to CTR, Ca^{2+} sparks showed reduced amplitude, width, duration and spark mass (Fig 5C), in agreement with a reduced SR Ca^{2+} content at resting. Istaroxime, by stimulating SERCA2a, partially restored Ca^{2+} sparks characteristics. In particular, istaroxime-induced SERCA2a stimulation emerged also by the analysis of Ca^{2+} sparks decay that significantly became faster in the presence of the compound. Sparks rate was not significantly affected by STZ and istaroxime (Fig 5B).

2.5. Discussion

Aim of the present study was to assess the effect of SERCA2a stimulation in improving intracellular Ca^{2+} dynamics in a diabetic rat model characterized by impaired diastolic function.

Several therapeutic approaches that increase SERCA2a function have been recently investigated. These include SERCA2a overexpression by gene transfer[38], PLN inactivation by expression of mutants with negative dominance[39], AdV-shRNA[40], siRNA[41] or antibodies[42]. As highlighted by the negative results of the largest phase IIb clinical trial applying SERCA2a gene delivery in HF (CUPID 2), these approaches suffer from major problems in construct delivery (viral vectors etc.) and dose adjustment that are far from being solved. Moreover, a small-molecule (pyridone derivative) inhibiting PLN has been recently described[19]. An improved diastolic function is expected to be achieved by a SERCA2a activator. However, despite of the intense research on discovering small molecules or gene therapy aimed at selectively activating SERCA2a, no promising clinical outcomes have been reached so far.

Istaroxime is the first-in-class original luso-inotropic agent targeting SERCA2a, in addition to NKA inhibition[22,24,28,29], that has shown excellent efficacy and good safety in clinical trials on patients with Acute heart Failure Syndrome (AHFS)[21]. At the same level of inotropy, the proarrhythmic effect of istaroxime is considerably lower than that of digoxin, a Na^+/K^+ pump inhibitor. Thus, by improving Ca^{2+} clearance from the cytosol[24], SERCA2a stimulation may also minimize the proarrhythmic effect of Na^+/K^+ pump blockade while preserving its inotropic effect.

In the past, *in vitro* istaroxime effects were largely characterized by testing the drug at concentrations showing dual mechanism of action[22,24,28,30]. In the present study, lusitropic SERCA2a-dependent istaroxime effects were evaluated *in vitro* by testing istaroxime at concentrations marginally affecting NKA. To this end, its affinity on NKA in rat was evaluated, by measuring it in cardiac (isolated myocytes) and renal (purified enzyme) preparations. Comparable IC_{50} were obtained and thus, a concentration marginally affecting NKA (100-500 nM) was chosen to isolate drug effects dependent on SERCA2a stimulation. Results obtained in cell-free system and in isolated myocytes clearly showed SERCA2a stimulation by istaroxime at 100-500 nM, thus suggesting higher affinity of istaroxime for SERCA2a than for NKA in rat preparation.

To our knowledge, no other small molecules active on SERCA2a at submicromolar concentration are available.

2.5.1. STZ model: DD associated to down-regulated SERCA2a expression and activity

STZ rats showed a clear DD highlighted by changes in mitral inflow, in line with published results[5], reporting that DCM often manifests first as DD (Table 2). It should be mentioned that the peak E velocity is directly correlated with HR[43] and the bradycardia we found in STZ rats is likely to affect E velocity. However, DT, DT/E and E/DT are not affected by HR changes and are considered robust indicators of diastolic function[43]. Our echo measurements evidenced marked alterations on these parameters in STZ rats. In particular, we showed a significant transmitral Doppler flow alteration of E wave velocity with prolonged E wave deceleration time (DT), increased mitral deceleration index (DT/E) and reduced deceleration slope (E/DT) in STZ rats. Analogously, TDI parameters, relatively unaffected by load, indicated a significant reduction of early diastolic myocardial velocity (e') and e'/a' with an increase of E/e' ratio in STZ rats, associated with an overall reduction of cardiac function (CO).

The E wave constitutes the energy dependent phase of LV relaxation; thus, its decrease could point to a reduction in SERCA2a activity, consistent with reported alterations in the expression and function of Ca^{2+} regulatory proteins and Ca^{2+} metabolism[7]. Consistently, in heart preparations and in cardiomyocytes from STZ rats we observed a clear reduction of SERCA2 protein expression level, an increase of mPLN/SERCA2 ratio and a reduction of Ser^{16} phosphorylated mPLN (pSer^{16}-mPLN/mPLN) (Fig 1 and Fig S3). These biochemical alterations are associated with the reduction of SERCA2a ATPase activity observed in heart preparations from STZ compared to CTR rats (Fig 1 and Fig S3) and indicate that these may translate into the impairment of diastolic function seen by the echocardiographic examination. The A wave reflects the late passive phase of LV relaxation, affected mainly by the myocardial viscoelastic properties, and DCM is reported to be associated with fibrosis[43]. However, in the present study, no effect on this parameter has been observed, indicating that 8 weeks after STZ injection may be a time not long enough to develop this alteration.

At 8 weeks of diabetes, systolic function appears to be preserved or even ameliorated in STZ as compared to CTR rats as indicated by a significant increase of FS (Table 2). This finding is at variance with most published results, although some authors report an unchanged FS (up to 16 weeks after STZ)[44] or increased cardiac output[45]. It should be noted that increased cardiac contractility in humans has been also reported[46,47]. One possible explanation for this is that the increased water intake due to polyuria requires the heart to deal with higher blood volume turnover. Given that heart rate is reduced, LV contractility must increase.

Moreover, we observed a marked bradycardia, consistent with the impaired autonomic function and down-regulation of the expression of the pacemaker channel HCN4[48] (Table 2).

Collectively, these results indicate that our model of STZ-induced DCM is characterized by impaired diastolic function associated with a downregulation of the SERCA2a expression and activity. This model is therefore suitable for testing the cardiac effects of SERCA2a stimulation by istaroxime on intracellular Ca^{2+} dynamics.

2.5.2. SERCA2a stimulation by istaroxime: improvement of STZ-induced intracellular Ca^{2+} handling anomalies

The effects of istaroxime on SERCA2a activity have been investigated both on CTR and STZ heart preparations. Istaroxime stimulates SERCA2a in cardiac preparations from STZ rats by re-establishing the STZ-induced reduction of its maximal activity (V_{max}) without affecting its affinity for Ca^{2+} (K_m). Moreover, no effects on SERCA2a activity were detected in CTR heart preparation (Fig 1). Similar results were obtained on SR vesicles from healthy and failing dogs[23], while a reduction in K_m was observed in SR vesicles from healthy guinea pig[22]. Thus, SERCA2a stimulation by istaroxime seems to occur in different ways depending on the species. This species-specific effect has to be further investigated through a full understanding of the molecular mechanism underlying SERCA2a stimulation by the drug.

In isolated SR vesicles, the number of targets potentially accounting for such an action is limited to SERCA2a itself and to its regulatory proteins, which remain associated with the SR membrane. Among them, PLN may be contained in variable amounts in SR vesicles prepared according to the present technique constituting a potential target for istaroxime action. Indeed, Ferrandi et al. showed that istaroxime stimulates SERCA2a activity through a direct interaction with SERCA2a/PLN complex, independently from cAMP/PKA and PLN phosphorylation[23]. Thus, it is reasonable to assume that the molecular mechanisms of action of istaroxime may involve targeting within a pocket generated by SERCA2a/PLN protein–protein interaction or a direct binding to one or more sites on PLN, favoring the dissociation of PLN from SERCA2a and the relief of SERCA2a inhibition. Anyway, further structural studies are still necessary to validate this hypothesis.

Istaroxime effects observed in cell free preparations were extensively reproduced in isolated STZ myocytes (Figs 2, 4, 5). In particular, the reduced SERCA2a activity and protein level in STZ animals was correlated to an increased Ca_D in intact myocytes, leaving unaltered all the other Ca^{2+} handling parameters (Fig 2). Istaroxime reverted the higher Ca_D by stimulating Ca^{2+} compartmentalization into the SR. This was fully remarkable by controlling membrane potential changes in voltage clamped myocytes (Fig 4). Indeed, by clamping myocytes at -40 mV, STZ-induced changes in Ca^{2+} handling emerged, such as reduced Ca_{SR} and Ca_T amplitude, that were unseen in intact field stimulated cells. Istaroxime, by stimulating SERCA2a, mostly restored Ca_{SR} and Ca_T amplitude, the last probably as a consequence of the higher SR Ca^{2+} content. Moreover, by measuring the SR reloading process after caffeine-induced depletion in the absence of the contribution of NCX, istaroxime accelerated it by blunting the opposite effects induced by STZ. This protocol allows direct measurement of SR Ca^{2+} uptake kinetics because of the inhibition of NCX function. Istaroxime effects were all compatible with a sharp enhancement of Ca^{2+} uptake by the SR, as expected from stimulation of SERCA2a activity. Indeed, the drug increased the magnitude and rate of Ca^{2+} reuptake, thus stimulating the SR reloading process. The marked increase in ER-gain caused by istaroxime may be secondary to larger increments in SR Ca^{2+} content during the reloading protocol.

Overall, due to the control of the membrane potential, we were able to highlight STZ induced direct effects on Ca^{2+} handling proteins and istaroxime effects on blunting them by stimulating SERCA2a. In particular, STZ model clearly showed SERCA2a downregulation not paralleled by an increment of NCX function, defined through the relationship between I_{NCX} and cytosolic Ca^{2+}, thus correcting for differences in cytosolic Ca^{2+} level (Fig 4B).

Abnormalities of the SR uptake function can be due to reduced SERCA2a activity or to increased Ca^{2+} leak through RyR channels. While functional and structural SERCA2a downregulation (increased inhibition by PLN and reduced SERCA2a protein level) was observed, RyR open probability was not significantly changed in STZ myocytes. Indeed, Ca^{2+} spark frequency (Fig 5A-B), the incidence of Ca^{2+} waves and the related DADs were not significantly increased in STZ myocytes, thus suggesting the absence of a sharp SR instability at this stage of STZ-induced DCM. These findings lead to limit the detection of potential antiarrhythmic effect of istaroxime as a direct consequence of SERCA2a stimulation. Intra-SR Ca^{2+} waves threshold is reported to increase following SERCA2a stimulation because it appears to exert a negative feedback on ER-gain mechanisms sustaining the waves[49]. Thus, istaroxime by stimulating SERCA2a can potentially become antiarrhythmic in condition of profound SR instability.

Moreover, STZ-induced changes in Ca^{2+} sparks characteristics are a mirror image of the reduced SR Ca^{2+} content in STZ myocytes (Fig 5). Indeed, in comparison to CTR myocytes, Ca^{2+} sparks became smaller in amplitude, spatial and time duration, resulting in a smaller spark mass. Istaroxime, by stimulating SERCA2a blunted these changes and even markedly accelerated Ca^{2+} sparks decay. The last event is relevant for the potential anti-arrhythmic efficacy of istaroxime because of a faster Ca^{2+} release unit (CRU) switch off, that can limit Ca^{2+} waves genesis. Moreover, the acceleration of Ca^{2+} spark decay induced by istaroxime seems independent on STZ-induced changes; thus, we cannot exclude direct effects of the drug on Ca^{2+} spark termination mechanisms.

Temporal dispersion of repolarization, quantified as short-term variability (STV) of APD, is a well-known proarrhythmic index because plays an important role in the initiation of ventricular arrhythmias like *torsade de point* (TdP)[50]. STV was significantly increased in STZ myocytes and this was mainly associated to APD prolongation (Fig 3B). Istaroxime blunted STV especially at high stimulation rates; this effect seems secondary to its effects on attenuating STZ-induced APD prolongation at these rates.

STZ induced marked APD prolongation at all stimulation rates (Fig 3A) suggesting voltage dependent K^+ channels down-regulation[35]. Moreover, since NKA plays an important role in setting E_{diast}, STZ-induced NKA down-regulation[37] was highlighted by the lack of E_{diast} rate dependent hyperpolarization in STZ myocytes. Surprisingly, istaroxime significantly depolarized E_{diast} at all stimulation rates and this effect was reproduced in CTR myocytes (Fig S6). Any potential direct ancillary effects of the drug beyond those dependent on its two direct targets (NKA and SERCA2a) have to be excluded in agreement to previous studies[22,30]. Thus, a significant E_{diast} depolarization can be ascribed to a partial inhibition of NKA at the concentration used (100 nM) or to membrane channels changes as a consequence of SERCA2a stimulation by the drug. The first hypothesis seems far from being realistic because the drug concentration used in the study (100 nM) is very low compared to the measured IC_{50} for NKA (32 µM, Fig S5). However, istaroxime depolarized E_{diast} in CTR myocytes too (Fig S6), while its effects on SERCA2a was practically absent at least in CTR cell-free system (Fig 1). Thus, even though 100 nM is a concentration of the drug not displaying a clear-cut inhibition of NKA in voltage clamped myocytes (Fig S5), we have to consider that NKA contribution to electrical activity is important and thus, marginal effects on it might be disclosed by analyzing E_{diast} especially at high pacing rates. Overall, further analysis should be performed to better understand istaroxime effect on E_{diast}.

Moreover, if a weak NKA inhibition is induced by 100 nM istaroxime, the reduced diastolic Ca^{2+} observed in intact myocytes (Fig 2) depending mainly on drug-induced SERCA2a stimulation, might be even underestimated.

2.5.3. Study limitation

The aim of the study was to test the effect of SERCA2a stimulation on STZ-induced Ca^{2+} handling anomalies in cell-free system and isolated ventricular myocytes. To this end, istaroxime was tested at a concentration marginally affecting NKA. We would like to stress that even though we cannot exclude marginal NKA inhibition by istaroxime, the general findings of the study are largely dependent on SERCA2a stimulation by the drug.

Although blood volumes alterations due to glycosuria might affect echocardiographic parameters interpretation in STZ rats, correlation between biochemical and functional changes in isolated myocytes is far from being influenced.

2.6. Conclusions

SERCA2a stimulation by istaroxime restores STZ-induced intracellular Ca^{2+} handling anomalies in isolated cardiomyocytes. Thus, SERCA2a stimulation can be considered a promising therapeutic approach for DCM treatment. The development of small molecules active on SERCA2a only ("pure/sole SERCA2a activators") might be clinically relevant to understand their effects especially *in vivo* when therapies are applied to stimulate the SERCA2a activity, i.e. DCM and in general DD related cardiac pathologies.

2.7. Funding

This work was supported by CVie Therapeutics Limited (Taipei, Taiwan) and University of Milano-Bicocca.

2.8. Conflict of interests

MF, PB, GB are Windtree employees, PF is a Windtree consultant.

2.9. References

1. Sherwin R, Jastreboff AM. Year in diabetes 2012: The diabetes tsunami. *J Clin Endocrinol Metab* 2012;**97**:4293–4301.

2. Schannwell CM, Schneppenheim M, Perings S, Plehn G, Strauer BE. Left ventricular diastolic dysfunction as an early manifestation of diabetic cardiomyopathy. *Cardiology* 2002;**98**:33–39.

3. Belke DD, Dillmann WH. Altered cardiac calcium handling in diabetes. *Curr Hypertens Rep* 2004;**6**:424–429.

4. Boudina S, Abel ED. Diabetic cardiomyopathy revisited. *Circulation* 2007;**115**:3213–3223.

5. Lebeche D, Davidoff AJ, Hajjar RJ. Interplay between impaired calcium regulation and insulin signaling abnormalities in diabetic cardiomyopathy. *Nat Clin Pract Cardiovasc Med* 2008;**5**:715–724.

6. Bers DM. Cardiac excitation-contraction coupling. *Nature* 2002;**415**:198–215.

7. Choi KM, Zhong Y, Hoit BD, Grupp IL, Hahn H, Dilly KW, Guatimosim S, Jonathan Lederer W, Matlib MA. Defective intracellular Ca2+ signaling contributes to cardiomyopathy in type 1 diabetic rats. *Am J Physiol - Hear Circ Physiol* 2002;**283**:H1398–H1408.

8. Vasanji Z, Dhalla NS, Netticadan T. Increased inhibition of SERCA2 by phospholamban in the type I diabetic heart. *Mol Cell Biochem* 2004;**261**:245–249.

9. Kranias EG, Hajjar RJ. Modulation of cardiac contractility by the phopholamban/SERCA2a regulatome. *Circ Res* 2012;**110**:1646–1660.

10. Zaza A, Rocchetti M. Calcium Store Stability as an Antiarrhythmic Endpoint. *Curr Pharm Des* 2015;**21**:1053–1061.

11. Malek V, Gaikwad AB. Telmisartan and thiorphan combination treatment attenuates fibrosis and apoptosis in preventing diabetic cardiomyopathy. *Cardiovasc Res* 2019;**115**:373–384.

12. Dobrin JS, Lebeche D. Diabetic cardiomyopathy: Signaling defects and therapeutic approaches. *Expert Rev Cardiovasc Ther* 2010;**8**:373–391.

13. Ng HH, Leo CH, Parry LJ, Ritchie RH. Relaxin as a therapeutic target for the cardiovascular complications of diabetes. *Front Pharmacol* 2018;**9**:501.

14. Jaski BE, Jessup ML, Mancini DM, Cappola TP, Pauly DF, Greenberg B, Borow K, Dittrich H, Zsebo KM, Hajjar RJ. Calcium Upregulation by Percutaneous Administration of Gene Therapy in Cardiac Disease (CUPID Trial), a First-in-Human Phase 1/2 Clinical Trial. *J Card Fail* 2009;**15**:171–181.

15. Clark RJ, McDonough PM, Swanson E, Trost SU, Suzuki M, Fukuda M, Dillmann WH. Diabetes and the Accompanying Hyperglycemia Impairs Cardiomyocyte Calcium Cycling through Increased Nuclear O-GlcNAcylation. *J Biol Chem* 2003;**278**:44230–44237.

16. Shao CH, Capek HL, Patel KP, Wang M, Tang K, DeSouza C, Nagai R, Mayhan W, Periasamy M, Bidasee KR. Carbonylation contributes to SERCA2a activity loss and diastolic dysfunction in a rat model of type 1 diabetes. *Diabetes* 2011;**60**:947–959.

17. Kho C, Lee A, Jeong D, Oh JG, Gorski PA, Fish K, Sanchez R, Devita RJ, Christensen G, Dahl R, Hajjar RJ. Small-molecule activation of SERCA2a SUMOylation for the treatment of heart failure. *Nat Commun* 2015;**6**:7229.

18. Peng BY, Dubey NK, Mishra VK, Tsai FC, Dubey R, Deng WP, Wei HJ. Addressing stem cell therapeutic approaches in pathobiology of diabetes and its complications. *J Diabetes Res* 2018;**2018**.

19. Kaneko M, Yamamoto H, Sakai H, Kamada Y, Tanaka T, Fujiwara S, Yamamoto S, Takahagi H, Igawa H, Kasai S, Noda M, Inui M, Nishimoto T. A pyridone derivative activates SERCA2a by attenuating the inhibitory effect of

phospholamban. *Eur J Pharmacol* 2017;**814**:1–8.

20. Bidasee KR, Zhang Y, Shao CH, Wang M, Patel KP, Dincer ÜD, Besch HR. Diabetes Increases Formation of Advanced Glycation End Products on Sarco(endo)plasmic Reticulum Ca2+-ATPase. *Diabetes* 2004;**53**:463–473.

21. Shah SJ, Blair JEA, Filippatos GS, MacArie C, Ruzyllo W, Korewicki J, Bubenek-Turconi SI, Ceracchi M, Bianchetti M, Carminati P, Kremastinos D, Grzybowski J, Valentini G, Sabbah HN, Gheorghiade M. Effects of istaroxime on diastolic stiffness in acute heart failure syndromes: Results from the Hemodynamic, Echocardiographic, and Neurohormonal Effects of Istaroxime, a Novel Intravenous Inotropic and Lusitropic Agent: A Randomized Controlled Trial in P. *Am Heart J* 2009;**157**:1035–1041.

22. Rocchetti M, Besana A, Mostacciuolo G, Micheletti R, Ferrari P, Sarkozi S, Szegedi C, Jona I, Zaza A. Modulation of sarcoplasmic reticulum function by Na+/K + pump inhibitors with different toxicity: Digoxin and PST2744 [(E,Z)-3-((2-aminoethoxy)imino)androstane-6,17-dione hydrochloride]. *J Pharmacol Exp Ther* 2005;**313**:207–215.

23. Ferrandi M, Barassi P, Tadini-Buoninsegni F, Bartolommei G, Molinari I, Tripodi MG, Reina C, Moncelli MR, Bianchi G, Ferrari P. Istaroxime stimulates SERCA2a and accelerates calcium cycling in heart failure by relieving phospholamban inhibition. *Br J Pharmacol* 2013;**169**:1849–1861.

24. Alemanni M, Rocchetti M, Re D, Zaza A. Role and mechanism of subcellular Ca2+ distribution in the action of two inotropic agents with different toxicity. *J Mol Cell Cardiol* 2011;**50**:910–918.

25. Adamson PB, Vanoli E, Mattera GG, Germany R, Gagnol JP, Carminati P, Schwartz PJ. Hemodynamic effects of a new inotropic compound, PST-2744, in dogs with chronic ischemic heart failure. *J Cardiovasc Pharmacol* 2003;**42**:169–173.

26. Micheletti R, Palazzo F, Barassi P, Giacalone G, Ferrandi M, Schiavone A, Moro B, Parodi O, Ferrari P, Bianchi G. Istaroxime, a Stimulator of Sarcoplasmic Reticulum Calcium Adenosine Triphosphatase Isoform 2a Activity, as a Novel Therapeutic Approach to Heart Failure. *Am J Cardiol* 2007;**99**:24A-32A.

27. Sabbah HN, Imai M, Cowart D, Amato A, Carminati P, Gheorghiade M.

Hemodynamic Properties of a New-Generation Positive Luso-Inotropic Agent for the Acute Treatment of Advanced Heart Failure. *Am J Cardiol* 2007;**99**:41A-46A.

28. Rocchetti M, Alemanni M, Mostacciuolo G, Barassi P, Altomare C, Chisci R, Micheletti R, Ferrari P, Zaza A. Modulation of sarcoplasmic reticulum function by PST2744 [Istaroxime; (E,Z)-3-((2-aminoethoxy)imino) androstane-6,17-dione hydrochloride] in a pressure-overload heart failure model. *J Pharmacol Exp Ther* 2008;**326**:957–965.

29. Micheletti R, Mattera GG, Rocchetti M, Schiavone A, Loi MF, Zaza A, Gagnol RJP, Munari S De, Melloni P, Carminati P, Bianchi G, Ferrari P. Pharmacological profile of the novel inotropic agent (E,Z)-3-((2-aminoethoxy)imino)androstane-6,17-dione hydrochloride (PST2744). *J Pharmacol Exp Ther* 2002;**303**:592–600.

30. Rocchetti M, Besana A, Mostacciuolo G, Ferrari P, Micheletti R, Zaza A. Diverse toxicity associated with cardiac Na+/K+ pump inhibition: Evaluation of electrophysiological mechanisms. *J Pharmacol Exp Ther* 2003;**305**:765–771.

31. Gheorghiade M, Ambrosy AP, Ferrandi M, Ferrari P. Combining SERCA2a activation and Na-K ATPase inhibition: a promising new approach to managing acute heart failure syndromes with low cardiac output. *Discov Med* 2011;**12**:141–151.

32. Bossu A, Kostense A, Beekman HDM, Houtman MJC, Heyden MAG van der, Vos MA. Istaroxime, a positive inotropic agent devoid of proarrhythmic properties in sensitive chronic atrioventricular block dogs. *Pharmacol Res* 2018;**133**:132–140.

33. Ferrandi M, Tripodi G, Salardi S, Florio M, Modica R, Barassi P, Parenti P, Shainskaya A, Karlish S, Bianchi G, Ferrari P. Renal Na,K-ATPase in genetic hypertension. *Hypertension* 1996;**28**:1018–1025.

34. Altomare C, Bartolucci C, Sala L, Bernardi J, Mostacciuolo G, Rocchetti M, Severi S, Zaza A. IKr Impact on Repolarization and Its Variability Assessed by Dynamic Clamp. *Circ Arrhythmia Electrophysiol* 2015;**8**:1265–1275.

35. Meo M, Meste O, Signore S, Sorrentino A, Cannata A, Zhou Y, Matsuda A, Luciani M, Kannappan R, Goichberg P, Leri A, Anversa P, Rota M. Reduction

in kv current enhances the temporal dispersion of the action potential in diabetic myocytes: Insights from a novel repolarization algorithm. *J Am Heart Assoc* 2016;**5**.

36. Howarth FC, Jacobson M, Qureshi MA, Shafiullah M, Hameed RS, Zilahi E, Haj A Al, Nowotny N, Adeghate E. Altered gene expression may underlie prolonged duration of the QT interval and ventricular action potential in streptozotocin-induced diabetic rat heart. *Mol Cell Biochem* 2009;**328**:57–65.

37. Ku DD, Sellers BM. Effects of streptozotocin diabetes and insulin treatment on myocardial sodium pump and contractility of the rat heart. *J Pharmacol Exp Ther* 1982;**222**:395–400.

38. Greenberg B, Butler J, Felker GM, Ponikowski P, Voors AA, Desai AS, Barnard D, Bouchard A, Jaski B, Lyon AR, Pogoda JM, Rudy JJ, Zsebo KM. Calcium upregulation by percutaneous administration of gene therapy in patients with cardiac disease (CUPID 2): A randomised, multinational, double-blind, placebo-controlled, phase 2b trial. *Lancet* 2016;**387**:1178–1186.

39. Hoshijima M, Ikeda Y, Iwanaga Y, Minamisawa S, Date MO, Gu Y, Iwatate M, Li M, Wang L, Wilson JM, Wang Y, Ross J, Chien KR. Chronic suppression of heart-failure progression by a pseudophosphorylated mutant of phospholamban via in vivo cardiac rAAV gene delivery. *Nat Med* 2002;**8**:864–871.

40. Suckau L, Fechner H, Chemaly E, Krohn S, Hadri L, Kockskamper J, Westermann D, Bisping E, Ly H, Wang X, Kawase Y, Chen J, Liang L, Sipo I, Vetter R, Weger S, Kurreck J, Erdmann V, Tschope C, Pieske B, Lebeche D, Schultheiss HP, Hajjar RJ, Poller WC. Long-term cardiac-targeted RNA interference for the treatment of heart failure restores cardiac function and reduces pathological hypertrophy. *Circulation* 2009;**119**:1241–1252.

41. Watanabe A, Arai M, Yamazaki M, Koitabashi N, Wuytack F, Kurabayashi M. Phospholamban ablation by RNA interference increases Ca2+uptake into rat cardiac myocyte sarcoplasmic reticulum. *J Mol Cell Cardiol* 2004;**37**:691–698.

42. Suzuki T, Wang JH. Stimulation of bovine cardiac sarcoplasmic reticulum Ca2+ pump and blocking of phospholamban phosphorylation and dephosphorylation by a phospholamban monoclonal antibody. *J Biol Chem* 1986;**261**:7018–7023.

43. Mihm MJ, Seifert JL, Coyle CM, Bauer JA. Diabetes related cardiomyopathy

time dependent echocardiographic evaluation in an experimental rat model. *Life Sci* 2001;**69**:527–542.

44. Weytjens C, Franken PR, D'Hooge J, Droogmans S, Cosyns B, Lahoutte T, Camp G Van. Doppler myocardial imaging in the diagnosis of early systolic left ventricular dysfunction in diabetic rats. *Eur J Echocardiogr* 2008;**9**:326–333.

45. Joffe II, Travers KE, Perreault-Micale CL, Hampton T, Katz SE, Morgan JP, Douglas PS. Abnormal cardiac function in the streptozotocin-induced, non-insulin- dependent diabetic rat: Noninvasive assessment with Doppler echocardiography and contribution of the nitric oxide pathway. *J Am Coll Cardiol* 1999;**34**:2111–2119.

46. Thuesen L, Sandahl Christiansen J, Falstie-Jensen N, Christensen CK, Hermansen K, Mogensen CE, Henningsen P. Increased myocardial contractility in short-term Type 1 diabetic patients: an echocardiographic study. *Diabetologia* 1985;**28**:822–826.

47. Gøtzsche O, Sørensen K, McIntyre B, Henningsen P. Reduced left ventricular afterload and increased contractility in children with insulin-dependent diabetes mellitus: An M-mode and Doppler-echocardiographic evaluation of left ventricular diastolic and systolic function. *Pediatr Cardiol* 1991;**12**:69–73.

48. Zhang Y, Wang Y, Yanni J, Qureshi MA, Logantha SJRJ, Kassab S, Boyett MR, Gardiner NJ, Sun H, Howarth FC, Dobrzynski H. Electrical Conduction System Remodeling in Streptozotocin-Induced Diabetes Mellitus Rat Heart. *Front Physiol* 2019;**10**:1–15.

49. Fernandez-Tenorio M, Niggli E. Stabilization of Ca2+ signaling in cardiac muscle by stimulation of SERCA. *J Mol Cell Cardiol* 2018;**119**:87–95.

50. Smoczynska A, Beekman HDM, Vos MA. The increment of short-term variability of repolarisation determines the severity of the imminent arrhythmic outcome. *Arrhythmia Electrophysiol Rev* 2019;**8**:166–172.

2.10. Figures and tables legends

Figure 1. Effect of STZ and istaroxime on SERCA2 level and activity in cell-free system. (A) Representative Western blot for SERCA2, monomeric (m) and pentameric (p) un-phosphorylated PLN in cardiomyocytes from STZ and CTR animals. Standard molecular weights are indicated as s1 and s2 respectively for SERCA2 and PLN. (B) Densitometric analysis of western blot for SERCA2, mPLN, pPLN protein level and mPLN/SERCA2 ratio. Values are expressed as optical density in arbitrary units. *=$p<0.05$ vs CTR (unpaired t-test); CTR N=6, STZ N=4. (C) Ca^{2+} activation curves of SERCA2a activity were measured as CPA sensitive component in cardiac SR homogenates from CTR and STZ (with or w/o istaroxime 500 nM) rats. (D) The kinetic parameter, maximum velocity (V_{max}), of the Ca^{2+} activation curves was determined by a sigmoidal fitting. *= $p<0.05$ vs CTR (unpaired *t*-test), #=$p<0.05$ vs STZ (paired *t*-test); CTR N=5, CTR + ista N=5, STZ N=5, STZ + ista N=5.

Figure 2. Effect of STZ and istaroxime on Ca^{2+} dynamics in field stimulated cardiomyocytes. (A) Representative recordings of Ca^{2+} transients (Ca_T) in field stimulated cells (2 Hz) from CTR and STZ (with or w/o istaroxime 100 nM) myocytes. (B) Average values of Ca_T parameters. (C) Changes in diastolic Ca^{2+} (Ca_D) during the reloading process after caffeine-induced SR depletion. Ca_D values ($Ca_{D,n}$) were normalized to the 1st pulse Ca_D ($Ca_{D,1}$); estimated steady state Ca_D ($ssCa_D$) and reloading kinetic (Tau) are shown on the right. *=$p<0.05$ vs CTR; #=$p<0.05$ vs STZ (two-way ANOVA, Tukey's multiple comparison); CTR N=3 / n=26, STZ N=4 / n=28, STZ + ista N=4 / n=30.

Figure 3. Effect of STZ and istaroxime on electrical activity. (A) Rate dependency of AP parameters (APD_{50}, APD_{90} and E_{diast}) in CTR and STZ (with or w/o istaroxime 100 nM) myocytes. (B) Rate-dependency of STV (left panel) and its correlation to APD_{90} values (right panel) for each experimental group (slope values in CTR=0.011, STZ=0.016 and STZ + ista=0.014, ns). *=$p<0.05$ vs CTR; #=$p<0.05$ vs STZ (two-way ANOVA, Tukey's multiple comparison); CTR N=4 / n=20-29, STZ N=3 / n=13-24, STZ + ista N=3 / n=16-19.

Figure 4. Effect of STZ and istaroxime on Ca^{2+} dynamics in patch-clamped cardiomyocytes. (A) Representative traces of simultaneously recorded transmembrane currents (top) and Ca^{2+} transients (Ca_T) (bottom) in voltage-clamped cells from CTR and

STZ (with or w/o istaroxime 100 nM) myocytes. (B) Average values of Ca_T amplitude, SR Ca^{2+} content (Ca_{SR}), fractional release (FR), Ca^{2+} influx through L-type Ca^{2+} channel (Ca_L influx), excitation release (ER)-gain and slope of I_{NCX}/Ca_{SR} relationship in each group. *=$p<0.05$ vs control; #=$p<0.05$ vs STZ (two-way ANOVA, Tukey's multiple comparison); CTR N=3 / n=20-25, STZ N=5 / n=15-33, STZ + ista N=3 / n=12-28. (C) Average values of Ca_T parameters measured during each pulse after SR depletion under NCX blockade (see methods) in CTR and STZ (with or w/o istaroxime 100 nM) myocytes. *=$p<0.05$ vs CTR; #=$p<0.05$ vs STZ (two-way ANOVA); CTR N=5 / n=13-21, STZ N=4 / n=13-28, STZ + ista N=4 / n=19-24.

Figure 5. Effect of STZ and istaroxime on Ca^{2+} sparks rate and characteristics. (A) Representative xt images showing Ca^{2+} sparks at resting in CTR and STZ (with or w/o istaroxime 100 nM) myocytes. (B) Average values of Ca^{2+} sparks rate for each group. (C) Average values of Ca^{2+} sparks characteristics for each group. *=$p<0.05$ vs control; #=$p<0.05$ vs STZ (two-way ANOVA, Tukey's multiple comparison); CTR N=7 /n=62 /sparks number=2789, STZ N=5 /n=53 /sparks number=2019, STZ + ista N=5 /n=47 /sparks number=1940.

Table 1. Glycaemia values and systemic parameters. Average values of fasting/non fasting glycaemia and systemic parameters (see methods) in CTR and STZ animals. Body weight (BW); heart weight (HW); kidney weight (KW); left ventricle weight (LVW); tibia length (TL). *=$p<0.05$ vs CTR (unpaired *t*-test); CTR N=15-21, STZ N=23-34.

Table 2. Echocardiographic and Tissue Doppler parameters. Average values of echocardiographic and tissue doppler parameters (see methods) in CTR and STZ animals. Telediastolic interventricular septum thickness (IVSTd); telediastolic posterior wall thickness (PWTd); left ventricle early-diastolic diameter (LVEDD); telesystolic interventricular septum thickness (IVSTs); telesystolic posterior wall thickness (PWTs); left ventricle early-systolic diameter (LVESD); fractional shortening (FS); early diastolic peak velocity (E, e'); late diastolic peak velocity (A, a'); deceleration time (DT); systolic peak velocity (s'); heart rate (HR); stroke volume (SV); cardiac output (CO); ejection fraction (EF). *=$p<0.05$ vs CTR, **=$p<0.01$ vs CTR, ns=not significant (unpaired *t*-test); CTR N=10-17, STZ N=16-24.

Figure 1

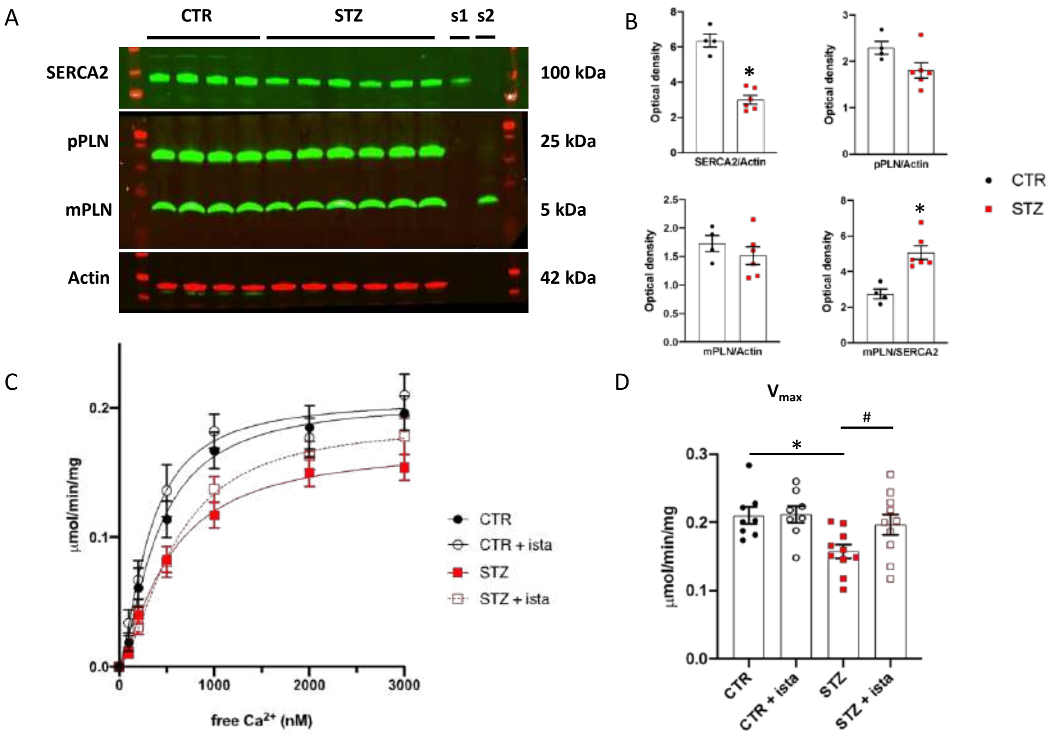
A
CTR
STZ
s1
s2
SERCA2
pPLN
mPLN
Actin
100 kDa
25 kDa
5 kDa
42 kDa
B
Optical density
SERCA2/Actin
pPLN/Actin
mPLN/Actin
mPLN/SERCA2
*
*
0
2
4
6
8
0
1
2
3
0.0
0.5
1.0
1.5
2.0
2.5
● CTR
■ STZ
C
μmol/min/mg
0.0
0.1
0.2
0
1000
2000
3000
free Ca²⁺ (nM)
CTR
CTR + ista
STZ
STZ + ista
D
Vmax
*
#
μmol/min/mg
0.0
0.1
0.2
0.3
CTR
CTR + ista
STZ
STZ + ista

Figure 2

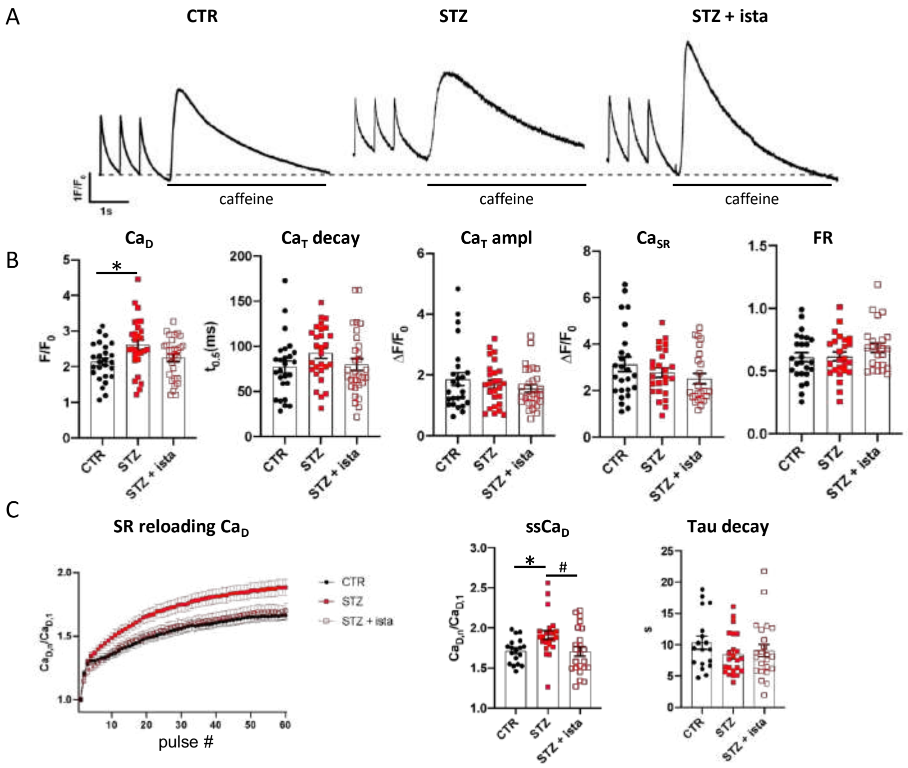
A
CTR
STZ
STZ + ista
1F/F0
1s
caffeine
caffeine
caffeine
B
CaD
*
F/F0
CaT decay
t0,5(ms)
CaT ampl
ΔF/F0
CaSR
ΔF/F0
FR
CTR
STZ
STZ + ista
C
SR reloading CaD
CaD,n/CaD,1
pulse #
CTR
STZ
STZ + ista
ssCaD
*
#
CaD,n/CaD,1
Tau decay
s

Figure 3

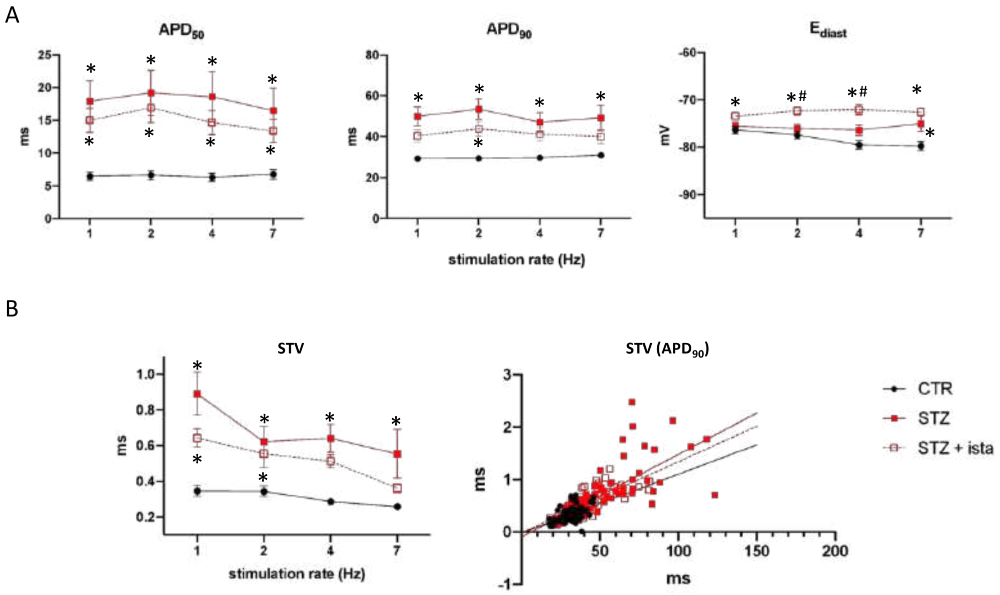
A
APD50
ms
APD90
ms
Ediast
mV
stimulation rate (Hz)
1
2
4
7
B
STV
ms
stimulation rate (Hz)
STV (APD90)
ms
ms
CTR
STZ
STZ + ista

Figure 4

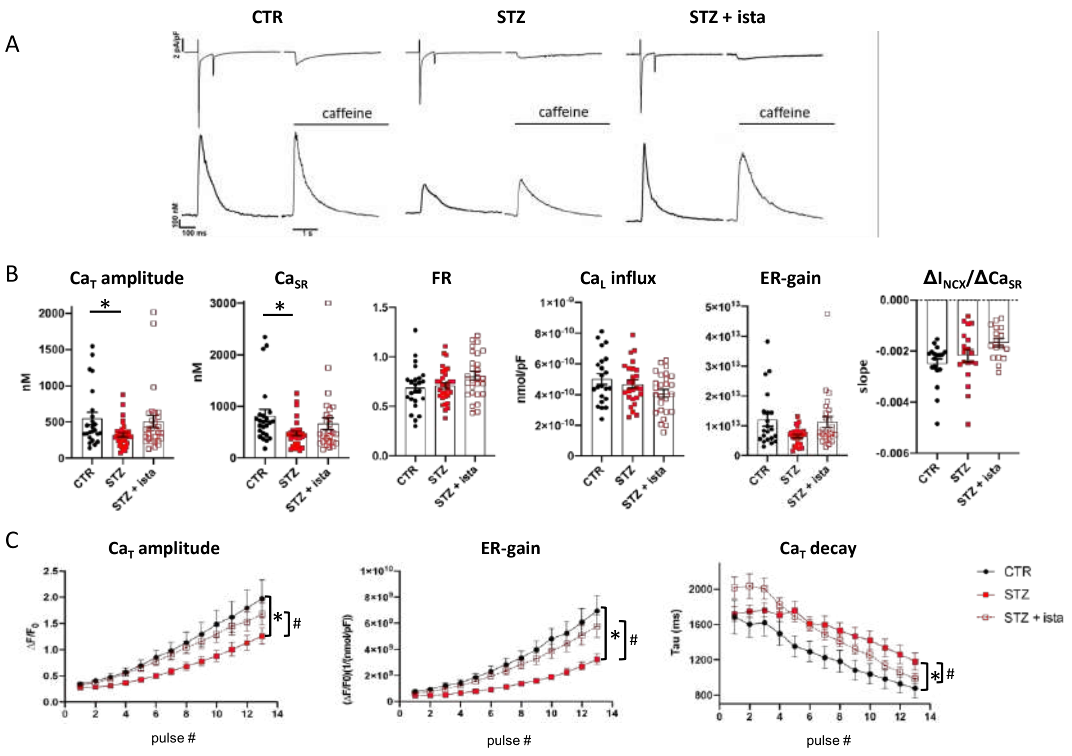
A
CTR
STZ
STZ + ista
2 pA/pF
caffeine
caffeine
caffeine
100 nM
100 ms
1 s
B
Ca_T amplitude
nM
0
500
1000
1500
2000
*
CTR
STZ
STZ + ista
Ca_{SR}
nM
0
1000
2000
3000
*
FR
0.0
0.5
1.0
1.5
Ca_L influx
nmol/pF
0
2×10^{-10}
4×10^{-10}
6×10^{-10}
8×10^{-10}
1×10^{-9}
ER-gain
0
1×10^{13}
2×10^{13}
3×10^{13}
4×10^{13}
5×10^{13}
$\Delta I_{NCX}/\Delta Ca_{SR}$
slope
0.000
-0.002
-0.004
-0.006
C
Ca_T amplitude
$\Delta F/F_0$
0.0
0.5
1.0
1.5
2.0
2.5
pulse #
*
#
ER-gain
$(\Delta F/F0)/(1/(nmol/pF))$
0
2×10^9
4×10^9
6×10^9
8×10^9
1×10^{10}
pulse #
*
#
Ca_T decay
Tau (ms)
800
1200
1600
2000
pulse #
*
#
0
2
4
6
8
10
12
14
CTR
STZ
STZ + ista

Figure 5

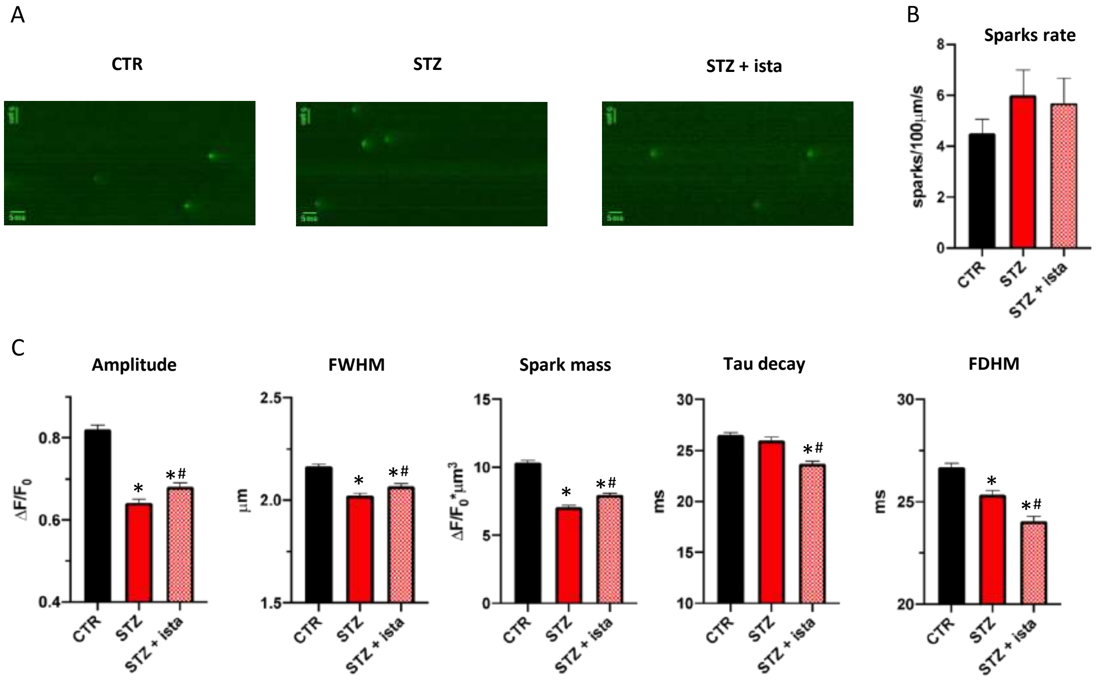
A
CTR
STZ
STZ + ista
5ms
B
Sparks rate
sparks/100μm/s
0
2
4
6
8
CTR
STZ
STZ + ista
C
Amplitude
ΔF/F0
0.4
0.6
0.8
*
*#
FWHM
μm
1.5
2.0
2.5
*
*#
Spark mass
ΔF/F0*μm3
0
5
10
15
*
*#
Tau decay
ms
10
15
20
25
30
*#
FDHM
ms
20
25
30
*
*#
CTR
STZ
STZ + ista

Table 1

	CTR	STZ	P vs CTR
Fasting glycaemia (mg/dL)	94 ± 2	390 ± 14	*
Non fasting glycaemia (mg/dL)	126 ± 4	560 ± 8	*
BW (g)	401 ± 7	202 ± 6	*
BW gain (g)	230 ± 18	26 ± 8	*
HW/TL (g/cm)	0.35 ± 0.02	0.28 ± 0.009	*
LVW/HW (%)	66.6 ± 1.1	63.4 ± 0.7	*
KW/TL (g/cm)	0.52 ± 0.02	0.6 ± 0.02	*

Table 2

	CTR	STZ	P vs CTR
IVSTd (mm)	1.67 ± 0.08	1.43 ± 0.05	*
PWTd (mm)	1.68 ± 0.10	1.41 ± 0.07	*
LVEDD (mm)	8.33 ± 0.27	7.82 ± 0.16	ns
IVSTs (mm)	2.12 ± 0.11	2.00 ± 0.07	ns
PWTs (mm)	2.04 ± 0.09	1.98 ± 0.09	ns
LVESD (mm)	5.84 ± 0.24	4.99 ± 0.19	**
FS (%)	30.06 ± 1.41	36.41 ± 1.77	**
E (m/s)	0.86 ± 0.03	0.75 ± 0.02	**
A (m/s)	0.46 ± 0.04	0.53 ± 0.03	ns
E/A	2.04 ± 0.18	1.54 ± 0.13	*
DT (ms)	42.35 ± 1.42	53.92 ± 1.38	**
DT/E (s^2/m)	50.60 ± 2.64	74.58 ± 3.57	**
E/DT (m/s^2)	20.74 ± 1.20	14.16 ± 0.71	**
s’ (mm/s)	45.42 ± 1.76	32.71 ± 1.33	**
e’ (mm/s)	52.87 ± 1.53	32.70 ± 2.41	**
a’ (mm/s)	31.79 ± 1.74	30.95 ± 2.26	ns
e'/a’	1.74 ± 0.10	1.19 ± 0.16	*
E/e'	16.37 ± 0.64	25.23 ± 1.63	**
HR (bpm)	264.82 ± 3.85	212.13 ± 4.84	**
SV (mL)	0.92 ± 0.08	0.81 ± 0.06	ns
CO (mL/min)	243.58 ± 22.01	178.86 ± 13.54	*
EF (%)	60.13 ± 3.19	69.52 ± 2.74	*

2.11. Supplementary methods

2.11.1. Echocardiography

Eight weeks after vehicle/STZ injection, rats were submitted to a transthoracic echocardiographic and Doppler evaluation, performed under ketamine-xylazine (130-7.5 mg/kg I.P.) anesthesia, (CX50 Echographer, Philips, equipped with a 12 MHz probe, S12-4 Transducer, Philips, Italy).

Two-dimensionally guided M-mode recordings were used to obtain short-axis measurements of left ventricular end-diastolic diameter (LVEDD), left ventricular end-systolic diameter (LVESD), posterior wall thickness in diastole (PWTd) and interventricular septum thickness in diastole (IVSTd) according to the American Society of Echocardiography guidelines. Fractional shortening was calculated as FS = (LVEDD - LVESD)/LVEDD.

Mitral inflow was measured by pulsed Doppler at the tips of mitral leaflets from an apical 4-chamber view to obtain early and late filling velocities (E, A), and deceleration time (DT) of early filling velocity. The deceleration slope was calculated as the ratio E/DT. The mitral deceleration index was calculated as the ratio DT/E.

Tissue Doppler Imaging (TDI) was evaluated from the apical 4 chamber view to record mitral annular movements, i.e., peak myocardial systolic (s'), and early and late diastolic velocity (e' and a').

End diastolic volume (EDV) and end systolic volume (ESV) were calculated from the diameters using the Teicholz formula. Ejection fraction, expressed as a percentage (EF%), was calculated by the formula: (EDV-ESV)/EDV*100.

2.11.2. Heart homogenate preparations

Rats were sacrificed at 9 weeks after STZ injection. Left ventricle (LV) tissues from control and STZ rats were rapidly excised, frozen in liquid nitrogen and stored at -80°C. Tissues were homogenized (1g/4ml buffer) in a medium containing 300 mM sucrose, 50 mM K-phosphate, pH 7, 10 mM NaF, 0.3 mM PMSF, 0.5 mM DTT and centrifuged at 35.000g for 30 min. The final pellet was suspended in the same medium and stored in aliquots at -80°C until use.

Protein concentration was determined by Lowry assay[1] using bovine serum albumin as standard, and molecular purity was checked using SDS-polyacrylamide gel electrophoresis.

2.11.3. Purification of renal Na-K ATPase

Rat kidneys were sliced and the outer medulla was dissected, pooled and suspended (1g/10 ml) in a sucrose-histidine solution containing 250 mM sucrose, 30 mM histidine and 5 mM EDTA, pH 7.2 and homogenized. The homogenate was centrifuged at 6,000 g for 15 min, the supernatant was decanted and centrifuged at 48,000 g for 30 min. The pellet was suspended in the sucrose-histidine buffer and incubated for 20 min with a sodium-dodecyl-sulphate (SDS) solution, dissolved in a gradient buffer, containing 25 mM imidazole and 1 mM EDTA, pH 7.5. The sample was layered on the top of a sucrose discontinuous gradient (10, 15 and 29.4%) and centrifuged at 60,000 g for 115 min. The final pellet was suspended in the gradient buffer.

2.11.4. SERCA2a and Na^+/K^+ pump activity measurement

SERCA2a activity was measured *in vitro* as ^{32}P-ATP hydrolysis at different Ca^{2+} concentrations (100-2000 nM) as previously described[2]. The heart homogenate (30 µg) was pre-incubated for 5 minutes at 4°C in 80 µL of a solution containing (mM): 100 KCl, 5 $MgCl_2$, 20 mM Tris, 5 mM NaN_3, 1 µM A23187, 1 µM Ruthenium red, at pH 7.4. After pre-incubation, 20 µl of a 5 mM Tris-ATP solution containing 50 nCi of ^{32}P-ATP (0.5-3 Ci/mmol, Perkin Elmer) were added. After 15 min at 37°C, the ATP hydrolysis was stopped by acidification with 100 µL ice-cold perchloric acid 20% v/v. ^{32}P-phosphate was separated by centrifugation with activated charcoal (Norit A, SERVA) and the radioactivity was measured by liquid scintillation counting in a beta counter (Microbeta Trilux, Perkin Elmer). SERCA2a-dependent activity was identified as the portion of total hydrolytic activity inhibited by 10 µM Cyclopiazonic Acid (CPA). Ca^{2+} concentration-response curves were fitted by using a logistic function to estimate SERCA2a Ca^{2+} affinity (K_d Ca^{2+}) and V_{max}.

Na/K-ATPase activity was assayed *in vitro* by measuring the release of ^{32}P-ATP, as previously described[3]. Increasing concentrations of the standard ouabain, or istaroxime, were incubated with 0.3 µg of purified rat kidney enzyme for 10 min at 37°C in 120 µl final volume of a medium, containing 140 mM NaCl, 3 mM $MgCl_2$, 50 mM Hepes-Tris, 3 mM ATP, pH 7.5. Then, 10 µl of incubation solution containing 10 mM KCl and 20 nCi of ^{32}P-ATP (3-10 Ci/mmol) were added, the reaction continued for 15 min at 37°C and was stopped by acidification with 20% v/v ice-cold perchloric acid. ^{32}P was separated by centrifugation with activated Charcoal (Norit A, Serva) and the radioactivity was measured. The inhibitory activity was expressed as percent of the control samples carried out in the absence of ouabain or tested compound. The concentration of compound causing 50% inhibition of the Na,K-ATPase activity (IC_{50}) was calculated by using by using a logistic function.

2.11.5. Western blot analysis

Samples of LV homogenates or isolated LV myocytes were separated by SDS-polyacrylamide gel electrophoresis (4-12% Bis-Tris Criterion BIO-RAD gels), blotted for 1h and incubated overnight at 4°C with specific primary antibodies, followed by 1h incubation with specific secondary antibodies, labelled with fluorescent markers (Alexa Fluor or IRDye) and quantified by Odyssey Infrared Imaging System (LI-COR).

Antibodies: polyclonal anti-SERCA2 (N-19; Santa Cruz Biotechnology); monoclonal anti-PLB (2D12, Abcam); polyclonal anti-phospho-Ser^{16}-PLB (Upstate Millipore, Milan, Italy); polyclonal anti-actin (Sigma).

2.11.6. Ventricular myocytes preparation

Male Sprague Dawley LV ventricular myocytes were isolated by using a retrograde coronary perfusion method previously published[4] with minor modifications. Rod-shaped, Ca^{2+}-tolerant myocytes were used within 12 h from dissociation.

2.11.7. Patch clamp measurements

Ventricular myocytes were clamped in the whole-cell configuration (Axopatch 200-A, Axon Instruments Inc., Union City, CA). During measurements, myocytes were superfused at 2 ml/min with Tyrode's solution containing 154 mM NaCl, 4 mM KCl, 2 mM $CaCl_2$, 1 mM $MgCl_2$, 5 mM HEPES/NaOH, and 5.5 mM d-glucose, adjusted to pH 7.35. A thermostated manifold, allowing for fast (electronically timed) solution switch, was used for cell superfusion. All measurements were performed at 35 ± 0.5°C. The pipette solution contained 110 mM K^+-aspartate, 23 mM KCl, 0.2 mM $CaCl_2$ (calculated free-$Ca^{2+}=10^{-7}$ M), 3 mM $MgCl_2$, 5 mM HEPES-KOH, 0.5 mM EGTA-KOH, 0.4 mM GTP-Na^+ salt, 5 mM ATP-Na^+ salt, and 5 mM creatine phosphate Na^+ salt, pH 7.3. Membrane capacitance and series resistance were measured in every cell but left uncompensated. Current signals were filtered at 2 KHz and digitized at 5 KHz (Axon

Digidata 1200). Trace acquisition and analysis was controlled by dedicated software (Axon pClamp 8.0).

2.11.8. Na^+/K^+ pump current (I_{NaK}) recordings

I_{NaK} was measured as the holding current recorded at -40 mV in the presence of Ni^{2+} (5 mM), nifedipine (5 µM), Ba^{2+} (1 mM) and 4-aminopyridine (2 mM) to minimize contamination by changes in Na^+/Ca^{2+} exchanger, Ca^{2+} and K^+ currents, respectively. Tetraethylammonium-Cl (20 mM) and EGTA (5 mM) were added to the pipette solution and intracellular K^+ was replaced by Cs^+. To optimize the recording conditions, I_{NaK} was enhanced by increasing intracellular Na^+ (10 mM) and extracellular K^+ (5.4 mM). In each cell, the current was recorded at steady state during exposure to increasing concentrations of the drug under test and, finally, to a saturating concentration of ouabain (1 mM) (Fig S5). All drugs were dissolved in dimethyl sulfoxide (DMSO). Control and test solutions contained maximum 1:200 DMSO. Because I_{NaK} inhibition was expressed as percentage of ouabain effect, the latter was used as the asymptote for the estimation of IC_{50} values whenever possible.

2.11.9. Intracellular Ca^{2+} dynamics

Myocytes were incubated in Tyrode solution for 30 min with the membrane-permeant form of the dye, Fluo4-AM (10 µmol/L), and then washed for 15 min to allow de-esterification. Fluo4 emission was collected through a 535 nm band pass filter, converted to voltage, low-pass filtered (100 Hz) and digitized at 2 kHz after further low-pass digital filtering (FFT, 50 Hz).

Protocol 1: Ca^{2+} dynamics in field stimulated cells

Intracellular Ca^{2+} dynamics were measured in Fluo4-loaded field-stimulated (2 Hz) cardiomyocytes superfused with Tyrode's solution. The SR Ca^{2+} content (Ca_{SR}) was estimated at steady-state by applying an electronically timed 10 mM caffeine pulse. The voltage-induced Ca^{2+} transient (Ca_T) was evaluated in terms of diastolic Ca^{2+} (Ca_D) and Ca_T amplitude. SR Ca^{2+} fractional release (FR) was obtained as the ratio between Ca_T amplitude and Ca_{SR}. Moreover, Ca_T decay kinetic was estimated by measuring decay $t_{0.5}$, a parameter indicative of both SERCA and NCX activity in this protocol setting. Furthermore, after SR Ca^{2+} depletion by caffeine, cells were de novo stimulated and Ca_D values during the reloading process were monitored. A quantification of the kinetic of Ca_D enhancement was obtained by mono-exponential fit of Ca_D values normalized to the 1st value recorded after SR depletion ($Ca_{D,n}/Ca_{D,1}$). Moreover, spontaneous Ca^{2+} release (SCR) events were evaluated in each group at resting and during diastole. A fluorescence increase > 3SD the resting fluorescence was considered a SCR. Protocol outline is shown in Fig S1.

Protocol 2: Ca^{2+} dynamics in patch-clamped cells under physiological condition

To better highlight changes in Ca^{2+} handling not affected by modifications of electrical activity, intracellular Ca^{2+} dynamic was evaluated in voltage-clamped cells. $BaCl_2$ (1 mM) and 4-aminopyridine (2 mM) were added to Tyrode's solution to block K^+ channels. Transmembrane current and cytosolic Ca^{2+} were simultaneously measured during a train of depolarizing (100 ms) pulses to 0 mV (0.25 Hz) applied from a holding of -40 mV. At steady state condition, an electronically timed 10 mM caffeine pulse was applied at the same cycle length to estimate SR Ca^{2+} content (Ca_{SR}). Fluorescence signal was converted to Ca_f (see above) and the following parameters were evaluated: Ca_T amplitude, SR Ca^{2+} content (Ca_{SR}) and FR (see above). SR Ca^{2+} content was also evaluated by integrating the NCX current (I_{NCX}) elicited by caffeine and similar results were obtained. The slope of the I_{NCX}/Ca_{SR} relationship during the final third of the caffeine-induced transient was used to estimate NCX 'conductance'. Ca^{2+} influx through L-type Ca^{2+} channel (Ca_L) was evaluated integrating the nifedipine (10μM)-sensitive current during the activation pulse and then converted to nmol of Ca^{2+}. Accordingly, the excitation-release (ER) gain was calculated as the ratio between the fraction of nmol of Ca^{2+} released by SR and nmol of Ca^{2+} entered in the cell ((Ca_T amplitude-Ca_L)/Ca_L).

Protocol 3: Ca^{2+} dynamics in patch-clamped cells under Na^+/Ca^{2+} exchanger (NCX) blockade

To estimate changes in SR function only, the NCX was blocked by removing Na^+ from both sides of the sarcolemma as previously described[5–7]. Cells were incubated in a Na^+/Ca^{2+}-free solution (replaced by equimolar Li^+ and 1 mM EGTA) added with 4-aminopyridine (2 mM) to block K^+ channels. The pipette solution was Na^+-free (Na^+ salts were replaced by Mg^{2+} or Tris salts). The protocol consisted in emptying the SR by a caffeine pulse (with 154 mM Na^+ to allow Ca^{2+} extrusion through NCX) and then progressively refilling it by voltage steps to 0 mV activating Ca^{2+} influx through I_{CaL} in the presence of 1 mM Ca^{2+} (Fig. S2). Similarly, to protocol 2, kinetics of SR Ca^{2+} reloading was evaluated but in the absence of NCX function. We thus considered the rate at which Ca_T amplitude and the ER gain increased during the loading protocol, reflecting the rate at which the SR refilled and the gain of the system. ER gain in this setting was simply evaluated as the ratio between Ca_T amplitude and Ca_L influx at the peak of Ca_T within each pulse. Moreover, the time constant of Ca_T decay (τ_{decay}) reflected Ca^{2+} transport rate across the SR membrane, that can be considered a functional index of SERCA2a activity.

The fluorescence values recorded at resting (*protocol 1*) and at -40 mV after emptying the SR (*protocol 3)* were used as reference (F_0) for signal normalization (F/F_0) after subtraction of background luminescence. In a set of experiments (*protocol 2*) fluorescence was calibrated in nmol/L by estimating in each cell the maximal fluorescence (F_{max}) by increasing at the end of the experiment the intracellular Ca^{2+} concentration through a gentle patch damage. Fluorescence was converted to $[Ca]_f$ according to Eq. S1:

$$[Ca]_f = F * K_d/(F_{max} - F) \qquad \text{(Eq. S1)}$$

assuming a dye Ca^{2+} dissociation constant (K_d) = 400 nmol/L.

2.11.10. Ca^{2+} sparks rate and characteristics

Spontaneous unitary Ca^{2+} release events (Ca^{2+} sparks) were recorded at room temperature in Fluo 4-AM (10μM) loaded myocytes at resting condition. Tyrode bath solution contained 1 mM $CaCl_2$. Images were acquired at x60 magnification in line-scan mode (*xt*) at 0.5 kHz by confocal Nikon A1R microscope. Each cell was scanned along a longitudinal line and #10 *xt* frames (512 pxls x 512 pxls) were acquired. Non-cell fluorescence was acquired too to allow background fluorescence measurement. Confocal setting parameters were kept constant throughout all experimental groups to permit group comparison analysis. Images were analyzed by SparkMaster plugin (Fiji) software[8]. Automatic spark detection threshold (criteria) was imposed to 3.8. Only in focus Ca^{2+} sparks (amplitude > 0.3) were considered to quantify their characteristics. In particular, the following spark parameters were measured: frequency (N of events/s/100μ), amplitude (DF/F0), full width at half-maximal amplitude (FWHM, μ), full duration at half-maximal amplitude (FDHM, ms), full width (FW) and full duration (FD), time to peak (ttp, ms) and decay time constant (τ, ms). Spark mass (spark amplitude*1.206* $FWHM^3$) was also calculated as index of Ca^{2+} spark volume[9].

2.11.11. Compounds

Stock Fluo4-AM solution (1 mM in DMSO) was diluted in Tyrode's solution. Istaroxime was dissolved in DMSO at 10-100 mM and then diluted to get a final concentration of 100 or 500 nM. The final DMSO did not exceed 0.1% (if it is not different specify).

Istaroxime was synthesized at SciAnda (/Changshu) Pharmaceuticals Ltd, Jiangsu (China). Fluo4-AM from Molecular Probes and all other chemicals from Merck (Darmstadt, Germany).

2.11.12. References

1. Lowry OH, Rosebrough NJ, Farr AL, Randall RJ. Protein measurement with the Folin phenol reagent. *J Biol Chem* 1951;**193**:265–275.
2. Micheletti R, Palazzo F, Barassi P, Giacalone G, Ferrandi M, Schiavone A, Moro B, Parodi O, Ferrari P, Bianchi G. Istaroxime, a Stimulator of Sarcoplasmic Reticulum Calcium Adenosine Triphosphatase Isoform 2a Activity, as a Novel Therapeutic Approach to Heart Failure. *Am J Cardiol* 2007;**99**:24A-32A.
3. Ferrandi M, Tripodi G, Salardi S, Florio M, Modica R, Barassi P, Parenti P, Shainskaya A, Karlish S, Bianchi G, Ferrari P. Renal Na,K-ATPase in genetic hypertension. *Hypertension* 1996;**28**:1018–1025.
4. Rocchetti M, Sala L, Rizzetto R, Irene Staszewsky L, Alemanni M, Zambelli V, Russo I, Barile L, Cornaghi L, Altomare C, Ronchi C, Mostacciuolo G, Lucchetti J, Gobbi M, Latini R, Zaza A. Ranolazine prevents INaL enhancement and blunts myocardial remodelling in a model of pulmonary hypertension. *Cardiovasc Res* 2014;**104**:37–48.
5. Rocchetti M, Besana A, Mostacciuolo G, Micheletti R, Ferrari P, Sarkozi S, Szegedi C, Jona I, Zaza A. Modulation of sarcoplasmic reticulum function by Na+/K + pump inhibitors with different toxicity: Digoxin and PST2744 [(E,Z)-3-((2-aminoethoxy)imino)androstane-6,17-dione hydrochloride]. *J Pharmacol Exp Ther* 2005;**313**:207–215.
6. Rocchetti M, Alemanni M, Mostacciuolo G, Barassi P, Altomare C, Chisci R, Micheletti R, Ferrari P, Zaza A. Modulation of sarcoplasmic reticulum function by PST2744 [Istaroxime; (E,Z)-3-((2-aminoethoxy)imino) androstane-6,17-dione hydrochloride] in a pressure-overload heart failure model. *J Pharmacol Exp Ther* 2008;**326**:957–965.
7. Alemanni M, Rocchetti M, Re D, Zaza A. Role and mechanism of subcellular Ca2+ distribution in the action of two inotropic agents with different toxicity. *J Mol Cell Cardiol* 2011;**50**:910–918.

8. Picht E, Zima A V., Blatter LA, Bers DM. SparkMaster: Automated calcium spark analysis with ImageJ. *Am J Physiol - Cell Physiol* 2007;**293**:C1073–C1081.

9. Hollingworth S, Peet J, Chandler WK, Baylor SM. Calcium sparks in intact skeletal muscle fibers of the frog. *J Gen Physiol* 2001;**118**:653–678.

2.12. Supplementary figures

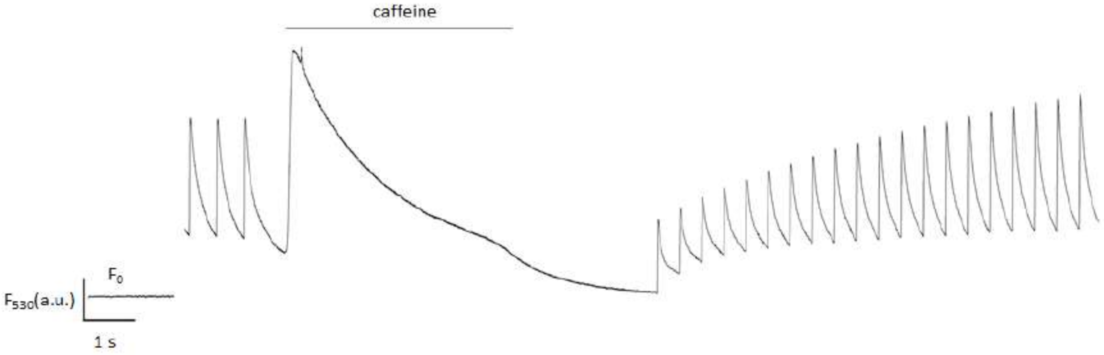

Figure S1. Protocol to evaluate intracellular Ca^{2+} dynamics in field-stimulated cardiomyocytes. Left ventricular myocytes were field stimulated (2Hz) and evocated Ca^{2+} transients were recorded before and after caffeine (10 mM)-induced SR depletion.

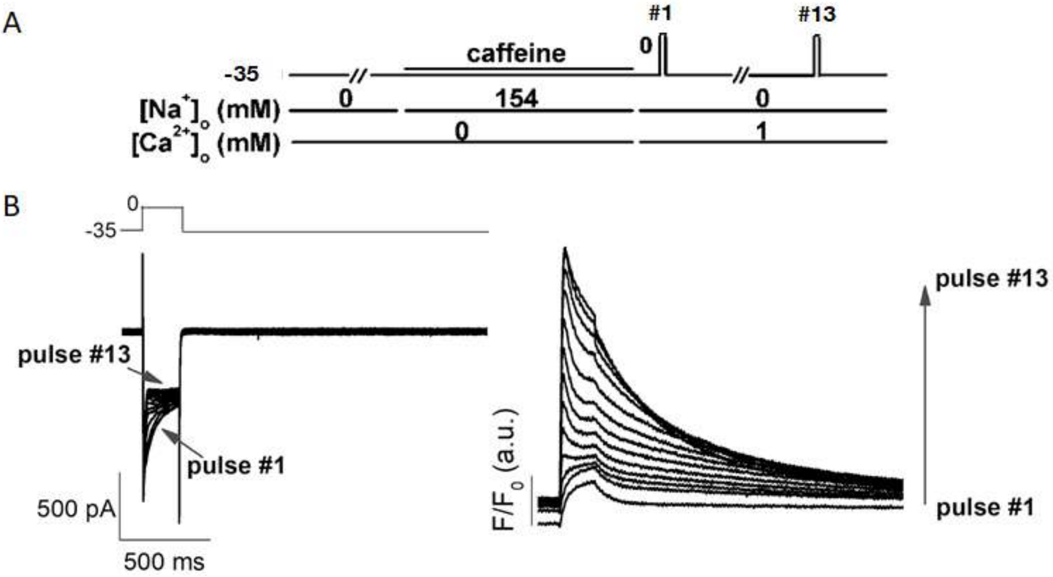

Figure S2. Protocol to evaluate intracellular Ca^{2+} dynamics in patch-clamped cells under Na^{+}/Ca^{2+} exchanger (NCX) blockade. (A) Protocol outline. (B) Transmembrane current (left) and Ca^{2+} transients (right) recordings during SR reloading after caffeine-induced SR depletion in patch-clamped cells.

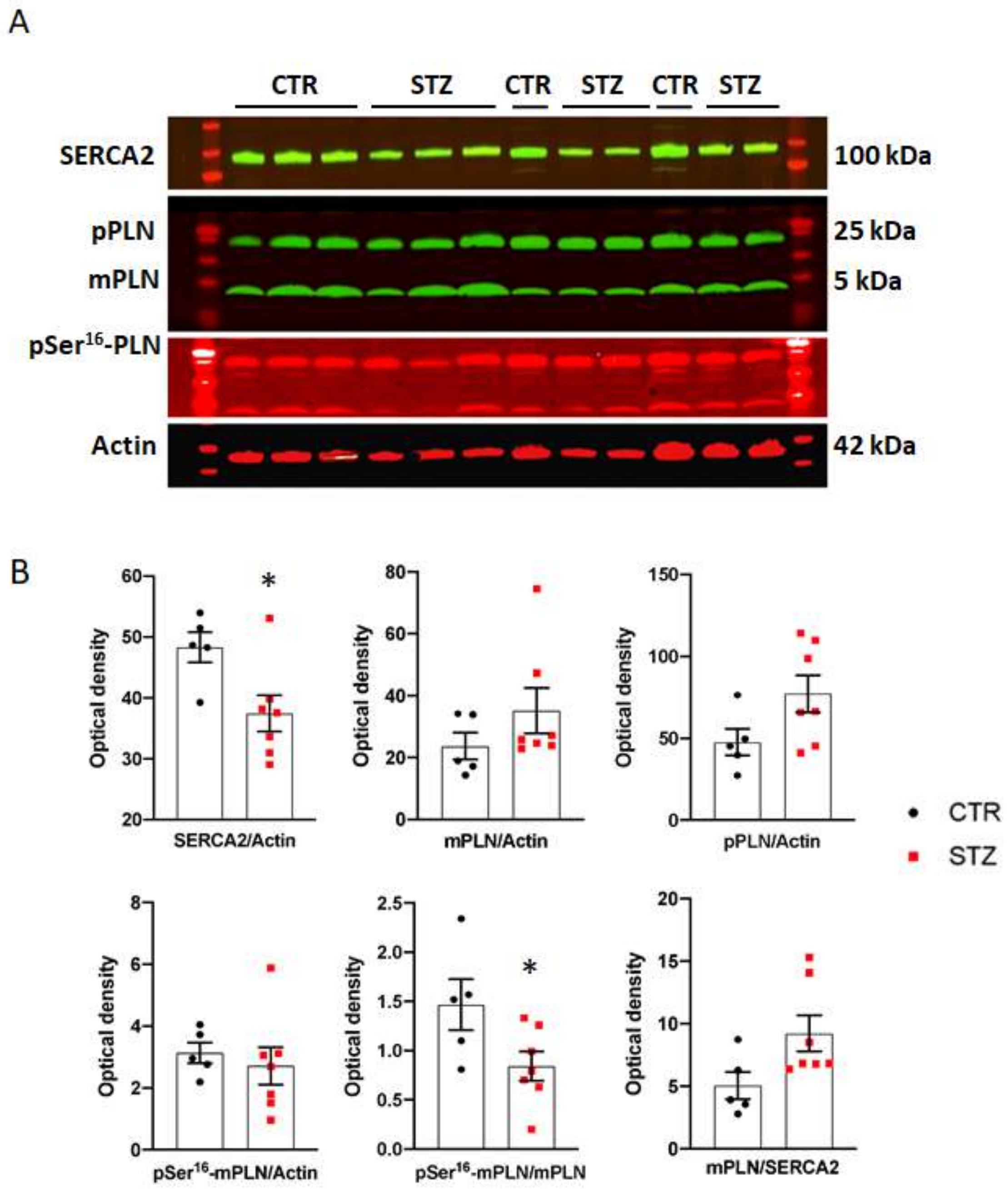

Figure S3. Effect of STZ and istaroxime on SERCA2 and PLN levels in cardiac homogenates. (A) Representative Western blot for SERCA2, monomeric (m) and pentameric (p) unphosphorylated and Ser^{16} phosphorylated (pSer^{16}) PLN in homogenates preparation from STZ and CTR hearts. (B) Densitometric analysis of Western blot for SERCA2, mPLN, pPLN, pSer^{16}-PLN protein level and mPLN/SERCA2 ratio. Values are expressed as optical density in arbitrary units. *=$p<0.05$ vs CTR (unpaired *t*-test); CTR N=5, STZ N=7.

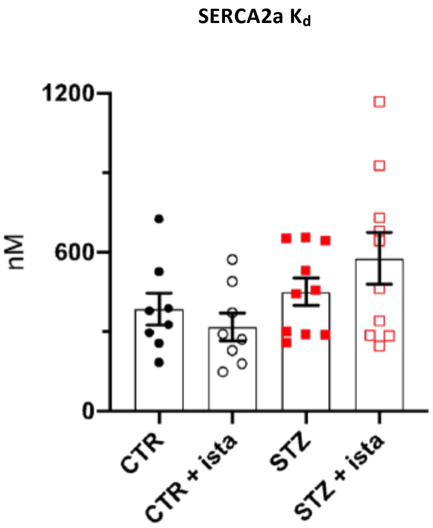

Figure S4. Effects of STZ and istaroxime on SERCA2a Ca^{2+} affinity (K_d) in cardiac homogenates. The kinetic parameter was estimated by fitting the Ca^{2+} activation curve through a logistic function. N=5 for each group.

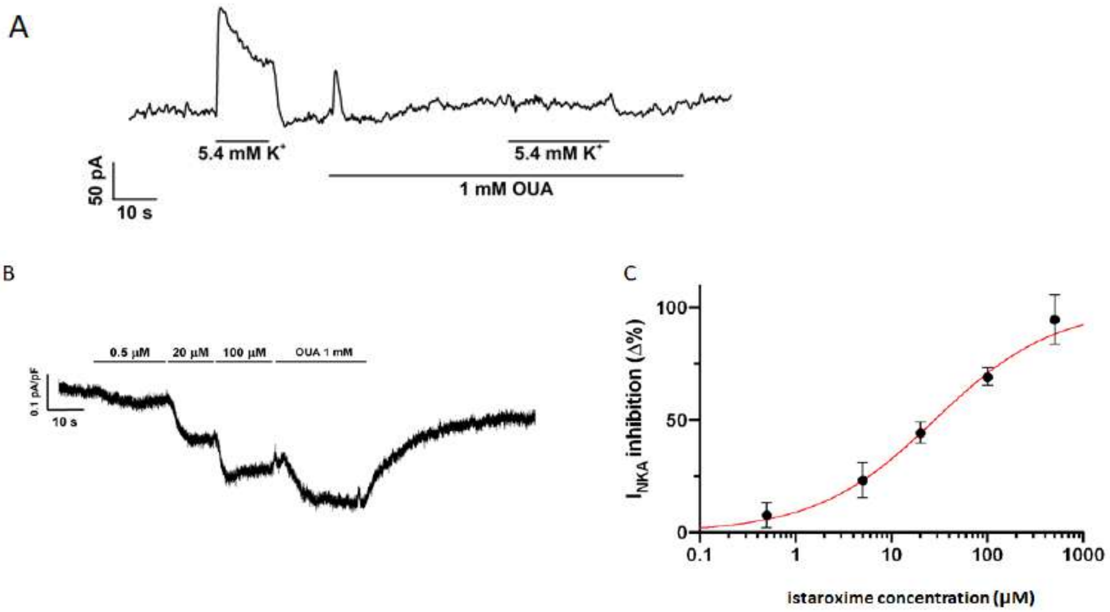

Figure S5. NKA inhibition by istaroxime in isolated cardiomyocytes. (A) Example of I_{NKA} evocated at -40 mV by 5.4 mM K^+, totally abolished by a saturating concentration of ouabain (1 mM) in CTR LV myocyte. (B) I_{NKA} recordings at -40 mV during exposure to increasing concentrations of istaroxime and, finally, to 1 mM ouabain. (C) Concentration-dependent I_{NKA} inhibition by istaroxime; the best logistic fit is shown in red (IC_{50} 32 ± 4 µM). CTR N=2/n=6-19.

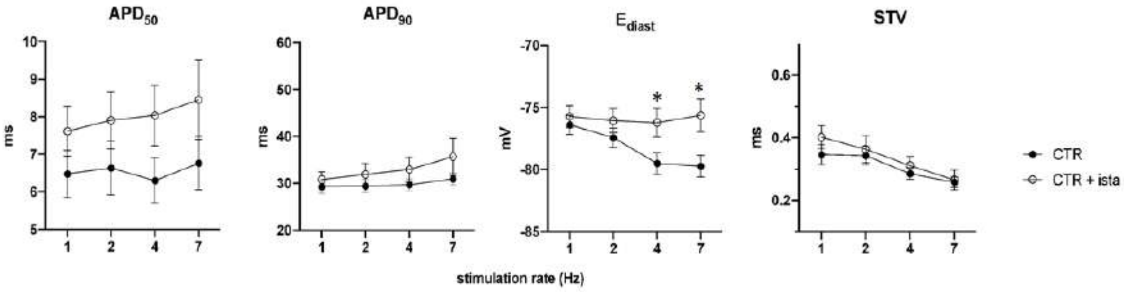

Figure S6. Effect of istaroxime on AP parameters in CTR myocytes. Average values of APD_{50}, APD_{90}, E_{diast} and STV at all pacing rates. *= $p<0.05$ vs basal condition (w/o istaroxime) (two-way ANOVA, Tukey's multiple comparison). CTR N=4 / n=20-29; CTR + ista N=4 / n=20-25.

Chapter 3

Role of cardiac L- and T-type voltage gated Ca^{2+} channels in heart automaticity

3.1. Cardiac conduction system

Pacemaker activity in the heart is generated by specialized myocytes, able to generate periodical oscillations of their membrane potential (V_m). These cells are thus called "pacemaker" cells[1].

In the mammalian heart, three major structures are endowed with automaticity and are able to drive the heartbeat: the sino-atrial node (SAN), the atrioventricular node (AVN), and the Purkinje fibers network (PFN) (Fig. 1). Under physiological conditions the cardiac impulse has origin in the SAN. The intrinsic SAN beating rate is normally faster than that of the cardiac conduction system and suppresses pacemaking in the AVN and Purkinje network. However, automaticity in AVN can become dominant in case of SAN block or failure. Purkinje fibers can also generate a viable rhythm in conditions of atrioventricular block [2]. For these reasons, the SAN region is indicated as the primary pacemaker, while the AVN and Purkinje fibers are indicated as secondary (or accessory) pacemakers.

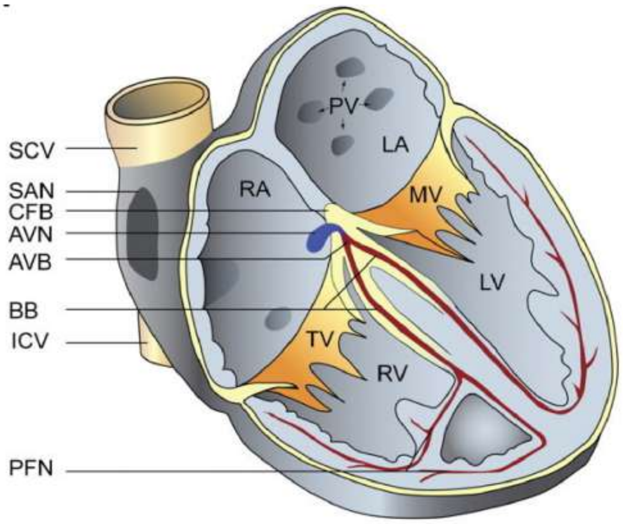

Figure 1: the mammalian heart with the cardiac conduction system. The sinoatrial node (SAN) is located at the entry of the superior vena cava (SCV) in the right atrium (RA). The atrioventricular node (AVN) extends in a region delimited by the inferior vena cava (ICV), the central fibrous body (CFB), and the tricuspid valve (TV). The atrioventricular bundle (AVB) divides in the bundle branches (BB) and originates the left and right Purkinje fibers network (PFN). Other abbreviations are: LA, left atrium; PV, pulmonary veins; MV, mitral valve; RV, right ventricle; LV, left ventricle. [Adapted from Moorman and Christoffels, 2003]

SAN pacemaker tissue is located in the intercaval region (between the inferior vena cava, IVC, and the superior vena cava, SVC) and extends towards the endocardial side of the crista terminalis (CT). Spontaneously active cells are found in the area delimited by the crista terminalis and the interatrial septum (IAS) (Fig. 2). CT mediates the cardiac impulse from the SAN to the AVN by high level of connexins (Cx) expression. Cx43 is the most abundant Cx of the gap junctions that allow the electrical coupling between the cells.

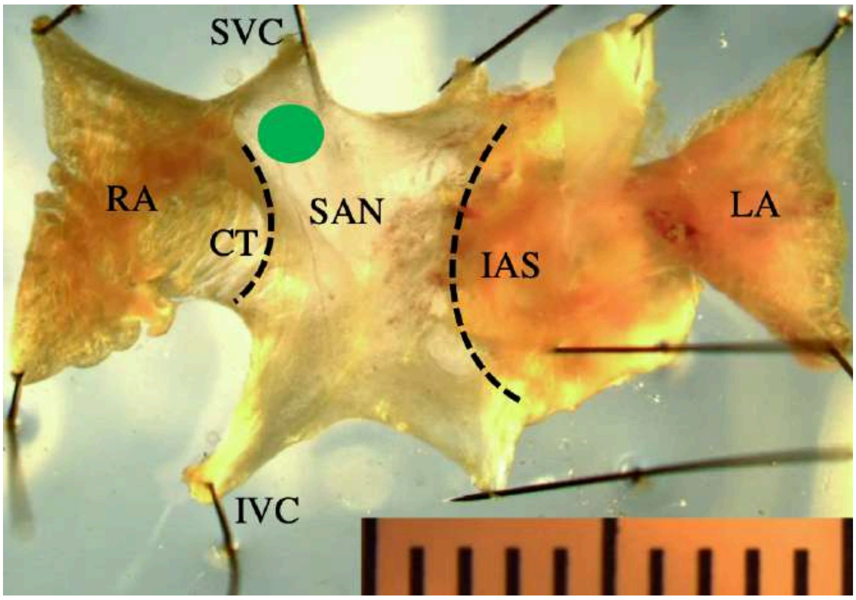

Figure 2: sino-atrial tissue in mouse. The green dot indicates the leading SAN pacemaking site. Abbreviations are: SVC, superior vena cava; IVC, inferior vena cava; LA, left atrium; RA, atrium; CT, crista terminalis; IAS, interatrial septum.

3.2. Cardiac automaticity: membrane and Ca^{2+} clocks

The pacemaker mechanism has been intensively studied for more than 40 years. The generation of the automaticity in cardiac pacemaker cells is due to the diastolic depolarization (DD), a spontaneous slowly depolarizing phase of the action potential (AP) cycle. During this phase the membrane potential progressively becomes less negative until it reaches the threshold for triggering a new action potential. Because the DD is an electrical phenomenon, pacemaking has been first interpreted in terms of activation of specific ionic currents. However, recently the Ca^{2+} release from the sarcoplasmic reticulum (SR) was proposed as an important player in the pacemaker mechanism.

Two main models of pacemaker activity have been proposed:

- the so-called "membrane (M) clock" that considers the activity of ion channels of the plasma as the trigger of the diastolic depolarization
- The "Ca^{2+} clock" model of pacemaker activity highlights a spontaneous phenomenon of local Ca^{2+} releases (LCRs) from the ryanodine receptors (RyRs). This spontaneous Ca^{2+} release stimulates the activity of the Na^+/Ca^{2+} exchanger which generates an inward current that initiates the diastolic depolarization.

The M clock model considers the pacemaker activity as a membrane potential oscillation that depends on periodically outward repolarizing and inward depolarizing currents fluctuations. The channel activation sequence acts as a clock to spontaneously initiate the mechanism that governs rhythm and heart rate.

In the M clock, the "funny current" (I_f) is consider as the key initiator of the diastolic depolarization. I_f is an inward Na^+/K^+ current carried by hyperpolarization-activated cyclic nucleotide-gated (HCN) (reversal potential of approximately -25 mV)[3]. I_f is originated specifically at the initial phase of the diastolic depolarization, following the deactivation of outward delayed rectifier K^+ current (I_{Kr}), and triggering the activation of inward currents. Inward currents include Na^+-dependent background current (i.e. $I_{Na\text{-}TTX\ sensitive}$); the T- and L-type Ca^{2+} currents, I_{CaT} and I_{CaL}; and possibly, sustained inward current, I_{st} (Fig. 3)[4].

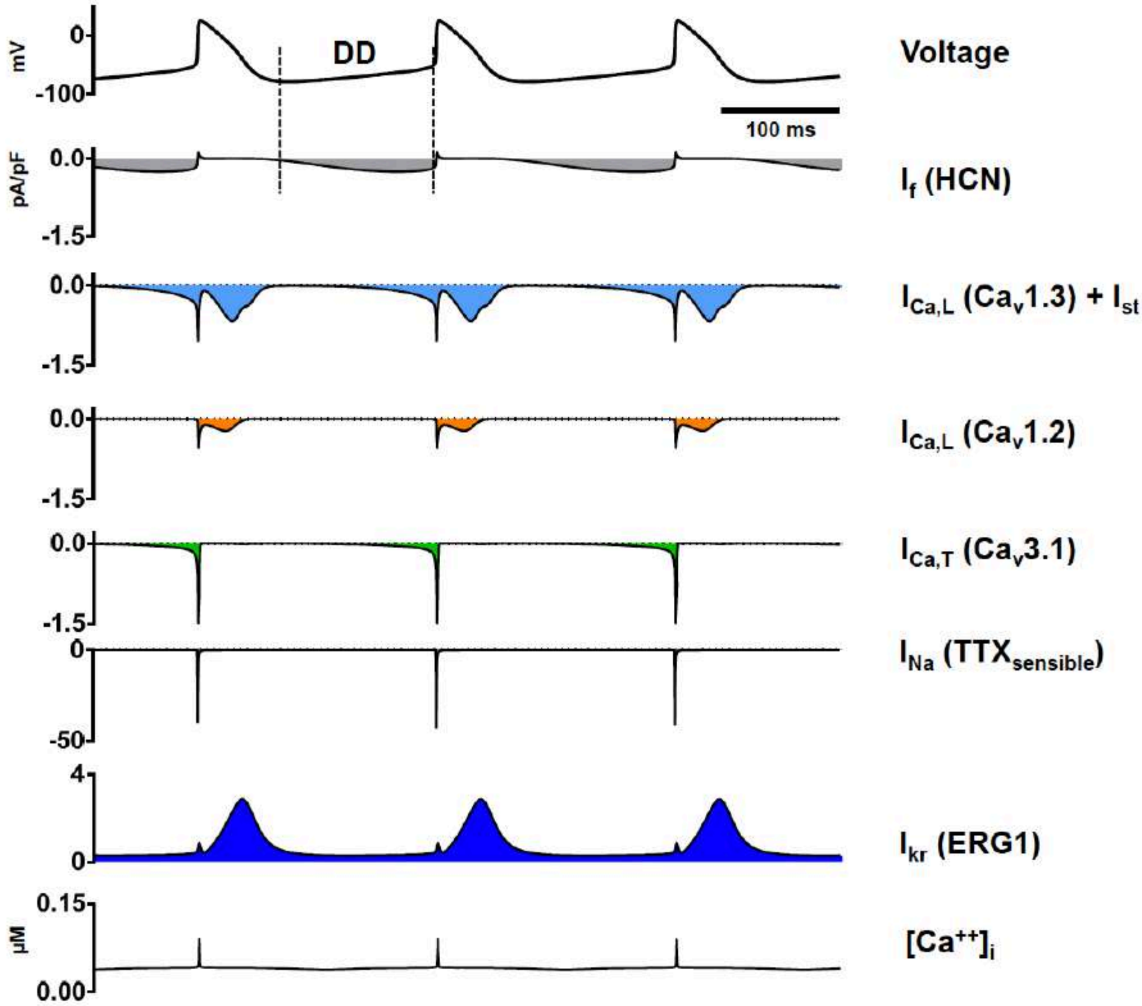

Figure 3: ion channels membrane clock. Numerical simulation of spontaneous activity of mouse pacemaker cells; ion channels involved in the pacemaker cells AP (Christel et al. J Physiol 2012). The model shows the sequential activation of ionic currents and SR Ca^{2+} release during the DD. At the beginning of the DD, both If and $Ca_v1.3$-mediated currents (I_{CaL} and I_{st}) carry inward current to generate the DD. $Ca_v3.1$-mediated I_{CaT} also contributes to the DD during the action potential upstroke phase, $Ca_v1.2$ mediated I_{CaL} is activated. The predominant repolarizing K^+ current in the absence of cholinergic activation is I_{Kr} [According to Mesirca et al., 2018]

In the "Ca^{2+} clock" model of pacemaking (Fig. 4), SAN cells exhibit spontaneous voltage-independent SR local Ca^{2+} releases (LCRs) from the ryanodine receptors (RyRs) during the late DD[5]. These LCRs induce a Na^+-Ca^{2+} exchanger (NCX)-mediated inward current (I_{NCX}), as each Ca^{2+} that is transported out of the cell is exchanged for $3Na^+$. The forward mode NCX, by generating inward I_{NCX}, couples LCRs to the late DD acceleration. The membrane current fluctuations generated by LCRs are sufficient to drive V_m oscillations that confer the exponential increase to the late phase of DD[6]. Consequently, the L-type Ca^{2+} channels (I_{CaL}) are rapidly activated (activation threshold is approximately -50 mV to -40 mV for $Ca_v1.3$-mediated I_{CaL}, see below) and the AP rapid upstroke is generated. Together with I_{CaL}, the T-type Ca^{2+} channels (I_{CaT}) cooperate to the diastolic depolarization (activation threshold is approximately -70 mV) with a slow-activated low current[7,8,9]. The action potential upstroke of pacemaker cells is mainly driven by Ca^{2+} rather than Na^+ channels (I_{Na}). In particular, I_{Na} does not participate in the generation of automaticity per se (in the central SAN), but can influence heart rate by contributing to impulse propagation with the SAN and from the SAN to the atrium[10].

Recently, Torrente et al., 2016[11] indicated that SR Ca^{2+} release events are triggered following the activation of a specific L-type Ca^{2+} channel ($Ca_V1.3$) in the mechanism of diastolic Ca^{2+}-induced Ca^{2+} release (CICR). SAN cells do not have T-tubules, so that AP-triggered Ca^{2+} release, resulting in a global subsarcolemmal and cytosolic Ca^{2+} transient, occurs via subsarcolemmal RyRs[12].

The relative importance of both the "membrane clock" and "Ca^{2+} clock" in pacemaker function remains controversial.

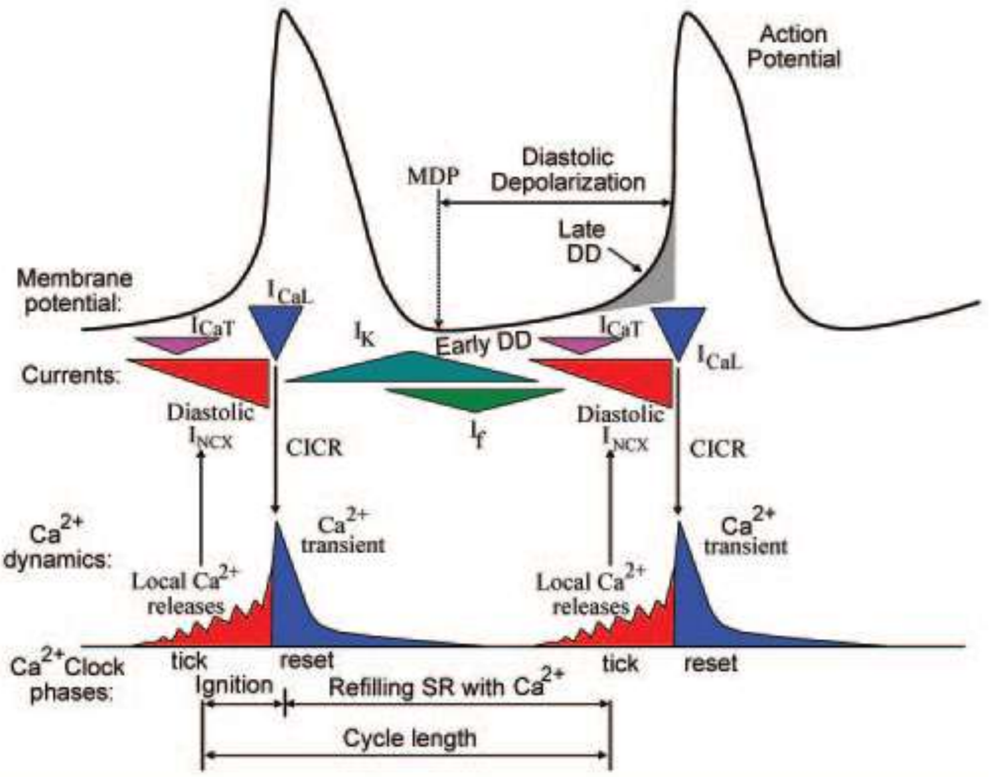

Figure 4: the Ca^{2+}-clock. Schematic illustration of the Ca^{2+} clock implication (red) in the late DD during the action potential [According to Lakatta et al., 2010].

3.3. Cardiac voltage gated Ca^{2+} channels: L- and T-type mediated Ca^{2+} currents

Voltage gated Ca^{2+} channels (VGCCs) are an important pathway for Ca^{+} entry in pacemaker cells. In the mammalian heart, L- and T-type mediated Ca^{2+} currents are expressed in SAN, AVN and PFN. L-type VGCCs are activated at more positive potentials than T-Type VGCCs. In particular I_{CaL} as a "high"- threshold Ca^{2+} current is activated from about -30mV and distinguished from T-type mediated Ca^{2+} current (I_{CaT}), a "low" threshold Ca^{2+} current activated at -50mV[13]. VGCCs channels are hetero-oligomeric complex of an α_1 subunit and an accessory α2, δ and β subunit (Fig. 5). The α_1 subunit comprises four homologous domains, I–IV, each containing six transmembrane segments (S1–6) and a pore region between segments S5 and S6; segment S4 in each domain has a net positive charge and serves as the voltage sensor[14].

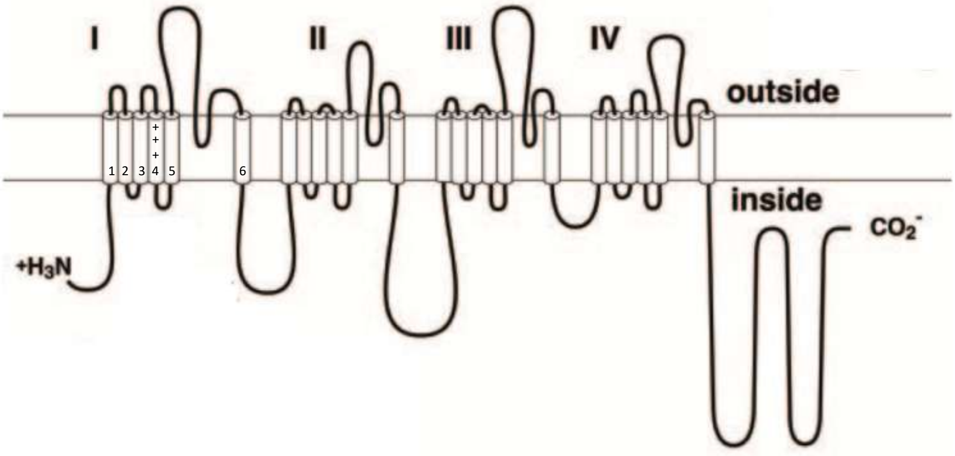

Figure 5: α_1 subunit structure. [Adapting from Catterall et al., 2005]

From the 10 different α_1 subunit isoforms, four are involved in the generation of the L-type Ca^{2+} channels and named α_{1S} ($Ca_v1.1$), α_{1C} ($Ca_v1.2$), α_{1D} ($Ca_v1.3$), and α_{1F} ($Ca_v1.4$) and they are highly sensitive to DHP (dihydropyridine) Ca^{2+} channels modulators[15]. $Ca_v1.1$ subunits are expressed in the skeletal muscle, where they couple membrane excitation to contraction[16], $Ca_v1.4$ expression is predominant in the retina, spinal cord and immune cells[17]. $Ca_v1.2$ and $Ca_v1.3$ are expressed in neurons, as well as in cells from the neuroendocrine and cardiovascular systems[18]. $Ca_v1.2$ is expressed in the whole heart but predominantly in atria and ventricles; $Ca_v1.3$ expression is predominant in the supraventricular regions with higher amounts of $Ca_v1.3$ in the rhythmogenic centers[19]. Electrophysiological measurements showed clear differences between $Ca_v1.3$ and $Ca_v1.2$

mediated I_{CaL}. $Ca_v1.3$-mediated I_{CaL} activates at more negative voltages and displays slower current inactivation during depolarization allowing these channels to mediate Ca^{2+} influx during weak depolarization[7] (Fig. 6). Recently, Toyoda et al. demonstrated the involvement of $Ca_v1.3$ in the generation of a voltage-dependent, DHP sensitive Na^+ current (I_{st}) in SAN cells. I_{st} is identified as a sustained inward current with several properties (low voltage for activation, DHP sensitivity, Na^+ permeability and slow inactivation). Their results suggest that $Ca_v1.3$ α_1-subunits in the SAN cell not only form underlies $Ca_V1.3$-mediated L-type Ca^{2+} current, but also mediates I_{st}[20]. Future studies will address if $Ca_v1.3$ are also permeable to Na^+ or whether a phenomenon of coupling between the $Ca_v1.3$ α_1 subunit and a Ca^{2+} activated cationic channel underlies I_{st}.

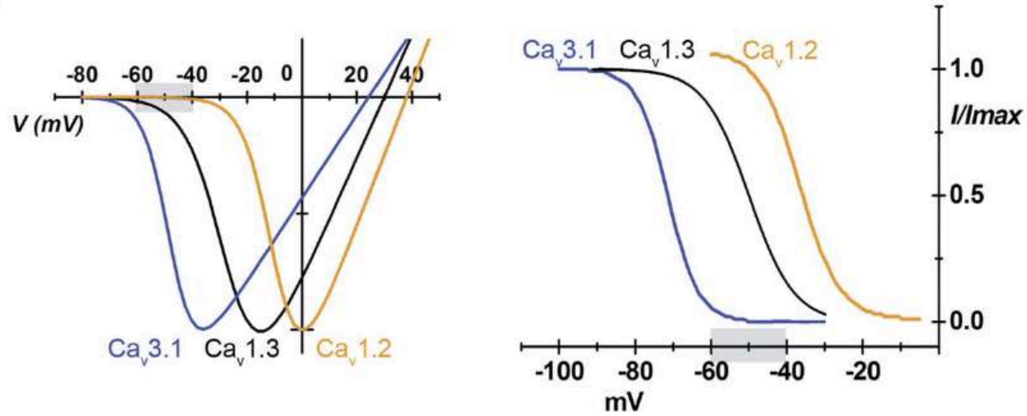

Figure 6: voltage-dependent Ca^{2+} currents in pacemaker SAN cells. Current-to-voltage relationships (left) and steady-state inactivation (right) of native SAN $Ca_v3.1$, $Ca_v1.3$, and $Ca_v1.2$ channels. [According to Mangoni et al., 2006]

Moreover, I_{CaT} show pure voltage-dependent inactivation and inactivation is complete at more negative membrane potentials than I_{CaL}[21]. Three genes encoding for T-type α-subunits have been cloned and named $Ca_v3.1$, $Ca_v3.2$ and $Ca_v3.3$. While the $Ca_v3.3$ isoform is not present in the heart, the expression of $Ca_v3.1$ and $Ca_v3.2$ isoforms in the myocardium varies according to the developmental status of the tissue. $Ca_v3.2$ constitutes the predominant T-type isoform in embryonic heart tissue[22]; $Ca_v3.1$ channels expression increases during perinatal period and reaches its maximal in adulthood[23]. In adult SAN $Ca_v3.1$ expression is higher than $Ca_v3.2$[24]. Contrary to the Ca_v1 family, the Ca_v3 family is almost insensitive to DHPs and at present, no selective inhibitor to discriminate the contribution of $Ca_v3.1$ and $Ca_v3.2$ channels to the total I_{CaT} is available (Tab. 1).

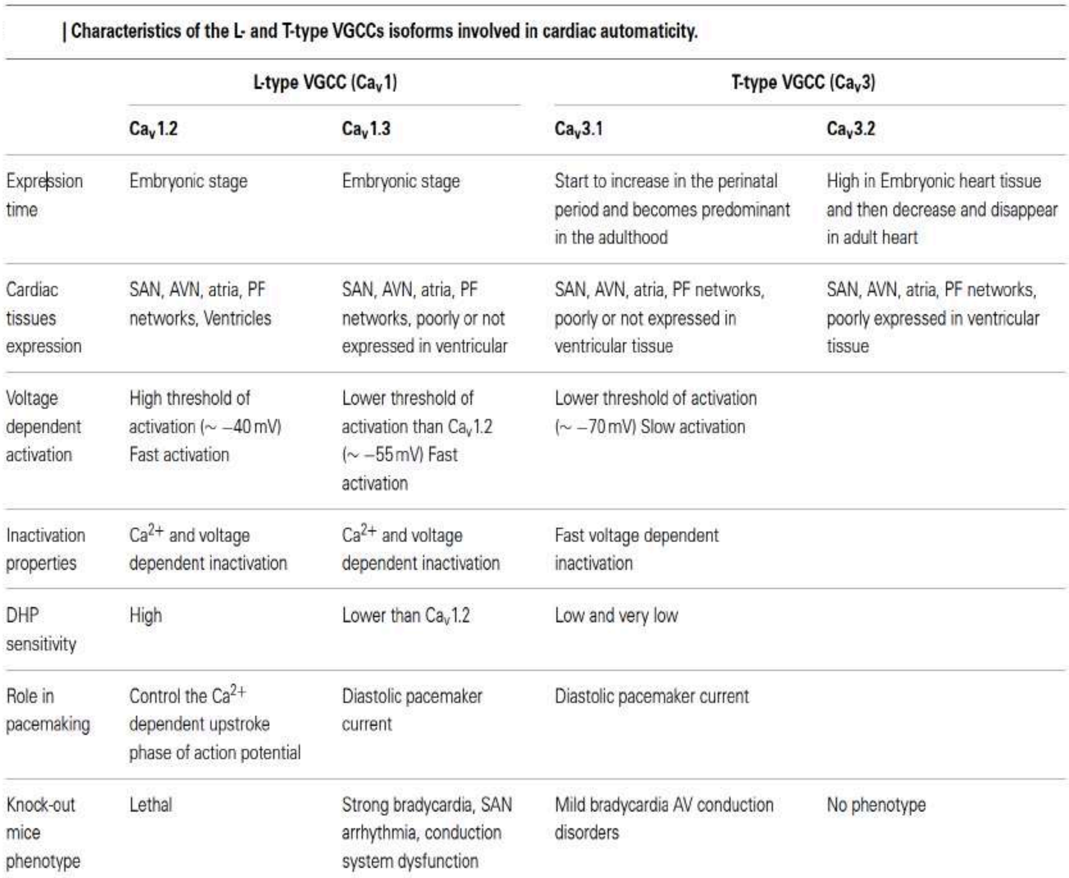

| Characteristics of the L- and T-type VGCCs isoforms involved in cardiac automaticity.

	L-type VGCC (Ca$_v$1)		T-type VGCC (Ca$_v$3)	
	Ca$_v$1.2	**Ca$_v$1.3**	**Ca$_v$3.1**	**Ca$_v$3.2**
Expression time	Embryonic stage	Embryonic stage	Start to increase in the perinatal period and becomes predominant in the adulthood	High in Embryonic heart tissue and then decrease and disappear in adult heart
Cardiac tissues expression	SAN, AVN, atria, PF networks, Ventricles	SAN, AVN, atria, PF networks, poorly or not expressed in ventricular	SAN, AVN, atria, PF networks, poorly or not expressed in ventricular tissue	SAN, AVN, atria, PF networks, poorly expressed in ventricular tissue
Voltage dependent activation	High threshold of activation (~ −40 mV) Fast activation	Lower threshold of activation than Ca$_v$1.2 (~ −55 mV) Fast activation	Lower threshold of activation (~ −70 mV) Slow activation	
Inactivation properties	Ca^{2+} and voltage dependent inactivation	Ca^{2+} and voltage dependent inactivation	Fast voltage dependent inactivation	
DHP sensitivity	High	Lower than Ca$_v$1.2	Low and very low	
Role in pacemaking	Control the Ca^{2+} dependent upstroke phase of action potential	Diastolic pacemaker current	Diastolic pacemaker current	
Knock-out mice phenotype	Lethal	Strong bradycardia, SAN arrhythmia, conduction system dysfunction	Mild bradycardia AV conduction disorders	No phenotype

Table 1: summary of the main characteristics of the L- and T-type VGCCs isoforms involved in cardiac automaticity. [According to Mesirca et al., 2015].

3.4. Regulation of L-type and T-type Ca^{2+} channels by autonomic nervous system in pacemaker cells

The autonomic nervous system (ANS) is the major extracardiac determinant of the heart rate. Sympathovagal control of cardiac automaticity is a complex phenomenon (Fig. 7). In the adult heart, the sympathetic branch of the autonomic nervous system accelerates heart rate, while the parasympathetic branch slows it. Autonomic fiber projections to the heart rhythmogenic centers are abundant. The SAN is enriched in adrenergic and muscarinic receptors.

Sympathetic regulation of pacemaker activity is mediated by catecholamines (i.e. norepinephrine) activating the β-adrenergic receptors (β_1/β_2 -AR). In 2003, Matteo Mangoni team demonstrated the $Ca_v1.3$ and $Ca_v1.2$ channels are directly regulated by the isoprenalin-mediated β-adrenergic receptors stimulation[7]. Moreover, activation of β-adrenergic receptors stimulates adenylyl cyclase (AC) activity, which converts ATP in cyclic AMP (cAMP). Elevated cAMP promotes voltage-dependent opening of f-channels and activates PKA (Protein Kinase A) [25]. The catalytic subunit of PKA enhances the activity of $Ca_v1.3$ and $Ca_v1.2$ channels by channel phosphorylation [26]. Regulation of T-type Ca^{2+} channels by cAMP dependent protein kinase A is still controversial[27], however, in a recent work Li and collaborators found that in cardiac myocytes the activity of $Ca_v3.1$ T-type VGCCs was significantly increased by β-adrenergic agonist, and that this regulation was strictly connected to the adenylate cyclase/cAMP/PKA machinery similar to L-Type Ca^{2+} channels[28].

The parasympathetic regulation of cardiac automaticity is mediated by the activation of muscarinic receptors following release of acetylcholine (ACh) from vagal nerve endings. The muscarinic M_2 receptor activates the inhibitory G protein α-subunit (α_i) which negatively couples to AC activity. Thus, downregulation of cAMP and, consequently, PKA phosphorylation reduction, reverses the signaling processes involved in sympathetic stimulation of heart rate in which $Ca_v1.3/Ca_v1.2$ and $Ca_v3.1$ were positively stimulated. Moreover, Petit-Jacques and collaborators have shown that muscarinic regulation of SAN I_{CaL} dependon the previous β-adrenergic stimulation and cAMP levels[29]. Indeed, moderate doses of ACh can significantly inhibit I_{CaL} if previously stimulated by β-adrenergic agonists. Moreover, Han et al. have demonstrated that the activation of the nitric oxide synthase (NOS) and the nitric oxide (NO) synthesis are involved in the muscarinic regulation of I_{CaL} in conditions of accentuated antagonism, when intracellular cAMP is increased by stimulation of β-adrenergic receptors[30] . In cardiac myocytes, muscarinic receptor activation is coupled to NO synthesis, which stimulates guanylyl cyclase (GC) activity. Elevated cyclic GMP (cGMP) production promotes phosphodiesterase activity (PDEII) that inhibits I_{CaL} by cAMP breakdown [31].

βγ-subunits of the G protein directly activate the acetylcholine-activated outward K^+ current (I_{KACh}) that induces a hyperpolarization of the membrane potential and consequently reduces the pacemaker rate [32].

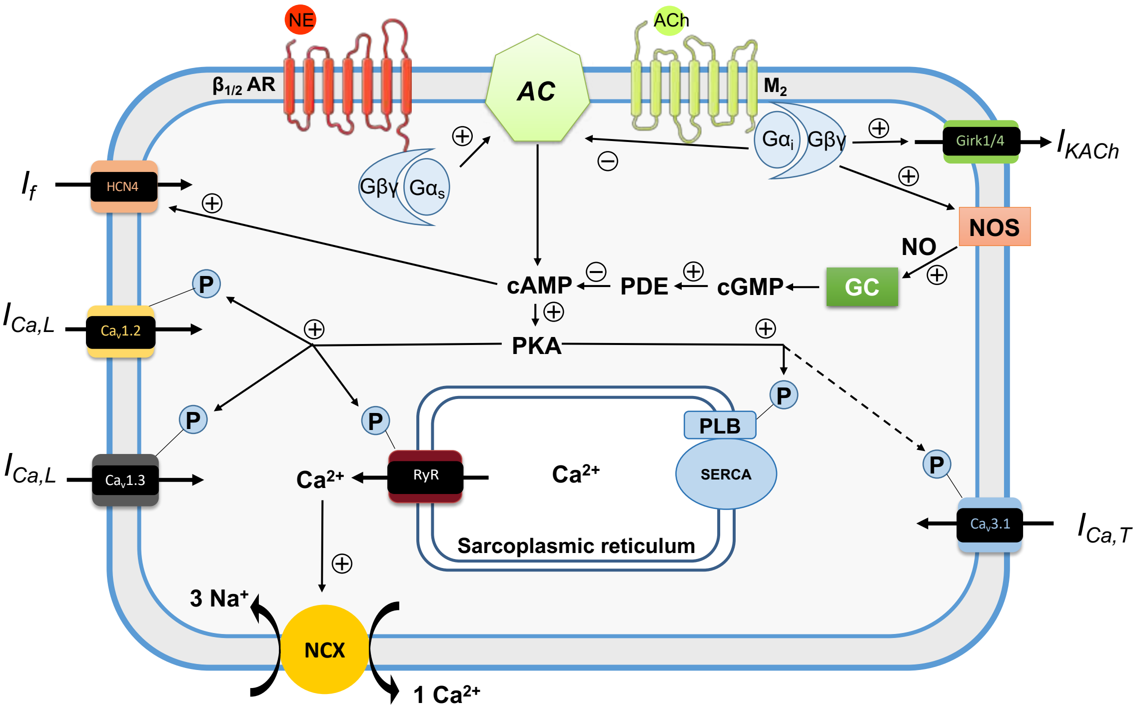

Figure 7: Summary of the signaling pathways involved in the adrenergic and muscarinic regulation of pacemaker activity. [Adapted from Mangoni and Nargeot, 2008].

3.5. Sino-atrial node dysfunction and voltage gated Ca^{2+} channels

SAN dysfunction (SND) as a clinical entity includes a variety of disorders, including inappropriate sinus bradycardia, sinus arrest, chronic atrial fibrillation, and tachycardia-bradycardia syndrome. It is a common problem in clinical cardiology, and one of the commonest indications for insertion of permanent pacing systems. Its frequency is expected to increase significantly as the general population continues to live longer. Its etiology includes structural abnormalities of the node, drug effects, and pathological autonomic influences. Rather than a single entity, SAN dysfunction is better conceptualized as a spectrum of disorders, whereby a number of different pathophysiological mechanisms lead to a very similar disease phenotype (Fig. 8) [33].

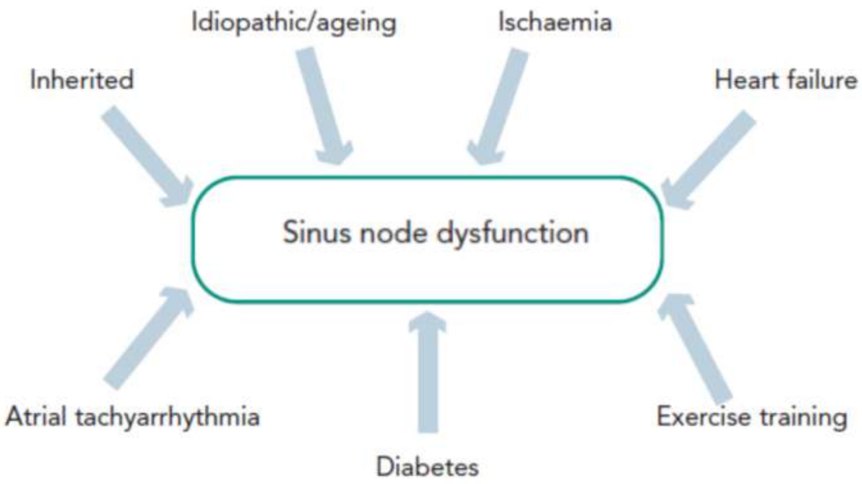

Figure 8: summary of the different etiologies surrounding SND. [Adapted from Choudhury et al., 2015]

During the last few years, mutations in ion channels contributing to SND in humans have been described [34]. In particular, several studies demonstrate that down regulation or loss-of-function of $Ca_v1.3$ and/or $Ca_v3.1$ lead to congenital pathologies of heart automaticity and atrioventricular conduction[35,36].

The sino-atrial node dysfunction and deafness (SANDD syndrome) results from loss of $Ca_v1.3$ function in humans and is associated with deafness and bradycardia. Indeed, together with the role in pacemaker cells, the $Ca_v1.3$ channels tightly control Ca^{2+}-dependent glutamate release at cochlear inner hair cell (IHC) ribbon synapses and are essential for hearing. In human $Ca_v1.3$ is encoded by CACNA1D and in SANDD syndrome, CACNA1D results in a splice mutated variant that is preferentially expressed in IHCs and the SAN [37].

SAN bradycardia has also been shown in association with congenital heart block (CHB). CHB is characterized by progressive complete atrioventricular block affecting fetuses and newborns. CHB is an autoimmune disease due to production of autoantibodies against intracellular soluble ribonucleoproteins. In 2002, Hu et al. have reported inhibition of I_{CaL} and I_{CaT} by IgG isolated from mothers having CHB-affected children. Thus, downregulation of $Ca_v1.3$ and $Ca_v3.1$ channels by maternal antibodies underlies SAN bradycardia in CHB[35]. In particular, Strandberg et al. shown that CHB maternal sera antibodies readily target an extracellular epitope of $Ca_v3.1$ in human fetal cardiomyocytes[38].

3.6. Genetically modified mice lacking L-type and T-type Ca^{2+} channels

In the early 2000s, advances in the field of genetics influenced research through the development of genetically modified animal models. Concerning $Ca_v3.1$ and $Ca_v1.3$ channels, the creation of genetically modified mouse models for these channels led to a better understanding of the pacemaker mechanism. These genetically modified organisms have become essential for studying the functional role of these channels and their interactions with other components in the pacemaker mechanism They highlight the function of a coding gene for an ion channel and its alteration.

In 2000, the Jörg Striessnig team generated a mutant mouse $Ca_v1.3^{-/-}$ and characterized it for the study of SANDD. The study of ECGs recorded in these mutant mice revealed bradycardia and sinus arrhythmias [39].

At the same time, in California, Z. Zhang and colleagues generated other similar $Ca_v1.3^{-/-}$ mice, and saw the same in vivo dysfunctions that was due to a SAN abnormal activity[40]. In 2003, Matteo Mangoni team indicated for the first time that loss of $Ca_v1.3$ function profoundly affected pacemaking. Indeed, slower and irregular pacing was found in all cells isolated from $Ca_v1.3^{-/-}$ mice in comparison with cells from wild-type mice[7].

The study of the functional role of $Ca_v3.1$ also required the creation of a genetically modified mouse model.

In 2001, the Korean D. Kim and collaborators generated in their laboratory a $Ca_v3.1^{-/-}$ mouse model to study the implication of this T-type Ca^{2+} channel in SWD (Spike-and-wave discharges) phenomena at the level of cortico-thalamic neurons[41].

In 2006, Matteo Mangoni team demonstrated for the first time the involvement of $Ca_v3.1$ in pacemaker activity and cardiac conduction by characterizing the $Ca_v3.1^{-/-}$ mouse in vivo and studying the electrophysiological properties of isolated SAN cells in vitro. In this $Ca_v3.1^{-/-}$ model, the mice show a low bradycardia of less than 10% of the normal rhythm and a slowing of the atrioventricular conduction[8].

From the studies described above, SAN is the major driver of conduction and automatism, and model mice provide a good deal of information about the functional roles of the ion channels involved.

In order to further understand the pacemaker mechanism, Matteo Mangoni team also generated cross-genotype between the $Ca_v3.1^{-/-}$ mouse and the $Ca_v1.3^{-/-}$ mouse.

3.7. Aim of the study

Previous studies showed that L-type $Ca_v1.3$ channels play a major role in the generation of cardiac pacemaker activity by contributing to diastolic depolarization in SAN pacemaker cells[39,7]. T-type $Ca_v3.1$ channels have also been shown to contribute directly in the setting of the mammalian cardiac impulse generation and propagation by contributing to both the diastolic depolarization in the SAN and impulse conduction through the AVN to automaticity[8]. However, it remains to be established whether L-type $Ca_v1.3$ and T-type $Ca_v3.1$ channels play distinct or partially overlapping roles in heart automaticity.

The aim of this study is to investigate the functional roles of L-type $Ca_v1.3$ and T-type $Ca_v3.1$ channels and study the consequences of concomitant genetic ablation of these channels ($Ca_v1.3^{-/-}/Ca_v3.1^{-/-}$) on heart automaticity.

3.8. References

1. Mangoni ME, Nargeot J. Genesis and regulation of the heart automaticity. *Physiol Rev* 2008;**88**:919–982.

2. James TN. Structure and function of the sinus node, AV node and his bundle of the human heart: Part II - Function. *Prog Cardiovasc Dis* 2003;**45**:327–360.

3. DiFrancesco D. The contribution of the 'pacemaker' current (if) to generation of spontaneous activity in rabbit sino-atrial node myocytes. *J Physiol* 1991;**434**:23–40.

4. Yu S, Li G, Huang CLH, Lei M, Wu L. Late sodium current associated cardiac electrophysiological and mechanical dysfunction. *Pflugers Arch Eur J Physiol* Pflügers Archiv - European Journal of Physiology; 2018;**470**:461–469.

5. Lakatta EG, Maltsev VA, Vinogradova TM. A Coupled SYSTEM of intracellular Ca2+ clocks and surface membrane voltage clocks controls the timekeeping mechanism of the heart's pacemaker. *Circ Res* 2010;**106**:659–673.

6. Bogdanov KY, Maltsev VA, Vinogradova TM, Lyashkov AE, Spurgeon HA, Stern MD, Lakatta EG. Membrane potential fluctuations resulting from submembrane Ca2+ releases in rabbit sinoatrial nodal cells impart an exponential phase to the late diastolic depolarization that controls their chronotropic state. *Circ Res* 2006;**99**:979–987.

7. Mangoni ME, Couette B, Bourinet E, Platzer J, Reimer D, Striessnig J, Nargeot J. Functional role of L-type Cav1.3 Ca2+ channels in cardiac pacemaker activity. *Proc Natl Acad Sci U S A* 2003;**100**:5543–5548.

8. Mangoni ME, Traboulsie A, Leoni AL, Couette B, Marger L, Quang K Le, Kupfer E, Cohen-Solal A, Vilar J, Shin HS, Escande D, Charpentier F, Nargeot J, Lory P. Bradycardia and slowing of the atrioventricular conduction in mice lacking CaV3.1/α1G T-type calcium channels. *Circ Res* 2006;**98**:1422–1430.

9. Mesirca P, Torrente AG, Mangoni ME. Functional role of voltage gated Ca2+ channels in heart automaticity. *Front Physiol* 2015;**6**:1–13.

10. Lei M, Jones SA, Liu J, Lancaster MK, Fung SSM, Dobrzynski H, Camelliti P, Maier SKG, Noble D, Boyett MR. Requirement of neuronal- and cardiac-type sodium channels for murine sinoatrial node pacemaking. *J Physiol* 2004;**559**:835–848.

11. Torrente AG, Mesirca P, Neco P, Rizzetto R, Dubel S, Barrere C, Sinegger-Brauns M, Striessnig J, Richard S, Nargeot J, Gomez AM, Mangoni ME. L-type Cav1.3 channels regulate ryanodine receptor-dependent Ca2+ release during sino-atrial node pacemaker activity. *Cardiovasc Res* 2016;**109**:451–461.

12. Chen B, Wu Y, Mohler PJ, Anderson ME, Song LS. Local control of Ca2+-induced Ca2+ release in mouse sinoatrial node cells. *J Mol Cell Cardiol* Elsevier Inc.; 2009;**47**:706–715.

13. Hagiwara N, Kameyama M. Contribution of two types of calcium currents to the pacemaker potentials of rabbit sino-atrial node cells. *J Physiol* 1988;**395**:233–253.

14. Zuccotti A, Clementi S, Reinbothe T, Torrente A, Vandael DH, Pirone A. Structural and functional differences between L-type calcium channels: Crucial issues for future selective targeting. *Trends Pharmacol Sci* Elsevier Ltd; 2011;**32**:366–375.

15. Striessnig J. Pharmacology, structure and function of cardiac L-type Ca 2+ channels. *Cell Physiol Biochem* 1999;**9**:242–269.

16. Tuluc P, Molenda N, Schlick B, Obermair GJ, Flucher BE, Jurkat-Rott K. A Cav1.1 Ca2+ channel splice variant with high conductance and voltage-sensitivity alters EC coupling in developing skeletal muscle. *Biophys J* Biophysical Society; 2009;**96**:35–44.

17. McRory JE, Hamid J, Doering CJ, Garcia E, Parker R, Hamming K, Chen L, Hildebrand M, Beedle AM, Feldcamp L, Zamponi GW, Snutch TP. The CACNA1F Gene Encodes an L-Type Calcium Channel with Unique Biophysical Properties and Tissue Distribution. *J Neurosci* 2004;**24**:1707–1718.

18. Catterall W a. Structure and regulation of voltage-gated ca2+ channels. *Annu Rev Cell Dev Biol* 2000;**16**:555.

19. Marionneau C, Couette B, Liu J, Li H, Mangoni ME, Nargeot J, Lei M, Escande D, Demolombe S. Specific pattern of ionic channel gene expression associated with pacemaker activity in the mouse heart. *J Physiol* 2005;**562**:223–234.

20. Toyoda F, Mesirca P, Dubel S, Ding WG, Striessnig J, Mangoni ME, Matsuura H. Ca V 1.3 L-type Ca 2+ channel contributes to the heartbeat by generating a dihydropyridine-sensitive persistent Na + current. *Sci Rep* Springer US; 2017;**7**:1–12.

21. Perez-Reyes E. Molecular physiology of low-voltage-activated T-type calcium channels. *Physiol Rev* 2003;**83**:117–161.

22. Ferron L, Capuano V, Deroubaix E, Coulombe A, Renaud JF. Functional and molecular characterization of a T-type Ca2 + channel during fetal and postnatal rat heart development. *J Mol Cell Cardiol* 2002;**34**:533–546.

23. Marshall PW, Rouse W, Briggs I, Hargreaves RB, Mills SD MBJ. ICI D7288, a novel sinoatrial node modulator. *J Cardiovasc Pharmacol* 1993;**21**:902–906.

24. Bohn G, Moosmang S, Conrad H, Ludwig A, Hofmann F KN. Expression of T- and L-type calcium channel mRNA in murine sinoatrial node. *FEBS Lett* 2000;**481**:73–76.

25. DiFrancesco D, Tortora P. Direct activation of cardiac pacemaker channels by intracellular cyclic AMP 1991 Nature Publishing Group. *Nature* 1991;**351**:145–147.

26. Ramadan O, Qu Y, Wadgaonkar R, Baroudi G, Karnabi E, Chahine M, Boutjdir M. Phosphorylation of the consensus sites of protein kinase a on α 1D L-type calcium channel. *J Biol Chem* 2009;**284**:5042–5049.

27. Chemin J, Traboulsie A, Lory P. Molecular pathways underlying the modulation of T-type calcium channels by neurotransmitters and hormones. *Cell Calcium* 2006;**40**:121–134.

28. Li Y, Wang F, Zhang X, Qi Z, Tang M, Szeto C, Li Y, Zhang H, Chen X. B-Adrenergic stimulation increases Cav3.1 activity in cardiac myocytes through protein kinase A. *PLoS One* 2012;**7**:1–10.

29. Petit-Jacques J, Bois P, Bescond J, Lenfant J. Mechanism of muscarinic control of the high-threshold calcium current in rabbit sino-atrial node myocytes. *Pflügers Arch Eur J Physiol* 1993;**423**:21–27.

30. Han X, Habuchi Y, Giles WR. Relaxin increases heart rate by modulating calcium current in cardiac pacemaker cells. *Circ Res* 1994;**74**:537–541.

31. Han X, Kobzik L, Severson D, Shimoni Y. Characteristics of nitric oxide-mediated cholinergic modulation of calcium current in rabbit sino-atrial node. *J Physiol* 1998;**509**:741–754.

32. Wickman K, Krapivinsky G, Corey S, Kennedy M, Nemec J, Medina I, Clapham DE. Structure, G protein activation, and functional relevance of the cardiac G protein-gated K+ channel, I(KACh). *Ann N Y Acad Sci* 1999;**868**:386–398.

33. Monfredi O, Dobrzynski H, Mondal T, Boyett MR, Morris GM. The anatomy and physiology of the sinoatrial node-A contemporary review. *PACE - Pacing Clin Electrophysiol* 2010;**33**:1392–1406.

34. Dobrzynski H, Boyett MR, Anderson RH. New insights into pacemaker activity: Promoting understanding of sick sinus syndrome. *Circulation* 2007;**115**:1921–1932.

35. Hu K, Qu Y, Yue Y, Boutjdir M. Functional basis of sinus bradycardia in congenital heart block. *Circ Res* 2004;**94**:1–7.

36. Qu Y, Baroudi G, Yue Y, Boutjdir M. Novel molecular mechanism involving α1D (Cav1.3) L-type calcium channel in autoimmune-associated sinus bradycardia. *Circulation* 2005;**111**:3034–3041.

37. Baig SM, Koschak A, Lieb A, Gebhart M, Dafinger C, Nürnberg G, Ali A, Ahmad I, Sinnegger-Brauns MJ, Brandt N, Engel J, Mangoni ME, Farooq M, Khan HU, Nürnberg P, Striessnig J, Bolz HJ. Loss of Ca v 1.3 (CACNA1D) function in a human channelopathy with bradycardia and congenital deafness. *Nat Neurosci* Nature Publishing Group; 2011;**14**:77–86.

38. Strandberg LS, Cui X, Rath A, Liu J, Silverman ED, Liu X, Siragam V, Ackerley C, Su B Bin, Yan JY, Capecchi M, Biavati L, Accorroni A, Yuen W, Quattrone F, Lung K, Jaeggi ET, Backx PH, Deber CM, Hamilton RM. Congenital Heart Block Maternal Sera Autoantibodies Target an Extracellular Epitope on the α1G T-Type Calcium Channel in Human Fetal Hearts. *PLoS One* 2013;**8**:10–16.

39. Platzer J, Engel J, Schrott-Fischer A, Stephan K, Bova S, Chen H, Zheng H, Striessnig J. Congenital deafness and sinoatrial node dysfunction in mice lacking class D L-type Ca2+ channels. *Cell* 2000;**102**:89–97.

40. Zhang Z, Xu Y, Song H, Rodriguez J, Tuteja D, Namkung Y, Shin HS, Chiamvimonvat N. Functional roles of Cav1.3 (α1D) calcium channel in sinoatrial nodes: Insight gained using gene-targeted null mutant mice. *Circ Res* 2002;**90**:981–987.

41. Kim D, Song I, Keum S, Lee T, Jeong MJ, Kim SS, McEnery MW, Shin HS. Lack of the burst firing of thalamocortical relay neurons and resistance to absence

seizures in mice lacking α1G T-type Ca2+ channels. *Neuron* 2001;**31**:35–45.

Chapter 4

Concomitant genetic ablation of L-type $Ca_v1.3$ and T-type $Ca_v3.1$ Ca^{2+} channels disrupts heart automaticity

M. Baudot[1,2], E. Torre[1,2,3], I. Bidaud[1,2], A.G. Torrente[1,2], L. Fossier[1,2], L. Talssi[1,2], H.S. Shin[4], J. Striessnig[5], J. Nargeot[1,2], S. Barrère-Lemaire[1,2], M. Rocchetti[3], P. Mesirca[1,2]*, M.E. Mangoni[1,2]*

[1]Institut de Génomique Fonctionnelle, Département de Physiologie, Université de Montpellier, CNRS, Inserm, 141 rue de la Cardonille, Montpellier, F-34094, France.

[2]LabEx ICST, Montpellier, France.

[3]Department of Biotechnology and Biosciences, Università degli Studi di Milano-Bicocca, Milan, Italy.

[4]Korea institute of science and technology, Seoul, South Korea.

[5]Department of Pharmacology and Toxicology, Institute of Pharmacy, Center for Molecular Biosciences, University of Innsbruck, Austria.

*Corresponding Author

[Under submission]

4.1. Abstract

Heart automaticity is generated in the sino-atrial node (SAN) by a functional interplay between ion channels of the plasma membrane and intracellular ryanodine receptor (RyR) -dependent Ca^{2+} release. SAN cells are characterized by the expression of voltage-gated L-type $Ca_v1.3$ and T-type $Ca_v3.1$ Ca^{2+} (Ca_v) channels in addition to L-type $Ca_v1.2$ channels, which are ubiquitously expressed in the heart. To investigate the significance of Ca_v expression for heart automaticity we used mutant mice carrying individual or concomitant genetic ablation of $Ca_v1.3$ and $Ca_v3.1$. Ca_v ablation additively reduced heart rate in mice: $Ca_v3.1^{-/-}$ (-8%, n=11), $Ca_v1.3^{-/-}$ (-24%, n=8), $Ca_v1.3^{-/-}/Ca_v3.1^{-/-}$ (-35%, n=11). ECG recordings of intact $Ca_v1.3^{-/-}/Ca_v3.1^{-/-}$ hearts showed atrioventricular rhythm dissociation and predominantly junctional, rather than SAN driven rhythmicity. Optical mapping of automaticity showed disruption of primary automaticity in $Ca_v1.3^{-/-}/Ca_v3.1^{-/-}$ SAN and a shift of the leading pacemaker sites outside the SAN area. We also investigated the role of hyperpolarization-activated f-(HCN) channels, TTX-sensitive Na^+ (Na_v) channels and RyR-dependent Ca^{2+} release in residual automaticity of mutant mice. Concomitant pharmacologic inhibition of f-HCN and TTX-sensitive Na_v channels slowed atrial automaticity in wild-type (-48%, n=7) and $Ca_v3.1^{-/-}$ (-37%, n=7), while arrested it in 4/6 of $Ca_v1.3^{-/-}$, 3/6 of $Ca_v1.3^{-/-}/Ca_v3.1^{-/-}$. When present, residual pacemaking was reduced by ~80%. In isolated $Ca_v1.3^{-/-}/Ca_v3.1^{-/-}$ SAN pacemaker cells automaticity was arrested in 5/9 cells tested or was reduced by 80% in 4/9 cells. This work contributes to elucidating the consequences of $Ca_v1.3$ and $Ca_v3.1$ Ca^{2+} channels deletion on heart automaticity that has never been investigated before. In particular, $Ca_v1.3$ and $Ca_v3.1$ Ca^{2+} channels deletion disrupts normal heart automaticity by inducing bradycardia and altering cardiac conduction. Moreover, in the concomitant absence of $Ca_v1.3$ and $Ca_v3.1$ channels, f-HCN channels and TTX-sensitive Na_v channels are the predominant mechanisms sustaining pacemaker activity. Finally, in $Ca_v1.3^{-/-}/Ca_v3.1^{-/-}$ SAN cells, RyR-dependent Ca^{2+} release cannot sustain SAN automaticity alone.

Keywords: Sino-atrial node, calcium channels, $Ca_v1.3$, $Ca_v3.1$, diastolic depolarization, pacemaker mechanism.

4.2. Introduction

Heart automaticity is a highly integrated mechanism that comprises the primary pacemaker activity of the sino-atrial node (SAN) and conduction of the impulse through the principal components of the cardiac conduction system, the atrioventricular node (AVN), the His bundle and the Purkinje fibres network[1]. The SAN generates the cardiac impulse under physiological conditions however the AVN and the Purkinje fibres network can generate viable automaticity in case of SAN failure. Automaticity in cardiac cells is due to the diastolic depolarization, a slow phase of the action potential cycle, which drives the membrane voltage from the end of the repolarization to the threshold of the following action potential[2].

Several aspects of the cardiac pacemaker mechanism are still incompletely understood however, there exists considerable agreement that the diastolic depolarization is generated by a functional interplay between the activity of ion channels of the plasma membrane and intracellular Ca^{2+} ($[Ca^{2+}]_i$) release from ryanodine receptors (RyRs) of the sarcoplasmic reticulum (SR)[3]. The contribution of RyR dependent Ca^{2+} release to automaticity is currently interpreted within the "Ca^{2+} clock" model of pacemaking [4]. In this model, an intracellular "Ca^{2+} clock" is generated by a phenomenon of spontaneous voltage-independent Ca^{2+} release from RyRs that stimulates the Na^+-Ca^{2+} exchanger (NCX)[5]. This electrogenic transport generates an inward current that initiates the diastolic depolarization[6]. According to the more recent version of this model, normal pacemaking is generated when the intracellular Ca^{2+} clock is synchronous (coupled) to the activity of ion channels of the plasma membrane[3]. Among plasmalemmal ion channels, hyperpolarization activated f-(HCN) channels[7], voltage gated Ca^{2+} channels (VGCCs)[8], voltage-dependent tetrodotoxin (TTX)-sensitive Na^+ channels mediating neuronal type Na^+ current ($I_{NaTTX\text{-}sensitive}$)[9] and transient receptor potential (TRPM) [10,11] channels have been shown to contribute to the cardiac automaticity.

The mammalian heart expresses three VGCC isoforms[8]: L-type $Ca_v1.2$ and $Ca_v1.3$ channels, as well as T-type $Ca_v3.1$ channels however, these isoforms show differential expression in the working myocardium and in automatic tissue. In particular, adult ventricular myocytes express L-type $Ca_v1.2$ channels[12], which couple excitation to contraction of the myocardium[13]. $Ca_v1.2$ channels are also ubiquitously expressed in the SAN and in the conduction system[12]. In contrast, L-type $Ca_v1.3$ channels are expressed in automatic tissue and, to a lower degree of expression, also in atria [12]. Finally, T-type

$Ca_v3.1$ channels are not functionally expressed in the adult working myocardium but show strong expression in the SAN and in the conduction system[14]. $Ca_v1.3$ functionally differs from the other cardiac L-type isoform, its threshold for activation being substantially more negative (-55 mV) than that of the excitation-contraction controlling isoform $Ca_v1.2$ (-30 mV)[15]. T-type $Ca_v3.1$ channels activate at more negative voltages than $Ca_v1.3$ (-60 mV) however, their half inactivation voltage is also more negative (-70 mV)[15]. Previous studies showed that L-type $Ca_v1.3$ channels play a major role in the generation of the diastolic depolarization[15]. T-type $Ca_v3.1$ channels have also been shown to contribute to automaticity[15]. The functional significance of the expression of distinct VGCCs isoforms in the SAN versus the working myocardium is not fully understood. In addition, their relevance in relation to other ion channels involved in automaticity has not been investigated in detail.

Here we created a mouse model of automaticity in which the two VGCCs expressed in the SAN have been ablated, leaving the excitation contraction coupling L-type $Ca_v1.2$ as the sole VGCCs isoform in the SAN. To this aim we ablated both L-type $Ca_v1.3$ and T-type $Ca_v3.1$ channels ($Ca_v1.3^{-/-}/Ca_v3.1^{-/-}$) and study the consequences of concomitant genetic ablation of these channels on heart automaticity. We also investigate the mechanism of residual pacemaker activity in $Ca_v1.3^{-/-}/Ca_v3.1^{-/-}$ mice. Finally, we tested whether intracellular Ca^{2+} clock and the excitation-contraction coupling L-type isoform $Ca_v1.2$ could sustain viable pacemaker activity. We show that concomitant ablation of $Ca_v1.3$ and $Ca_v3.1$ disrupts heart automaticity, by preventing formation of the SAN impulse and inducing severe heart block. In addition, we find that residual pacemaker activity in $Ca_v1.3^{-/-}/Ca_v3.1^{-/-}$ SANs was predominantly sustained by f-channels. Finally, we report that the intracellular Ca^{2+} clock cannot generate viable pacemaker activity following concomitant targeting of L-type $Ca_v1.3$ and f-channels. Our results indicate that co-expression L-type $Ca_v1.3$ and T-type $Ca_v3.1$ channels is required from the proper genesis and conduction of the cardiac impulse. In addition, association between $Ca_v1.3$ and f-(HCN) channels constitutes the predominant mechanism to generate the basal SAN rate.

4.3. Methods

Mutant mice harboring genetic ablation of Ca_v: $Ca_v3.1^{-/-}$, $Ca_v1.3^{-/-}$ and $Ca_v1.3^{-/-}/Ca_v3.1^{-/-}$ were generated in the IGF animal facility from C57B/6J genetic background. $Ca_v1.3^{-/-}/Ca_v3.1^{-/-}$ mice were obtained by crossing C57B/6J $Ca_v1.3^{-/-}$ [16] with C57B/6J $Ca_v3.1^{-/-}$ [17] mice. The investigation conforms to the Guide for the Care and Use of Laboratory Animals published by the US national Institute of Health (NIH Publication No. 85–23, revised 1996) and European directives (2010/63/EU). The experimental procedure was approved by the Ethical committee of the University of Montpellier and the French Ministry of agriculture (protocol n°: 2017010310594939). Animals were housed in individual cages with free access to food and water and were exposed to 12-hour light/dark reverse cycles (light, 20:00 h to 8:00 h) in a thermostatically controlled room.

4.3.1. ECG recordings in conscious mice

Mice undergoing telemetric ECG recordings were anesthetized with 2% isoflurane (Forene®, Abbott, UK). A midline incision was made on the back along the spine to insert a telemetric transmitter (ETA-F10, Data Sciences International) into a subcutaneous pocket. Paired wire electrodes were placed over the thorax (chest bipolar ECG lead) in DII derivation against the heart axis. To manage post-surgery pain, Advil (ibuprofen, 7 mL/l) was added to the drinking water for 4 days after implantation. Mice were left to recover for 10 days before ECG recordings. ECG signals were recorded using a telemetry receiver and an analog-to-digital conversion data acquisition system for display and analysis by Dataquest™ A.R.T.™ software (Data Sciences International). Heart rates (HR) were determined from RR intervals. For evaluating drug effects, the HR was first recorded for 4-h in basal condition. Following drug intraperitoneal (IP) injection, mean HR values were calculated in each mouse by analyzing periods of 5 min at different time points corresponding to the peak effect of the drug. ECG parameters were measured with ECG Auto 1.5.7 software (EMKA Technologies). Atrial rates were determined from PP intervals.

4.3.2. Langendorff-perfused hearts

Mice were deeply anesthetized by IP injection of 0.3 mL of solution constituting Ketamine (0.1mg/g, Imalgène) and Xylazine (0.01mg/g, Rompun 2%, Bayer AG), followed by a second injection of Pentobarbital (150μL Euthasol Vet in 10 mL NaCl physiological solution). To avoid blood clots in the heart, we injected 0.5 mL of NaCl solution containing Heparin (25000 U.I). Hearts were removed via thoracotomy when the tail sensitivity test become negatives. Excised hearts with aortic cannula were quickly mounted on a Langendorff apparatus (Isolated heart system; EMKA Technologies) at a pressure of 70-80 mm Hg imposed by the working heart with normal Tyrode's solution containing (mM): NaCl, 140; KCl, 5.4; $MgCl_2$, 1; $CaCl_2$, 1.8; Hepes, 5 and glucose, 5.5 (pH adjusted to 7.4 with NaOH). Perfused hearts were immersed in the water-jacked bath and maintained at 36°C. The ECG was continuously recorded by two Ag-AgCl electrodes; the first was placed on the epicardial side of the right atrium close to the SAN area and the second near the ventricular apex. The heart rate was allowed to stabilize for at least 30 min before perfusion of drugs. ECG parameters were measured with ECG Auto 3.3.3.8 software (EMKA Technologies).

4.3.3. Intact SAN/atria preparations

We obtained SAN-atria preparations from excised hearts as previously described [18]. Briefly, we placed the entire SAN/atrial preparation in pre-warmed (36 °C) Tyrode's solution containing heparin (10 U/mL). We used a stereomicroscope (SZX16; Olympus) with low magnification (7×) to transilluminate and visualize directly the isolated SAN/atria preparation. We identified the SAN region using the superior and inferior vena cava, the crista terminalis, and the interatrial septum as landmarks[18]. The SAN/atrial preparation including right and left atria (RA and LA) was pinned to the bottom of an optical chamber (Fluorodish, FD35PDL-100; WPI) coated with ~2 mm of clear Sylgard (Sylgard 184 Silicone elastomer kit; Dow Corning). To maintain the SAN in a flat plane, we pinned the atrial preparation.

4.3.4. Optical mapping of membrane voltage in SAN/atria preparations

To analyze changes in membrane voltage in SAN/atrial tissue, the entire preparation, including the SAN, LA, and RA, was loaded by immersing the tissue in a Tyrode's solution containing the voltage-sensitive indicator/dye Di-4-ANEPPS (10 µM; Biotium) for at least 30 min at room temperature (20–22 °C). The preparation was placed on agitated plate during loading to maintain proper oxygenation of the tissue and load it uniformly. After the loading step, the tissue was washed 3 times in dye-free Tyrode's solution. The SAN/atrial tissue was then constantly perfused at 34–36 °C and imaged by high speed optical voltage mapping (2 ms per frame) on a MiCAM Ultima-L complementary metal oxide semiconductor (CMOS) camera (100×100-pixel CMOS sensor, 10×10 mm, SciMedia). This camera was mounted on a THT microscope, with two objectives (2×and 1.6×) that generated a field of view of 12.5×12.5 mm. A 150-W halogen light system with built-in shutter (SciMedia) was used as an excitation light source for the voltage dye. The filter set included a 531/50-nm excitation filter, 580-nm dichroic mirror, and 580 long-pass emission filter. To avoid motion artifacts, we blocked mechanical activity using blebbistatin (1.5–5μM; Tocris Bioscience). We usually limited our recording times to 32.768 s (16,384 frames at 2 ms per frame) to avoid phototoxic effects of the dye. Optical raw data were analyzed using dedicated software from the camera developer, BVAna Analysis Software (Brainvision).

4.3.5. Isolation of SAN cells

SAN pacemaker cells were isolated as previously described[19]. Briefly, SAN tissue was immersed into a "low-Ca^{2+}" Tyrode's solution containing 140 mM NaCl, 5.4 mM KCl, 0.5 mM $MgCl_2$, 0.2 mM $CaCl_2$, 1.2mM KH_2PO_4, 50 mM taurine, 5.5 mM D-glucose, 1 mg/mL BSA, and 5 mM Hepes-NaOH (adjusted to pH 6.9 with NaOH) for 4 min and set aside for 2 min. The tissue was then transferred into the low-Ca^{2+} solution containing purified collagenase and protease (Liberase TM; 229 U/mL; Roche). 1.9 U/ml elastase (Boehringer Mannheim). Digestion was carried out for 15-20 min at 36 °C. To stop the digestion process, the SAN was washed in a modified "Kraftbrühe" (KB) medium containing 70 mM L-glutamic acid, 20 mM KCl, 80 mM KOH, 10 mM KH_2PO_4, 10 mM taurine, 1 mg/mL BSA, and 10 mM Hepes-KOH (adjusted to pH 7.4 with KOH). Single cells were isolated from the SAN tissue by manual agitation using a flame-forged Pasteur's pipette in KB solution at 36 °C. To recover the automaticity of the SAN cells, Ca^{2+} was gradually reintroduced in the cells' storage solution to a final concentration of 1.8 mM. Normal Tyrode's solution containing 1 mg/ml BSA was added to finish the readaptation[19]. Cells were then stored at room temperature until use.

4.3.6. Patch-clamp recordings of SAN cells

For electrophysiological recordings, SAN cells were harvested in special custom-made recording chambers with glass bottoms for proper cell attachment. The storage solution was rinsed with normal Tyrode's solution warmed at 36°C before recording. ICa was recorded in standard whole cell patch-clamp configuration. Extracellular recording solution contained (mM): 135 tetraethylammonium chloride (TEA-Cl), 10 4-

aminopyridine (4-AP), 1 $MgCl_2$, 0.03 tetrodotoxin (TTX), 1 g/L Glucose, 2 $CaCl_2$, 10 Hepes, (adjusted to pH = 7.2 with CsOH). Electrodes had a resistance of about 3 MΩ when filled with an intracellular solution containing (in mM): 125 CsOH, 20 TEA-Cl, 1.2 $CaCl_2$, 5 Mg-ATP, 0.1 Li_2-GTP, 5 EGTA, and 10 HEPES (pH adjusted to 7.2 with aspartate). Seal resistances were in the range of 2–5 GΩ. Pacemaker activity of SAN cells was recorded under perforated patch conditions by adding 50 µM β-Escin to the pipette intracellular solution. Patch-clamp electrodes had a resistance of 3–5 MΩ when filled with an intracellular solution containing (in mM): 130 K^+-aspartate; 10.0 NaCl; 2 ATP-Na^+ salt, 6.6 creatine phosphate, 0.1 GTP-Mg^{2+}, 0.04 $CaCl_2$ (pCa = 7.0), and 10.0 HEPES-KOH (adjusted to pH 7.2 with KOH). Perfusion of pre-warmed (36 °C) experimental solutions was performed by using a multi- MPRE8 heating pen (Cell Micro Controls,). Data acquisition was performed using a Multiclamp 700A patch clamp amplifier connected to Digidata 1550B interface (Molecular Devices).

4.3.7. Ca^{2+} imaging in isolated SAN cells

We harvested SAN cells in a glass Fluorodish (FD3510-100, WPI), coated overnight with laminin (1 mg/ml; Sigma-Aldrich) for 1 h before recordings. SAN cells loading was performed by removing the bath solution and replacing it by Tyrode's solution containing the Ca^{2+} indicator CAL-520 (1 µM, from a stock solution containing DMSO/Pluronic F-127 0.13%; Invitrogen) during 25 min at room temperature. Images were obtained with confocal microscopy (Zeiss LSM 780), by scanning SAN cells with an Argon laser in line-scan configuration. To avoid phototoxicity we generally recorded the SAN cells at a line rate of 1.53 or 3.78 ms to obtain 10,000 lines. Fluorescence was excited at 488 nm and emissions were collected at >505 nm. A 63x oil immersion objective was used to record $[Ca^{2+}]_i$ in isolated SAN myocytes. We suppressed the background noise and analyzed the time-courses of Ca^{2+} fluorescence by pClamp software (ver.10.6.2.2, Molecular Devices). $[Ca^{2+}]_i$ transients and LCRs were analyzed using ImageJ software 8.

4.3.8. Statistical analysis

Statistical analysis was performed using Prism 8.0 (GraphPad Software). Data are represented as mean ± SEM. Statistical tests used in each experiment are specified throughout the figure legends. Statistical significance was defined as $p<0.05$. *$p < 0.05$, **$p < 0.01$, ***$p < 0.001$ and ****$p < 0.0001$.

4.4. Results

4.4.1. Concomitant ablation of L-type $Ca_v1.3$ and T-type $Ca_v3.1$ channels silences the VDCCs mediated Ca^{2+} current in the voltage range of the diastolic depolarization

In order to validate our model, we recorded L- and T-type Ca^{2+} currents in isolated SAN pacemaker cells from control and mutant mice. I_{Ca} was first recorded from a holding potential (HP) of -80 mV to record I_{CaL} and I_{CaT})[15]. Samples traces of I_{Ca} are reported in Fig.1A for wild-type, $Ca_v3.1^{-/-}$, $Ca_v1.3^{-/-}$ and $Ca_v1.3^{-/-}/Ca_v3.1^{-/-}$ SAN cells. To separate I_{CaL} from I_{CaT}, we switched the HP to -55 mV to inactivate I_{CaT} (Fig.1A). Current-to-voltage relationship curves for each genotype are reported in Fig.1B. Black symbols represent values recorded using the depolarizing step protocol starting from HP = -80 mV and red symbols values recorded from HP of -55 mV. In wild-type SAN myocytes the net T-type Ca^{2+} current was calculated as the difference between traces obtained at HP of -55 mV from those at HP -80 mV[15] (Fig. 1B-a, dashed line). In $Ca_v3.1^{-/-}$ SAN cells only L-type current flowing through $Ca_v1.3$ and $Ca_v1.2$ subunits was recorded, whereas T-type Ca^{2+} current was totally absent (Fig.1B-b). In $Ca_v1.3^{-/-}$ SAN cells, the total I_{Ca} (black dots, Fig.1B-c) was the sum of $Ca_v3.1$ mediated T-type and the $Ca_v1.2$ mediated L-Type Ca^{2+} current (red dots, Fig.1B-c). Similar to wild-type, I_{CaT} was quantified by subtracting traces obtained at the two different HPs (Fig.1B-c, dashed line). In $Ca_v1.3^{-/-}/Ca_v3.1^{-/-}$ SAN cells the only residual I_{Ca} recorded was $Ca_v1.2$ mediated I_{CaL} (recognizable by its activation at more positive potentials, Fig.1B-d). A comparison between Ca^{2+} current intensity recorded in different mutants with respect to wild-type animals is depicted in Fig.1Ca-c (for data collected with HP = -80 mV) and Fig.1Da-c (HP=-55 mV). These data were in line with our previous results showing the presence of $Ca_v1.3$ mediated I_{CaL} at diastolic membrane voltages between -55 mV and -35 mV[15]. Furthermore, our results show the absence of residual Ca^{2+} current in $Ca_v1.3^{-/-}/Ca_v3.1^{-/-}$SAN cells at voltages spanning the diastolic depolarization.

4.4.2. Deep bradycardia and heart block in and $Ca_v1.3^{-/-}/Ca_v3.1^{-/-}$ mice

We first compared *in vivo* SAN rates (P wave rate) with ventricular heart rates (HRs) in mutant mice, under control conditions (ANS+) and following combined injection of atropine and propranolol (ANS-) to inhibit the autonomic nervous system input (Fig. 2A and B). All mutant mice displayed significant slowing of SAN rates: $Ca_v3.1^{-/-}$ (~-10%),

$Ca_v1.3^{-/-}$ (~-30%) and $Ca_v1.3^{-/-}/Ca_v3.1^{-/-}$ (~-35%) in comparison to wild-type counterparts (Fig. 2A-E). The standard deviation of the SAN interbeat time was increased in $Ca_v1.3^{-/-}/Ca_v3.1^{-/-}$ mice (Fig. S1), indicating erratic SAN automaticity. The atrioventricular (AV) conduction time (PR interval) was increasingly prolonged in mutant $Ca_v3.1^{-/-}$, $Ca_v1.3^{-/-}$ and $Ca_v1.3^{-/-}/Ca_v3.1^{-/-}$ mice (Fig. S1). The uncorrected QT interval was also significantly prolonged in $Ca_v1.3^{-/-}$ and $Ca_v1.3^{-/-}/Ca_v3.1^{-/-}$ mice (Fig. 1). $Ca_v1.3^{-/-}$ and $Ca_v1.3^{-/-}/Ca_v3.1^{-/-}$ mice showed also a high incidence of 2nd degree AV blocks (Fig. 2A). Furthermore, 6/23 $Ca_v1.3^{-/-}/Ca_v3.1^{-/-}$ mice presented with complete 3rd degree AV block and dissociated atrial and ventricular rhythm (Fig. 2A). In comparison, any of the 24 $Ca_v1.3^{-/-}$mice studied presented complete 3rd degree AV block. Inhibition of the autonomic nervous system input reduced SAN rates in all genotypes tested and abolished 2nd and 3rd degree AV blocks in mutant mice (Fig. 2B). We recorded deep SAN bradycardia in $Ca_v1.3^{-/-}/Ca_v3.1^{-/-}$ mice under autonomic nervous system inhibition (~240 bpm), suggesting that the sympathetic activity was important in sustaining pacemaker activity in double-mutant animals (Fig. 2B-D). The averaged SAN rates of $Ca_v1.3^{-/-}$ and $Ca_v1.3^{-/-}/Ca_v3.1^{-/-}$ mice did not differ significantly. However, HRs of $Ca_v1.3^{-/-}/Ca_v3.1^{-/-}$ were significantly lower than those of $Ca_v1.3^{-/-}$ mice because of a higher incidence of 2nd degree AV blocks and the presence of dissociated rhythms in double mutant animals (Fig. 2E and F).

Thus we investigated the consequences of concomitant ablation of $Ca_v1.3$ and $Ca_v3.1$ on intrinsic heart automaticity using intact Langendorff perfused hearts to reduce ANS influence (Fig.3). Similar to observations *in vivo*, the rates of P waves in mutant hearts were lower than that of wild-type counterparts however, complete 3rd degree AV block and rhythm dissociation characterized $Ca_v1.3^{-/-}/Ca_v3.1^{-/-}$ hearts (Fig. 3A and B). Rhythm dissociation was evidenced by the difference between measured atrial and ventricular rates in $Ca_v1.3^{-/-}$ and $Ca_v1.3^{-/-}/Ca_v3.1^{-/-}$ hearts (Fig. 3C). Concomitant ablation of $Ca_v1.3$ and $Ca_v3.1$ was strongly proarrhythmic. Indeed, $Ca_v1.3^{-/-}/Ca_v3.1^{-/-}$ hearts showed inversed P waves associated with atrial and ventricular escape rhythms, suggesting extranodal impulse generation. Furthermore, all $Ca_v1.3^{-/-}/Ca_v3.1^{-/-}$ hearts showed episodes of ventricular tachycardia (Fig.S2). Taken together, these observations indicated that concomitant ablation of $Ca_v1.3$ and $Ca_v3.1$ channels disrupted heart automaticity by strongly reducing SAN pacemaking and by severely compromising atrioventricular conduction and ventricular rhythmicity. In conclusion, concomitant ablation of $Ca_v1.3$

and $Ca_v3.1$ disrupts heart automaticity by inducing SAN dysfunction and heart block. In addition, coexpression of $Ca_v1.3$ and $Ca_v3.1$ is necessary to ensure conduction and stabilizing ventricular automaticity.

4.4.3. Concomitant ablation of $Ca_v1.3$ and $Ca_v3.1$ channels disrupts SAN automaticity and induces shift of pacemaker leading sites to extranodal locations

Since we recorded limited residual SAN driven heart automaticity in $Ca_v1.3^{-/-}/Ca_v3.1^{-/-}$ hearts we attempted to study SAN impulse formation and localization using optical mapping (OM) of membrane voltage in isolated SAN/atria preparations (see methods). All wild-type SAN/atria preparations displayed consistent positioning of the pacemaker leading site in a limited region of the central cranial side of the SAN at the entry of the superior cava vein in the right atrium and close to the border of the *Crista Terminalis* (Fig.4A). In contrast, we found that automaticity in $Ca_v3.1^{-/-}$ and $Ca_v1.3^{-/-}$ SAN/atria preparations was characterized by the presence of at least two leading sites with alternating dominance in 3 out of 7 and in 4 out of 7 tissues tested, respectively (Fig.4A, table S1). In addition, 2 out of 4 $Ca_v1.3^{-/-}$ SAN/atria preparations displayed 3 alternating leading sites. Finally, all $Ca_v1.3^{-/-}/Ca_v3.1^{-/-}$ preparations studied displayed alternating automaticity between two or three leading sites (Fig.4A, supplementary table 1). In $Ca_v3.1^{-/-}$ preparations, secondary leading sites appeared in the correspondence of the nodal extension caudally to the inferior vena cava[20]. In $Ca_v1.3^{-/-}$ and $Ca_v1.3^{-/-}/Ca_v3.1^{-/-}$ preparations secondary leading sites were also found in the right or left atrium (Fig.4A). Emergence of multiple extranodal leading sites was accompanied by increasing slowing of automaticity in $Ca_v3.1^{-/-}$, $Ca_v1.3^{-/-}$ and $Ca_v1.3^{-/-}/Ca_v3.1^{-/-}$ SAN/atria preparations (Fig.4B). The coefficient of variability of atrial rate also increased with concomitant genetic ablation of $Ca_v1.3$ and $Ca_v3.1$in comparison to wild-type counterparts (Fig.4C). The rate of atrial impulse was negatively correlated with the distance between the alternating leading sites (Fig.4D). Taken together, these observations indicate that concomitant ablation of $Ca_v1.3$ and $Ca_v3.1$ channels disrupted primary SAN automaticity and shifted pacemaker activity to extranodal leading sites generating slow atrial rates.

4.4.4. f-channels sustain automaticity in $Ca_v1.3^{-/-}$ and $Ca_v1.3^{-/-}/Ca_v3.1^{-/-}$ in vivo

Since we observed automaticity arising in $Ca_v1.3^{-/-}$ and $Ca_v1.3^{-/-}/Ca_v3.1^{-/-}$ hearts, either in the SAN or in extranodal regions (Fig.4), we attempted to identify the mechanisms underlying residual pacemaking. Hyperpolarization-activated f-channels underlie the cardiac I_f current[21,22]. Because of their direct sensitivity to intracellular cAMP they constitute a primary targets of the opposite regulation of heart rate by catecholamines and acetylcholine[2]. We thus hypothesized that the decrease in HR observed in $Ca_v1.3^{-/-}$ and $Ca_v1.3^{-/-}/Ca_v3.1^{-/-}$ mice following inhibition of the autonomic nervous system was generated by atropine induced I_{KACh} inhibition[23,24] and a shift of I_f activation to more negative voltages by blockade of β-adrenergic receptors by propranolol (Fig.2B). We thus administered to wild-type and mutant mice the selective I_f blocker ivabradine and recorded HR under these conditions (Fig.5). Ivabradine decreased the HR in all the genotypes tested (Fig.5A-C). The HR recorded in $Ca_v1.3^{-/-}/Ca_v3.1^{-/-}$ mice under ivabradine administration was similar to that observed in the same mice under atropine and propranolol, which suggested that I_f was playing a major role in establishing HR in $Ca_v1.3^{-/-}$ and $Ca_v1.3^{-/-}/Ca_v3.1^{-/-}$ mice in vivo under the action of the autonomic nervous system. In addition, the difference in HR before and after ivabradine administration was similar among wild-type and mutant mice (Fig.5D), which indicated that genetic ablation of $Ca_v1.3$ and $Ca_v3.1$ channels did not affect the relative contribution of I_f to HR. Since ivabradine induced strong bradycardia in $Ca_v1.3^{-/-}$ and $Ca_v1.3^{-/-}/Ca_v3.1^{-/-}$ mice we decided to investigate the origin of the residual SAN automaticity under ex vivo conditions, to prevent lethal bradycardia. Similarly to in vivo conditions, ivabradine (10 μM) induced low HRs in isolated hearts from mutant $Ca_v1.3^{-/-}$ and $Ca_v1.3^{-/-}/Ca_v3.1^{-/-}$ mice (<100 bpm; Fig.6A). TTX-sensitive Na^+ channels (I_{NaTTX}) are expressed in the SAN, where they have been shown to contribute to basal heart rate and to SAN pacemaker activity[9,25]. We thus employed a moderate concentration of TTX (100 nM) I_{NaTTX} to investigate the contribution of these channels to the residual automaticity of $Ca_v1.3^{-/-}$ and $Ca_v1.3^{-/-}/Ca_v3.1^{-/-}$ hearts under conditions of I_f block by ivabradine. TTX further reduced heart rate in $Ca_v1.3^{-/-}$ hearts (<50 bpm; Fig. 6B) however, upon 7 hearts tested, we failed to observe complete arrest of cardiac automaticity. Since part of the residual automaticity could come from extranodal impulse leading regions (Fig.5), we directly investigated SAN automaticity by OM of the pacemaker impulse following pharmacological blockade of I_f (Fig.6C) or concomitant I_f and TTX-sensitive Na^+ channels (Fig.6D). Ivabradine slowed the SAN rate in wild-type and mutant mice and reduced the number of preparations presenting alternating leading sites (table S1). However, ivabradine significantly increased the variability of SAN rate in wild-type and mutant mice (supplementary Fig. 3). Blockade of TTX-sensitive Na^+ channels in ivabradine perfused SANs arrested automaticity in 5/7 $Ca_v1.3^{-/-}$ and 4/7 $Ca_v1.3^{-/-}$/$Ca_v3.1^{-/-}$ preparations (Fig.6D, table S1). Very low rate was recorded in 5 SANs from $Ca_v1.3^{-/-}$ and $Ca_v1.3^{-/-}$/$Ca_v3.1^{-/-}$ mice still presenting residual automaticity (<40 bpm, Fig.6D). In contrast, ivabradine and TTX did not affect the impulse conduction times to the right and left atria (Fig. S3).

We obtained similar results using spontaneously beating isolated SAN cells (Fig. 7). Indeed, concomitant inhibition of I_f and TTX-sensitive Na^+ channels slowed pacemaker activity in wild-type and $Ca_v3.1^{-/-}$cells (Fig. 7A and B, supplementary table 2), while arrested automaticity in 3/6 $Ca_v1.3^{-/-}$ and in 7/14 $Ca_v1.3^{-/-}$/$Ca_v3.1^{-/-}$ cells (Fig. 7C and D, supplementary table 2). Consistently with OM recordings in intact SAN/atria preparations, very slow automaticity was recorded in $Ca_v1.3^{-/-}$ cells that maintained residual pacemaking under these conditions (<30 bpm). Pharmacological inhibition of T-type channels (namely $Ca_v3.1$ channels) and $Ca_v1.3$ L-type channels in isolated pacemaker cells confirmed the results obtained in the experiments where same channels were inactivated genetically. $Ca_v1.2^{DHP-/-}$ mouse model ($Ca_v1.2$ subunits of L-type Ca^{2+} channels insensitive to dihydropyridine) was used for the experiments. 1 µM TTA-A_2, a selective T-type channel blocker, reduced action potential rate of approximatively 10% in isolated SAN cells from $Ca_v1.2^{DHP-/-}$ mice (Fig. 8A, supplementary table 3). Nifedipine highly affected (70% action potential rate decrease) automaticity in $Ca_v1.2^{DHP-/-}$ pacemaker cells (Fig. 8B, supplementary table 3). Finally, concomitant perfusion of TTA-A_2 and nifedipine stopped spontaneous sinoatrial action potential firing on 3 out of 6 $Ca_v1.2^{DHP-/-}$ SAN cells with a total residual action potential rate of about 25 bpm (Fig. 8C, supplementary table 3). The action potential parameters are reported in the supplementary table 3.

4.4.5. $Ca_v1.3$ channels silencing decreased spontaneous intracellular Ca^{2+} transient frequency and augmented SR Ca^{2+} load in SAN myocytes

To further characterize the Ca^{2+}-dependence of cardiac automaticity we recorded intracellular Ca^{2+} release ($[Ca^{2+}]_i$) by line-scan imaging of Fluo-4-loaded myocytes in control and in mutant SAN cells. Similar to current clamps results (Fig. 7), 3 µM ivabradine significantly reduced the spontaneous $[Ca^{2+}]_i$ transient frequency in SAN cells from all genotypes studied. In addition, perfusion of 50 nM TTX further decreased automaticity (Fig. 9). Even if we recorded a variation in the number of local Ca^{2+} release events in basal condition between $Ca_v1.3^{-/-}$ and $Ca_v1.3^{-/-}/Ca_v3.1^{-/-}$ cells (supplementary Fig. 4A), we failed to detect any differences in the LCRs number between control condition, ivabradine perfusion and perfusion of ivabradine plus TTX (supplementary Fig. 4B).

4.5. Discussion

Our study reports, at first, that genetic inactivation of $Ca_v1.3$ and $Ca_v3.1$ subunits abolished Ca^{2+} current, at least, at voltages spanning the diastolic depolarization range, in SAN cells. Second, we show that concomitant ablation of L-type $Ca_v1.3$ and T-type $Ca_v3.1$ Ca^{2+} channels disrupts heart automaticity in vivo by inducing prominent SAN bradycardia and severe atrioventricular dysfunction. Third, we show that $Ca_v3.1$ channels play an important role in stabilizing atrial and ventricular rhythmicity in isolated $Ca_v1.3^{-/-}$ hearts. Indeed, $Ca_v1.3^{-/-}/Ca_v3.1^{-/-}$ mice present slow SAN rates associated with both atrial and ventricular arrhythmias. Fourth, we report that in both $Ca_v1.3^{-/-}$ and $Ca_v1.3^{-/-}/Ca_v3.1^{-/-}$ SAN/atria preparations, residual pacemaker activity is predominantly generated in nodal and extranodal sites by f-channels and TTX-sensitive Na^+ channels. Finally, we show that spontaneous RyR-dependent $[Ca^{2+}]_i$ release cannot sustain viable automaticity following concomitant genetic ablation of $Ca_v1.3$ channels and pharmacologic inhibition of f-channels.

4.5.1. Concomitant genetic ablation of $Ca_v1.3$ and $Ca_v3.1$ channels abolishes Ca^{2+} current at voltages spanning the diastolic depolarisation range and disrupts heart automaticity

Our results indicate that genetic inactivation of both $Ca_v3.1$ and $Ca_v1.3$ abolishes I_{Ca} at voltages between -65 mV and -40 mV (diastolic depolarisation membrane potential range) (Fig. 1). Previous work showed that $Ca_v3.1$ channels activate at more negative voltages than $Ca_v1.3$ channels[8,15]. However, their limited steady-state availability at the maximum diastolic potential predicts smaller $Ca_v3.1$-mediated I_{CaT} than $Ca_v1.3$-mediated I_{CaL}[14]. Consistently with this prediction, we did not observe additivity between $Ca_v1.3$ and $Ca_v3.1$ ablation on SAN rhythm in vivo (Fig. 2). In contrast, we observed lower ventricular rates in $Ca_v1.3^{-/-}/Ca_v3.1^{-/-}$ in comparison with $Ca_v1.3^{-/-}$ mice. Decreased ventricular rate was due to worsening of atrioventricular conduction in double mutant mice, because pharmacologic inhibition of the autonomic nervous system input by atropine and propranolol reduced atrioventricular blocs leading to similar ventricular rates in $Ca_v1.3^{-/-}$ and $Ca_v1.3^{-/-}/Ca_v3.1^{-/-}$ mice. The differential effect of concomitant, versus individual genetic ablation of VGCCs on SAN automaticity and atrioventricular conduction suggests that in the SAN $Ca_v1.3$ and $Ca_v3.1$ channels converge to a common intracellular mechanism of pacemaking. Indeed, the absence of additivity of $Ca_v1.3$ and $Ca_v3.1$ ablation on SAN rate in vivo could be explained by convergence in the control of RyR dependent Ca^{2+} release by I_{CaT}[26] and $Ca_v1.3$-mediated I_{CaL}[16]. On the other hand, the additive effect on atrioventricular conduction of $Ca_v3.1$ deletion in double mutant mice is explained by the loss of depolarization reserve mediated by I_{CaT} in the $Ca_v1.3^{-/-}$ genetic background. The importance of $Ca_v3.1$ channels in atrioventricular conduction is stressed by the prevalence of dissociated atrial and ventricular rhythms in Langendorff-perfused $Ca_v1.3^{-/-}/Ca_v3.1^{-/-}$ hearts (Fig. 4). In addition, our data show that expression of $Ca_v3.1$ channels is essential to maintain normal atrial and ventricular rhythmicity in hearts lacking $Ca_v1.3$. The observation that $Ca_v1.3^{-/-}/Ca_v3.1^{-/-}$ hearts ex vivo present with junctional atrial and ventricular rhythmicity rather than SAN rate as observed in vivo led us to investigate automaticity using isolated SAN/atria preparations. In comparison with $Ca_v1.3^{-/-}$ hearts, $Ca_v1.3^{-/-}/Ca_v3.1^{-/-}$ hearts showed an increased frequency of alternating impulse initiation in the SAN and in extranodal sites, which was associated with slower automaticity in double mutant hearts (Fig. 5). These observations indicate that concomitant ablation of $Ca_v1.3$ and $Ca_v3.1$ channels disrupts primary SAN automaticity, shifting impulse initiations to extranodal sites. Shifting of leading pacemaker sites to extranodal locations can explain atrial ectopic and atrial rhythmicity observed in Langendorff-perfused $Ca_v1.3^{-/-}/Ca_v3.1^{-/-}$ hearts. The discrepancy between the additivity of the effect of $Ca_v1.3$ and $Ca_v3.1$ loss in isolated $Ca_v1.3^{-/-}/Ca_v3.1^{-/-}$ SAN/atria preparations and the observations in vivo and in intact hearts could be explained by the action of the autonomic nervous system and/or the presence of the mechanoelectrical feedback. In conclusion, our data show for the first time that $Ca_v1.3$ channels are necessary to maintain atrial automaticity in the SAN region. $Ca_v3.1$ channels contribute to sustain SAN automaticity and to maintain SAN dominance towards extranodal sites (Fig. 5).

4.5.2. Automaticity in $Ca_v1.3^{-/-}$ and $Ca_v1.3^{-/-}/Ca_v3.1^{-/-}$ SANs is sustained by f- and TTX-sensitive Na^+ channels

Concomitant ablation of $Ca_v1.3$ and $Ca_v3.1$ reduce the heart rate in vivo by about 200 bpm, which corresponds to ~30% of the heart rate measured in wild-type mice under control conditions (Fig. 2). Inhibition of I_f by ivabradine reduced the heart rate about 200 bpm in all genotypes studied, a value which corresponds to the decrease in heart rate induced by inhibition of the autonomic nervous system. This observation suggests that I_f was controlling heart rate under the action of the autonomic nervous system in $Ca_v1.3^{-/-}$ and $Ca_v1.3^{-/-}/Ca_v3.1^{-/-}$ mice. In addition, these results indicate that I_f is responsible for ~ one third of the total rate of pacemaker activity. Consequently, I_f inhibition in $Ca_v1.3^{-/-}$ and $Ca_v1.3^{-/-}/Ca_v3.1^{-/-}$ mice reduced heart rate by two-thirds leaving an averaged heart rate of about 240 bpm. Heart rate in some $Ca_v1.3^{-/-}/Ca_v3.1^{-/-}$ mice was lower than 100 bpm, which corresponds to a reduction of more than 85%, in comparison to the initial heart rate measured in wild-type mice under control condition. While such a prominent reduction in heart rate would be lethal in humans, this residual pacemaking was sufficient to sustain heart function in mice. Taken, together, these observations indicate that L-type $Ca_v1.3$ and f-channels are the two predominant ion channel mechanisms underlying pacemaker activity in mice.

Beside VGCCs and I_f, other plasmalemmal ion channels, as well as RyR-dependent Ca^{2+} release have been proposed to participate to the generation of the diastolic depolarization and pacemaker activity. We thus hypothesized that the residual pacemaker activity observed in vivo in $Ca_v1.3^{-/-}$ and $Ca_v1.3^{-/-}/Ca_v3.1^{-/-}$ mice or ex vivo in mutant hearts and SAN/atrial preparations was sustained by TTX-sensitive Nav1 channels and RyR-dependent Ca^{2+} release. Our data show that inhibition of $I_{Na(TTX)}$ arrests automaticity in a majority of isolated SAN/atria preparations and in isolated SAN cells. This observation indicates that TTX-sensitive Na_v1 channels are the predominant mechanisms sustaining pacemaker activity in the concomitant absence of L-type $Ca_v1.3$, T-type $Ca_v3.1$ channels and pharmacologic inhibition of I_f (Fig. 6 and 7). We may expect that spontaneous RyR-dependent $[Ca^{2+}]_i$ release could still sustain viable pacemaking under combined inhibition of I_f and and $I_{Na(TTX)}$ and concomitant genetic ablation of $Ca_v1.3$ and $Ca_v3.1$ channels. Indeed, the ubiquitous excitation-contraction coupling cardiac I_{CaL} isoform $Ca_v1.2$ is still expressed in $Ca_v1.3^{-/-}/Ca_v3.1^{-/-}$ hearts and could ensure proper SR Ca^{2+} load to activate the spontaneous "Ca^{2+} clock". In this regard, we showed previously that

$Ca_v1.3^{-/-}$ SAN cells present normal SR Ca^{2+} load[16]. However, we showed in the same study that diastolic RyR-dependent Ca^{2+} release is diminished in $Ca_v1.3^{-/-}$ SAN cells and that ablation of $Ca_v1.3$ channels disrupts synchronous recruitment of diastolic Ca^{2+} releasing sites[16]. It is thus possible that individual $Ca_v1.3$ and/or concomitant ablation of $Ca_v1.3$ and $Ca_v3.1$ channels disables the "Ca^{2+} clock" mechanism. We cannot exclude that RyR-dependent $[Ca^{2+}]_i$ release was still effective in the fraction of SAN/atria preparations generating automaticity at very low rates, probably in cooperation with TRPM4 channels[10]. However, our results show that $Ca_v1.3$ and f-channels account for 70-80% of the SAN rate, highlighting these channels as the predominant mechanisms in the generation of SAN pacemaker activity.

4.6. Conclusions

As stressed above our study demonstrates that L-type $Ca_v1.3$ and T-type $Ca_v3.1$ channels are essential for generating normal heart automaticity, atrioventricular conduction, as well as to stabilize atrial and ventricular rhythmicity and generating SAN pacemaker activity. As a corollary, we show that normal heart automaticity necessitates the expression of low-voltage activated VGCCs and would not be possible with the sole expression of the ubiquitous L-type $Ca_v1.2$ isoform in association with f-channels. On the other hand, $Ca_v1.3$ and f-channels appear to constitute the two predominant cardiac pacemaker mechanisms. Furthermore, our study suggests that co-expression of $Ca_v1.3$, $Ca_v3.1$ and f-channels could be the cornerstone to develop "biological" pacemakers with proper rate[27]. Finally, our data in mice suggest that $Ca_v1.3$ and $Ca_v3.1$ channels could underlie several still-to-be identified forms of idiopathic bradycardia and atrioventricular dysfunction in humans [28].

4.7. References

1. Mangoni ME, Nargeot J. Genesis and regulation of the heart automaticity. *Physiol Rev* 2008;**88**:919–982.
2. DiFrancesco D. Pacemaker Mechanisms in Cardiac Tissue. *Annu Rev Physiol* 1993;**55**:455–472.
3. Lakatta EG, Maltsev VA, Vinogradova TM. A Coupled SYSTEM of intracellular Ca2+ clocks and surface membrane voltage clocks controls the timekeeping mechanism of the heart's pacemaker. *Circ Res* 2010;**106**:659–673.
4. Lakatta EG, Vinogradova T, Lyashkov A, Sirenko S, Zhu W, Ruknudin A, Maltsev VA. The integration of spontaneous intracellular Ca2+ cycling and surface membrane ion channel activation entrains normal automaticity in cells of the heart's pacemaker. *Ann N Y Acad Sci* 2006;**1080**:178–206.
5. Vinogradova TM, Zhou YY, Maltsev V, Lyashkov A, Stern M, Lakatta EG. Rhythmic Ryanodine Receptor Ca 2+ Releases during Diastolic Depolarization of Sinoatrial Pacemaker Cells Do Not Require Membrane Depolarization. *Circ Res* 2004;**94**:802–809.
6. Bogdanov KY, Vinogradova TM, Lakatta EG. Sinoatrial Nodal Cell Ryanodine Receptor and Na+-Ca2+ Exchanger. *Circ Res* 2001;**88**:1254–1258.
7. Difrancesco D. The role of the funny current in pacemaker activity. *Circ Res* 2010;**106**:434–446.
8. Mangoni ME, Couette B, Marger L, Bourinet E, Striessnig J, Nargeot J. Voltage-dependent calcium channels and cardiac pacemaker activity: From ionic currents to genes. *Prog Biophys Mol Biol* 2006;**90**:38–63.
9. Lei M, Jones SA, Liu J, Lancaster MK, Fung SSM, Dobrzynski H, Camelliti P, Maier SKG, Noble D, Boyett MR. Requirement of neuronal- and cardiac-type sodium channels for murine sinoatrial node pacemaking. *J Physiol* 2004;**559**:835–848.
10. Demion M, Bois P, Launay P, Guinamard R. TRPM4, a Ca2+-activated nonselective cation channel in mouse sino-atrial node cells. *Cardiovasc Res* 2007;**73**:531–538.
11. Rajan Saha, Pietro Mesirca, Marjolein Van den Boogert, Jonathan Rosen, John Mably MEM and DEC. Ion channel-kinase TRPM7 is required for maintaining cardiac automaticity. *Proc Natl Acad Sci U S A* 2013;**111**:E3037–E3046.

12. Marionneau C, Couette B, Liu J, Li H, Mangoni ME, Nargeot J, Lei M, Escande D, Demolombe S. Specific pattern of ionic channel gene expression associated with pacemaker activity in the mouse heart. *J Physiol* 2005;**562**:223–234.
13. Bers DM. Cardiac Excitation-Contraction Coupling. *Nature* 2002;**415**:198–205.
14. Mangoni ME, Traboulsie A, Leoni AL, Couette B, Marger L, Quang K Le, Kupfer E, Cohen-Solal A, Vilar J, Shin HS, Escande D, Charpentier F, Nargeot J, Lory P. Bradycardia and slowing of the atrioventricular conduction in mice lacking CaV3.1/α1G T-type calcium channels. *Circ Res* 2006;**98**:1422–1430.
15. Mangoni ME, Couette B, Bourinet E, Platzer J, Reimer D, Striessnig J, Nargeot J. Functional role of L-type Cav1.3 Ca2+ channels in cardiac pacemaker activity. *Proc Natl Acad Sci U S A* 2003;**100**:5543–5548.
16. Torrente AG, Mesirca P, Neco P, Rizzetto R, Dubel S, Barrere C, Sinegger-Brauns M, Striessnig J, Richard S, Nargeot J, Gomez AM, Mangoni ME. L-type Cav1.3 channels regulate ryanodine receptor-dependent Ca2+ release during sino-atrial node pacemaker activity. *Cardiovasc Res* 2016;**109**:451–461.
17. Marger L, Mesirca P, Alig J, Torrente A, Dubel S, Engeland B, Kanani S, Fontanaud P, Striessnig J, Shin HS, Isbrandt D, Ehmke H, Nargeot J, Mangoni ME. Functional roles of Cav1.3, Cav3.1 and HCN channels in automaticity of mouse atrioventricular cells: Insights into the atrioventricular pacemaker mechanism. *Channels* 2011;**5**:251–261.
18. Neco P, Torrente AG, Mesirca P, Zorio E, Liu N, Priori SG, Napolitano C, Richard S, Benitah JP, Mangoni ME, Gómez AM. Paradoxical effect of increased diastolic Ca2+ release and decreased sinoatrial node activity in a mouse model of catecholaminergic polymorphic ventricular tachycardia. *Circulation* 2012;**126**:392–401.
19. Mangoni ME, Nargeot J. Properties of the hyperpolarization-activated current (I f) in isolated mouse sino-atrial cells. *Cardiovasc Res* 2001;**52**:51–64.
20. Dobrzynski H, Nikolski VP, Sambelashvili AT, Greener ID, Yamamoto M, Boyett MR, Efimov IR. Site of Origin and Molecular Substrate of Atrioventricular Junctional Rhythm in the Rabbit Heart. *Circ Res* 2003;**93**:1102–1110.
21. Difrancesco D. Characterization of single pacemaker channels in cardiac sino-atrial node cells. *Nature* 1986;**324**:470–473.
22. DiFrancesco D, Ferroni A, Mazzanti M, Tromba C. Properties of the hyperpolarizing-activated current (if) in cells isolated from the rabbit sino-atrial

node. *J Physiol* 1986;**377**:61–88.

23. Mesirca P, Bidaud I, Mangoni ME. Rescuing cardiac automaticity in L-type Cav1.3 channelopathies and beyond. *J Physiol* 2016;**594**:5869–5879.
24. Mesirca P, Bidaud I, Briec F, Evain S, Torrente AG, Quang K Le, Leoni AL, Baudot M, Marger L, Chong ACY, Nargeot J, Striessnig J, Wickman K, Charpentier F, Mangoni ME. G protein-gated IKACh channels as therapeutic targets for treatment of sick sinus syndrome and heart block. *Proc Natl Acad Sci U S A* 2016;**113**:E932-941.
25. Maier SKG, Westenbroek RE, Yamanushi TT, Dobrzynski H, Boyett MR, Catterall WA, Scheuer T. An unexpected requirement for brain-type sodium channels for control of heart rate in the mouse sinoatrial node. *Proc Natl Acad Sci U S A* 2003;**100**:3507–3512.
26. Hüser J, Blatter LA, Lipsius SL. Intracellular Ca2+ release contributes to automaticity in cat atrial pacemaker cells. *J Physiol* 2000;**524** pt **2**:415–422.
27. Rosen MR, Robinson RB, Brink PR, Cohen IS. The road to biological pacing. *Nat Rev Cardiol* 2011;**8**:656–666.
28. Baig SM, Koschak A, Lieb A, Gebhart M, Dafinger C, Nürnberg G, Ali A, Ahmad I, Sinnegger-Brauns MJ, Brandt N, Engel J, Mangoni ME, Farooq M, Khan HU, Nürnberg P, Striessnig J, Bolz HJ. Loss of Ca v 1.3 (CACNA1D) function in a human channelopathy with bradycardia and congenital deafness. *Nat Neurosci* Nature Publishing Group; 2011;**14**:77–86.

4.8. Figure legends

Figure 1. I_{Ca} in isolated SAN cells. (A). Sample traces obtained using a HP at -80 mV (top) and at -55 mV (bottom) in SAN myocytes from wild-type (a), $Ca_v3.1^{-/-}$ (b), $Ca_v1.3^{-/-}$ (c) and $Ca_v1.3^{-/-}/Ca_v3.1^{-/-}$ mice (d). (B) I-V relationship of Ca^{++} current recorded at HP = -80 mV (black circles) and at HP = -55 mV (red circles) in SAN cells from different genotypes: wild -type (a, n=11), $Ca_v3.1^{-/-}$ (b, n=6), $Ca_v1.3^{-/-}$ (c, n=11) and $Ca_v1.3^{-/-}/Ca_v3.1^{-/-}$ mice (d, n=10). In (a) and (b) dotted line indicates the net $I_{Ca,T}$ I-V curve calculated as difference between values obtained at HP of -55 mV from those at HP -80 mV. (C) Relative density of $I_{Ca,T}$ and $I_{Ca,L}$ at different test potentials measured in pacemaker cells, at HP = -80 mV, from wild type (black bars, n=11), $Ca_v3.1^{-/-}$ (a, open bars, n=6), $Ca_v1.3^{-/-}$ (b, open bars, n=11) and $Ca_v1.3^{-/-}/Ca_v3.1^{-/-}$ mice (c, open bars, n=10). (D) Same as C but with a HP = - 55 mV.

Figure 2. ECG recordings in wild-type and mutant mice. (A). Sample dot plots of heart rate (left panels) and ECG recordings (left panels) under control conditions in n=11 wild-type (WT), n=11 $Ca_v3.1^{-/-}$, n=8 $Ca_v1.3^{-/-}$ and n=10 $Ca_v1.3^{-/-}/Ca_v3.1^{-/-}$ mice. (B). Dot plots of heart rate (left panels) and ECG recordings (right panels) following intraperitoneal injection of atropine (1 mg/Kg) and propranolol (5 mg/Kg) to inhibit autonomic nervous system influence (ANS-) in n=10 WT, n=12 $Ca_v3.1^{-/-}$, n=7 $Ca_v1.3^{-/-}$, and n=8 $Ca_v1.3^{-/-}/Ca_v3.1^{-/-}$mice. Averaged rate of P waves (atrial rate) in wild-type and mutant mice under control conditions (C) or following atropine and propranolol injection (D). (E). Heart rates (ventricular rates) in wild-type and mutant mice Statistics: One-way ANOVA followed by Tukey's multiple comparisons test. (F). Number of atrioventricular blocks (AVB) under control and atropine and propranolol inhibition conditions in n=6 $Ca_v1.3^{-/-}$, and n=7 $Ca_v1.3^{-/-}/Ca_v3.1^{-/-}$ mice. Statistics: unpaired t-test. (#) indicates comparison with wild-type.

Figure 3. **Consequences of concomitant ablation of $Ca_v1.3$ and $Ca_v3.1$ on intrinsic heart automaticity using intact Langendorff perfused hearts**. Dot plots of heart rates and sample ECGs recorded before (A) and after (B) intraperitoneal (IP) injection of ivabradine (IVA, 6mg/kg) in n=10 wild-type, n=5 $Ca_v3.1^{-/-}$, n=8 $Ca_v1.3^{-/-}$ and n=10 $Ca_v1.3^{-/-}/Ca_v3.1^{-/-}$ mice. (C). Plotted averaged heart rates measured before and after IVA injection in all genotypes. Whiskers indicate mean ± the SEM. (D).

Relative effect of IVA 6mg/kg IP injection on heart rates measured in all genotypes. Statistics: one-way ANOVA followed by Tukey's multiple comparisons test. (#) indicates comparison with wild-type

Figure 4. (A). Line plots of atrial (red line) and ventricular (blue line) rates (left panel) and sample ECGs (right panel) recorded *ex vivo* on isolated Langendorff perfused heart under control conditions in n=8 wild-type, n=6 Ca$_v$3.1$^{-/-}$, n=8 Ca$_v$1.3$^{-/-}$ and n=7 Ca$_v$1.3$^{-/-}$/Ca$_v$3.1$^{-/-}$. (B). P wave rates in isolated wild-type and mutant hearts under control conditions. (C). Differences between atrial and ventricular rates of isolated hearts. Statistics: one-way ANOVA followed by Tukey's multiple comparisons. Whiskers indicate mean ± the SEM. (#) indicates comparison with wild-type.

Figure 5. Distribution of pacemaker leading sites in SAN/atria preparations and automaticity. (A). Sample snapshots of SAN/atria preparations with points showing the position of the pacemaking leading region. Connecting lines indicate alternating leading regions in in the same mutant SAN. (B). Comparison between atrial rates of n=8 wild-type, n=8 Ca$_v$3.1$^{-/-}$, n=7 Ca$_v$1.3$^{-/-}$ and n=7 Ca$_v$1.3$^{-/-}$/Ca$_v$3.1$^{-/-}$ SAN/atria preparations. (C). Coefficient of variability of atrial rates from the same mice as in (B). Statistics: one-way ANOVA followed by Tukey's multiple comparisons test. Whiskers indicate mean ± the SD. (D). Linear regression between the rate from the leading region and the distance from the normal leading region recorded in wild-type preparations. (#) indicates comparison with wild-type.

Figure 6. Pacemaker arrest by concomitant inhibition of I_f and $I_{Na\ TTX\text{-}sensitive}$ in Ca$_v$1.3$^{-/-}$ SAN/atria preparations. (A). Atrial rates of n=7 wild-type, n=6 Ca$_v$3.1$^{-/-}$, n=7 Ca$_v$1.3$^{-/-}$ and n=7 Ca$_v$1.3$^{-/-}$/Ca$_v$3.1$^{-/-}$ isolated Langendorff hearts under ivabradine (IVA, 10 µM) perfusion. (B). Atrial rates of isolated hearts under IVA 10 µM + TTX 100 nM perfusion. (C). Sample snapshots of the localization of leading regions under IVA 10 µM perfusion (left panels) and averaged rates of depolarization in n=7 wild-type, n=7 Ca$_v$3.1$^{-/-}$, n=6 Ca$_v$1.3$^{-/-}$ and n=6 Ca$_v$1.3$^{-/-}$/Ca$_v$3.1$^{-/-}$ SAN/atria preparations. (D): Same representation as in (C) with leading region in IVA 10 µM + TTX 100 nM perfusion. Statistics: one-way ANOVA followed by Tukey's multiple comparisons test. Whiskers indicate mean ± the SD. (#) indicates comparison with wild-type.

Figure 7. **Pacemaker activity in SAN cells from different mutant mice.** (A). Sample perforated-patch action potential recordings of SAN cells of wild-type and mutant mice under control conditions or following perfusion of IVA or IVA+TTX 100 nM. (B). Averaged rates of action potentials recorded on SAN cells under conditions in (A). Under control conditions: wild-type n=14, $Ca_v3.1^{-/-}$ n=8, $Ca_v1.3^{-/-}$ n=6 and $Ca_v1.3^{-/-}/Ca_v3.1^{-/-}$ n= 14. Statistics: one-way ANOVA followed by Holm-Sidak multiple comparisons test. Whiskers indicate mean ± the SD.

Figure 8. **Automaticity in isolated $Ca_v1.2^{DHP-/-}$ SAN cells perfused with T- and L-type Ca^{2+} channel blockers.** Sample perforated-patch action potential recordings (left) and averaged rates (right) from $Ca_v1.2^{DHP-/-}$ SAN cells in control conditions (n=6) and under perfusion of 1 µM TTA-A_2 (A, n=5), 3µM nifedipine (B, n=5) or both (C, n=6). Statistics: paired t-test. Whiskers indicate mean ± the SD.

Figure 9. **$[Ca^{2+}]_i$ handling in isolated pacemaker cells from different mutant mice**. Confocal line scan images (left) and averaged frequency of spontaneous $[Ca^{2+}]_I$ transients of SAN myocytes form wild-type (A, n=13), $Ca_v3.1^{-/-}$ (B, n=8), $Ca_v1.3^{-/-}$ (C, n=13) and $Ca_v1.3^{-/-}/Ca_v3.1^{-/-}$ (D, n=7) loaded with Fluo-4 and perfused with Tyrode's solution (left) or IVA 3µM (center) or IVA 3µM + TTX 50nM (right). Statistics: one-way ANOVA followed by Holm-Sidak multiple comparisons test. Whiskers indicate mean ± the SD.

Figure 1

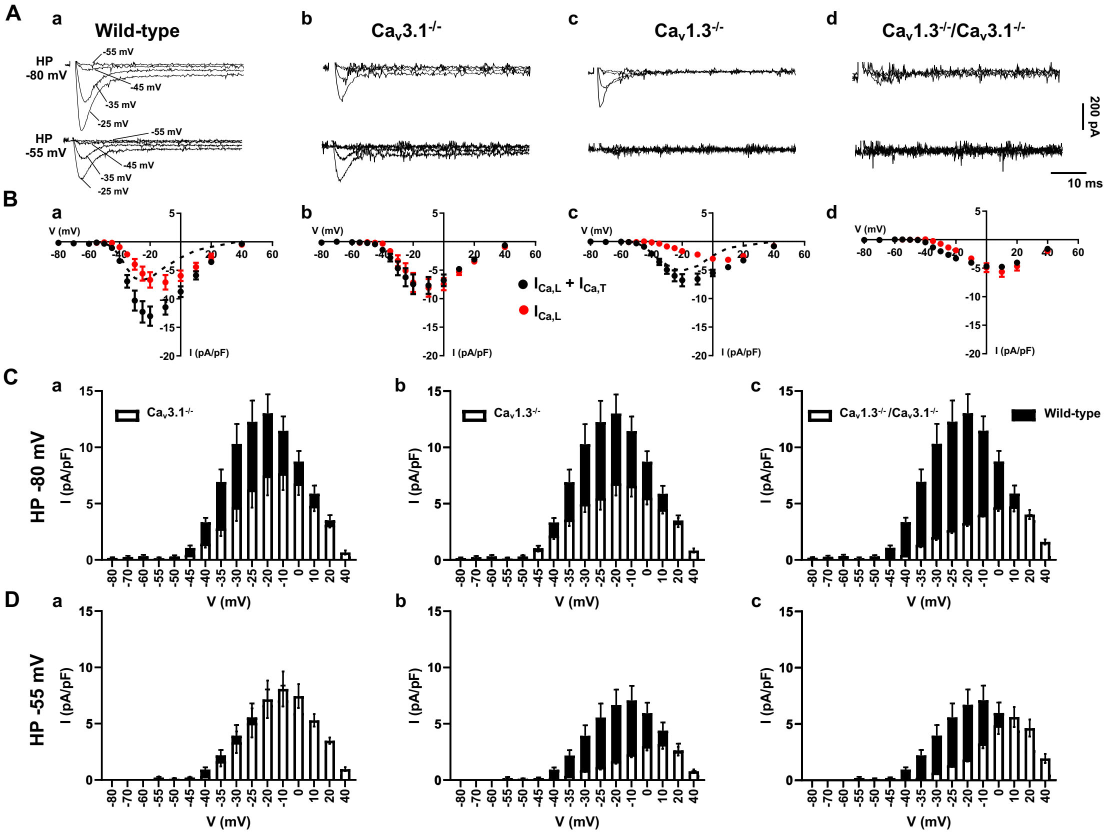
A
a
Wild-type
b
$Ca_v3.1^{-/-}$
c
$Ca_v1.3^{-/-}$
d
$Ca_v1.3^{-/-}/Ca_v3.1^{-/-}$
HP -80 mV
-55 mV
-45 mV
-35 mV
-25 mV
HP -55 mV
-55 mV
-45 mV
-35 mV
-25 mV
200 pA
10 ms
B
V (mV)
I (pA/pF)
$I_{Ca,L} + I_{Ca,T}$
$I_{Ca,L}$
C
HP -80 mV
I (pA/pF)
V (mV)
$Ca_v3.1^{-/-}$
$Ca_v1.3^{-/-}$
$Ca_v1.3^{-/-}/Ca_v3.1^{-/-}$
Wild-type
D
HP -55 mV
I (pA/pF)
V (mV)

Figure 2

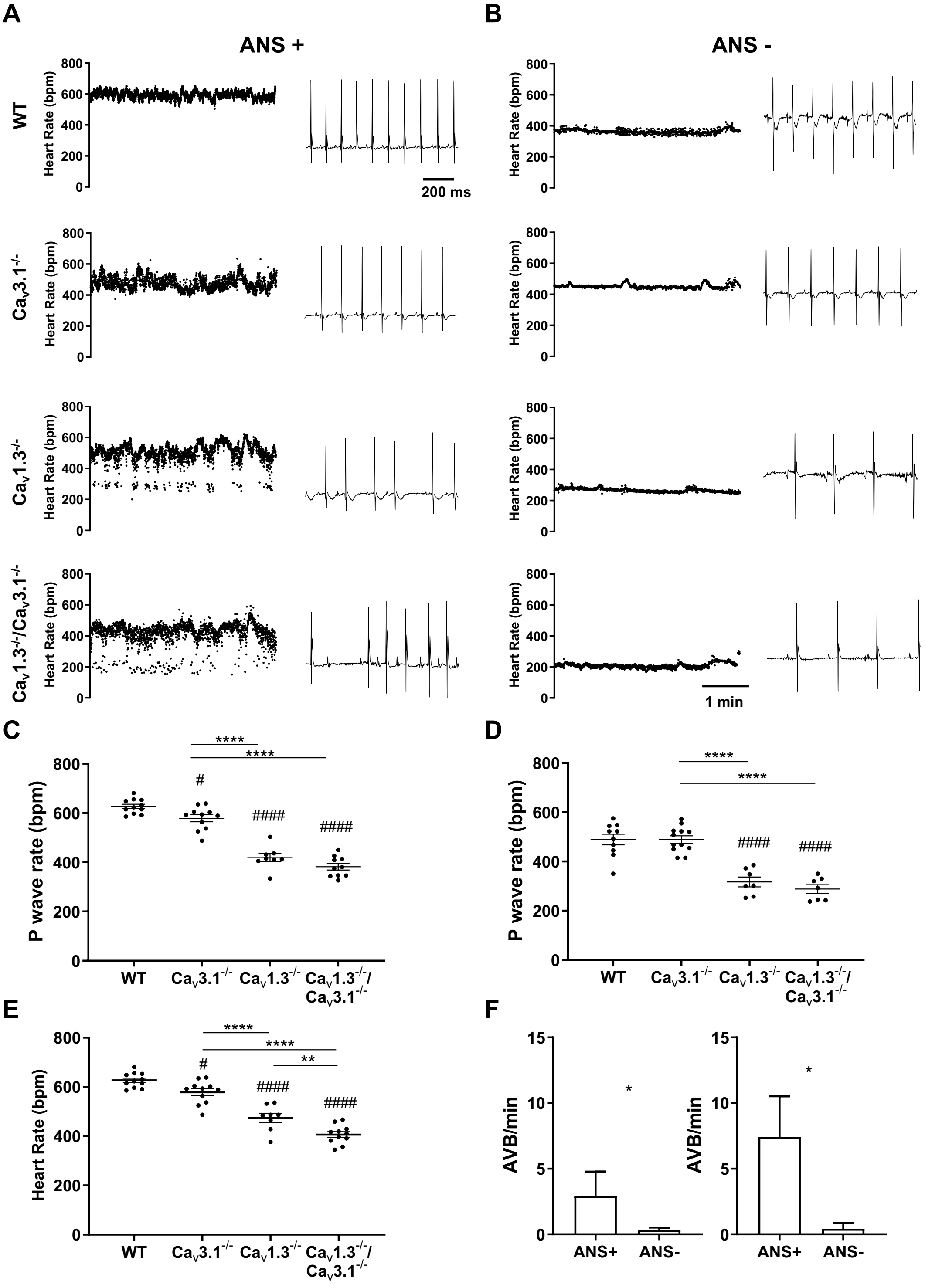
A
ANS +
B
ANS -
WT
Cav3.1-/-
Cav1.3-/-
Cav1.3-/-/Cav3.1-/-
Heart Rate (bpm)
800
600
400
200
0
200 ms
1 min
C
D
P wave rate (bpm)
WT
Cav3.1-/-
Cav1.3-/-
Cav1.3-/-/Cav3.1-/-
****
#
####
E
Heart Rate (bpm)
**
F
AVB/min
15
10
5
0
ANS+
ANS-
*

Figure 3

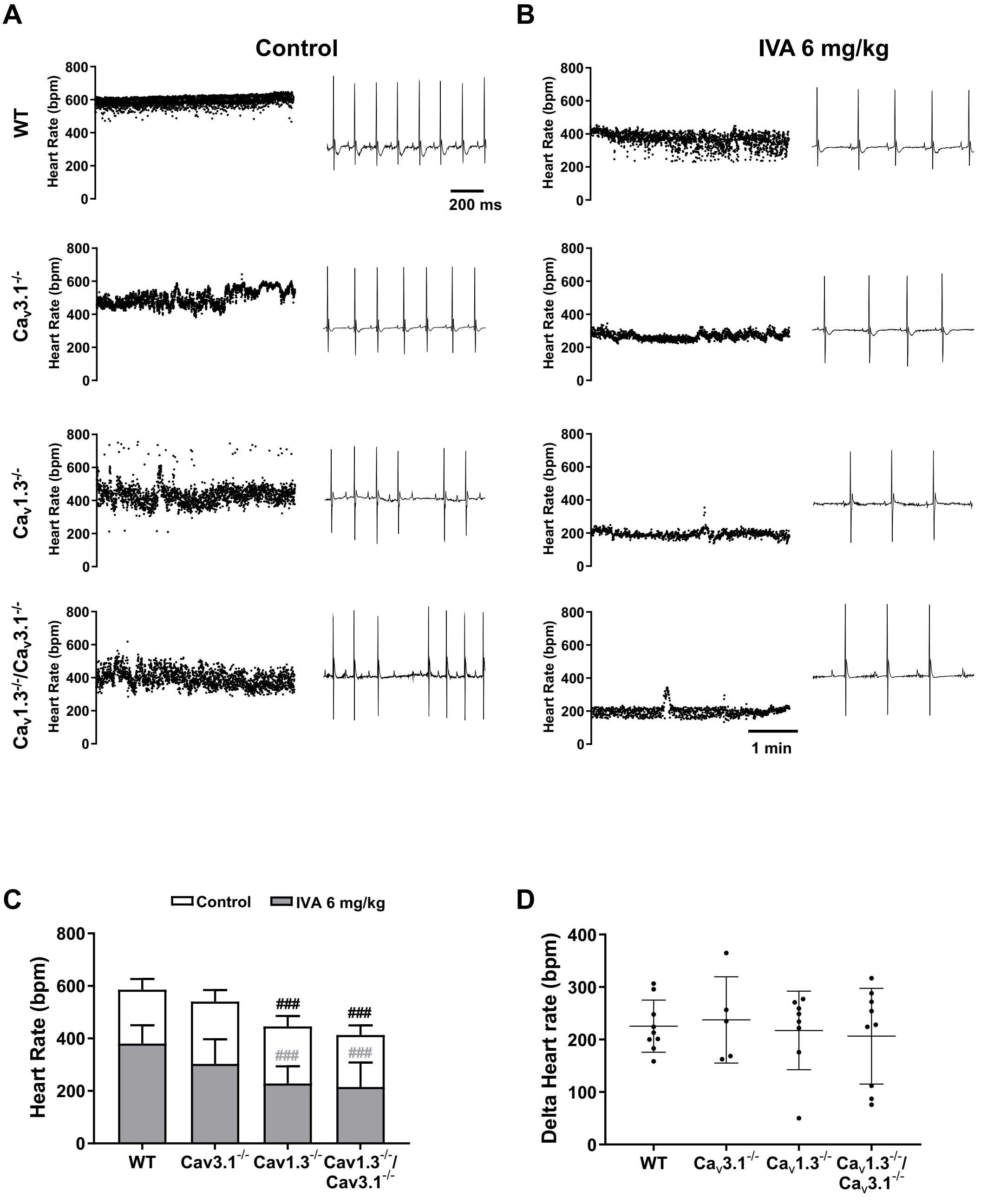
A
B
Control
IVA 6 mg/kg
WT
$Ca_v3.1^{-/-}$
$Ca_v1.3^{-/-}$
$Ca_v1.3^{-/-}/Ca_v3.1^{-/-}$
Heart Rate (bpm)
800
600
400
200
0
200 ms
1 min
C
Control
IVA 6 mg/kg
Heart Rate (bpm)
###
###
###
###
WT
$Cav3.1^{-/-}$
$Cav1.3^{-/-}$
$Cav1.3^{-/-}/Cav3.1^{-/-}$
D
Delta Heart rate (bpm)
400
300
200
100
0
WT
$Ca_v3.1^{-/-}$
$Ca_v1.3^{-/-}$
$Ca_v1.3^{-/-}/Ca_v3.1^{-/-}$

Figure 4

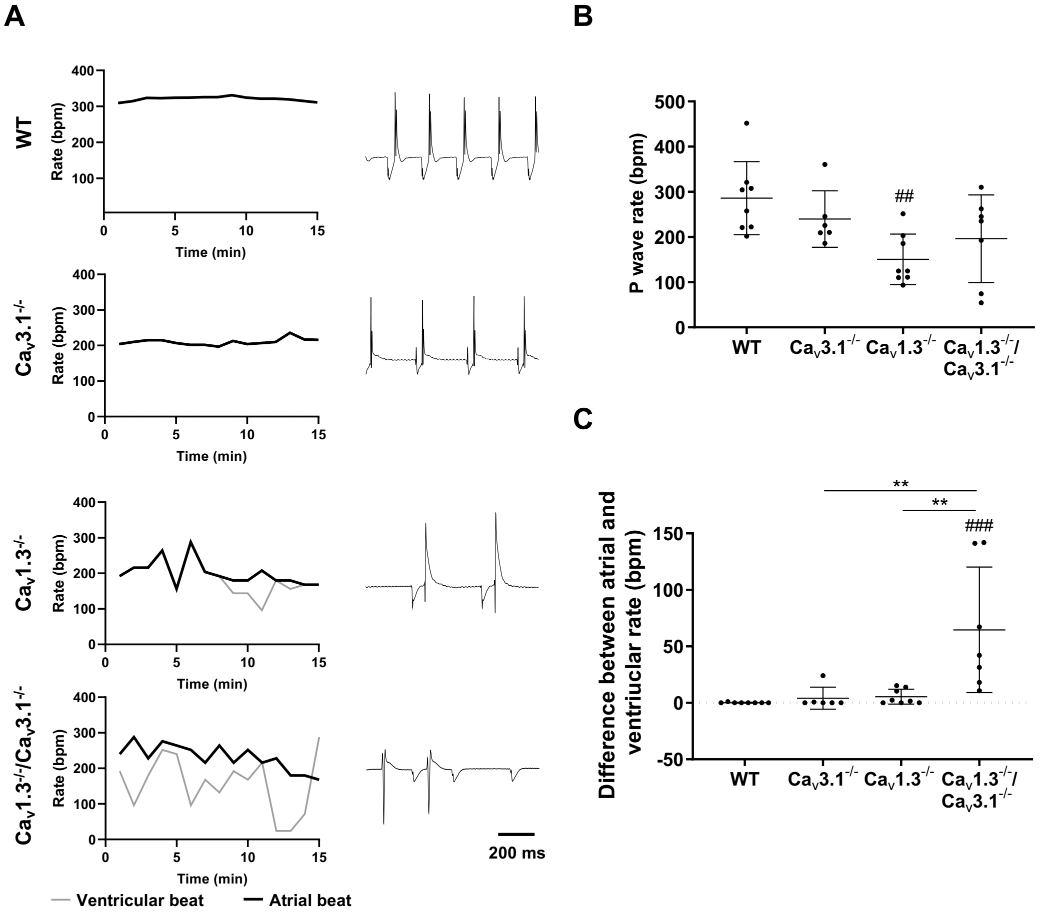
A
B
C
WT
Ca$_V$3.1$^{-/-}$
Ca$_V$1.3$^{-/-}$
Ca$_V$1.3$^{-/-}$/Ca$_V$3.1$^{-/-}$
Rate (bpm)
400
300
200
100
0
0
5
10
15
Time (min)
200 ms
Ventricular beat
Atrial beat
P wave rate (bpm)
500
400
300
200
100
0
WT
Ca$_V$3.1$^{-/-}$
Ca$_V$1.3$^{-/-}$
Ca$_V$1.3$^{-/-}$/ Ca$_V$3.1$^{-/-}$
##
Difference between atrial and ventriuclar rate (bpm)
150
100
50
0
-50
**
**
###

Figure 5

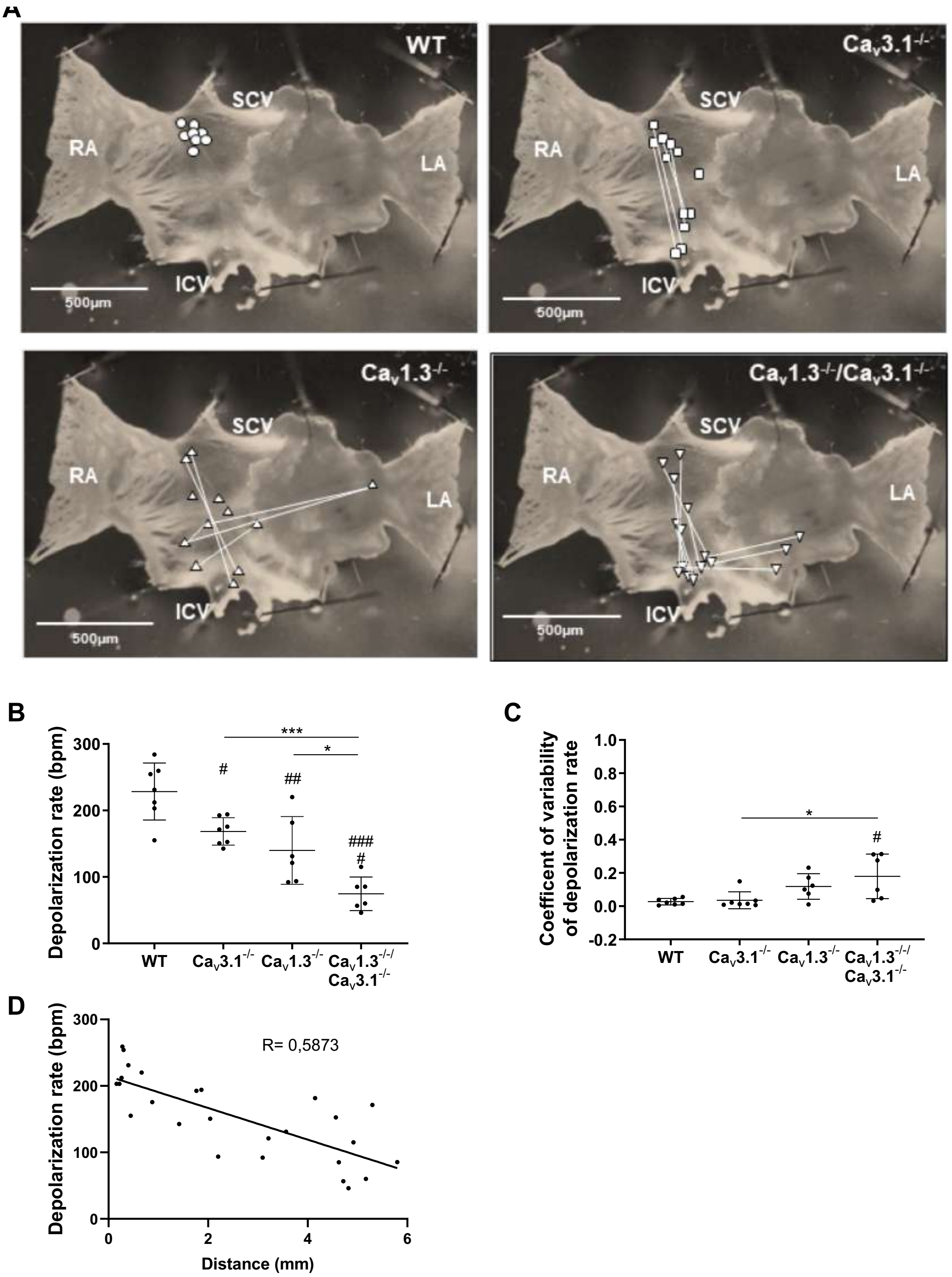
A
WT
SCV
RA
LA
ICV
500µm
Ca$_v$3.1$^{-/-}$
Ca$_v$1.3$^{-/-}$
Ca$_v$1.3$^{-/-}$/Ca$_v$3.1$^{-/-}$
B
Depolarization rate (bpm)
300
200
100
0
***
*
#
##
###
#
WT
Ca$_v$3.1$^{-/-}$
Ca$_v$1.3$^{-/-}$
Ca$_v$1.3$^{-/-}$/ Ca$_v$3.1$^{-/-}$
C
Coefficent of variability of depolarization rate
1.0
0.8
0.6
0.4
0.2
0.0
-0.2
*
#
WT
Ca$_v$3.1$^{-/-}$
Ca$_v$1.3$^{-/-}$
Ca$_v$1.3$^{-/-}$/ Ca$_v$3.1$^{-/-}$
D
Depolarization rate (bpm)
300
200
100
0
R= 0,5873
0
2
4
6
Distance (mm)

Figure 6

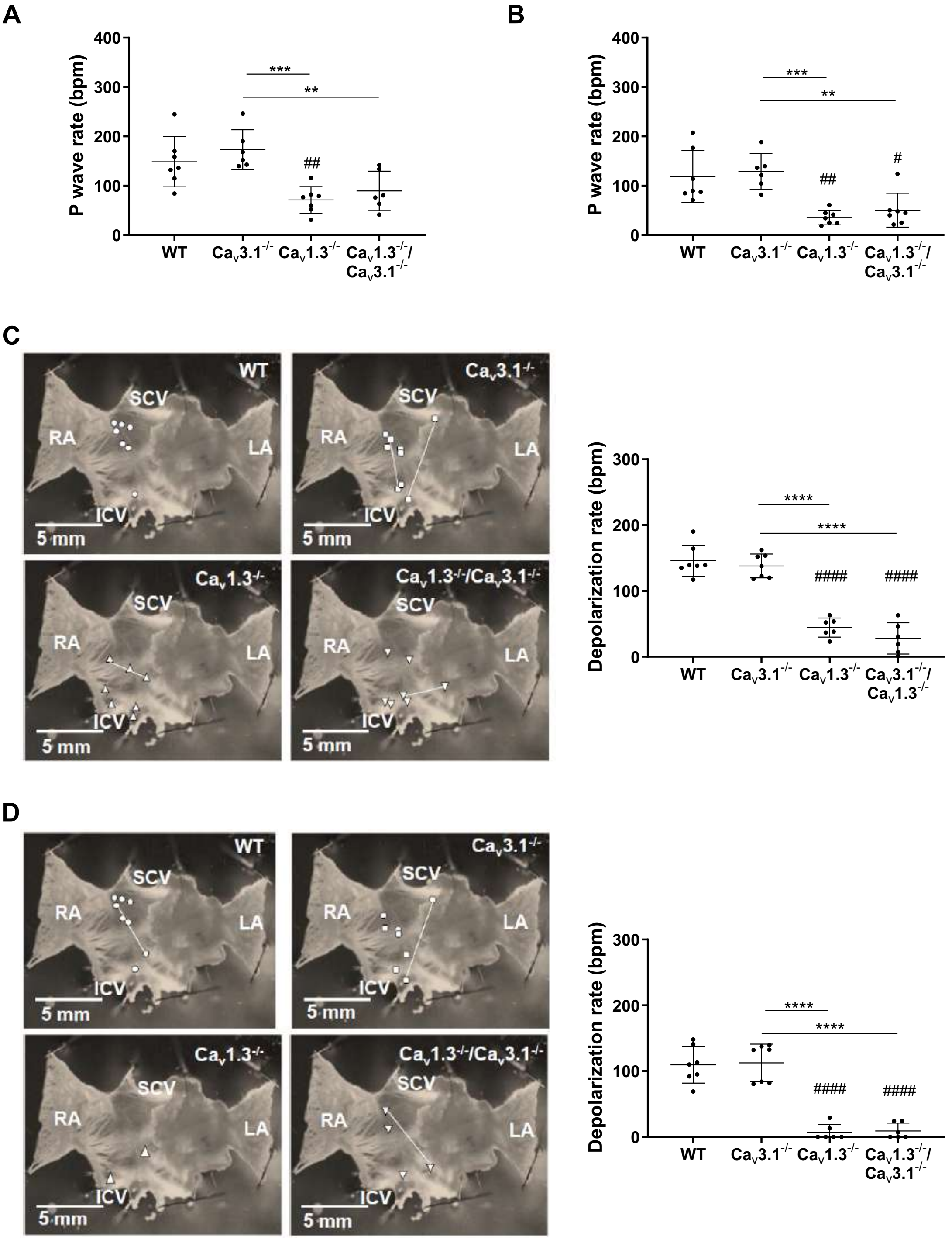
A
P wave rate (bpm)
0
100
200
300
400
***
**
##
WT
Cav3.1-/-
Cav1.3-/-
Cav1.3-/-/Cav3.1-/-
B
P wave rate (bpm)
0
100
200
300
400
***
**
##
#
WT
Cav3.1-/-
Cav1.3-/-
Cav1.3-/-/Cav3.1-/-
C
WT
Cav3.1-/-
Cav1.3-/-
Cav1.3-/-/Cav3.1-/-
SCV
RA
LA
ICV
5 mm
Depolarization rate (bpm)
0
100
200
300
****
****
####
####
WT
Cav3.1-/-
Cav1.3-/-
Cav3.1-/-/Cav1.3-/-
D
WT
Cav3.1-/-
Cav1.3-/-
Cav1.3-/-/Cav3.1-/-
SCV
RA
LA
ICV
5 mm
Depolarization rate (bpm)
0
100
200
300
****
****
####
####
WT
Cav3.1-/-
Cav1.3-/-
Cav1.3-/-/Cav3.1-/-

Figure 7

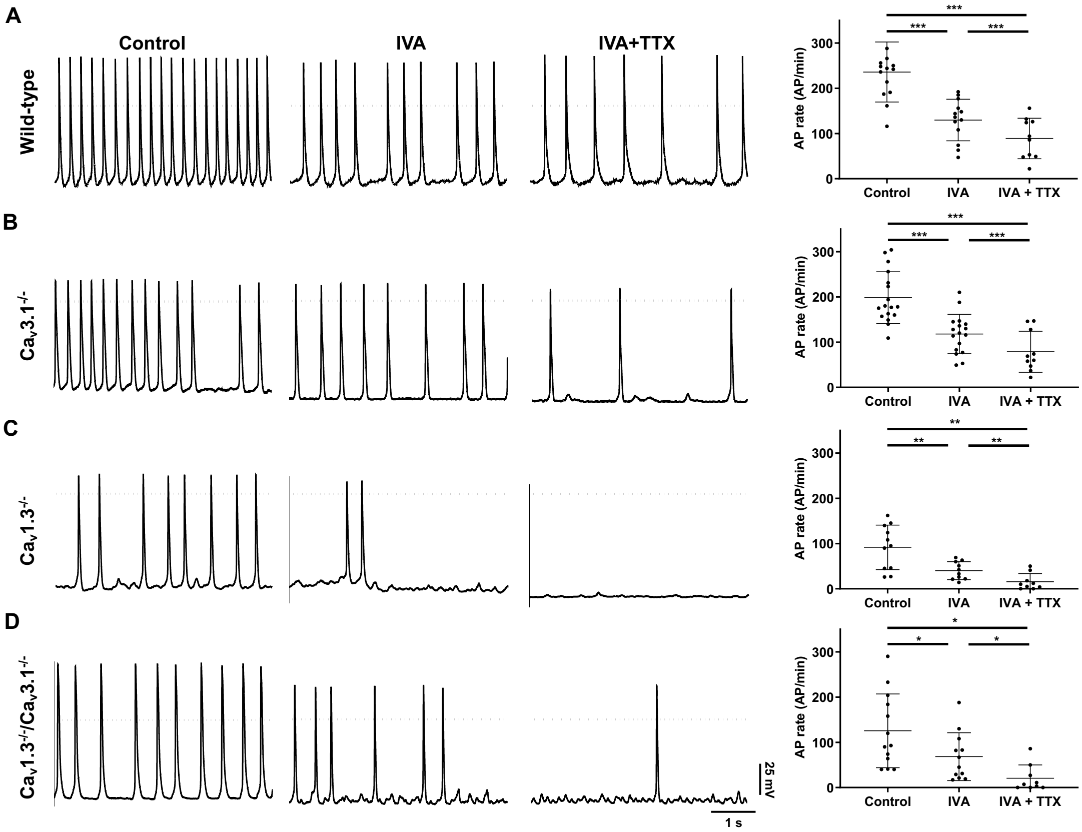
A
Control
IVA
IVA+TTX
Wild-type
***
***
***
AP rate (AP/min)
300
200
100
0
Control
IVA
IVA + TTX
B
Ca$_v$3.1$^{-/-}$
***
***
***
AP rate (AP/min)
300
200
100
0
Control
IVA
IVA + TTX
C
Ca$_v$1.3$^{-/-}$
**
**
**
AP rate (AP/min)
300
200
100
0
Control
IVA
IVA + TTX
D
Ca$_v$1.3$^{-/-}$/Ca$_v$3.1$^{-/-}$
*
*
*
AP rate (AP/min)
300
200
100
0
Control
IVA
IVA + TTX
25 mV
1 s

Figure 8

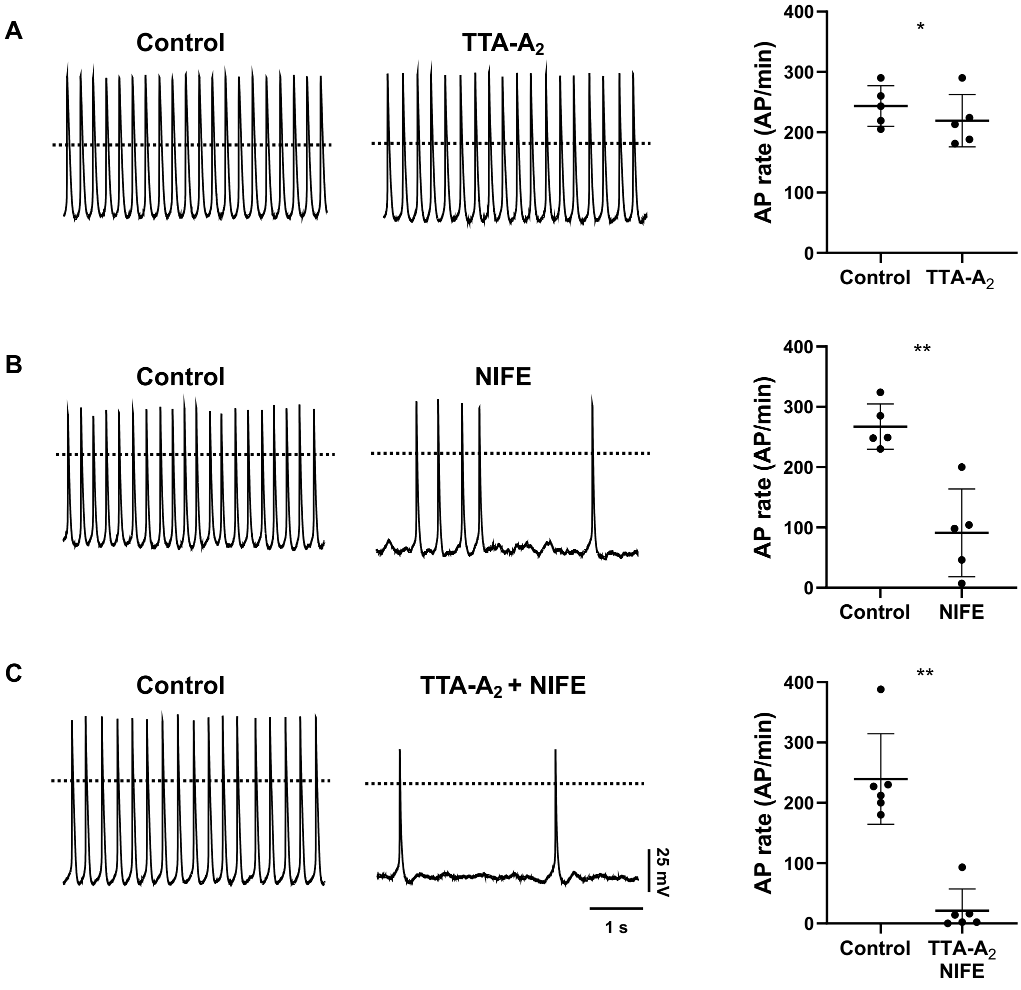
A
Control
TTA-A₂
AP rate (AP/min)
400
300
200
100
0
*
Control
TTA-A₂
B
Control
NIFE
AP rate (AP/min)
400
300
200
100
0
**
Control
NIFE
C
Control
TTA-A₂ + NIFE
25 mV
1 s
AP rate (AP/min)
400
300
200
100
0
**
Control
TTA-A₂
NIFE

Figure 9

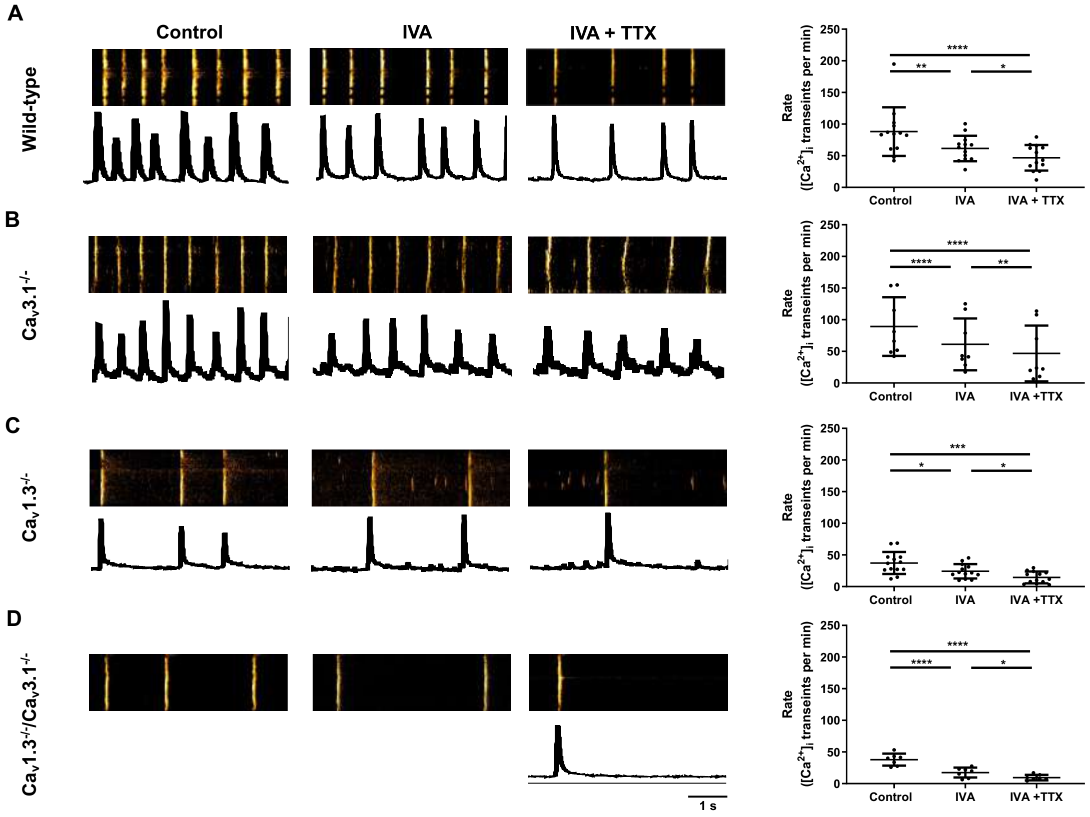
A
Control
IVA
IVA + TTX
Wild-type
B
Ca$_V$3.1$^{-/-}$
C
Ca$_V$1.3$^{-/-}$
D
Ca$_V$1.3$^{-/-}$/Ca$_V$3.1$^{-/-}$
1 s
Rate
([Ca^{2+}]$_i$ transeints per min)
0
50
100
150
200
250
Control
IVA
IVA + TTX
IVA +TTX
****
**
*
***

4.9. Supplementary figures legends

Figure S1. ECG in wild-type and mutant mice. (A) Standard deviation of the heart rate (top), averaged PR (center) and QT (bottom) intervals under basal conditions (ANS+) and after pharmacologic inhibition of the autonomic nervous system (ANS-). Wild-type (WT) n=11, $Ca_v3.1^{-/-}$ n=11, $Ca_v1.3^{-/-}$ n=8, $Ca_v1.3^{-/-}/Ca_v3.1^{-/-}$ n=10. Statistics: one-way ANOVA followed by Tukey's multiple comparisons test. (#) indicates comparison with WT.

Figure S2. Examples of ECGs from isolated heart. Sample ECGs recordings from Langendorff perfused WT hearts (A) and hearts from $Ca_v1.3^{-/-}/Ca_v3.1^{-/-}$ mice (B) showing atrial and ventricular arrhythmias, including premature ventricular contraction, atrioventricular blocks and ventricular tachycardia.

Figure S3. Parameters of pacemaker activity and conduction in SAN/atria preparations. (A) Coefficient of variability of SAN rate (top), conduction time between the leading site toward right (middle) and left (bottom) atria calculated in tissues from different mutants perfused with tyrode solution (control), with 10 µM ivabradine or with 10 µM ivabradine plus 100 nM TTX. WT n=8, $Ca_v3.1^{-/-}$ n=8, $Ca_v1.3^{-/-}$ n=7, $Ca_v1.3^{-/-}/Ca_v3.1^{-/-}$ n=7. Statistics: One-way ANOVA followed by Tukey's test. (B) Leading region position in SAN/atria preparations. SAN/atria tissue activation maps isolated from different mouse strains (color gradient, 4 msec/color). Multiple leading regions are recorded in $Ca_v1.3^{-/-}$ and $Ca_v1.3^{-/-}/Ca_v3.1^{-/-}$ SAN/atria preparations (bottom).

Figure S4. Frequency of local Ca^{2+} release (LCRs) in SAN cells. (A) LCRs recorded in pacemaker cells from WT (n=11), $Ca_v3.1^{-/-}$ (n=7), $Ca_v1.3^{-/-}$ (n=12) and $Ca_v1.3^{-/-}/Ca_v3.1^{-/-}$ (n=7) in control condition. (B) same as (A) but after perfusion of 3µM ivabradine or 3µM ivabradine plus 50 nM TTX. Statistics: One-way ANOVA followed by Holm-Sidak multicomparison test.

Table S1. Conduction alterations in SAN/atria preparations from different mouse strains. Pacemaker and conduction dysfunctions recorded in isolated SAN/atria preparations in control condition, after perfusion of 10 µM ivabradine or perfusion of 10 µM ivabradine + 100nM TTX.

Table S2. Action potential (AP) parameters recorded in isolated SAN cells from wild-type, $\mathrm{Ca_v3.1^{-/-}}$, $\mathrm{Ca_v1.3^{-/-}}$ and $\mathrm{Ca_v1.3^{-/-}/Ca_v3.1^{-/-}}$ mice. MDP: maximal diastolic potential (mV); Eth: AP threshold (mV); APA: AP amplitude (mV); APD: AP duration (ms); SLDD: slope of the linear part of the diastolic depolarization (mV/ms); EDD: slope of the exponential part of the diastolic depolarization (mV/ms); dV/dt: AP upstroke (mV/ms). Statistics: one-way ANOVA followed by Tukey's multiple comparisons test. Data are represented as mean±SEM.

Table S3. **Action potential (AP) parameters recorded in isolated SAN cells from $\mathrm{Cav1.2^{DHP-/-}}$ mice**. AP parameters calculated in pacemaker cells from Cav1.2DHP-/- mice in control condition, after perfusion of 1 µM TTA-A_2, 3µM nifedipine or both. Statistics: paired t-test. Data are represented as mean±SEM.

Figure S1

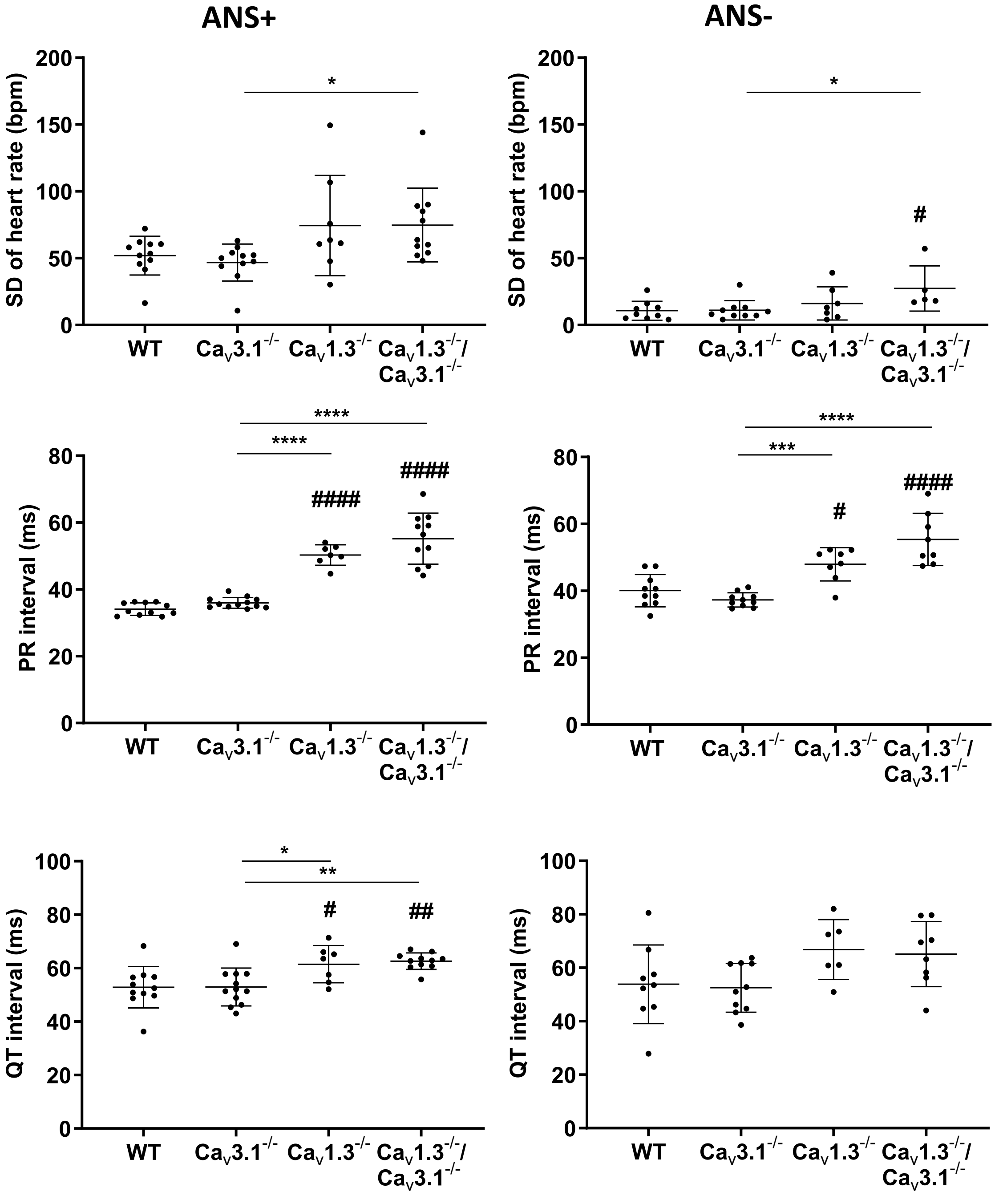
ANS+
ANS-
SD of heart rate (bpm)
0
50
100
150
200
*
#
PR interval (ms)
0
20
40
60
80
****
***
####
QT interval (ms)
0
20
40
60
80
100
**
##
WT
$Ca_V3.1^{-/-}$
$Ca_V1.3^{-/-}$
$Ca_V1.3^{-/-}$/ $Ca_V3.1^{-/-}$

Figure S2

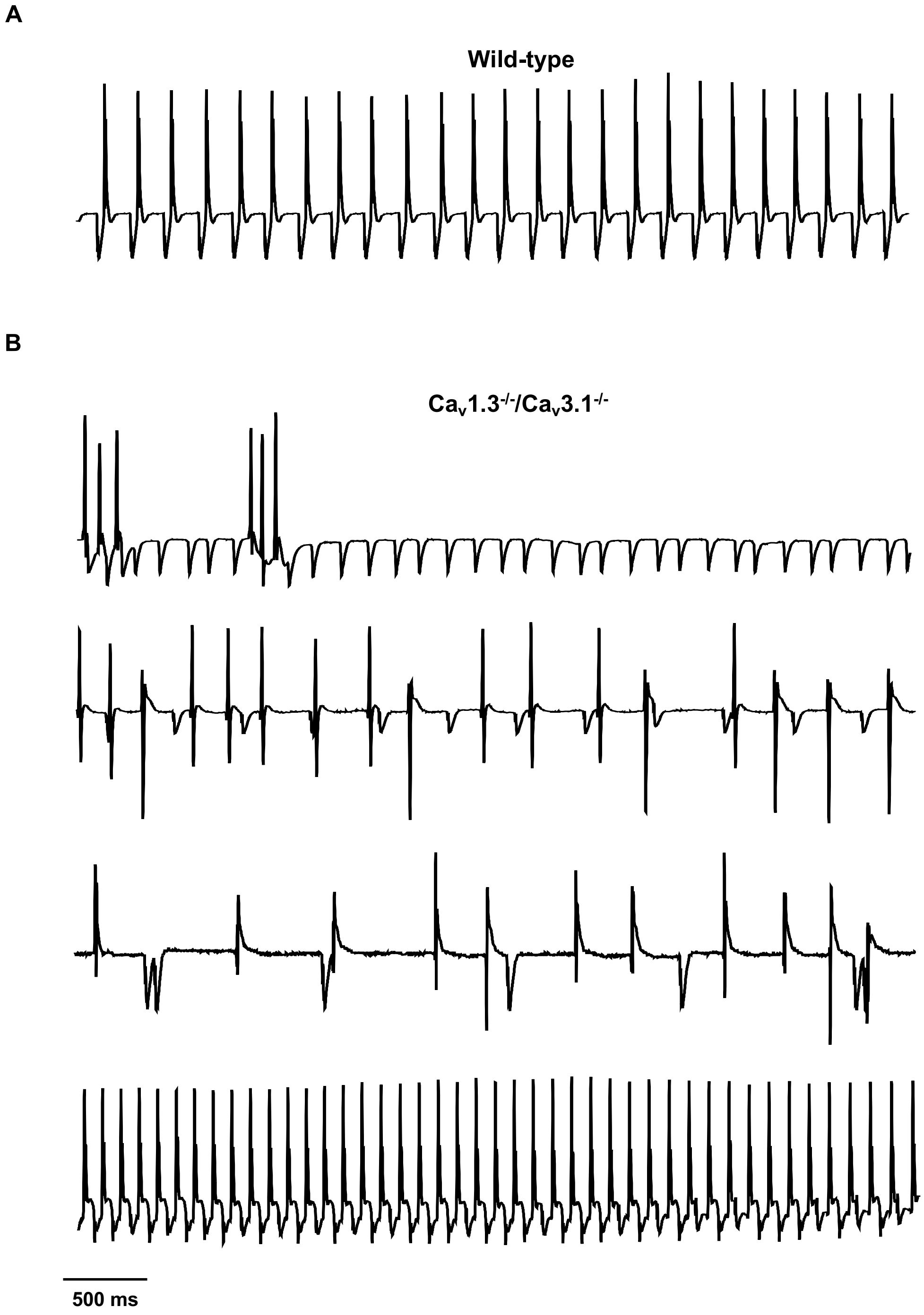

Figure S3

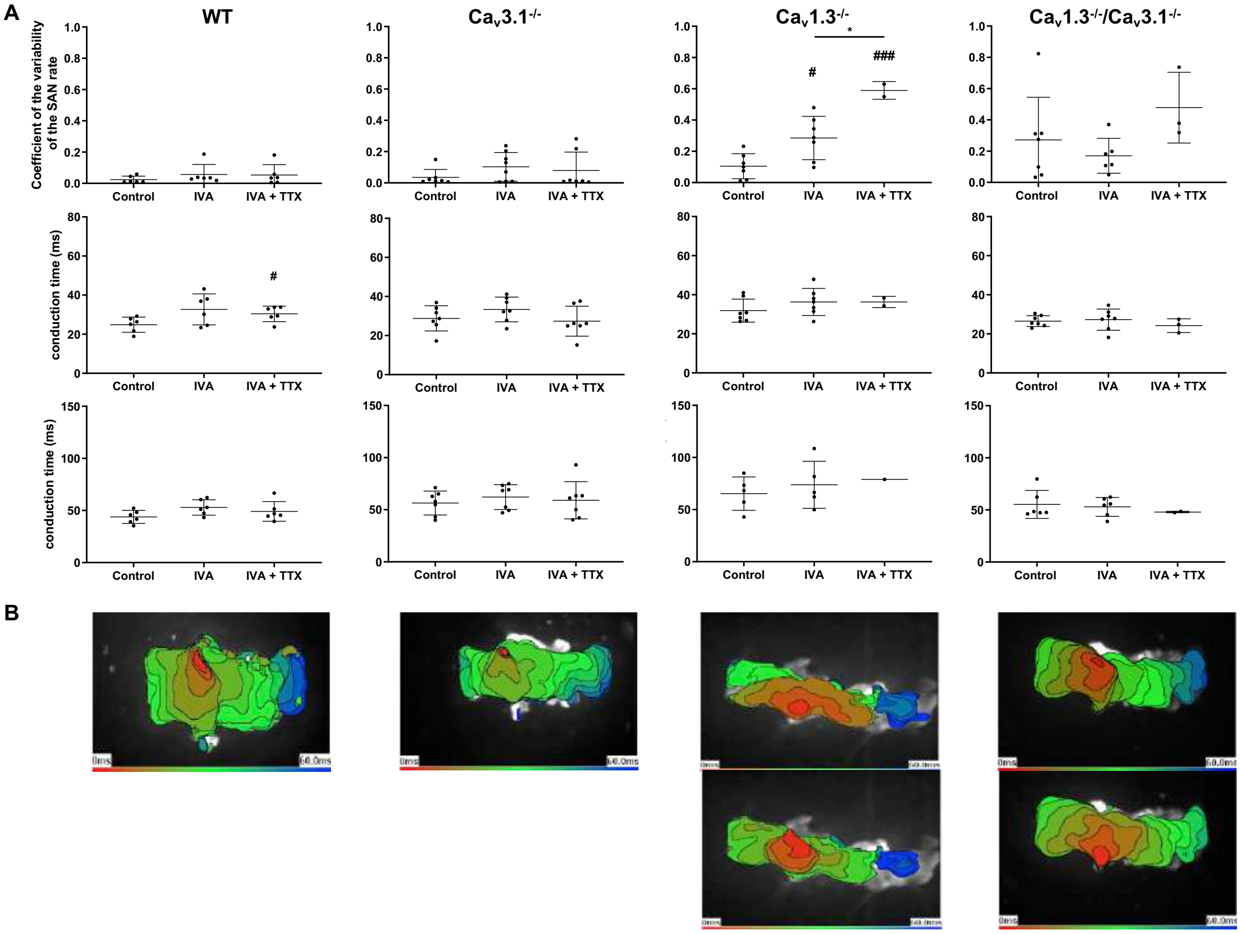

A
WT
$Ca_v3.1^{-/-}$
$Ca_v1.3^{-/-}$
$Ca_v1.3^{-/-}/Ca_v3.1^{-/-}$
Coefficient of the variability of the SAN rate
1.0
0.8
0.6
0.4
0.2
0.0
Control
IVA
IVA + TTX
*
#
###
conduction time (ms)
80
60
40
20
0
#
conduction time (ms)
150
100
50
0
B
0ms
60.0ms

Figure S4

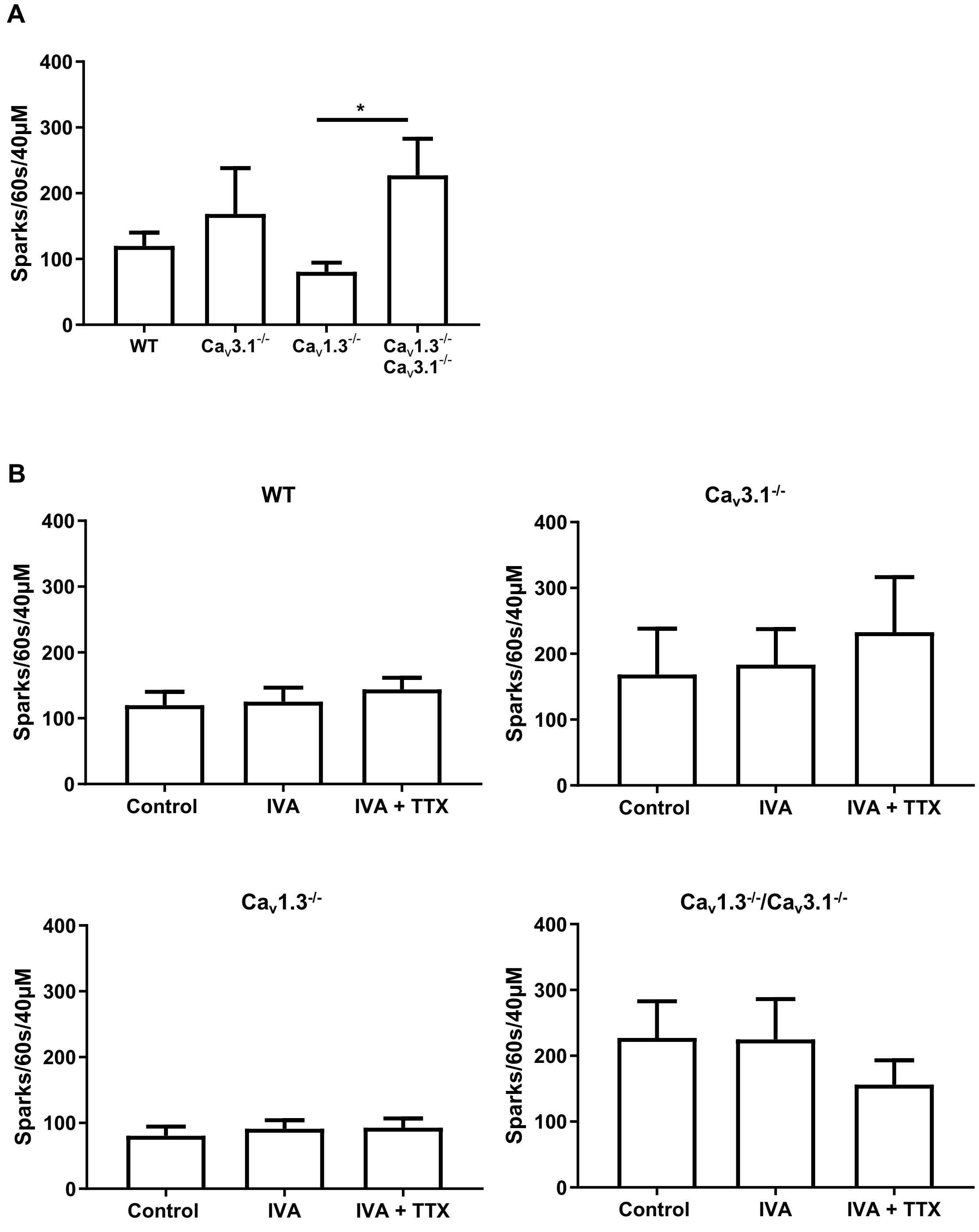
A
Sparks/60s/40µM
0
100
200
300
400
*
WT
Ca$_v$3.1$^{-/-}$
Ca$_v$1.3$^{-/-}$
Ca$_v$1.3$^{-/-}$ Ca$_v$3.1$^{-/-}$
B
WT
Ca$_v$3.1$^{-/-}$
Ca$_v$1.3$^{-/-}$
Ca$_v$1.3$^{-/-}$/Ca$_v$3.1$^{-/-}$
Sparks/60s/40µM
0
100
200
300
400
Control
IVA
IVA + TTX

Table S1

	Pacemaker activity	Multiple leading region	Ectopic leading reagion	No conduction towards left atrium
CONTROL				
Wild-type	8/8	0/8	0/8	0/8
$\mathrm{Ca_v3.1^{-/-}}$	7/7	3/7	0/7	0/7
$\mathrm{Ca_v1.3^{-/-}}$	7/7	4/7	1/7	3/7
$\mathrm{Ca_v1.3^{-/-}/Ca_v3.1^{-/-}}$	7/7	7/7	3/7	1/7
10 µM IVABRADINE				
Wild-type	8/8	0/8	0/8	0/8
$\mathrm{Ca_v3.1^{-/-}}$	7/7	2/7	1/7	0/7
$\mathrm{Ca_v1.3^{-/-}}$	7/7	1/7	0/7	3/7
$\mathrm{Ca_v1.3^{-/-}/Ca_v3.1^{-/-}}$	7/7	1/7	1/7	1/7
10 µM IVABRADINE + 100nM TTX				
Wild-type	8/8	1/8	1/8	0/8
$\mathrm{Ca_v3.1^{-/-}}$	7/7	1/7	1/7	1/7
$\mathrm{Ca_v1.3^{-/-}}$	2/7	0/2	1/2	0/2
$\mathrm{Ca_v1.3^{-/-}/Ca_v3.1^{-/-}}$	3/7	1/3	1/3	1/3

Table S2

	WT (A) n=22	$Ca_v3.1^{-/-}$ (B) n=17	$Ca_v1.3^{-/-}$ (C) n=16	$Ca_v1.3^{-/-}/Ca_v3.1^{-/-}$ (D) n=25	A vs B	A vs C	A vs D	B vs C	B vs D	C vs D
MDP (mV)	**-62±2**	**-61±2**	**-61±1**	**-63±1**	**ns**	**ns**	**ns**	**ns**	**ns**	**ns**
Eth (mV)	**-37±1**	**-37±1**	**-42±1**	**-45±1**	**ns**	*****	********	*****	********	**ns**
APA (mV)	**91±3**	**93±4**	**81±12**	**90±5**	**ns**	**ns**	**ns**	**ns**	**ns**	**ns**
APD (ms)	**150±16**	**156±9**	**199±24**	**194±13**	**ns**	**ns**	**ns**	**ns**	**ns**	**ns**
SLDD (mV/ms)	**0.11±0.02**	**0.08±0.02**	**0.02±0.01**	**0.02±0.01**	**ns**	********	********	*****	******	**ns**
EDD (mV/ms)	**1.0±0.2**	**0.8±0.1**	**0.3±0.1**	**0.2±0.1**	**ns**	*******	********	*****	******	**ns**
dV/dt (mV/ms)	**39±7**	**39±7**	**31±5**	**26±4**	**ns**	**ns**	**ns**	**ns**	**ns**	**ns**

Table S3

	Ctrl	TTA-A$_2$	Ctrl	NIFE	Ctrl	TTA-A$_2$+NIFE
	n=5	n=5	n=5	n=5	n=6	n=6
MDP (mV)	-44±2	-43±1	-50±2	-51±2	-52±2	-52±3
Eth (mV)	-25±2	-26±2	-31±2	-32±1	-31±3	-29±4
APA (mV)	81±5	86±7	77±5	76±7	82±5	74±7
APD (ms)	131±13	135±14	133±9	146±10*	130±10	161±21
SLDD (mV/ms)	0.06±0.01	0.05±0.01	0.07±0.01	0.04±0.01	0.06±0.01	0.06±0.01
EDD (mV/ms)	0.5±0.1	0.4±0.1	0.6±0.1	0.4±0.1*	0.5±0.1	0.3±0.1*
dV/dt (mV/ms)	22±6	35±12	22±8	22±10	35±9	24±9

Chapter 5

Published papers

1. Benzoni P, Campostrini G, Landi S, Bertini V, Marchina E, Iascone M, Ahlberg G, Olesen MS, Crescini E, Mora C, Bisleri G, Muneretto C, Ronca R, Presta M, Poliani PL, Piovani G, Verardi R, Pasquale E Di, Consiglio A, Raya A, **Torre E**, Lodrini AM, Milanesi R, Rocchetti M, Baruscotti M, DiFrancesco D, Memo M, Barbuti A, Dell'Era P. Human iPSC modeling of a familial form of atrial fibrillation reveals a gain of function of If and ICaL in patient-derived cardiomyocytes. *Cardiovasc Res* 2019;
2. Rocchetti M, Sala L, Dreizehnter L, Crotti L, Sinnecker D, Mura M, Pane LS, Altomare C, **Torre E**, Mostacciuolo G, Severi S, Porta A, Ferrari GM De, George AL, Schwartz PJ, Gnecchi M, Moretti A, Zaza A. Elucidating arrhythmogenic mechanisms of long-QT syndrome CALM1-F142L mutation in patient-specific induced pluripotent stem cell-derived cardiomyocytes. *Cardiovasc Res* 2017;**113**:531–541.
3. Ronchi C, **Torre E**, Rizzetto R, Bernardi J, Rocchetti M, Zaza A. Late sodium current and intracellular ionic homeostasis in acute ischemia. *Basic Res Cardiol* 2017;**112**:1-12 (12).

European Society of Cardiology

Cardiovascular Research
doi:10.1093/cvr/cvz217

Human iPSC modelling of a familial form of atrial fibrillation reveals a gain of function of I_f and I_{CaL} in patient-derived cardiomyocytes

Patrizia Benzoni[1‡], Giulia Campostrini[1†‡], Sara Landi[1], Valeria Bertini[2], Eleonora Marchina[2], Maria Iascone[3], Gustav Ahlberg[4], Morten Salling Olesen[4], Elisabetta Crescini[2], Cristina Mora[2], Gianluigi Bisleri[5], Claudio Muneretto[6], Roberto Ronca[2], Marco Presta[2], Pier Luigi Poliani[2], Giovanna Piovani[2], Rosanna Verardi[7], Elisa Di Pasquale[8], Antonella Consiglio[2,9,10], Angel Raya[11,12,13], Eleonora Torre[14], Alessandra Maria Lodrini[14], Raffaella Milanesi[1], Marcella Rocchetti[14], Mirko Baruscotti[1], Dario DiFrancesco[1], Maurizio Memo[2], Andrea Barbuti[1]*, and Patrizia Dell'Era[2]*

[1]Department of Biosciences, Università degli Studi di Milano, via Celoria 26, 20133 Milan, Italy; [2]Department of Molecular and Translational Medicine, cFRU lab, Università degli Studi di Brescia, viale Europa 11, 25123 Brescia, Italy; [3]USSD Laboratorio di Genetica Medica, Azienda Socio Sanitaria Territoriale Papa Giovanni XXIII, Piazza OMS, 1, 24127 Bergamo, Italy; [4]The Heart Centre, Rigshospitalet, Laboratory for Molecular Cardiology, Blegdamsvej 9, 2100 Copenhagen, Denmark; [5]Department of Surgery, Division of Cardiac Surgery, Queen's University, 99 University Avenue, Kingston, Ontario K7L 3N6, Canada; [6]Clinical Department of Cardiovascular Surgery, University of Brescia, viale Europa 11, 25123 Brescia, Italy; [7]Department of Trasfusion Medicine, Laboratory for Stem Cells Manipulation and Cryopreservation, ASST Spedali Civili, viale Europa 11, 25123 Brescia, Italy; [8]Department of Cardiovascular Medicine, Humanitas Clinical and Research Center, Via Rita Levi Montalcini, 4, 20090 Pieve Emanuele, Milan, Italy; [9]Department of Pathology and Experimental Therapeutics, Bellvitge University Hospital-IDIBELL, 08908 Hospitalet de Llobregat, C/Feixa Larga s/n, 08907 Barcelona, Spain; [10]Institute of Biomedicine of the University of Barcelona (IBUB), Carrer Baldiri Reixac 15-21, Barcelona 08028, Spain; [11]Center of Regenerative Medicine in Barcelona (CMRB), Hospital Duran i Reynals, Hospitalet de Llobregat, 08908 Barcelona, Spain; [12]Catalan Institution for Research and Advanced Studies (ICREA), Passeig Lluís Companys 23 08010 Barcelona, Spain; [13]Networking Center of Biomedical Research in Bioengineering, Biomaterials and Nanomedicine (CIBER-BBN), 28029 Madrid, Spain; and [14]Department of Biotechnology and Biosciences, Università degli Studi di Milano-Bicocca, iazza dell'Ateneo Nuovo 1, 20126 Milan, Italy

Received 15 November 2018; revised 19 July 2019; editorial decision 14 August 2019; accepted 26 August 2019

Time for primary review: 40 days

Aims Atrial fibrillation (AF) is the most common type of cardiac arrhythmias, whose incidence is likely to increase with the aging of the population. It is considered a progressive condition, frequently observed as a complication of other cardiovascular disorders. However, recent genetic studies revealed the presence of several mutations and variants linked to AF, findings that define AF as a multifactorial disease. Due to the complex genetics and paucity of models, molecular mechanisms underlying the initiation of AF are still poorly understood. Here we investigate the pathophysiological mechanisms of a familial form of AF, with particular attention to the identification of putative triggering cellular mechanisms, using patient's derived cardiomyocytes (CMs) differentiated from induced pluripotent stem cells (iPSCs).

Methods and results Here we report the clinical case of three siblings with untreatable persistent AF whose whole-exome sequence analysis revealed several mutated genes. To understand the pathophysiology of this multifactorial form of AF we generated three iPSC clones from two of these patients and differentiated these cells towards the cardiac lineage. Electrophysiological characterization of patient-derived CMs (AF-CMs) revealed that they have higher beating rates compared to control (CTRL)-CMs. The analysis showed an increased contribution of the I_f and I_{CaL} currents. No differences were observed in the repolarizing current I_{Kr} and in the sarcoplasmic reticulum calcium handling. Paced AF-CMs presented significantly prolonged action potentials and, under stressful conditions, generated both delayed after-depolarizations of bigger amplitude and more ectopic beats than CTRL cells.

---

* Corresponding authors. Tel: +39 02 50314941; fax: +39 02 50314932, E-mail: andrea.barbuti@unimi.it (A.B.); Tel: +39 030 3717539; fax: +39 030 3717 539, E-mail: patrizia.dellera@unibs.it (P.D.E.)

† Present address. Department of Anatomy and Embryology, Leiden University Medical Center, Einthovenweg 20, 2333ZC Leiden, The Netherlands.

‡ The first two authors contributed equally to the study.

Conclusions Our results demonstrate that the common genetic background of the patients induces functional alterations of I_f and I_{CaL} currents leading to a cardiac substrate more prone to develop arrhythmias under demanding conditions. To our knowledge this is the first report that, using patient-derived CMs differentiated from iPSC, suggests a plausible cellular mechanism underlying this complex familial form of AF.

Keywords Ion channels • Arrhythmias • Atrial fibrillation • iPSC-derived cardiomyocytes • Precision medicine

Graphical Abstract

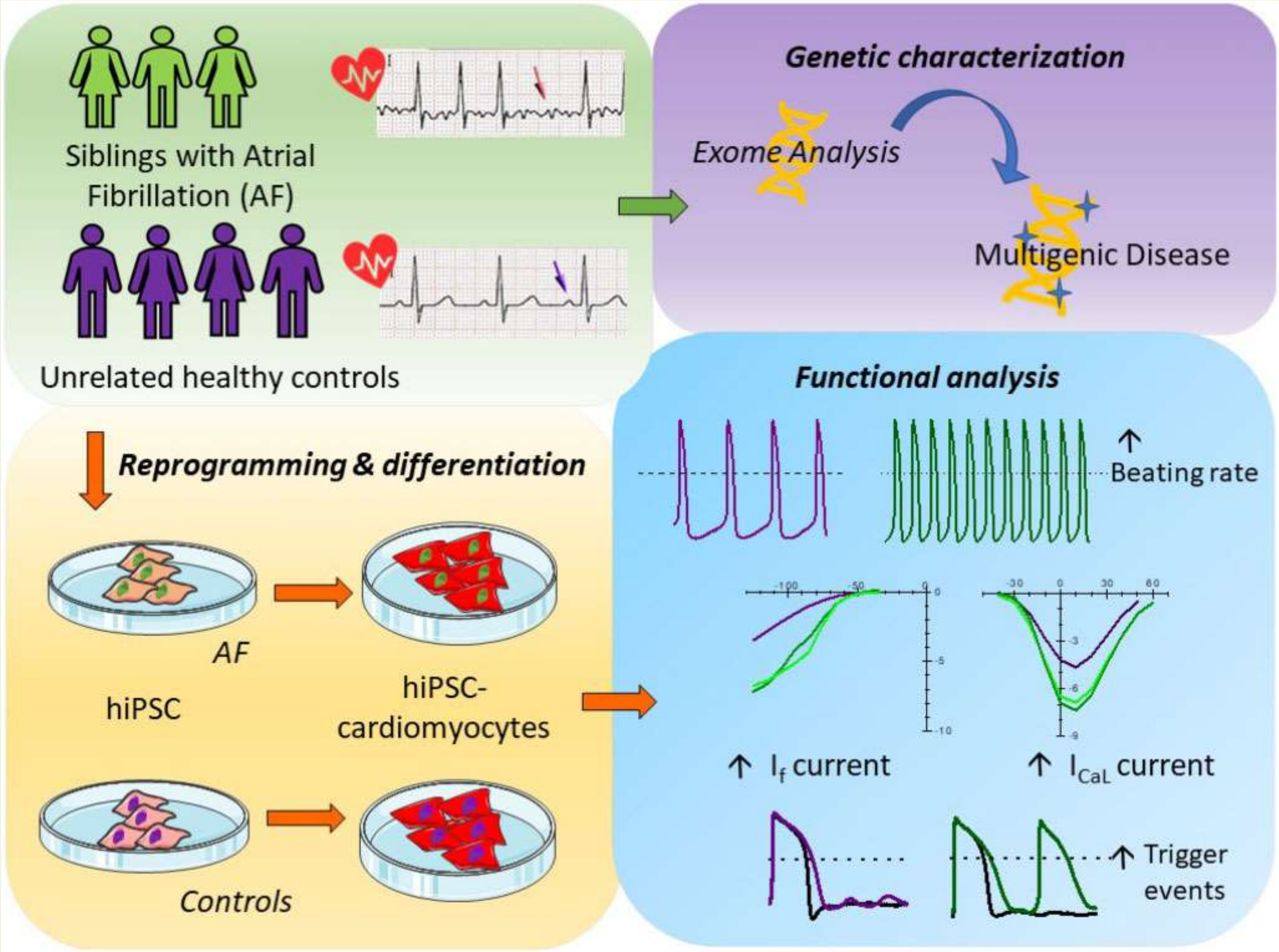

1. Introduction

Atrial fibrillation (AF) is the most common cardiac arrhythmia, occurring in 1–2% of the general population, but with a greater incidence in the elderly. In this type of arrhythmia, ectopic activity originating outside the sinoatrial node, gives rise to a disorganized electrical activation due to a cellular substrate susceptible to re-entrant circuits. While AF is commonly associated with structural heart diseases and is a major cause of cardiovascular morbidity and mortality in the elderly, it sometimes develops in a subset of patients younger than 60, with no evidence of associated cardiopulmonary or other diseases.

In recent years, evidence for inheritable forms of AF has grown. Beyond the rare cases of monogenic forms of AF and linkage analysis that revealed several genetic loci associated with AF,[1] population-based studies have shown that having first degree relatives with AF increases significantly the probability to develop AF.[2] Familial AF is likely associated with a complex genetic background that predisposes to this arrhythmia and that may or may not manifest itself depending on other non-genetic contributors.

Because of this genetic complexity, the molecular mechanisms underlying the initiation of AF are still poorly understood and possibly involve a complex interplay of various effectors.[3] In addition, electrical disturbances typical of AF cause the remodelling of the atria in a way that may sustain the arrhythmic phenotype.[4] This remodelling, in turn, makes it impossible to discriminate between causes and effects of AF when analysing cardiomyocytes (CMs) obtained from patient's biopsies. Human induced pluripotent stem cells-derived CMs (hiPSCs-CMs) may represent a valuable model to study AF, since they carry the exact genetic background of the patient but are free from the AF-dependent remodelling. hiPSC-CMs are now recognized as a useful human model that recapitulates the functional alterations underlying inherited arrhythmogenic diseases.[5]

In this work, we describe the first iPSC-derived model of human AF, generated from two out of three siblings that developed a drug-resistant form of AF at a relatively young age (<55 years). Using this model, we compared molecular and electrophysiological properties of hiPSC-CMs from AF patients (AF-CMs) and controls (CTRL-CMs), revealing alterations in ionic currents that may represent one of the cellular mechanisms that contribute to AF initiation.

2. Methods

2.1 AF patients

The three siblings were referred to Spedali Civili of Brescia (Italy), where they were diagnosed for AF (for details on method see Supplementary material online). Since all three patients were non-responsive to antiarrhythmic medication and failed previous transcatheter ablation, they underwent surgical ablation as described in Supplementary material online. A detailed clinical history of the patients is reported in the Supplementary material online, *Table S1*.

2.2 Generation of hiPSCs and cardiac differentiation

Blood and skin biopsies have been obtained from all three siblings following approved protocols by the Ethical Committee of Brescia (protocol number 1737) and a written consent obtained from the patients, in agreement with the declaration of Helsinki. hiPSC were generated as reported in Supplementary material online.

Cardiac differentiation of hiPSC was carried out either by embryoid bodies (EBs), as previously described[6] or by monolayer culture using the PSC Cardiomyocyte Differentiation Kit (Thermo Fisher Scientific). Differentiation in EBs was used for experiments on beating clusters to record the spontaneous rate. All the other experiments were carried out using the monolayer differentiation.

2.3 Electrophysiological and Ca^{2+} handling analysis

Electrophysiological and Ca^{2+} handling experiments were performed on dissociated hiPSC-CMs from at least three independent differentiation experiments, using the patch-clamp technique in whole-cell configuration. For protocols and solutions see Supplementary material online.

2.4 Statistics

Statistical analysis was carried out with Origin Pro 9, IBM SPSS Statistics and R software. Groups were compared with one-way ANOVA followed by pairwise comparison using Fisher's test or by nested one-way ANOVA with Holm *P*-value adjustment. Difference in events percentage among groups was assessed by Fisher's exact test, adjusting the *P*-value with Bonferroni correction. *P*-value <0.05 defines statistical significance. Data are presented as mean ± SEM.

3. Results

3.1 Characteristics of patients: genetic screening for mutations in AF-related genes

We identified three siblings with untreatable AF (see exemplified electrocardiogram in Supplementary material online, *Figure S1* and clinical characteristics in Supplementary material online, *Table S1*) who, due to failure of pharmacological treatment, underwent surgical ablation. Although they present other comorbidities (e.g. high body mass index and hypertension) that may importantly contribute to the poor control of the pathology, the familiarity, and their young age of onset of AF, strongly support a genetic basis for this form of arrhythmia.

In an attempt to identify potential AF-related mutations within the family we performed a whole exome sequencing in which data obtained from the three siblings (dubbed AF1, AF2, and AF3) were compared with 6000 human reference genomes (GRC37/hg19). We identified more than one hundred variants common only to the three siblings (see Supplementary material online, *Table S2*). Only few of these variants were in genes previously associated with AF (*ZFHX3*) and expressed also in the heart (*PDE4DIP*, *CNN2*, *RYR3*, *NEFM*, *FLNC*, and *MYLK*). Because of the complex genetic background of the family and the lack of unquestionably healthy relatives, we decided to address the molecular basis of this form of AF from a functional point of view.

3.2 Generation of hiPSC clones

To highlight possible common functional cardiac alterations in these patients, we generated patient-derived iPSCs and differentiated them into CMs. The reprogramming procedure was effective for fibroblasts obtained from AF1 and AF2, which allowed the generation of three hiPSC clones (AF1 $n = 2$; AF2 $n = 1$).

In the absence of unquestionably healthy parental or isogenic controls, AF clones were compared with at least three of four different unrelated control clones: one derived from dermal fibroblasts of an age-matched healthy woman[7] (CTRL1); one derived from epidermal keratinocytes[8] (CTRL2); one derived from dermal fibroblasts of a young male (CTRL3 shown in *Figure 1B* and *C*); and the last one from blood cells of a 62-year-old male not affected by AF or other cardiac pathologies (CTRL4).

The clones obtained from AF1 and AF2 were tested for the expression of both exogenous (t) and endogenous (e) pluripotency genes *OCT4*, *SOX2*, *NANOG*, and *REX1* by qPCR (*Figure 1A*) or by immunocytochemistry (*Figure 1B*). They were further screened for morphological properties typical of pluripotent colonies, such as sharp borders, the absence of a central dark area, and the expression of alkaline phosphatase (*Figure 1B*). The maintenance of a normal karyotype was also verified by quinacrine staining of metaphase plates (*Figure 1B*). Finally, the capacity to differentiate towards the three germ layers was confirmed by immunostaining with specific antibodies recognizing the ectodermal protein Nestin or Class III beta-Tubulin (TUJ1), the mesodermal protein smooth muscle actin, and the endodermal protein alpha fetoprotein (*Figure 1C*).

3.3 AF and CTRL hiPSCs differentiate into CMs with similar efficiency

For the experiments evaluating beating rate of clusters of hiPSC-CMs, clones were differentiated towards the cardiac lineage using a previously published procedure that involves spontaneous formation of EBs.[6] For all remaining experiments, we switched to a commercially available cardiac differentiation kit that ensured a higher yield of CMs.

Besides the appearance of beating areas, CMs in AF and CTRL groups were evaluated for the expression of the cardiac troponin gene (TNNT2) and the atrial gene sarcolipin (SLN) at day 30 of differentiation, by qPCR. The plots in *Figure 2A* (top panels) show that the levels of TNNT2 and SLN were similar in all groups.

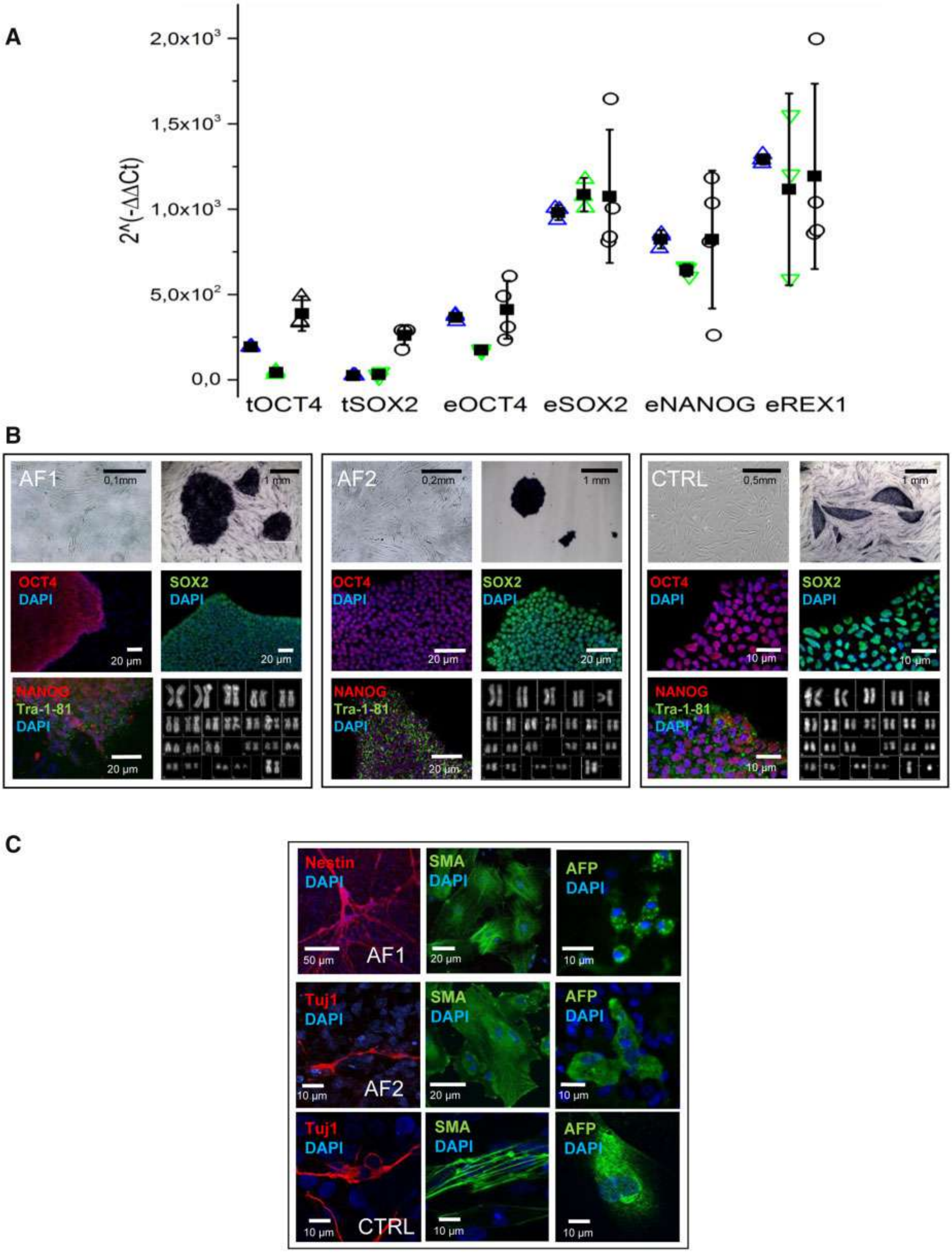

Figure 1 Pluripotency characterization. (*A*) qPCR analysis of pluripotency gene expression in hiPSC using dermal fibroblasts as reference control equal to 1. *tOCT4* and *tSOX2* indicate the specific expression of transgenes, while *eOCT4* and *eSOX2* refer to expression of endogenous genes. Differences in gene expression levels were compared using one-way ANOVA followed by Fisher's *T*-test. (*B*) Summary panels for AF1, AF2, and CTRL hiPSC lines, as indicated (from left to right): bright-field images of primary fibroblasts, alkaline phosphatase activity in hiPSC-colonies, immunostaining of hiPSC for pluripotency markers and karyotype. (*C*) Immunostaining of differentiated hiPSCs with antibodies recognizing ectodermal, mesodermal, and endodermal markers as indicated.

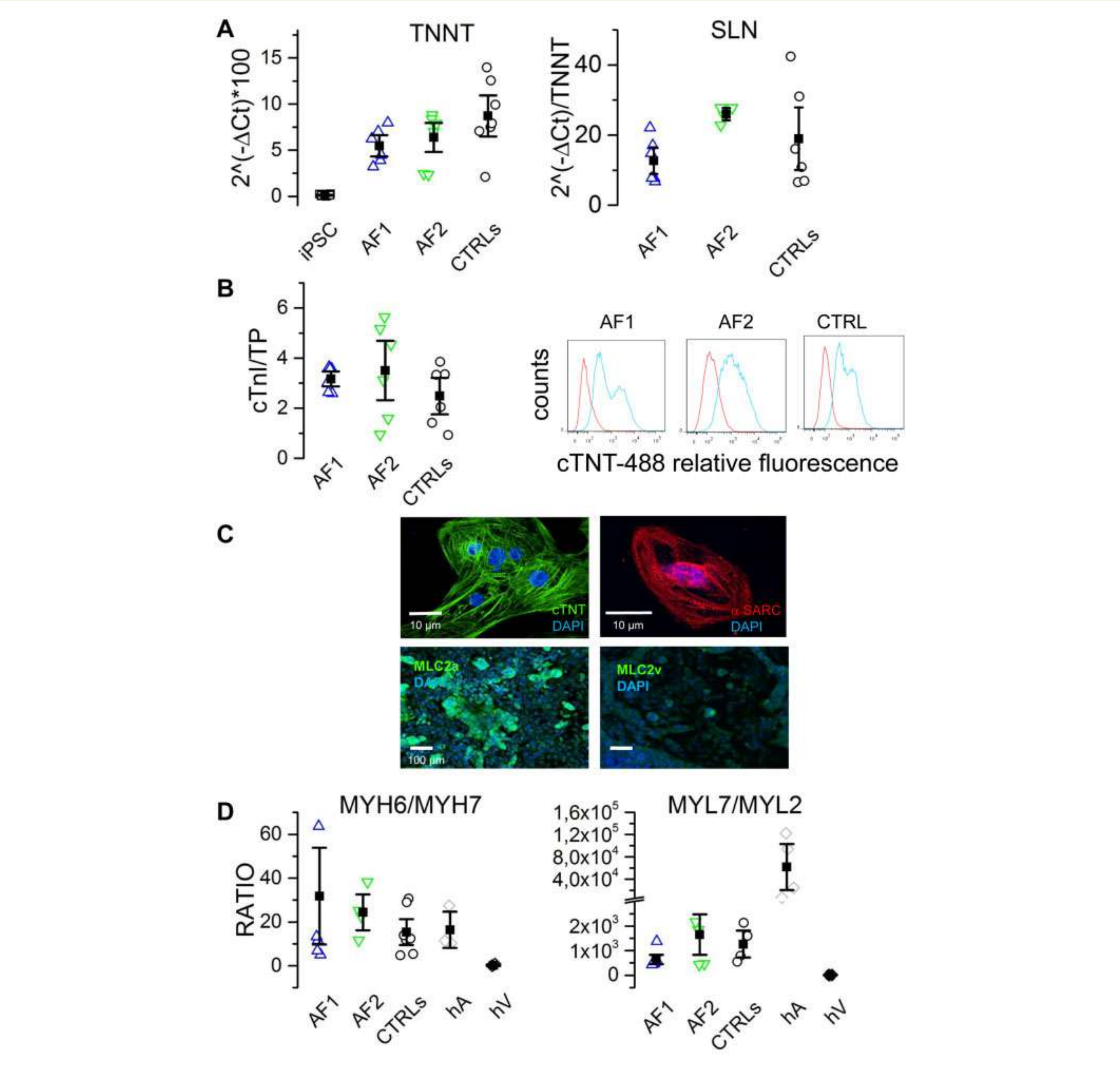

Figure 2 hiPSC-derived cardiomyocyte differentiation. (*A*) qPCR analysis of cardiac troponin T (TNNT2) and sarcolipin (SLN) expression at day 30 of differentiation for AF1-, AF2-, and CTRL-CMs, as indicated. Undifferentiated hiPSC were used as negative control. (*B*) Quantification of cardiac troponin I (µg) on total protein content (TP, mg) of AF1 (2.9 ± 0.46; *n* = 3), AF2 (2.4 ± 1.37; *n* = 3), CTRL (2.36 ± 1.08; *n* = 6), and hiPSCs (0.002 ± 0.01; *n* = 2) (left). Representative flow cytometry analysis on hiPSC-differentiated cells using an anti-cardiac troponin T antibody: AF1 (45.1 ± 11 *n* = 3), AF2 (55.2 ± 19 *n* = 3), CTRL (52 ± 12 *n* = 6) (right). (*C*) Representative images of isolated AF1-CM and AF1-differentiated monolayers stained for cardiac troponin T (cTNT), sarcomeric actin (α-SARC), atrial (MLC2a), and ventricular (MLC2v) myosin light chains; nuclei were counterstained with DAPI. (*D*) Ratios between the qPCR expression levels of heavy (left) and light (right) chain isoforms of myosin. Human atria (hA) and ventricles (hV) were used as positive and negative controls, respectively. Differences in gene expression and protein quantification were assessed by one-way ANOVA followed by Fisher's *T*-test.

We further investigated cardiac differentiation at the protein level by assessing the expression of cardiac troponin I in cellular lysates using a commercially available diagnostic kit (*Figure* 2*B*, left panel), finding no differences among clones. CMs yield was evaluated by flow cytometry using an anti-cardiac troponin T (cTNT) antibody. This analysis revealed that around half of the population was composed by CMs (*Figure* 2*B*, right panel). Again, no significant differences were found between AF and CTRL clones. Top panels of *Figure* 2*C* show representative images of isolated AF1-CMs, stained with cTNT and sarcomeric actin, displaying clear sarcomeric structures. In differentiating monolayers (*Figure* 2*C*, bottom panels), we evaluated the expression of the atrial myosin light chain (MLC2a) typical of immature/atrial CMs; conversely, very poor staining was obtained using anti-ventricular light chain (MLC2v) antibodies.

To better characterize the maturation stage reached at 30 days and the subtype of CM obtained, we measured the expression of the genes corresponding to the alfa (atrial) and beta (ventricular) myosin heavy chain (MYH6 and MYH7, respectively) and atrial and ventricular light chains (MYL7 and MYL2, respectively) by qPCR. *Figure 2D* shows that the mean MYH6/MYH7 ratio values were similar among hiPSC-CMs and comparable to values found in human adult atrium but not human ventricles. These data together with SLN expression, further suggest an immature/atrial rather than a ventricular phenotype for hiPSC-CMs.

Taken together these data confirm the reproducibility of the differentiating procedure among different groups and indicate that no significant differences in CM differentiation were found between AF and CTRL hiPSC lines.

3.4 hiPSC-CMs from AF patients display a higher beating rate than CTRL

In order to investigate the molecular mechanisms contributing to AF in our patients, we compared the electrophysiological properties of AF- and CTRL-CMs. Because data obtained from CMs of different CTRL clones were similar (Supplementary material online, *Figure S2* and *Tables S3–S5*), they were pooled together.

Representative action potential (AP) traces, recorded from spontaneously beating hiPSC-CM aggregates derived from AF1, AF2, and CTRL lines are shown in *Figure 3A*; even if the intra-clone variability was relatively large, on average aggregates derived from the two patients were beating at significantly higher rates than those derived from control lines (*Figure 3B*; see also Supplementary material online, *Movies S1 and S2*).

No significant differences in maximum diastolic potential, amplitude, and rate-corrected duration[9] were observed (Supplementary material online, *Table S3*). To test if the higher rate could result from elevated concentrations of intracellular cyclic AMP (cAMP), cells were challenged with a saturating concentration of the β-adrenergic agonist isoproterenol (Iso 1 μM). Panels of *Figure 3C* show representative time courses of spontaneous action potential rate in control, during superfusion of isoproterenol and after washout. The mean graph of *Figure 3D* shows that the fractional rate acceleration caused by isoproterenol was similar in all groups, suggesting that the higher basal beating rate does not depend on the modulatory pathway but likely derives from an intrinsic modification of the pacemaking mechanisms. On the other hand, we evaluated the effect of superfusion of the bradycardic agent ivabradine (3 μM). Panels in *Figure 3E* show representative time courses of spontaneous action potential rate in control, during ivabradine perfusion and after washout. The mean graph of *Figure 3F* shows that the fractional rate reduction caused by ivabradine was significantly higher in AF groups, abolishing the rate difference. These data suggest a higher than normal contribution of I_f to the pacemaker activity of beating AF-CMs.

3.5 hiPSC-CMs from AF patients show a gain of function of f-channels

Since the I_f current is a major contributor to control beating rate,[10,11] we measured the pacemaker I_f current in isolated AF-CMs at day 15 and day 30 of differentiation, while controlling at the same time the expression of the HCN genes responsible for this current (*Figure 4*). Expression analysis revealed that HCN1, HCN2, and HCN3 isoforms were expressed at comparable low levels in all groups while HCN4, the most abundant isoform, was significantly more expressed in CTRL than in AF1- and AF2-CMs (*Figure 4A*).

Such increase in HCN4 expression could not be confirmed by immunofluorescence analysis; representative confocal images shown in *Figure 4B* display similar HCN4 expression in CMs derived from the various hiPSC lines.

Functional data instead demonstrated a significant gain of function of f-channels in AF-CMs compared to CTRL cells, as shown by the representative families of I_f traces recorded from 30-day-old hiPSC-CMs (*Figure 4C*) and by the mean current density-voltage relations for AF1-, AF2-, and CTRL-CMs (*Figure 4D*, top). Interestingly, besides having higher density, f-channels of AF-CMs also activated at significantly more positive potentials than in CTRL-derived cells, as apparent from the mean activation curves shown in *Figure 4D* (bottom). It is noteworthy that at an earlier stage of differentiation (between day 15 and 20), while the current density does not differ among groups, f-channels activation is already shifted by 7 and 10 mV towards more positive potentials in AF1- and AF2-CMs, respectively, compared to CTRL (see Supplementary material online, *Figure S3*). Superfusion with isoproterenol (100 nM), which is known to cause a cAMP-dependent positive shift of I_f activation curve,[12] had similar effects in all groups (shift: AF1 = 4.0 ± 0.5 mV, *n* = 15; AF2 = 4.1 ± 0.5 mV, *n* = 21; CTRL = 5.0 ± 0.7 mV, *n* = 9), indicating that the more positive activation depends on changes in the intrinsic properties of the channel rather than a functional modulation due to alteration in cytosolic cAMP homeostasis. Since a mis-interaction of HCN channels with caveolin-3 (CAV3) may cause both a shift of their voltage dependence and decrease in membrane expression,[13,14] we evaluated if the more positive activation in AF-CMs could be due to either a decreased expression of CAV3 or a mis-localization of the channel and CAV3. We found that CAV3 was equally expressed in AF- and CTRL-CMs and HCN4 co-localized with CAV3 (Supplementary material online, *Figure S4*).

3.6 AF-CMs display an increase in the L-type calcium current with a preserved calcium handling

Antiarrhythmic drugs aimed at controlling heart rhythm often target calcium currents and in particular L-type calcium currents. We thus evaluated the expression levels and functional properties of calcium channels. qPCR analysis revealed that CACNA1C and CACNA1D genes, responsible for the I_{CaL} current, were similarly expressed in AF- and CTRL-CMs with CACNA1C as the prevalent isoform (*Figure 5A*). Electrophysiological analysis revealed instead that AF-derived cells show a significantly larger nifedipine-sensitive I_{CaL} current than CTRL-CMs as shown by representative traces in *Figure 5B* and by the mean current density-voltage relations plotted in *Figure 5C* (top). All samples had similar activation and inactivation curves (*Figure 5C*, bottom).

Notably, the difference in I_{CaL} density was already detectable at an early stage of differentiation (see Supplementary material online, *Figure S3*). We did not detect the expression of CACNA1G gene (*Figure 5A*) and indeed we could never record a T-type calcium current (data not shown).

To verify whether I_{CaL} enhancement in AF-CMs might alter the excitation-contraction coupling mechanism, intracellular Ca^{2+} handling was evaluated. In order to analyse only the primary effects on the intracellular Ca^{2+} handling, cells were voltage-clamped and stimulated at 1 Hz and diastolic calcium (Ca_{diast}), Ca^{2+} transient (CaT) amplitude, and sarcoplasmic reticulum (SR) Ca^{2+}content (CaSR) measured. In *Figure 5D* left, representative traces are shown together

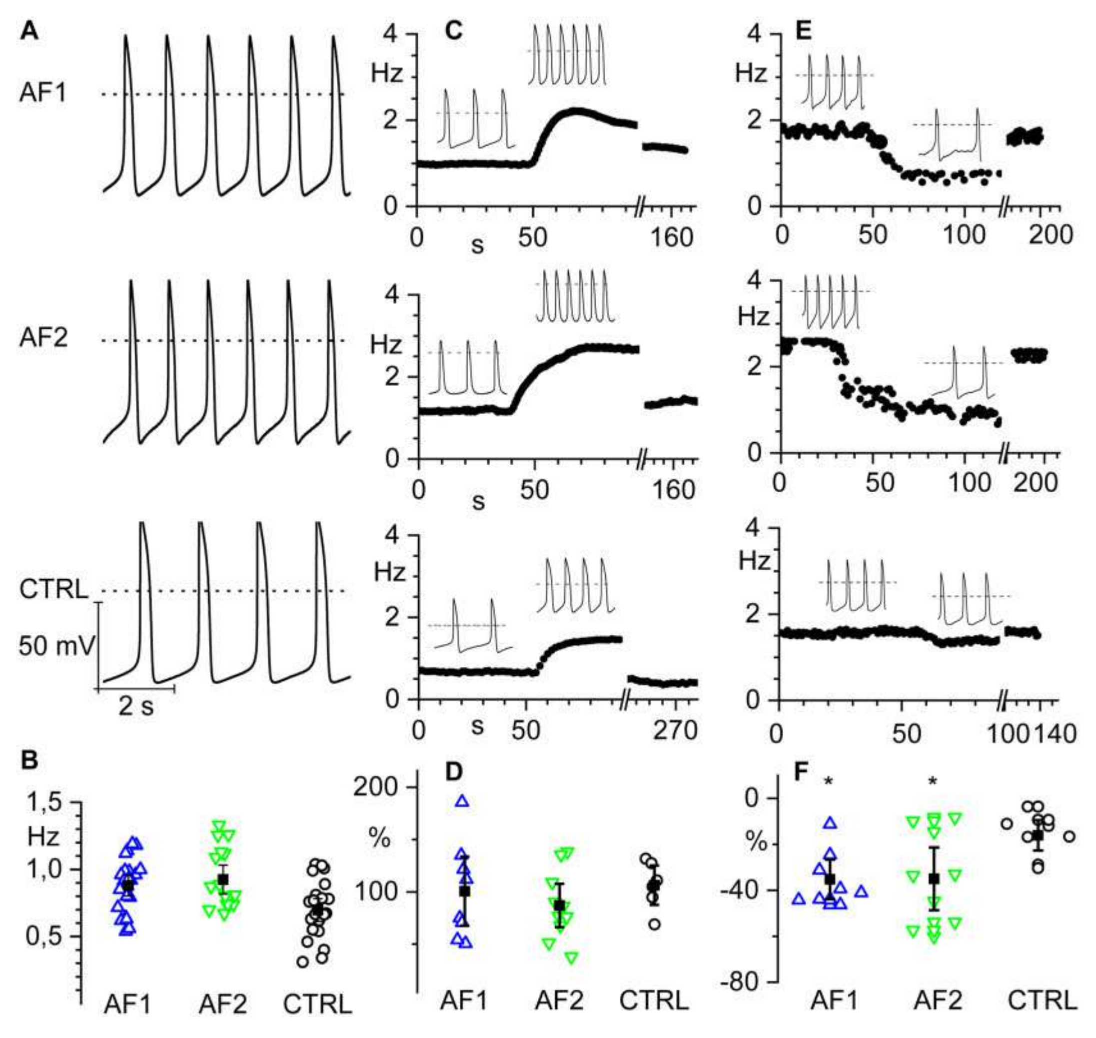

Figure 3 hiPSC-CMs from AF patients show increased spontaneous firing rate and similar response to β-adrenergic stimulation compared to controls. (*A*) Representative voltage traces of spontaneous firing recorded from hiPSC-CM clusters from AF1 and AF2 patients and CTRL as indicated. (*B*) Scatter plot of the firing rate (open circles) and mean values (filled squares) of AF1 (0.88 ± 0.04 Hz, *n*/exp = 24/6), AF2 (0.99 ± 0.07 Hz, *n*/exp = 19/8), and CTRL (0.72 ± 0.05 Hz, *n*/exp = 25/9) hiPSC-CMs. (*C*) Time course of the firing rate of representative hiPSC-CM clusters from AF1, AF2, and CTRL from top to bottom, respectively; the black line indicates the time of isoproterenol perfusion. Insets show representative voltage traces before and during isoproterenol stimulation. (*D*) Dot plot graph of the percentage increase in firing rate after isoproterenol stimulation. (AF1 100.6 ± 16.5%; *n*/exp = 8/3, AF2 87.0 ± 10.4%; *n*/exp = 10/6, and CTRL 106.4 ± 9.4%; *n*/exp = 6/5). (*E*) Time course of the firing rate of representative hiPSC-CM clusters from AF1, AF2, and CTRL before, during, and after ivabradine superfusion. Insets show representative voltage traces before and during ivabradine stimulation. (*F*) Dot plot of the percentage decrease in firing rate after ivabradine superfusion (AF1 -35.2 ± 4.3%; *n*/exp = 8/3; AF2 -34.9 ± 6.8%; *n*/exp = 9/3; CTRL -16 ± 3.3%; *n*/exp = 8/3). Data were compared using nested one-way ANOVA $^*P < 0.05$.

with the protocol. The analysis revealed that Ca_{diast} was similar in all groups, while AF1-CMs showed an increased CaT amplitude and an increase in CaSR, compared to CTRL-CMs and AF2-CMs. AF2-CMs values were similar to those of CTRL-CMs. However, fractional release (FR) did not change among groups, suggesting a preserved SR stability in AF as in CTRL cells under resting condition (*Figure 5D*, right). The Ca^{2+} parameters for the three separate CTRL lines can be found in Supplementary material online, *Table S5*. In agreement with these data, Western blot analyses on SERCA2 and phospholamban did not reveal any difference (Supplementary material online, *Figure S5*).

3.7 AF-CMs show longer action potential duration without changes in repolarizing currents

Once isolated, the great majority of hiPSC-CMs were quiescent but when stimulated (at 1 Hz) they fired action potentials. In *Figure 6*, the histograms of action potential duration (APD)90 obtained from AF1-, AF2-, and CTRL-CMs show that, despite the large variability of data, intrinsic to this cell model, AF-CMs have a wider distribution of APD (*Figure 6A*) with action potentials lasting as much as 300 ms, while none of the action potentials recorded from CTRL-CMs lasted more than 200 ms. In *Figure*

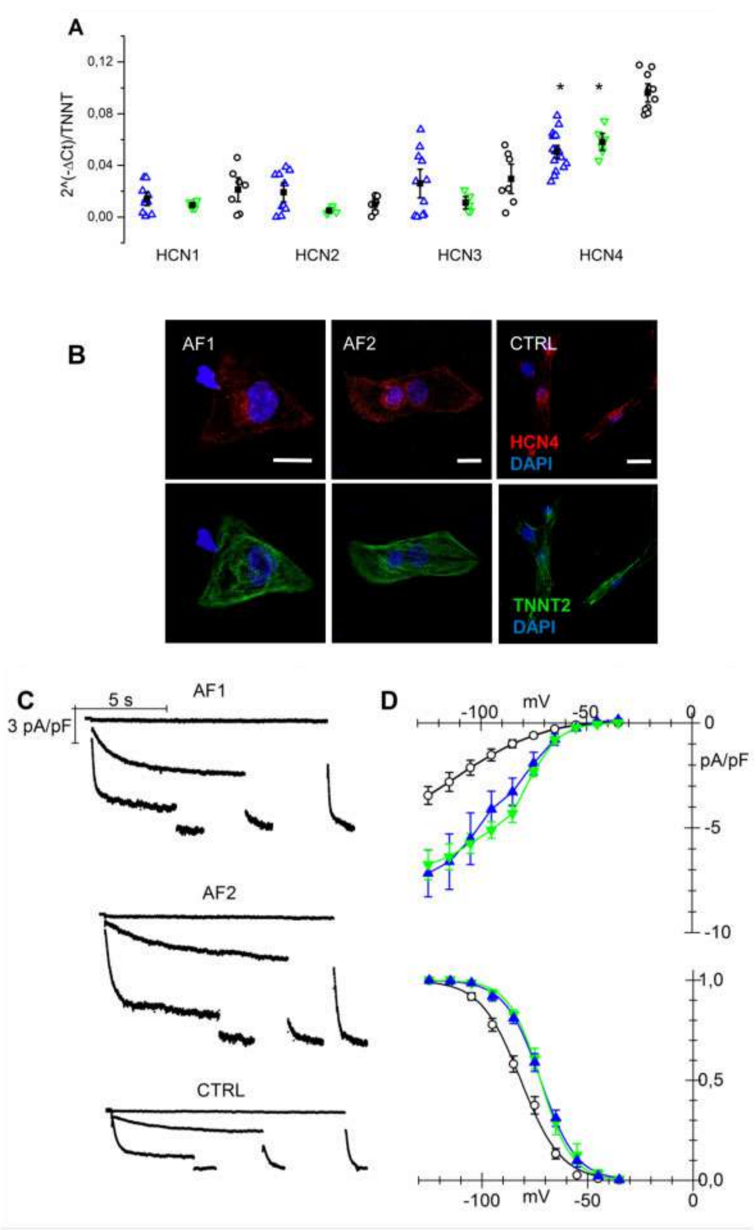

Figure 4 I_f current is increased in AF-CMs. (*A*) qPCR analysis of *HCN* isoforms normalized to troponin T expression at day 30 of differentiation. (*B*) Representative images of isolated AF1-, AF2-, and CTRL-CMs stained for HCN4 and cardiac troponin T (calibration bar = 10µm). (*C*) Representative traces of I_f current density recorded at -35, -75, and -105 mV followed by a step at -125 mV from AF1-, AF2-, and CTRL-CMs. (*D* Top) Plot of mean I_f current density voltage relation from AF1-CMs (blue triangles), AF2-CMs (green inverted triangles), and CTRL-CMs (white circles); Peak current density (at -125mV): AF1 = -7.17 ± 1.1*pA/pF, *n*/exp = 14/8; AF2 = -6.75 ± 0.72*pA/pF, *n*/exp = 13/3; CTRL = -3.45 ± 0.43 pA/pF, *n*/exp = 28/9. (Bottom) Mean activation curves of I_f current from AF1-CMs, AF2-CMs, and CTRL-CMs (symbols as in top panel). $V_{1/2}$ values: AF1 = -71.2 ± 1.6* mV, *n*/exp = 21/6; AF2 = -72.7 ± 1.3* mV, *n*/exp = 15/4; CTRL = -81.5 ± 1.4 mV, *n*/exp = 28/9. Inverse slope factor values: AF1 = 8.4 ± 0.25, *n* = 21; AF2 = 7.5 ± 0.5, *n* = 15; CTRL = 9.5 ± 0.5, *n* = 28. *P < 0.005. Data were compared using nested one-way ANOVA *P < 00.5.

6*B* representative traces recorded from the three groups highlight the prolongation of APD in AF-CMs.

On average patient-derived cells displayed significantly longer APD at 30, 50, and 90% of repolarization (see *Table 1*), in agreement with the presence of a larger I_{CaL}.

Because of this APD prolongation, we decided not to categorize the CM population in nodal-, atrial-, or ventricular-like cells based on the APD ratio. Indeed, the classifications based on either the APD90/APD50[15] or the APD30–40/APD70–80 ratios,[16] revealed that 66.5 or 68.5% of CTRL-CMs seems to be atrial-like, while these percentages were substantially lower for AF1-CMs (52.5–47.5%) and AF2-CMs (48.7–41.0%). However, as apparent in the Supplementary material online, *Figure S6*, most of the AF-derived CMs fall close to the cut-off values separating atrial from ventricular cells. Since AF-CMs

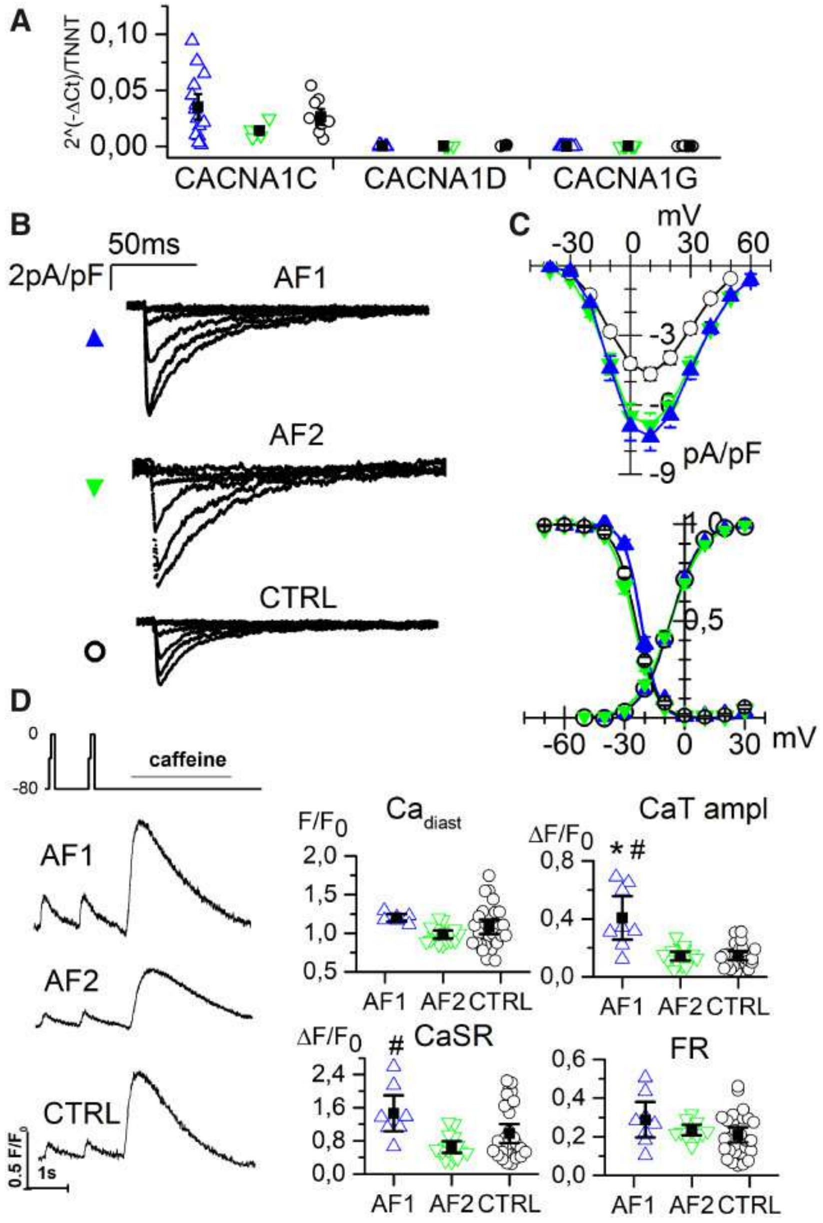

Figure 5 L-type calcium current is increased in AF-CMs. (*A*) qPCR analysis of L-type calcium channel isoforms (1C, 1D) and T-type isoform (1G) expression normalized to troponin level at day 30 of differentiation. (*B*) Representative traces of I_{CaL} current density recorded by 10 mV steps to the range of -40/ +10 mV from AF1-, AF2-, and CTRL-CMs. (*C* Top) Plot of mean I_{CaL} current density voltage relation from AF1-CMs (blue triangles), AF2-CMs (green inverted triangles), and CTRL-CMs (white circles). Peak current density (at 10 mV): AF1 = -7.4 ± 0.6*pA/pF, *n*/exp = 34/6; AF2 = -6.9 ± 0.5*pA/pF, *n*/exp = 30/8; CTRL = -4.7 ± 0.3 pA/pF, *n*/exp = 52/11. (Bottom) Mean activation and inactivation curves of I_{CaL} current from AF1-CMs, AF2-CMs, and CTRL-CMs (symbols as in top panel) $V_{1/2}$ values of activation: AF1 = -6.6 ± 1.2 mV, *n*/exp = 29/6; AF2 = -6.8 ± 1.0 mV, *n*/exp = 31/8; CTRL = -7.4 ± 0.5 mV, *n*/exp = 51/11. $V_{1/2}$ values of inactivation: AF1 = -21.8 ± 0.7 mV, *n*/exp = 16/6; AF2 = -25.4 ± 0.8 mV, *n*/exp = 25/8; CTRL = -24.5 ± 0.5 mV, *n*/exp = 36/11. (*D*) Left, examples of calcium transients recorded from AF1-, AF2-, and CTRL-CMs applying the protocol shown. Right, dot blot graphs of the Ca diast, CaT amplitude, CaSR, and FR data in the three groups, as indicated. For values see Supplementary material online, *Table S5*. Data were compared using nested one-way ANOVA $^*P < 0.05$ vs. CTRL; $^{\#}P < 0.05$ vs. AF2.

show a larger ICaL and, as a consequence, a APD prolongation, a certain number of atrial-like cells would indeed pass the threshold and enter the 'ventricular-like' category even if they are not actually ventricular cells. Therefore, in this specific case, a selection of cells based on these criteria would obviously introduce a bias in the results.

Of the main repolarizing currents, we were able to analyse the delayed rectifier current I_{Kr}, whose density and kinetics did not differ between AF- and control-CMs (Supplementary material online, *Figure S7*). Under our differentiation conditions I_{Ks} was absent while, in agreement with the depolarized resting potential, I_{K1} was expressed at very low levels (data not shown), as previously reported.[17]

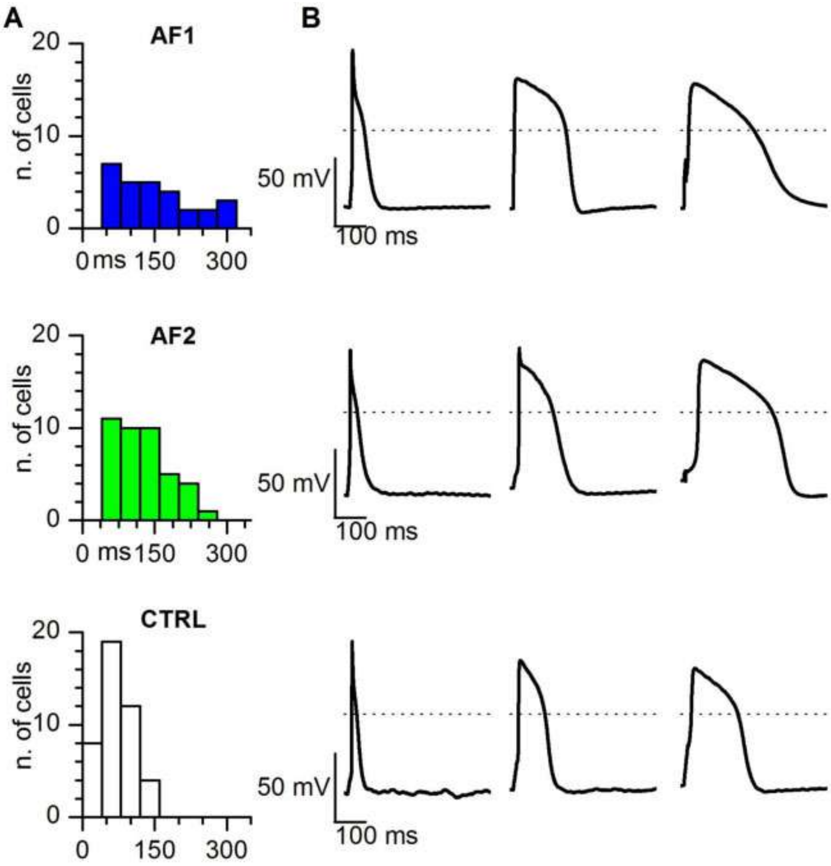

Figure 6 Action potential duration is longer in AF-CMs compared to CTRL-CMs. (*A*) Histograms of the distribution of the APD90 in AF1, AF2, and CTRL cells, as indicated. Bin size = 40 ms. (*B*) Representative action potentials with the shortest (left), average (centre), and longest (right) APD90 recorded at 1 Hz stimulation in AF1 (top), AF2 (middle), and CTRL (bottom) CMs. Dashed lines indicate the 0 mV level.

Table 1 Stimulated action potential analysis

	APD30 (ms)	APD50 (ms)	APD90 (ms)	MDP (mV)	dV/dT	APA (mV)
AF1 (*n*/exp = 40/11)	80.2 ± 9.4*	105.1 ± 11.2*	137.3 ± 12.7*	-55.7 ± 1.4	57.6 ± 11.9	92.78 ± 3.9
AF2 (*n*/exp = 39/12)	71.2 ± 6.7*	92.6 ± 8.2 *	120.6 ± 8.8*	-58.8 ± 0.9	46.6 ± 6.6	93.9 ± 3.4
CTRLs (*n*/exp = 61/13)	39.9 ± 3.2	52.4 ± 3.7	74.1 ± 4.1	-56.9 ± 0.9	41.3 ± 8.4	86.7 ± 2.4

Stimulated action potential properties of hiPSC-CMs paced at 1 Hz: action potential duration (APD30, 50, and 90), maximum diastolic potential (MDP), slope (dV /dT), and action potential amplitude (APA) *$P< 0.05$ by one-way ANOVA.

Because of the difference in the L-type calcium current, we evaluated the presence of calcium-dependent K^+ currents. Application of both apamin (100 nM), a specific blocker of the SK3 channel and charybdotoxin (100 nM), a blocker of the BK channel, did not have any effect on stimulated action potentials, thus suggesting a negligible expression of these channels (data not shown).

3.8 AF-CMs display larger delayed-after-depolarizations and an increased number of ectopic beats under stressful conditions

Finally, we evaluated if the electrophysiological alterations found in AF-CMs may be pro-arrhythmic by pacing both CTRL- and AF-CMs at 0.5 Hz and superfusing them with isoproterenol (100 nM) and E4031 (300 nM). This treatment, as expected, caused a significant prolongation of the APD and eventually the development of delayed-after-depolarizations (DADs) and/or triggered AP (*Figure 7A*). In *Figure 7B*, the proportion of CMs showing DADs, triggered AP, or the APD prolongation only (no events) for AF1, AF2, and CTRL-CMs is plotted. A significantly higher percentage of AF cells displayed triggered AP than CTRL cells, under this stressful condition (*Figure 7B*).

Furthermore, even if the proportion of cells with DADs was not different among the three cell populations, on average, DADs from AF1 and AF2 cells had a higher amplitude than those from CTRL cells (*Figure 7C*).

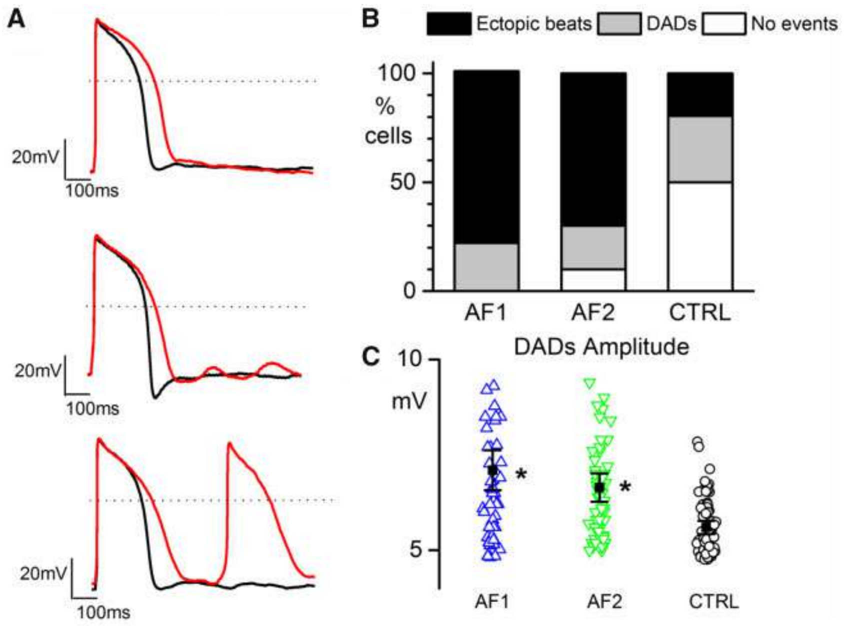

Figure 7 AF-CMs are more arrhythmogenic. (*A*) Representative action potentials in Tyrode (black line) and during perfusion of 100 nM isoproterenol + 300 nM E4031 (red line) showing no events (top), DADs (middle), and ectopic beats (bottom) recorded from AF2-CMs paced at 0.5 Hz; dashed lines indicate the 0 mV level. (*B*) Plot of the percentage of cells showing ectopic beats (AF1 7 out of 9/3 cells/exp, 78.8%*; AF2 7 out of 10/3 cells/exp, 70.0%*; CTRL 7 out of 36/6 cell/exp, 19.5%), DADs (AF1 2 out of 9, 22.2%; AF2 2 out of 10, 20.0%; CTRL 11 out of 36, 30.5%), and no events (AF1 0 out of 9, 0%; AF2 1 out of 10, 10.0%; CTRL 18 out of 36, 50%). (*C*) Plot of DADs amplitude in AF1-CMs (blue triangles), AF2-CMs (green inverted triangles), and CTRL-CMs (white circles). Values are AF1 = 6.95 ± 0.62* mV, *n*/exp = 60/3; AF2 = 6.73 ± 0.26* mV, *n*/exp = 66/3; CTRL = 5.66 ± 0.16 mV, *n*/exp = 70/6. Percentage data were compared using Fisher's exact test, adjusting the *P*-value with Bonferroni correction. Amplitude data were compared using nested one-way ANOVA $^*P < 0.05$.

4. Discussion

4.1 Whole exome screening reveals a complex genetic background in the siblings affected by AF

Although AF is the most prevalent cardiac arrhythmia in the developed world,[18] the pathophysiology of this complex heart rhythm disorder is still incomplete. The changes leading to the initial occurrence of AF are still elusive because (i) it is a progressive disease, (ii) human cardiac diseased tissues have undergone extensive remodelling, and (iii) no animal models fully recapitulate the disease.

The discovery of genetic forms of AF, linked to single gene mutations, and genome-wide association studies have improved our knowledge of causative mechanisms underlying AF.[1] Monogenic forms of AF are rare but, since the probability to develop AF increases in the presence of affected relatives,[2] a complex genetic background can be hypothesized. Indeed, we described a family in which three siblings, diagnosed with AF, share several mutations that can contribute to determine this arrhythmia.

Among these genes, only *ZFHX3* has been previously associated with AF in GWAS studies.[1] Nevertheless, the contribution of the other cardiac and non-cardiac mutated genes to AF onset is hard to dissect.

4.2 Generation of functional hiPSC-CMs overcomes the problems linked to genetic complexity of the disease

Because of this genetic complexity, an approach based on the evaluation of the contribution of each single mutation is clearly unfeasible and unlikely to provide a comprehensive description of the pathology. In order to estimate the full range of the effects of genetic alterations, we thus approached the problem from a functional point of view. We decided to use patient-derived hiPSCs to obtain a human cardiac cell model that possesses the entire patient's genetic background. Although the limitation linked to the well-known phenotypic immaturity of hiPSC-CMs,[19] these cells have already been widely used to study monogenic forms of cardiomyopathies and arrhythmias.[5] On the contrary, their use for modelling complex genetic pathologies is a rarely adopted approach.[20,21]

Here, we analysed for the first-time hiPSC-CMs from patients with a complex genetic form of AF. It must be emphasized that this model does not intend to recapitulate either the complexity of the atria or the entire clinical aspects of the disease but represents a novel tool to understand the molecular mechanisms underlying excitability alterations in diseased human CMs.

Because of the lack of healthy controls within the family and the unfeasibility to generate isogenic hiPSCs, due to the complex genetic alterations, AF clones were compared with four different lines generated from unrelated healthy controls. These controls were chosen based on different variables that could potentially affect the comparison with CMs derived from our patients: sex (female and male), age (middle aged), and reprogramming procedure (retroviral infection from skin fibroblast and keratinocyte).

Once established the pluripotency of the clones, we choose those clones displaying a good cardiac differentiation capacity for further characterization. Our molecular data on the expression of the myosin heavy and light chain isoforms indicate that hiPSC-CMs are mainly immature/atrial rather than ventricular cells, independently of the cell line. Because a certain degree of maturation can be achieved in culture, especially in the electrical properties,[19] we decided to compare the AF and control lines at an early (15–20 days) and at a late stage of differentiation (30–35 days).

4.3 AF-CMs show a high beating rate due to increased I_f and I_{CaL} currents

We started to analyse the spontaneous beating rate of small aggregates and found that AF-CMs beat at a significantly higher rate than those from the controls, while no differences were found in the other parameters. Since the beating rate is physiologically modulated by the β-adrenergic/adenylate cyclase/cAMP pathway and an increase in rate may derive from an imbalance of this system, we tested the ability of the cells to respond to the β-adrenergic agonist isoproterenol. A saturating concentration of isoproterenol caused similar increases in rate in all the lines thus excluding differences in intracellular cAMP concentration as a cause of the higher rate in AF-CMs. AF onset is often associated with elevated heart rates. A few studies have indeed shown that initiation of post-operative AF, in patients undergoing coronary artery bypass surgery, was preceded by a significant increase in sinus rate mediated by either high levels of circulating norepinephrine[22] or by an unbalance of the autonomic tone towards the sympathetic input.[23]

The funny current is the pacemaker current critical to the initiation and regulation of cardiac pacemaker activity[10] and an increase in its contribution can indeed be arrhythmogenic.[24] The expression of f-channels (HCN1–HCN4) has been demonstrated also in non-pacemaker cardiac cells and in the working myocardium where it is abundant during fetal and neonatal life or under pathological conditions.[25] We found that the *HCN4* gene is the most expressed isoform in hiPSC-CMs and is less expressed in AF-CMs than in control-CMs. Direct recording of the I_f current from isolated hiPSC-CMs, however, demonstrated a significant gain of function of f-channels due to both a rightward shift of the activation curve (both at early and late differentiation time-points) and an increase in current density (at later stages of differentiation) in AF compared to controls. Although molecular and functional data are discordant, they are in agreement with previous data from Stillitano *et al.*[26] These authors found that mRNA of HCN4 was down-regulated in chronic atrial fibrillation (cAF) CMs while the protein level tended to be higher. Although they have found similar current densities, the cAF cells displayed f-channels with activation curve shifted to more positive potentials than control cells by about 10 mV,[26] similar to our results.

Since CAV3 is known to interact with HCN4[13] and it has been already reported in pluripotent-derived CMs that different expression of CAV3 can shift I_f activation curve,[14] we analysed the CAV3 expression both at mRNA and protein levels without detecting any difference between AF and CTRL groups (Supplementary material online, *Figure S4*).

A possible contribution of an increased I_f current to abnormal automaticity in the atrium in paroxysmal AF has been described by Nattel and Dobrev[4] in a recent review.

Our results on L-type calcium current seem to be less in accordance with the evidence that AF induces a reduction of calcium currents. Indeed, atrial CMs derived either from patients with AF or from animal models of fast atrial pacing show a significant reduction of the effective refractory period (ERP) and of the I_{CaL} current, compared to controls.[4,27] The reduction of calcium current and ERP seems, however, the consequence rather than the cause of AF and is attributable to the maladaptive remodelling of atrial tissue. In support of a role of an increased I_{CaL} to AF, a few studies have shown that an initial calcium overload can be the stimulus that triggers maladaptive changes in atrial protein expression, based on the evidence that the calcium blocker verapamil prevents such remodelling.[28,29]

Albeit the magnitude of I_{CaL} density has not been regularly associated with a higher probability to develop post-cardiac surgery AF,[30] it is interesting to note that Van Wagoner *et al.*[27] have shown that patients in sinus rhythm who developed AF following cardiac surgery had a significantly higher pre-operative I_{CaL} density than those that did not experience post-operative AF. This observation, together with our data showing that CMs from AF patients display an I_{CaL} twice as big as that of controls, is consistent with the concept that calcium overload may be an important factor in the initiation of AF, while I_{CaL} depression is a consequence of AF.

4.4 AF-CMs display a prolonged APD and an increased susceptibility to arrhythmic activity

Despite the lack of any evident modulation of specific calcium channel isoforms, many mechanisms may contribute to an increased I_{CaL} current such as, for example: miRNA-mediated modulation of expression,[31] altered channel trafficking/recycling,[32] channel oligomerization,[33] and modulation by accessory subunits.[34] The observed increase of the inward calcium current not accompanied by a counterbalancing increase in outward currents is expected to prolong the APD. Indeed, Sato *et al.*[35] has shown that an increased cooperative gating of L-type calcium channels increases current density and causes APD prolongation, in *in silico* experiments. Despite the large variability in APD duration typical of the CMs derived from hiPSCs (*Figure 6*),[17] we observed a significant prolongation of the APD in paced AF-CMs compared to controls. Usually, variability in APD is decreased by dividing CMs in nodal-, atrial-, and ventricular-like cell based on the slope of fast depolarization and APD ratio.[15,16] In our specific case, the selection of the cardiac cell type using the criteria based on the APD ratio is not applicable since APD is in fact exactly the parameter which is altered in AF-CMs, according to our results.

Although data on calcium handling do not indicate a significant instability of the SR, at least under 'basal' conditions (fixed stimulus duration and Tyrode solution), this situation may, however, be quite different in a scenario in which calcium dynamics are affected by the duration of the action potential and/or under the prevalence of sympathetic tone. It is known from the literature, for example, that the catecholamine-mediated trigger for inducing AF involves a significant increase of atrial I_{CaL}.[36] In agreement with this situation, our data on paced cells show that under stressful conditions (isoproterenol + E4031) AF-CMs are significantly more prone to generate arrhythmic events than CTRL-CMs, as indicated by larger DADs that more easily give rise to ectopic beats. The underlying mechanism may be related to the very long action potential during β-adrenergic stimulation in AF-CMs in which the contribution of I_{CaL} become more relevant than in CTRL-CMs. Together, our data suggest that the increase in I_{CaL} and in I_f current are likely to be the trigger for the initiation of AF.

4.5 Study limitations

Because sibling's parents are deceased, and their sons/daughters are still too young for ruling out AF, we could not derive hiPSCs from healthy relatives. We bypassed this limitation by comparing data with those obtained from at least three unrelated healthy controls, which displayed similar results among them. At the time we started to collect data, no protocols for selecting specifically atrial-like hiPSC-derived CMs were available. However, even if we did not select a specific hiPSC-CM atrial subpopulation, and despite the fact that the arrhythmogenesis due to a gain of function of inward currents can be more easily demonstrated in hiPSC-CMs lacking I_{K1}, we believe that the changes observed in I_f and I_{CaL} could induce triggered automaticity also *in vivo*, specifically in the atria, due to the fact that the adult atrium shows a significantly lower conductance than ventricle, near the resting potential.[3,37]

5. Conclusions

In conclusion, we provide in the present work the first demonstration that hiPSCs can be used as a cellular model of a human cardiac pathology with a complex genetic background. Independently of the genetic alterations, we demonstrated that hiPSC-CMs from two sisters with AF show a higher spontaneous rate of contraction and a gain of function of both the I_f and the I_{CaL} currents relative to CMs derived from any of four control individuals. We suggest that the increase of these depolarizing currents and other still unknown factors can contribute to the induction of abnormal automaticity in atrial cells and can thus be the triggering event of this specific type of AF.

Supplementary material

Supplementary material is available at *Cardiovascular Research* online.

Acknowledgements

We acknowledge Angela De Luca, Marialaura Serzanti, Giulia Savio, and Laura Tononi for technical assistance; Gianluigi Condorelli for helpful discussions; and Paola Aldegheri for the informations on patients' clinical history.

Conflict of interest: none declared

Funding

E.C. was a recipient of the Giuseppe Marai INN fellowship. This work was supported by the European Research Council-ERC (2012-StG-311736-PD-HUMMODEL) to A.C., the Spanish Ministry of Economy and Competitiveness-MINECO (SAF2015-69706-R and BFU2016-80870-P), Instituto de Salud Carlos III-ISCIII/FEDER (Red de Terapia Celular - TerCel RD16/0011/0024), AGAUR (2014-SGR-1460) to A.R. and A.C. and CERCA Programme / Generalitat de Catalunya to A.R. Fondazione Cariplo (Grant numbers 2014-0822 to P.D.E.; 2014-1090 to A.B.; and 2014-0728 to D.D.).

References

1. Tucker NR, Ellinor PT. Emerging directions in the genetics of atrial fibrillation. *Circ Res* 2014;**114**:1469–1482.
2. Mahida S, Lubitz SA, Rienstra M, Milan DJ, Ellinor PT. Monogenic atrial fibrillation as pathophysiological paradigms. *Cardiovasc Res* 2011;**89**:692–700.
3. Iwasaki YK, Nishida K, Kato T, Nattel S. Atrial fibrillation pathophysiology: implications for management. *Circulation* 2011;**124**:2264–2274.
4. Nattel S, Dobrev D. Electrophysiological and molecular mechanisms of paroxysmal atrial fibrillation. *Nat Rev Cardiol* 2016;**13**:575–590.
5. Dell'Era P, Benzoni P, Crescini E, Valle M, Xia E, Consiglio A, Memo M. Cardiac disease modeling using induced pluripotent stem cell-derived human cardiomyocytes. *World J Stem Cells* 2015;**7**:329–342.
6. Di Pasquale E, Song B, Condorelli G. Generation of human cardiomyocytes: a differentiation protocol from feeder-free human induced pluripotent stem cells. *J Vis Exp* 2013;**76**:e50429.
7. Nakahama H, Di Pasquale E. Generation of cardiomyocytes from pluripotent stem cells. *Methods Mol Biol* 2016;**1353**:181–190.
8. Aasen T, Raya A, Barrero MJ, Garreta E, Consiglio A, Gonzalez F, Vassena R, Bilic J, Pekarik V, Tiscornia G, Edel M, Boue S, Izpisua Belmonte JC. Efficient and rapid generation of induced pluripotent stem cells from human keratinocytes. *Nat Biotechnol* 2008;**26**:1276–1284.
9. Cordeiro JM, Nesterenko VV, Sicouri S, Goodrow RJ Jr, Treat JA, Desai M, Wu Y, Doss MX, Antzelevitch C, Di Diego JM. Identification and characterization of a transient outward K+ current in human induced pluripotent stem cell-derived cardiomyocytes. *J Mol Cell Cardiol* 2013;**60**:36–46.
10. DiFrancesco D, Noble D. The funny current has a major pacemaking role in the sinus node. *Heart Rhythm* 2012;**9**:299–301.
11. Baruscotti M, Barbuti A, Bucchi A. The cardiac pacemaker current. *J Mol Cell Cardiol* 2010;**48**:55–64.
12. DiFrancesco D, Tortora P. Direct activation of cardiac pacemaker channels by intracellular cyclic AMP. *Nature* 1991;**351**:145–147.
13. Barbuti A, Scavone A, Mazzocchi N, Terragni B, Baruscotti M, Difrancesco D. A caveolin-binding domain in the HCN4 channels mediates functional interaction with caveolin proteins. *J Mol Cell Cardiol* 2012;**53**:187–195.
14. Bosman A, Sartiani L, Spinelli V, Del Lungo M, Stillitano F, Nosi D, Mugelli A, Cerbai E, Jaconi M. Molecular and functional evidence of HCN4 and caveolin-3 interaction during cardiomyocyte differentiation from human embryonic stem cells. *Stem Cells Dev* 2013;**22**:1717–1727.
15. Moretti A, Bellin M, Welling A, Jung CB, Lam JT, Bott-Flügel L, Dorn T, Goedel A, Höhnke C, Hofmann F, Seyfarth M, Sinnecker D, Schömig A, Laugwitz K-L. Patient-specific induced pluripotent stem-cell models for long-QT syndrome. *N Engl J Med* 2010;**363**:1397–1409.
16. Ma J, Guo L, Fiene SJ, Anson BD, Thomson JA, Kamp TJ, Kolaja KL, Swanson BJ, January CT. High purity human-induced pluripotent stem cell-derived cardiomyocytes: electrophysiological properties of action potentials and ionic currents. *Am J Physiol Heart Circ Physiol* 2011;**301**:H2006–H2017.
17. Barbuti A, Benzoni P, Campostrini G, Dell'Era P. Human derived cardiomyocytes: a decade of knowledge after the discovery of induced pluripotent stem cells. *Dev Dyn* 2016;**245**:1145–1158.
18. Schnabel RB, Yin X, Gona P, Larson MG, Beiser AS, McManus DD, Newton-Cheh C, Lubitz SA, Magnani JW, Ellinor PT, Seshadri S, Wolf PA, Vasan RS, Benjamin EJ, Levy D. 50 year trends in atrial fibrillation prevalence, incidence, risk factors, and mortality in the Framingham Heart Study: a cohort study. *Lancet* 2015;**386**:154–162.
19. Robertson C, Tran DD, George SC. Concise review: maturation phases of human pluripotent stem cell-derived cardiomyocytes. *Stem Cells* 2013;**31**:829–837.
20. Brennand KJ, Simone A, Jou J, Gelboin-Burkhart C, Tran N, Sangar S, Li Y, Mu Y, Chen G, Yu D, McCarthy S, Sebat J, Gage FH. Modelling schizophrenia using human induced pluripotent stem cells. *Nature* 2011;**473**:221–225.
21. Laksman Z, Wauchop M, Lin E, Protze S, Lee J, Yang W, Izaddoustdar F, Shafaattalab S, Gepstein L, Tibbits GF, Keller G, Backx PH. Modeling atrial fibrillation using human embryonic stem cell-derived atrial tissue. *Sci Rep* 2017;**7**:5268.
22. Kalman JM, Munawar M, Howes LG, Louis WJ, Buxton BF, Gutteridge G, Tonkin AM. Atrial fibrillation after coronary artery bypass grafting is associated with sympathetic activation. *Ann Thorac Surg* 1995;**60**:1709–1715.
23. Dimmer C, Tavernier R, Gjorgov N, Van Nooten G, Clement DL, Jordaens L. Variations of autonomic tone preceding onset of atrial fibrillation after coronary artery bypass grafting. *Am J Cardiol* 1998;**82**:22–25.
24. Baruscotti M, Bucchi A, Milanesi R, Paina M, Barbuti A, Gnecchi-Ruscone T, Bianco E, Vitali-Serdoz L, Cappato R, DiFrancesco D. A gain-of-function mutation in the cardiac pacemaker HCN4 channel increasing cAMP sensitivity is associated with familial inappropriate sinus tachycardia. *Eur Heart J* 2017;**38**:280–288.
25. Cerbai E, Mugelli A. I(f) in non-pacemaker cells: role and pharmacological implications. *Pharmacol Res* 2006;**53**:416–423.
26. Stillitano F, Lonardo G, Giunti G, Del Lungo M, Coppini R, Spinelli V, Sartiani L, Poggesi C, Mugelli A, Cerbai E. Chronic atrial fibrillation alters the functional properties of If in the human atrium. *J Cardiovasc Electrophysiol* 2013;**24**:1391–1400.
27. Van Wagoner DR, Pond AL, Lamorgese M, Rossie SS, McCarthy PM, Nerbonne JM. Atrial L-type Ca2+ currents and human atrial fibrillation. *Circ Res* 1999;**85**:428–436.

28. Daoud EG, Knight BP, Weiss R, Bahu M, Paladino W, Goyal R, Man KC, Strickberger SA, Morady F. Effect of verapamil and procainamide on atrial fibrillation-induced electrical remodeling in humans. *Circulation* 1997;**96**:1542–1550.
29. Tieleman RG, De Langen C, Van Gelder IC, de Kam PJ, Grandjean J, Bel KJ, Wijffels MC, Allessie MA, Crijns HJ. Verapamil reduces tachycardia-induced electrical remodeling of the atria. *Circulation* 1997;**95**:1945–1953.
30. Workman AJ, Pau D, Redpath CJ, Marshall GE, Russell JA, Kane KA, Norrie J, Rankin AC. Post-operative atrial fibrillation is influenced by beta-blocker therapy but not by pre-operative atrial cellular electrophysiology. *J Cardiovasc Electrophysiol* 2006;**17**: 1230–1238.
31. Barana A, Matamoros M, Dolz-Gaitón P, Pérez-Hernández M, Amorós I, Núñez M, Sacristán S, Pedraz Á, Pinto Á, Fernández-Avilés F, Tamargo J, Delpón E, Caballero R. Chronic atrial fibrillation increases microRNA-21 in human atrial myocytes decreasing L-type calcium current. *Circ Arrhythm Electrophysiol* 2014;**7**:861–868.
32. Ghosh D, Nieves-Cintron M, Tajada S, Brust-Mascher I, Horne MC, Hell JW, Dixon RE, Santana LF, Navedo MF. Dynamic L-type CaV1.2 channel trafficking facilitates CaV1.2 clustering and cooperative gating. *Biochim Biophys Acta Mol Cell Res* 2018; **1865**:1341–1355.
33. Dixon RE, Yuan C, Cheng EP, Navedo MF, Santana LF. Ca2+ signaling amplification by oligomerization of L-type Cav1.2 channels. *Proc Natl Acad Sci USA* 2012;**109**:1749–1754.
34. Kashihara T, Nakada T, Kojima K, Takeshita T, Yamada M. Angiotensin II activates CaV 1.2 Ca(2+) channels through beta-arrestin2 and casein kinase 2 in mouse immature cardiomyocytes. *J Physiol (Lond)* 2017;**595**:4207–4225.
35. Sato D, Dixon RE, Santana LF, Navedo MF. A model for cooperative gating of L-type Ca2+ channels and its effects on cardiac alternans dynamics. *PLoS Comput Biol* 2018; **14**:e1005906.
36. Workman AJ. Cardiac adrenergic control and atrial fibrillation. *Naunyn Schmiedebergs Arch Pharmacol* 2010;**381**:235–249.
37. Opthof T. The membrane current (I(f)) in human atrial cells: implications for atrial arrhythmias. *Cardiovasc Res* 1998;**38**:537–540.

Translational perspective

This is the first time a human cellular model of atrial fibrillation (AF), based on the analysis of iPSC-derived cardiomyocytes from patients, is presented. Comparing cells from two sisters of a family with a complex genetic form of AF with those from healthy controls, we found peculiar alterations in two ion currents potentially involved in AF aetiology. Despite progresses in the management of AF, efficacy in maintaining sinus rhythm is modest. Human-based models elucidating the molecular mechanisms underlying AF will help define the best therapeutic approach. We propose to personalize AF therapy based on functional alterations found in patient-specific cardiomyocytes.

Cardiovascular Research (2017) **113**, 531–541
doi:10.1093/cvr/cvx006

Elucidating arrhythmogenic mechanisms of long-QT syndrome *CALM1*-F142L mutation in patient-specific induced pluripotent stem cell-derived cardiomyocytes

Marcella Rocchetti[1†], Luca Sala[1,2†], Lisa Dreizehnter[3†], Lia Crotti[2,4], Daniel Sinnecker[3], Manuela Mura[4,5], Luna Simona Pane[3], Claudia Altomare[1], Eleonora Torre[1], Gaspare Mostacciuolo[1], Stefano Severi[6], Alberto Porta[7,8], Gaetano M. De Ferrari[4,5], Alfred L George Jr[9], Peter J. Schwartz[2], Massimiliano Gnecchi[4,5,10], Alessandra Moretti[3,11†], and Antonio Zaza[1,*†]

[1]Department of Biotechnology and Bioscience, University of Milano-Bicocca, Milan, Italy; [2]Center for Cardiac Arrhythmias of Genetic Origin and Laboratory of Cardiovascular Genetics, IRCCS Istituto Auxologico Italiano, Milan, Italy; [3]I. Medical Department - Cardiology, Klinikum Rechts der Isar- Technische Universität München, Munich, Germany; [4]Department of Molecular Medicine – Unit of Cardiology, University of Pavia, Pavia, Italy; [5]Department of Cardiothoracic and Vascular Sciences – Coronary Care Unit and Laboratory of Clinical and Experimental Cardiology, Fondazione IRCCS Policlinico San Matteo, Pavia, Italy; [6]Biomedical Engineering Laboratory D.E.I, University of Bologna, Cesena, Italy; [7]Department of Biomedical Sciences for Health, University of Milan, Milan, Italy; [8]Department of Cardiothoracic, Vascular Anesthesia and Intensive Care, IRCCS Policlinico San Donato, Milan, Italy; [9]Department of Pharmacology, Northwestern University Feinberg School of Medicine, Chicago, Illinois, USA; [10]Department of Medicine, University of Cape Town, Cape Town, South Africa; and [11]DZHK (German Centre for Cardiovascular Research) - Partner Site Munich Heart Alliance, Munich, Germany

Received 19 April 2016; revised 3 January 2017; editorial decision 11 January 2017; accepted 15 January 2017; online publish-ahead-of-print 2 February 2017

Time for primary review: 50 days

Aims Calmodulin (CaM) is a small protein, encoded by three genes (*CALM1-3*), exerting multiple Ca^{2+}-dependent modulatory roles. A mutation (F142L) affecting only one of the six *CALM* alleles is associated with long QT syndrome (LQTS) characterized by recurrent cardiac arrests. This phenotypic severity is unexpected from the predicted allelic balance. In this work, the effects of heterozygous *CALM1*-F142L have been investigated in human induced pluripotent stem cell-derived cardiomyocytes (hiPSC-CMs) obtained from a LQTS patient carrying the F142L mutation, i.e. in the context of native allelic ratio and potential gene modifiers.

Methods and Results Skin fibroblasts of the mutation carrier and two unrelated healthy subjects (controls) were reprogrammed to hiPSC and differentiated into hiPSC-CMs. Scanty I_{K1} expression, an hiPSC-CMs feature potentially biasing repolarization, was corrected by addition of simulated I_{K1} (Dynamic-Clamp). Abnormalities in repolarization rate-dependency (in single cells and cell aggregates), membrane currents and intracellular Ca^{2+} dynamics were evaluated as putative arrhythmogenic factors. *CALM1*-F142L prolonged repolarization, altered its rate-dependency and its response to isoproterenol. This was associated with severe impairment of Ca^{2+}-dependent inactivation (CDI) of I_{CaL}, resulting in augmented inward current during the plateau phase. As a result, the repolarization of mutant cells failed to adapt to high pacing rates, a finding well reproduced by using a recent hiPSC-CM action potential model. The mutation failed to affect I_{Ks} and I_{NaL} and changed I_f only marginally. Intracellular Ca^{2+} dynamics and Ca^{2+} store stability were not significantly modified. Mutation-induced repolarization abnormalities were reversed by verapamil.

Conclusion The main functional derangement in *CALM1*-F142L was prolonged repolarization with altered rate-dependency and sensitivity to β-adrenergic stimulation. Impaired CDI of I_{CaL} underlined the electrical abnormality, which was

---

* Corresponding author. Dipartimento di Biotecnologie e Bioscienze Università Milano-Bicocca, P.za della Scienza 2, 20126 Milano, Italy. Tel: +39 02 6448 3307; fax: +39 02 6448 3565, E-mail: antonio.zaza@unimib.it

[†] The first three authors and the last two authors contributed equally to the study.

sensitive to I_{CaL} blockade. High mutation penetrance was confirmed in the presence of the native genotype, implying strong dominance of effects.

Keywords LQTS • Calmodulin • Mutations • Sudden death • hiPSC-CMs

1. Introduction

The congenital long QT syndrome (LQTS) is a genetic disorder characterized by QT interval prolongation and by propensity to life-threatening arrhythmias.[1] We recently provided the first evidence of a malignant form of LQTS associated with calmodulin (CaM) mutations[2]; other reports of CaM mutations in arrhythmogenic syndromes have followed.[3–5] CaM is a small Ca^{2+}-binding protein essential for multiple signalling processes in eukaryotic cells.[6] Mammals have three CaM genes (*CALM1*, *2*, and *3*) that encode identical amino acid sequences.[7] In the heart, CaM transduces Ca^{2+} signals to regulate, either directly or through CaMKII, electrophysiology and Ca^{2+} handling.[8]

Ca^{2+}-binding affinity is variably altered by CaM mutations linked to arrhythmogenic syndromes. Whereas the LQTS phenotype prevails among those with reduced Ca^{2+} affinity, mutations with normal Ca^{2+} affinity are often associated with catecholaminergic polymorphic ventricular tachycardias (CPVT).[3,9,10]

In the setting of LQTS, heterologous expression of mutated *CALM* is associated with delayed I_{CaL} inactivation, prolonged repolarization and perturbed intracellular Ca^{2+} handling.[11,12] However, heterologous expression of mutant constructs cannot reproduce the amount and subcellular localization of the abnormal protein. Therefore, albeit unveiling mutation effects potentially involved in arrhythmogenesis, previous studies did not clarify whether these effects are truly present in mutation carriers and to which extent they may contribute to electrical instability.

The present study evaluates the effects of an heterozygous *CALM1*-F142L mutation with reduced Ca^{2+} affinity, first identified in a LQTS patient suffering multiple cardiac arrests since infancy,[2] using 'induced pluripotent stem cell-derived cardiomyocytes' (hiPSC-CMs) generated from patient's skin fibroblasts. This allowed to test mutation effects in the context of the patient's own genotype, including potential adaptive transcriptional or post-transcriptional remodelling. The results demonstrate that defective I_{CaL} inactivation is the dominant mutation consequence and suggest the resulting repolarization delay as the most likely arrhythmogenic effect.

2. Methods

The Ethical Committee of the Fondazione IRCCS Policlinico San Matteo approved the study, which was performed in accordance with the Declaration of Helsinki. All samples were collected after obtaining informed consent from the donors. The investigation conforms to the Guide of the Care and Use of Laboratory Animals (NIH publication No. 85-23, revised 2011) and to the guidelines for animal care endorsed by Università Milano-Bicocca. An expanded Methods section is available in the Supplementary material online.

2.1 Generation and differentiation of induced pluripotent stem cells

Human induced pluripotent stem cells (hiPSCs) were generated by Sendai virus-mediated reprogramming of dermal fibroblasts and differentiated into cardiac bodies (CB)[13] (see Supplementary material online, *Figures S1* and *S2* for details). For patch-clamp measurements, mature CBs were dissociated into single hiPSC-CMs and analysed within 3–5 days. The presence of the *CALM1*-F142L mutation was verified by PCR on skin fibroblasts, hiPSCs and hiPSC-CMs (see Supplementary material online, *Figure S1*, primer sequences in *Table S1*).

2.2 Molecular studies

Gene expression was quantified by qRT-PCR, the results were normalized to *GAPDH*. Total CaM protein level was quantified by densitometric analysis of western blots. CaMKII activity was measured in hiPSC-CMs by a FRET assay based on the biosensor Camui-CR[14] cloned into a lentiviral vector.

2.3 Electrical activity in multicellular preparations and single cells

Extracellular field-potentials were recorded at 37 °C in spontaneously beating CBs by Multiple Electrode Array (MEA). Field-potential duration, reflecting electrical systole, was measured from the onset of the sharp positive deflection to the peak of the secondary slow deflection[15]; for simplicity, we will refer to this measurement as QT, which was rate-corrected (QTc) by Bazett's formula. CBs contraction was recorded with a Video Edge detection System.

Action potentials (APs) were recorded by whole-cell patch-clamp in hiPSC-CM paced at 0.5, 1, 2, and 3.3 Hz during Tyrode superfusion (36.5 °C). Under native conditions, hiPSC-CM had partially depolarized diastolic potentials (E_{diast} -50.5 ± 3.7 mV at 0.5 Hz), a likely consequence of low I_{K1} expression in immature myocytes.[16] Thus, numerically modelled I_{K1}[17] (see Supplementary material online, *Table S2*) was injected in the hiPSC-CM by Dynamic Clamp (DC).[18,19] AP measurements under DC are described in the manuscript, those in native conditions in the Supplementary material online.

2.4 Characterization of membrane currents

I_{CaL} was recorded in voltage-clamped hiPSC-CMs at room temperature to minimize current rundown. Peak *I/V* relationships, steady-state activation/inactivation, and recovery kinetics were obtained by standard protocols (detail in Supplementary material online); mid activation/inactivation potential ($V_{0.5}$) and the reciprocal slope factors (*k*, in mV) were estimated by Boltzmann fitting. The magnitude of I_{CaL} 'window', defined as the overlap of steady-state activation and inactivation curves, was quantified (*Table 1*) as overlap area (Area), voltage (V@Peak) and open probability at curves intersection (Po_{max}). To quantify Ca^{2+}-dependent inactivation (CDI), I_{CaL} was recorded, within each cell, with Ca^{2+} (I_{CaL}) or equimolar Ba^{2+} (I_{BaL}) as charge carriers. CDI was expressed as the difference between I_{BaL} and I_{CaL} at 100 ms (r_{100}) and 300 ms (r_{300}). Rate-dependent I_{CaL} facilitation (CDF) was measured at 36.5 °C, as progressive enhancement of I_{CaL} (measured during the first 50 ms of the activating step) following initiation of repetitive activations at 0.05 and 1 Hz.

Table 1 Comparison of I_{CaL} parameters between CTR1 and the *CALM1*-F142L c1 and c2 clones separately

	CTR1	F142L			
		c1	*P* vs. CTR1	c2	*P* vs. CTR1
Activation curve					
$V_{0.5}$ (mV)	-11.3 ± 0.78	-9.9 ± 1.12	NS	-8.9 ± 1.42	NS
k (mV)	6.7 ± 0.27	7.7 ± 0.31	<0.05	7.8 ± 0.35	<0.05
G_{max} (nS/pF)	0.22 ± 0.03	0.25 ± 0.03	NS	0.26 ± 0.05	NS
Inactivation curve					
$V_{0.5}$ (mV)	-30.2 ± 0.62	-27.8 ± 0.7	<0.05	-28.1 ± 0.8	<0.05
k (mV)	4.8 ± 0.29	5.5 ± 0.29	NS	5.8 ± 0.16	<0.05
G_{min}/G_{max}	0.03 ± 0.005	0.09 ± 0.01	<0.05	0.08 ± 0.01	<0.05
Window					
Area (a.u.)	2.9 ± 0.34	5.2 ± 0.36	<0.05	4.8 ± 0.78	<0.05
V@Peak (mV)	-21.9 ± 0.84	-17.8 ± 0.86	<0.05	-19.2 ± 1.4	NS
Po_{max} (10^{-3})	31.6 ± 3.8	64.7 ± 4.4	<0.05	62.0 ± 11.5	<0.05

$V_{0.5}$, mid activation/inactivation potential; *k*, reciprocal slope factor (in mV) of activation/inactivation curves; G_{max} = maximal conductance; Area, 'window' area (in arbitrary units); *V*@Peak = membrane potential at which activation and inactivation curves intersect; Po_{max}: maximal open probability within the window range. Significance ($P < 0.05$) between CTR1 and each mutant clone was assessed by Student's *t*-test for unpaired measurements.

The delayed rectifier K^+ current (I_{Ks}), the late Na^+ current (I_{NaL}) and the pacemaker current (I_f) were recorded at physiological temperature by standard V-clamp protocols (detail in Supplementary material online). I_{Ks} and I_{NaL} were isolated as HMR1556 (1 µM)- and TTX (30 µM)-sensitive currents.

2.5 Intracellular Ca^{2+} measurements

Cytosolic Ca^{2+} and membrane current were simultaneously recorded in V-clamped hiPSC-CMs loaded with 10 µM Fluo4-AM; K^+ currents were blocked. Diastolic fluorescence was used as reference (F_0) for signal normalization (F/F_0) after subtraction of background. Ca^{2+} transients (CaT) were recorded during 300 ms steps to 0 mV (holding -50 mV), applied every 5 s.

Sarcoplasmic reticulum (SR) Ca^{2+} content (Ca_{SR}) was estimated by integrating the Na/Ca exchanger (NCX) current (I_{NCX}) elicited by 10 mM caffeine.[20] The slope of the I_{NCX}/Ca^{2+} relationship during the final third of the caffeine-induced transient was used to estimate NCX 'conductance'.[20]

The 'gain' of the coupling between membrane excitation and Ca^{2+} release was calculated as the ratio between CaT amplitude (F/F_0) and Ca^{2+} influx, obtained by integrating I_{CaL} up to the time of CaT peak.

The composition of experimental solutions is reported in the Supplementary material online.

2.6 Numerical simulations

Results of current clamp experiments were simulated *in silico* using a recently published hiPSC-CM AP model.[21] The I_{CaL} kinetic, as characterized in hiPSC-CMs in CTR1 and F142L was included into the model (see Supplementary material online). An additional amount of I_{K1}, based on the O'Hara–Rudy model of adult myocyte,[17] was incorporated in both CTR and F142L to mimic DC experimental conditions.

2.7 Statistics

Student's *t*-test or ANOVA for paired or unpaired measurements were applied as appropriate, with Bonferroni's correction in post-hoc comparisons. χ^2 statistics was used for comparison of categorical variables (GraphPad Prism 5). Data are expressed as mean ± SE; $P < 0.05$ defines significance, sample size is reported in figure legends.

3. Results

3.1 Characteristics of hiPSC-CMs donors

The proband under study is a young boy who suffered multiple syncopal events and cardiac arrest at the age of 14 years old. His QTc was very prolonged (between 600 and 700 ms) with episodes of T wave alternans often recorded by ECG Holter monitoring. When he was 9, mean HR was 66 b/min during the day, but at night HR dramatically dropped to less than 40 b/min. As compared with that of a normal subject, his QT/RR relationship was strongly non-linear, becoming significantly steeper at short RR intervals (see Supplementary material online, *Figure S3* and *Table S3*). Family history is unknown since he was adopted.

Two mutant hiPSC-CMs clones (c1 and c2) were obtained from patient's biopsy. Data from c1 and c2 are reported separately for I_{CaL} characterization (*Figure 2*) and, being closely comparable, have been pooled for the remaining studies. Because proband's relatives were unavailable, we used as healthy controls two genetically unrelated subjects: a 32-year-old Caucasian female (CTR1) and a 27-year-old Afro-American male (CTR2). For I_{CaL} characterization mutant hiPSC-CMs were compared to those of both CTR1 and CTR2; in the remaining studies CTR1 was used as control.

Molecular characterization of hiPSC-CMs demonstrated cardiomyocyte-like patterns of mRNA and protein expression (*Figure 1*), as also detailed in the Supplementary material online.

3.2 Transcriptional effects

To test for transcriptional changes secondary to the mutation, gene expression of CaM isoforms, ion channels, Ca^{2+} handling proteins and other Ca^{2+} binding proteins was analysed in CTR1 and mutant hiPSC-CMs. As shown in *Figure 1*, the mutation did not affect the expression of any of these genes (*Figure 1*). Also the levels of total CaM protein were

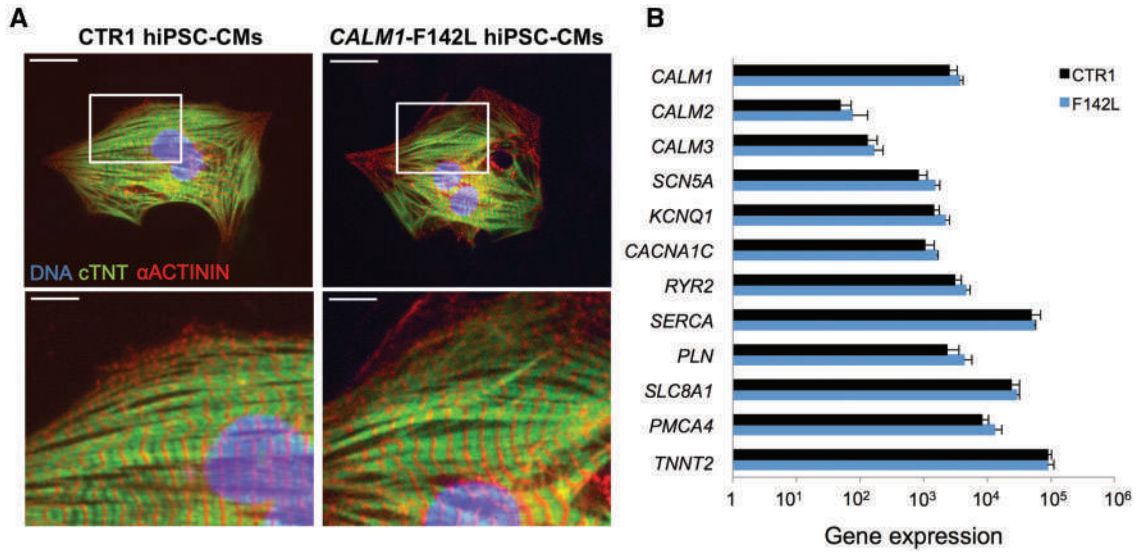

Figure 1 *CALM1*-F142L mutation does not affect the expression of CaM isoforms, ion channels and Ca^{2+} handling proteins. (*A*) Immunostaining for cardiac Troponin T (cTNT, green) and α-actinin (red) of CTR1 (left) and *CALM1*-F142L (right) hiPSC-CMs (nuclei in blue). Bottom panels are a magnification of the area framed in the upper images. (*B*) Quantitative RT-PCR analysis of *CALM* and cardiac-specific genes in CTR1 (black bars) and *CALM1*-F142L hiPSC-CMs (blue bars, clones c1 and c2 pooled). Data normalized to *GAPDH* and presented as mean ± SEM of three replicas. No significant differences were detected in the transcription pattern (Student's *t*-test for unpaired measurements). SCN5A: Na$_V$1.5 channel; KCNQ1: K$^+$ channel; CACNA1C: Ca$_V$1.2 channel; RyR2: Ryanodine receptor channel; SERCA: sarcoplasmic reticulum Ca^{2+} ATP-ase; PLN: phospholamban; SLC8A1: plasmalemmal Na$^+$/Ca^{2+} exchanger; PMCA4 plasmalemmal Ca^{2+} ATPase; TNNT2: troponinT.

similar in CTR1 and F142L hiPSC-CMs (see Supplementary material online, *Figure S4*).

3.3 Effects on I_{CaL} properties

We analysed I_{CaL} properties in c1 and c2 mutant hiPSC-CMs clones and in CTR1 hiPSC-CMs. In both mutant clones peak I_{CaL} density (*Figure 2A*) was similar to that of CTR1, but the sustained I_{CaL} component was significantly larger. In both mutant clones inactivation was positively shifted and incomplete, thus widening the voltage 'window' over which sustained I_{CaL} was present (*Table 1*). In mutant clones I_{CaL} inactivation was also slower than in CTR1 cells; as indicated by r_{100} and r_{300} values (*Figure 2*), this was due to weaker CDI. The wider 'window' and slower inactivation converged to enhance I_{CaL} sustained component in mutant hiPSC-CMs.

I_{CaL} recovery from inactivation is regulated by CaMKII[22] and relevant to I_{CaL} rate-dependency. Recovery time-course was tested for total I_{CaL} and after subtraction of the non-inactivating component (see Supplementary material online, *Figure S5*). As expected from defective CDI, a larger proportion of total I_{CaL} was available at short diastolic intervals in mutant hiPSC-CMs (see Supplementary material online, *Figure S5B*); when the inactivating component was analysed separately, recovery kinetics was similar between CTR1 and mutant cells (see Supplementary material online, *Figure S5C*). Recovery was faster, and the weight of the non-inactivating component smaller, at -80 mV than at -50 mV.

To rule out interindividual variability as a source of CDI differences, we analysed I_{CaL} properties in hiPSC-CMs from a second healthy control (CTR2) (see Supplementary material online, *Figure S6* and *Table S4*). Albeit in CTR2 I_{CaL} was larger and its properties were marginally different from those of CTR1, CDI and 'window' parameters were closely comparable.

CaMKII is a downstream signal mediating many effects of the Ca-CaM complex.[23] CaMKII activation was unexpectedly stronger in mutant hiPSC-CMs than in CTR1 ones (see Supplementary material online, *Figure S7*).

Rate-dependent and CaMKII-mediated I_{CaL} facilitation (CDF) can be detected in ventricular myocytes of different species.[24] However, CDF could not be induced even in CTR1 hiPSC-CMs (see Supplementary material online, *Figure S8A*). On the other hand, CDF was elicited by the same protocol in adult rat ventricular myocytes (see Supplementary material online, *Figure S8B*).

3.4 Effects on slow delayed rectifier K$^+$ current (I_{Ks}) and late Na$^+$ current (I_{NaL})

Given that both I_{Ks} and I_{NaL} are implicated in LQTS[25] and are modulated by CaM and/or CaMKII,[26,27] we analysed whether changes in these currents could contribute to this specific type of LQTS phenotype. As shown in *Figure 3A* and *B*, I_{Ks} *I–V* relationships and its steady-state activation were similar in CTR1 and mutant hiPSC-CMs. Non-inactivating components of I_{Na}, Na$^+$ 'window current' (I_{Naw}) and I_{NaL}, were evaluated by applying slow voltage ramps (*Figure 3C* and *D*) as previously reported.[28] TTX-sensitive current peaking at -38.0 ± 2.1 mV (CTR1, NS vs. F142L), mostly representing I_{Naw}, was less expressed in mutant cells, while no differences between groups were observed in the current activated at 0 mV, mostly representing I_{NaL}. Overall, in comparison to CTR1 hiPSC-CM, mutant cells showed smaller sustained I_{Na}, a finding opposite to what required to account for QT prolongation.

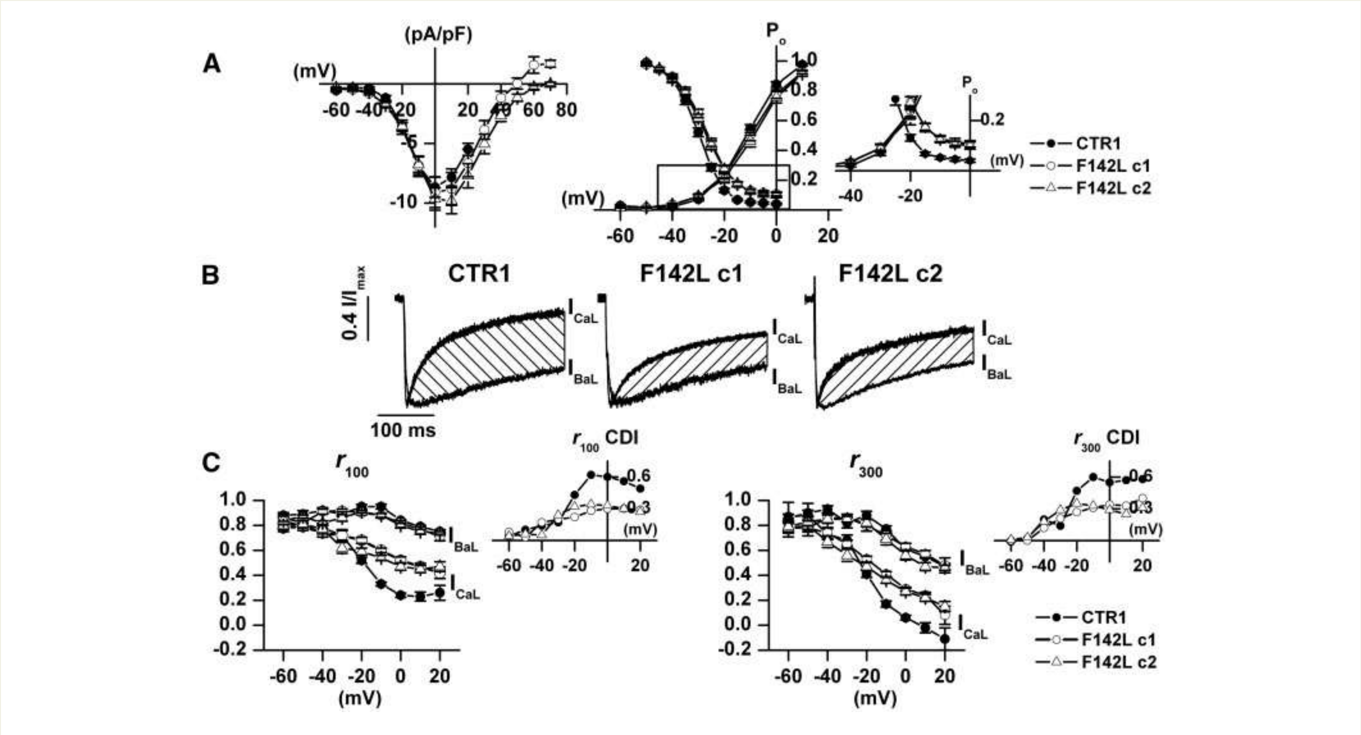

Figure 2 Steady-state I_{CaL} inactivation is positively shifted and CDI is reduced in *CALM1*-F142L hiPSC-CMs. I_{CaL} characterization in CTR1 (filled dots $N = 11$) and in the two *CALM1*-F142L clones (c1, open dots $N = 12$ and c2, open triangles $N = 13$) hiPSC-CMs separately. (*A*) *Left*: peak I_{CaL} I/V relationships; *Right*: I_{CaL} steady-state activation and inactivation curves; the 'window' range of potentials is zoomed in the inset (average data and statistics in *Table 1*). (*B*) I_{CaL} and I_{BaL} tracings recorded within the same cell at 0 mV; traces are normalized for their peak value; CDI was measured as the difference between I_{BaL} and I_{CaL} (dashed area). (*C*) Proportion of peak I_{CaL} and I_{BaL} remaining at 100 ms (r_{100}) and 300 ms (r_{300}), plotted as a function of the test potential. The insets show CDI as a function of test potential.

3.5 Effects on cardiac bodies and pacemaking

To reproduce tissue environment, field-potentials were recorded from spontaneously beating CBs at baseline and during β-adrenergic stimulation by isoproterenol (Iso 0.05–1.6 μM). The RR and QT intervals of CBs from the two mutant clones (c1 and c2) were similarly prolonged ($P < 0.05$ vs. CTR1, *Figure 4A*), reproducing both the bradycardic and LQTS phenotype of the patient. The relation between QT and RR intervals, evaluated by linear fitting (*Figure 4B*), was steeper in mutant CBs than in CTR1 ones (slope 0.22 ± 0.05 vs. 0.09 ± 0.02, $P < 0.05$) with a similar intercept. QTc was prolonged in mutant CBs (*Figure 4B*, inset). Isoproterenol effect on QT and RR saturated already at 0.05 μM and, at this concentration, it was larger in mutant than in CTR1 CBs (*Figure 4C*). Isoproterenol significantly increased QT/RR steepness in mutant CBs (*Figure 4D*, 0.49 ± 0.07, $P < 0.05$ vs. –Iso) while had no effect on CTR1 ones (*Figure 4D*, 0.08 ± 0.04, NS vs. –Iso).

Consistent with repolarization differences, contraction was more sustained and relaxation was slower in mutant CBs (see Supplementary material online, *Figure S9*).

In spite of the slow beating rate in mutant CBs, the pacemaker current (I_f) was grossly similar in CTR1 and F142L hiPSC CMs (see Supplementary material online, *Figure S10*). The I_f activation curve was slightly shallower in mutant cells (*k* from 7.7 to 9.7 mV, $P < 0.05$), a finding that can unlikely account alone for the huge difference in beating rate between groups.

3.6 Effect on electrical activity in isolated hiPSC-CMs

Mutation effects on AP repolarization and its rate-dependency were evaluated in hiPSC-CMs with ventricular-like APs (observed in > 80% of cells). The effect of DC on AP parameters is shown in Supplementary material online, *Figure S11*. Cells were studied under native conditions (see Supplementary material online, *Figure S12*) and during I_{K1} injection via DC (*Figure 5*). I_{K1} injection resulted in 'mature', ventricular-like AP contours, reduced AP duration (APD) variability and highlighted mutation-induced differences. Under DC, mutant hiPSC-CMs had significantly longer APD compared to CTR1 at all pacing rates below 3.3 Hz (*Figure 5A* and *B*). Whereas injected I_{K1} density during diastole was similar between control and mutant hiPSC-CMs, peak I_{K1} during the late AP repolarization phase was smaller in mutant ones, particularly at low pacing rate (see Supplementary material online, *Figure S13*), probably as a consequence of shallower AP repolarization in these cells[29] (see Supplementary material online).

In 20% of mutant cells, stimulation at 2 Hz induced APD alternans, which was never observed in CTR1 ones. At 3.3 Hz, 10% of CTR1 cells and 50% of mutant ones ($P < 0.05$, *Figure 5C* and *D*) could not follow stimulation because of failure of APD to shorten adequately. Numerical simulations showed that, at variance with the normal model, in the mutant one APD failed to adapt to 3.3 Hz pacing rate (mF142L trace in *Figure 5E*). Notably, the defect in I_{CaL} CDI was alone sufficient to account for the abnormality (mF142L CDIonly trace in *Figure 5E*). After

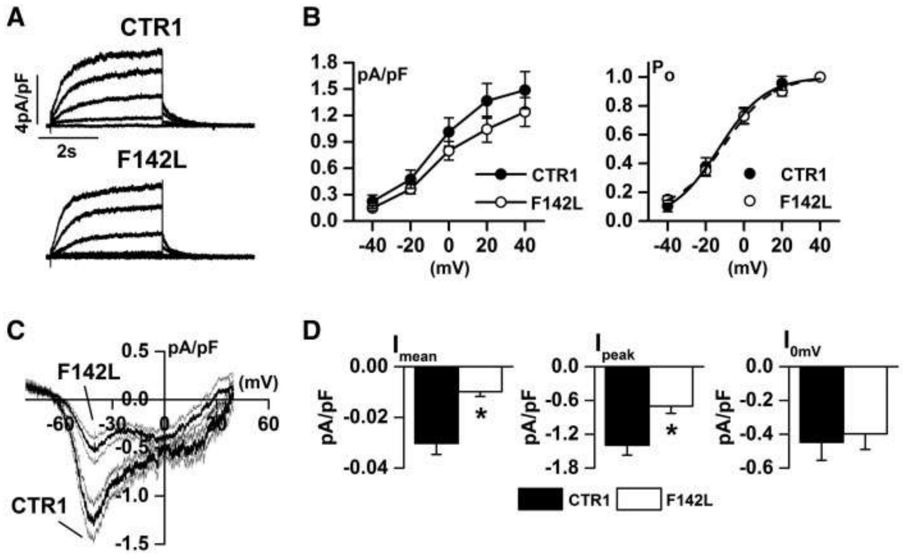

Figure 3 Steady-state I_{Ks} activation is unchanged and sustained I_{Na} is reduced in *CALM1*-F142L hiPSC-CMs. (*A*) HMR1556 (1 μM)-sensitive current (I_{Ks}) activated during voltage steps from a holding potential of - 40 mV in CTR1 and *CALM1*-F142L hiPSC-CMs. (*B*) I_{Ks} I/V relationships and steady state activation curves; Boltzmann fittings are represented by continuous and dashed lines for CTR1 (*N* = 19) and CALM1-F142L (*N* = 25) hiPSC-CMs respectively. (*C*) TTX (30 μM)-sensitive current (I_{TTX}) activated during slow voltage ramps (28 mV/sec) from a holding potential of - 100 mV, mean traces and SEM are shown. (*D*) Statistics for mean I_{TTX} (I_{mean}), peak I_{TTX} (I_{peak}, representative of I_{Naw}) and I_{TTX} activated at 0 mV (representative of I_{NaL}). CTR1: *N* = 14, *CALM1*-F142L: *N* = 13. **P* < 0.05 vs. CTR1 (Student's *t*-test for unpaired measurements).

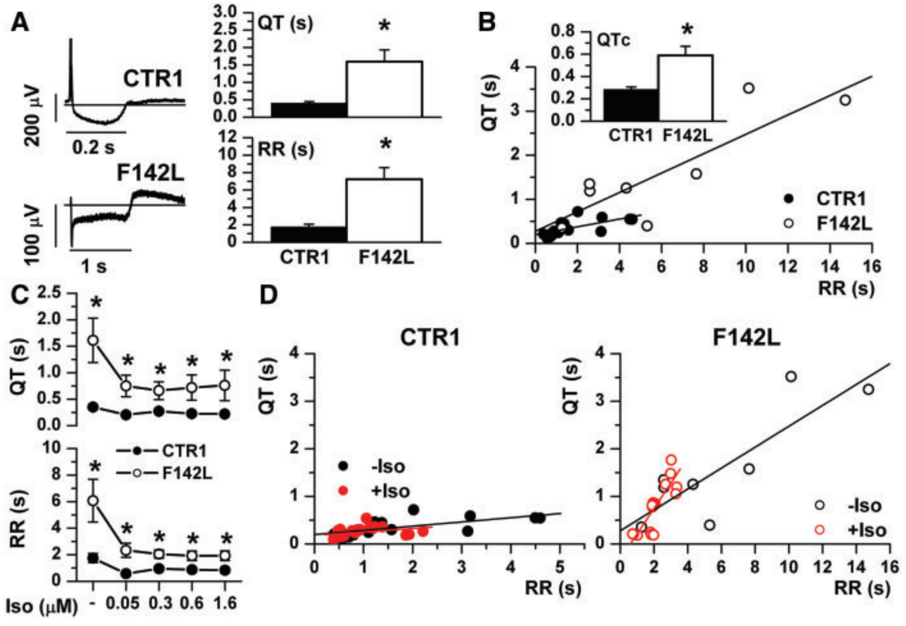

Figure 4 *CALM1*-F142L CBs show prolonged QTc and higher sensitivity to isoproterenol than CTR1 CBs. (*A*) *Left*: examples of field potentials from CTR1 and *CALM1*-F142L CBs. Arrows mark timepoints for QT measurement. *Right*: Statistics for QT and RR intervals (CTR1 *N* = 18, *CALM1*-F142L *N* = 8, data from mutant clones c1 and c2 pooled) under basal conditions. (*B*) QT-RR relationship; QTc statistics in the inset.). (*C*) Modulation of QT and RR by isoproterenol (Iso) (N > 5 at all concentrations in both groups). (*D*) QT-RR relationships at baseline (-Iso; black symbols) and during increasing Iso concentrations (+Iso red symbols) in CTR1 (left) and *CALM1*-F142L (right) CBs. **P* < 0.05 vs. CTR1 (Student's *t*-test for unpaired measurements).

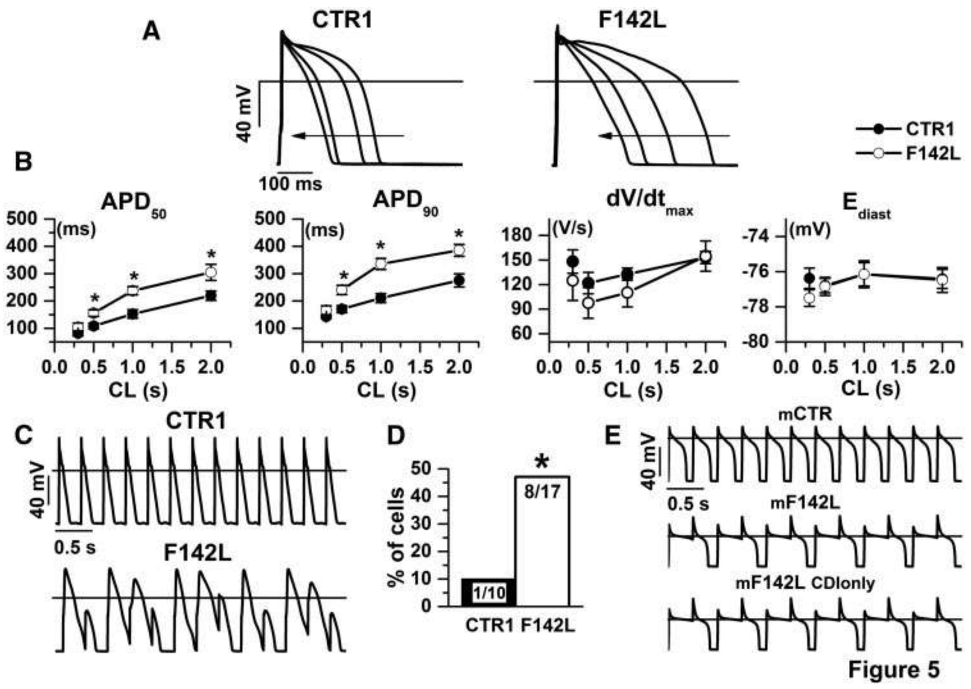

Figure 5 Isolated *CALM1*-F142L hiPSC-CMs show prolonged APD and failure of APD to shorten at high pacing rates, a finding reproduced by numerical simulations. (*A*) Action potential recorded at different pacing rates under DC; arrows indicate the direction of rate increase. (*B*) Statistics for APD_{50}, APD_{90}, dV/dt_{max} and E_{diast} in CTR1 (filled dots, $N \geq 6$) and *CALM1*-F142L (open dots, $N \geq 10$) ($^*P < 0.05$ vs. CTR1, two-way ANOVA with Bonferroni's correction). The point at the shortest CL (rate = 3.3 Hz) refers only to cells that followed pacing (see text and panel D). (*C*) Sequences of action potentials evoked at 3.3 Hz in a CTR1 (top) and a *CALM1*-F142L (bottom) hiPSC-CMs. (*D*) Percentage of cells failing to follow pacing at 3.3 Hz. $^*P < 0.05$ vs. CTR1 (χ^2 test). (*E*) Model (m) based simulation of the experimental protocol of panel C in CTR (top), *CALM1*-F142L (middle) and when only the F142L-related CDI reduction was incorporated into the computational model (bottom).

potentials, which would suggest spontaneous Ca^{2+} release events, were not observed, even at the highest pacing rate.

Cells studied under native conditions showed a qualitatively similar pattern (see Supplementary material online, *Figure S12*); however, mutation-induced differences were less pronounced and partially obscured by intercellular variability.

3.7 Effect on intracellular Ca^{2+} handling

CaM participates in the regulation of intracellular Ca^{2+} dynamics[8] which, in turn, may affect electrical stability.[30]

CaT amplitude was larger in mutant hiPSC-CMs than in CTR1 cells, however, because Ca^{2+} influx through I_{CaL} was also increased, the excitation-release (ER)-gain was unchanged (*Figure 6A-B*). In spite of the large difference in sarcolemmal Ca^{2+} influx, SR Ca^{2+} content was not affected by the mutation (*Figure 6C-E*). The kinetics of Ca^{2+} decay during the caffeine pulse (τ decay 1.88 ± 0.26 s vs. 1.93 ± 0.35 s, NS) and NCX 'conductance', were also similar between mutant and CTR1 cells (*Figure 6E*).

3.8 Pharmacological induction and rescue of the LQT phenotype

Failure of I_{CaL} CDI was pharmacologically induced by buffering subsarcolemmal Ca^{2+}. CTR1 and F142L hiPSC-CMs were incubated with the membrane permeable Ca^{2+} chelator BAPTA-AM (5 μM) for about 45 min. As shown in *Figure 7A*, at low pacing rates the repolarization was dramatically prolonged and unstable in both cell types; early after depolarizations (EADs) occurred and APD adaptation failed in most of cells at 2 Hz. Overall, removal of CDI by Ca^{2+} chelation abolished differences between CTR and mutant cells.

Rescue of LQTS phenotype was then tested by analysing the sensitivity of repolarization to verapamil and amlodipine in CBs by MEA recordings. Verapamil 50 nM shortened QTc significantly in mutant CBs, but had no effect on CTR1 ones (*Figure 7B*). Also amlodipine shortened QTc in mutant CBs (see Supplementary material online, *Figure S14*), but only at ≥900 nM, i.e. well above the EC_{50} for inhibition of contraction (10 nM).[31]

4. Discussion

The present work provides functional characterization of F142L-CaM in hiPSC-CMs derived from a symptomatic mutation carrier. The experimental strategy allowed to identify derangements, and relate them to clinical manifestations, in the context of native allelic balance and in the presence of all the factors, which might affect mutation expressivity. The mutation affected I_{CaL} time-course in a way consistent with delayed repolarization, the hallmark of the syndrome. I_{Ks} was unaffected and sustained I_{Na} was even smaller in mutant cells. Handling of intracellular Ca^{2+} was not directly altered, thus suggesting that the arrhythmogenic potential of this mutation may primarily reside in the electrophysiological

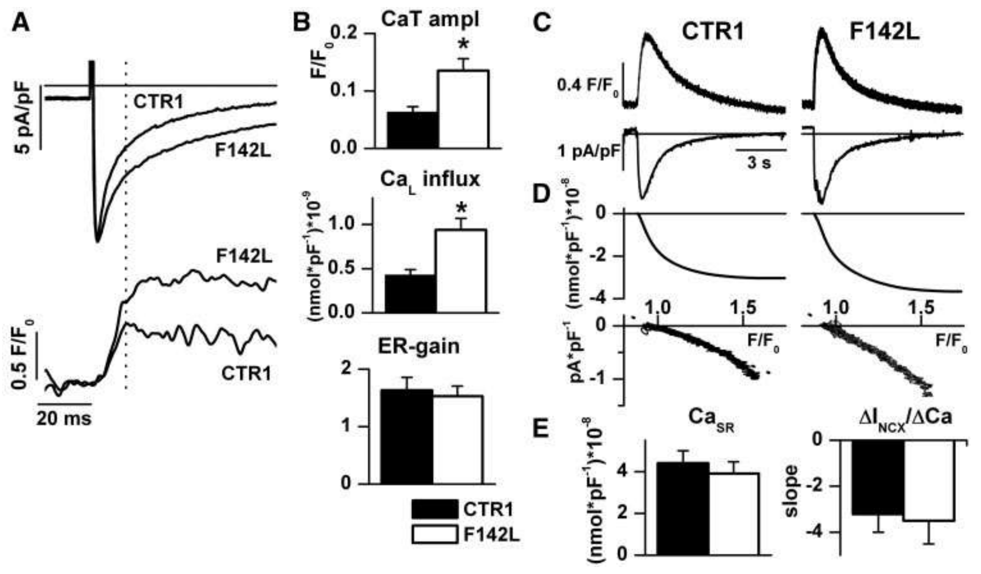

Figure 6 Intracellular Ca^{2+} handling and Ca^{2+} store stability are not significantly altered in V-clamped *CALM1*-F142L hiPSC-CMs. (*A*) Examples of I_{CaL} (top) and Ca^{2+} transients (CaT, bottom), evoked by voltage steps from -50 mV to 0 mV. Ca^{2+} influx (Ca_L) was measured from I_{CaL} up to the CaT peak (dotted line, see methods). (*B*) Statistics of CaT amplitude, Ca_L, and their ratio (ER-gain, see methods) in CTR1 ($N > 12$) and *CALM1*-F142L ($N > 9$; c1 and c2 pooled). (*C*) Caffeine-induced Ca^{2+} and current (I_{NCX}) transients (at - 50 mV). (*D*) Cumulative I_{NCX} integrals (top, used to estimate Ca_{SR}) and plots of I_{NCX} vs Ca^{2+} (bottom, slope used to estimate NCX 'conductance'). (*E*) Statistics for SR Ca^{2+} content (Ca_{SR}) and slope of I_{NCX}/Ca^{2+} relations in CTR1 ($N = 12$) and *CALM1*-F142L ($N = 13$, clones pooled) hiPSC-CMs. $^*P < 0.05$ vs. CTR1 (Student's *t*-test for unpaired measurements).

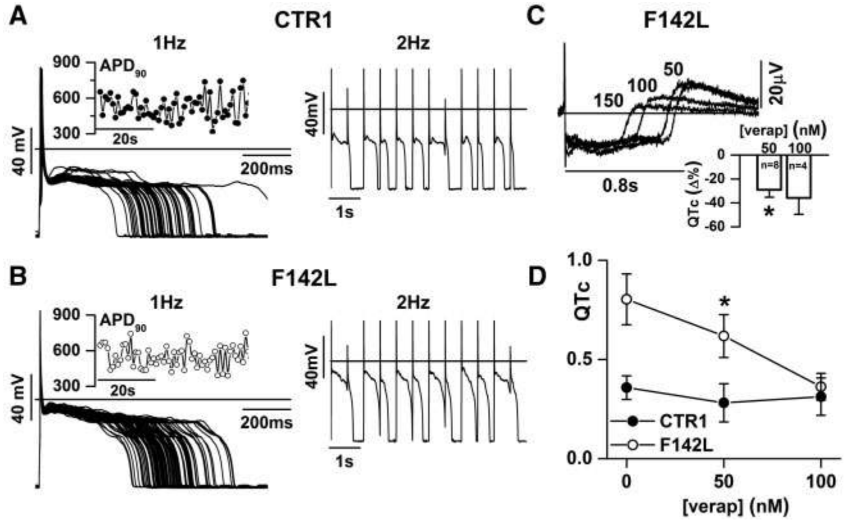

Figure 7 Intracellular Ca^{2+} buffering induces prolonged and unstable APDs in both *CALM1*-F142L and CTR1 hiPSC-CMs; verapamil shortens QTc in *CALM1*-F142L CBs only. Sequences of action potentials recorded at 1 Hz (left panels) or 2 Hz (right panels) in CTR1 (*A*) and *CALM1*-F142L (*B*) hiPSC-CMs pre-incubated with BAPTA-AM (5 μM). APD instability at 1 Hz is highlighted in insets; failing of APD to adapt at 2 Hz is shown on the right. Similar findings were observed in the majority of treated hiPSC-CMs (CTR1: 5 of 6, *CALM1*-F142L: 5 of 7). (*C*) Dose-dependent effects of verapamil on the field potential of a *CALM1*-F142L CB; tracings at various verapamil concentrations (numbers) are aligned on the time axis. Comparison of QTc shortening (Δ% from baseline) by verapamil at 50 and 100 nM respectively ($N \geq 4$, clones pooled). (*D*) Concentration-dependency of verapamil effect on QTc in CTR1 ($N \geq 5$) and *CALM1*-F142L CBs. $^*P < 0.05$ vs. baseline (Student's *t*-test for paired measurements).

abnormality. Even in the presence of the native allelic balance, F142L-CaM caused marked CDI abnormality to imply strong negative dominance of the mutant protein.

4.1 Target specificity and negative dominance

Beside $Ca_v1.2$ channels, also $K_v7.1$ channels, responsible for I_{Ks}, require functional CaM for their correct assembly and gating.[26] Heterologous F142L CaM mutation did not affect I_{Ks}, thus implying compensation by wild-type CaM.

Moreover, ryanodine receptor (RyR) channels and CaMKII are direct downstream CaM targets. As suggested by unchanged ER-gain and SR Ca^{2+} content (*Figure 6*), the mutation did not cause RyRs instability, which would be expected from loss of modulation by CaM.[8] The latter would also be expected to reduce CaMKII activity, which was nevertheless increased in mutant hiPSC-CMs.[10] On the other hand, CDI was strongly impaired by a mutation affecting only 1/6 of CaM alleles. Altogether, these findings imply that mutant CaM selectively interacts with $Ca_v1.2$ with strong negative dominance. Both selectivity and negative dominance may be interpreted by considering that modulation of $Ca_v1.2$ is mediated by a pre-bound apoCaM pool, formed independent of Ca^{2+}-induced activation.[32] Because of its increased affinity for $Ca_v1.2$ channels,[12] mutant apoCaM may dominate the pre-bound pool even in the presence of the unfavourable concentration ratio. CaM also binds RyR2 as apoCaM,[33] but heterologous expression studies suggest that high affinity Ca^{2+} binding to CaM C-lobe is essential for diastolic RyR2 stabilization.[34] Therefore, rather than reflecting irrelevance of F142L to RyR2 gating, normal RyRs function may result from compensation by wild-type CaM. The latter likely accounts also for lack of negative effects on CaMKII; the observed increase in CaMKII activity may simply be secondary to CDI impairment, i.e. reflect upregulation of residual wild-type CaM-CaMKII complexes by enhanced Ca^{2+} influx.

Phosphorylation by CaMKII may facilitate opening of RyRs[35] and $Ca_V1.2$ channels (Ca^{2+}-induced I_{CaL} facilitation, CDF),[8,22] and destabilize $Na_v1.5$ channel inactivation (I_{NaL} enhancement).[27] RyR facilitation, if present, was not large enough to be functionally relevant. I_{CaL} facilitation (CDF) was absent even in control hiPSC-CMs (see Supplementary material online, *Figure S8*). The present data provide the first comparative measurement of I_{CaL} CDF in human and rodent cells; nevertheless, the absence of the phenomenon in the former might also reflect hiPSC-CMs immaturity (e.g. lack of T-tubules).[36] Therefore, the present observation should not be considered conclusive for the absence of I_{CaL} facilitation in mature human cardiomyocytes.

Moreover, I_{NaL} was unaffected and I_{Naw} was even decreased in mutant hiPSC-CMs; thus, changes in these currents are unlikely to contribute to mutation-induced QT prolongation. CaMKII activity was found to be enhanced in F142L hiPSC-CMs, but still inadequate to induce the expected functional changes (RyR and I_{CaL} facilitation, I_{NaL} enhancement).

Defective CDI and prolonged repolarization might increase SR Ca^{2+} content, which was instead unaffected by the mutation (*Figure 6E*). While this might reflect adaptive upregulation of Ca^{2+} efflux, NCX 'conductance' was unchanged (*Figure 6D* and *E*) and, at least at transcriptional level, other Ca^{2+} transports were also unmodified (*Figure 1*). Therefore, we propose that, under the present conditions, the functional reserve of existing NCX, recruited by the larger Ca^{2+} transients, was adequate to balance the extra Ca^{2+} influx. This interpretation is consistent with previous work showing that Ca_{SR} is largely independent of sarcolemmal Ca^{2+} influx.[37]

4.2 Reproduction of clinical phenotype and pro-arrhythmic mechanism

The mutation carrier had prolonged QTc and a markedly non-linear QT/RR relationship, reflecting enhanced QT rate-dependency during tachycardia which, in turn, likely mirrors sympathetic activation. All these features were also present in mutant CBs (and hiPSC-CMs), in which QTc was prolonged, QT/RR (and APD/CL) relation was steeper and abnormally sensitive to isoproterenol. T wave alternans also occurred in the patient, possibly matching the higher incidence of repolarization irregularities in mutant hiPSC-CMs.

As most LQTS patients, the proband was bradycardic and this was reproduced *in vitro* by measuring spontaneous rate in CBs. Pacemaking can originate from pacemaker current (I_f) and/or from an intracellular Ca^{2+} clock.[38] I_f was comparable between control and mutant hiPSC-CMs and, if anything, we would expect increased Ca^{2+} influx to accelerate a Ca^{2+} clock. Therefore, by exclusion, we speculate that the low beating rate may be due to APD prolongation.

The present data point to inadequate CDI, and the resulting repolarization abnormality, as the primary cause of arrhythmias; indeed, failure of ER-gain to change in the presence of constant Ca_{SR} argues against primary SR instability.

Because of homeostatic regulation of intracellular Ca^{2+}, Ca_{SR} may be rather insensitive to changes in sarcolemmal Ca^{2+} influx[37]; therefore, failure of Ca_{SR} to increase significantly is not surprising. Nevertheless, Ca_{SR} was measured here under V-clamp, a condition not representative of in-vivo electrical activity; we cannot rule out that prolonged repolarization might change the Ca^{2+} influx/efflux balance at short cycle lengths. Limpitikul et al.[12] found *CALM-F142L* overexpression to increase Ca_{SR} in guinea-pig myocytes even at very low pacing rates (0.1 Hz) and suggested instead that SR instability might contribute to arrhythmogenesis. Notably, these experiments were performed at room temperature, at which myocytes were incompletely polarized and had extremely slow repolarization; such conditions are clearly inadequate to provide information on Ca^{2+} influx/efflux balance *in vivo*. On the other hand, Yin *et al.*[11] reported unchanged Ca_{SR} at 1 Hz in foetal murine myocytes. Whether or not the mutation may result in intracellular Ca^{2+} overload, the complete absence of afterpotentials in I-clamp recordings (even at high pacing rates), argues against SR instability as a mechanism contributing to arrhythmogenesis.

Repolarization was affected by two apparently antithetical abnormalities. In a large fraction of mutant isolated hiPSC-CMs, APD failed to shorten at high rates (3.3 Hz, *Figure 5D*), likely because of abnormal persistence of I_{CaL} availability (see Supplementary material online, *Figure S5*); this caused failure, or major distortion of subsequent excitations (*Figure 5C*). This defect was not observed in mutant CBs (*Figure 4*), possibly because delayed repolarization limited spontaneous beating rate. The second abnormality consisted of steeper QT/RR and APD/CL relations (*Figures 4 and 5*). Strong rate-dependency of repolarization is known to entail proarrhythmic risk.[39] APD prolongation on its own causes steeper APD rate-dependency,[29] but defective CDI might contribute to enhance sensitivity to β-adrenergic stimulation.

Simulation results confirmed that failure of APD adaptation to high pacing rates occurs in the presence of defective CDI of I_{CaL}. Separation of the CDI defect from the other abnormalities detected in F142L hiPSC-CMs suggest that the former alone is adequate to account for the phenotype (*Figure 5E*).

4.3 Clinical implications

The present results suggest that, in the case of *CALM1*-F142L, arrhythmogenesis may strictly result from the effect of excess I_{CaL} on repolarization. If this is the case, I_{CaL} blockade may be a logical therapeutic approach. The observation that verapamil reversed the mutation phenotype is consistent with this view. Thus, the identification of the arrhythmogenic mechanisms in the context of patient's genotype may enable the development of tailored therapeutic strategies.

Previous studies found QT-prolonging CaM mutations (e.g. D130G) to impair the ability of foetal murine cells to follow pacing even at slow rates.[11] This potentially arrhythmogenic feature was reversed by β-adrenergic stimulation, which was thus suggested as a therapeutic approach.[11] However, this abnormality was rare in the case of F142L-CaM[11] and, also in the present study, occurred at high rates only. On the other hand, enhanced sensitivity of repolarization to β-adrenergic stimulation might entail proarrhythmic risk.[39] Therefore, the present data do not support the view that β-adrenergic stimulation may represent a therapeutic approach, at least in the case of F142L-CaM.

4.4 Study limitations

A limitation in modelling arrhythmogenic syndromes with hiPSC-CM is represented by the degree of maturity of these cells, which often are more similar to foetal rather than adult CMs. Low I_{K1} expression is an important aspect of electrical immaturity, which we compensated by I_{K1} injection (DC technique). Other aspects of immaturity could not be corrected; consequently, extrapolation of our results should be done with caution.

Isogenic control hiPSC-CMs were not available for this study. To provide a comparison adequate to identify mutation-induced abnormalities, the opposite strategy of using multiple controls with maximal genetic heterogeneity was adopted. To this end, two iPSC-CMs control lines were generated from healthy donors with different gender and ethnicity, factors known to be involved in setting channels expression and AP duration. Except for different peak I_{CaL} magnitude, a complete consistency between CTR cell lines was found in I_{CaL} properties relevant to repolarization course, such as window current and CDI. This sharply contrasts with the obvious abnormality in the persistent I_{CaL} component observed in F142L hiPSC-CMs.

Generalization of the mechanisms identified in the present study to all cases of the F142L CaM mutation is limited by the fact that all mutant cell lines originated from a single mutation carrier.

Supplementary material

Supplementary material is available at *Cardiovascular Research* online.

Acknowledgements

The Authors are grateful to Dr Gabi Lederer (Cytogenetic Department, Technical University Munich) for providing karyotype data, and to Dr Vlasta Bari (Department of Biomedical Sciences for Health, University of Milan, Milan, Italy) for analysing 24 h Holter recordings.

Conflict of interest: none declared.

Funding

This work was supported by grants from the Italian Ministry of University and Research (MIUR-PRIN 2010BWY8E9_005 to G.M. and R.M.), Italian Ministry of Health (GR-2010-2305717 to C.L. and M.G.), the German Research Foundation, Research Unit 923 (Mo 2217/1-1 to M.A. and Si 1747/1-1 to S.D.), and the Academic Research Fund (F.A.R Milano-Bicocca to Z.A.).

References

1. Schwartz PJ, Ackerman MJ, George AL, Jr, Wilde AA. Impact of genetics on the clinical management of channelopathies. *J Am Coll Cardiol* 2013;**62**:169–180.
2. Crotti L, Johnson CN, Graf E, De Ferrari GM, Cuneo BF, Ovadia M, Papagiannis J, Feldkamp MD, Rathi SG, Kunic JD, Pedrazzini M, Wieland T, Lichtner P, Beckmann BM, Clark T, Shaffer C, Benson DW, Kaab S, Meitinger T, Strom TM, Chazin WJ, Schwartz PJ, George AL, Jr. Calmodulin mutations associated with recurrent cardiac arrest in infants. *Circulation* 2013;**127**:1009–1017.
3. Marsman RF, Barc J, Beekman L, Alders M, Dooijes D, van den WA, Ratbi I, Sefiani A, Bhuiyan ZA, Wilde AA, Bezzina CR. A mutation in CALM1 encoding calmodulin in familial idiopathic ventricular fibrillation in childhood and adolescence. *J Am Coll Cardiol* 2014;**63**:259–266.
4. Makita N, Yagihara N, Crotti L, Johnson CN, Beckmann BM, Roh MS, Shigemizu D, Lichtner P, Ishikawa T, Aiba T, Homfray T, Behr ER, Klug D, Denjoy I, Mastantuono E, Theisen D, Tsunoda T, Satake W, Toda T, Nakagawa H, Tsuji Y, Tsuchiya T, Yamamoto H, Miyamoto Y, Endo N, Kimura A, Ozaki K, Motomura H, Suda K, Tanaka T, Schwartz PJ, Meitinger T, Kaab S, Guicheney P, Shimizu W, Bhuiyan ZA, Watanabe H, Chazin WJ, George AL, Jr. Novel calmodulin mutations associated with congenital arrhythmia susceptibility. *Circ Cardiovasc Genet* 2014;**7**:466–474.
5. Reed GJ, Boczek NJ, Etheridge SP, Ackerman MJ. CALM3 mutation associated with long QT syndrome. *Heart Rhythm* 2015;**12**:419–422.
6. Chin D, Means AR. Calmodulin: a prototypical calcium sensor. *Trends Cell Biol* 2000;**10**:322–328.
7. Fischer R, Koller M, Flura M, Mathews S, Strehler-Page MA, Krebs J, Penniston JT, Carafoli E, Strehler EE. Multiple divergent mRNAs code for a single human calmodulin. *J Biol Chem* 1988;**263**:17055–17062.
8. Saucerman JJ, Bers DM. Calmodulin binding proteins provide domains of local Ca^{2+} signaling in cardiac myocytes. *J Mol Cell Cardiol* 2012;**52**:312–316.
9. Nyegaard M, Overgaard MT, Sondergaard MT, Vranas M, Behr ER, Hildebrandt LL, Lund J, Hedley PL, Camm AJ, Wettrell G, Fosdal I, Christiansen M, Borglum AD. Mutations in calmodulin cause ventricular tachycardia and sudden cardiac death. *Am J Hum Genet* 2012;**91**:703–712.
10. Hwang HS, Nitu FR, Yang Y, Walweel K, Pereira L, Johnson CN, Faggioni M, Chazin WJ, Laver D, George AL, Jr., Cornea RL, Bers DM, Knollmann BC. Divergent regulation of ryanodine receptor 2 calcium release channels by arrhythmogenic human calmodulin missense mutants. *Circ Res* 2014;**114**:1114–1124.
11. Yin G, Hassan F, Haroun AR, Murphy LL, Crotti L, Schwartz PJ, George AL, Satin J. Arrhythmogenic calmodulin mutations disrupt intracellular cardiomyocyte Ca^{2+} regulation by distinct mechanisms. *J Am Heart Assoc* 2014;**3**:e000996.
12. Limpitikul WB, Dick IE, Joshi-Mukherjee R, Overgaard MT, George AL, Jr., Yue DT. Calmodulin mutations associated with long QT syndrome prevent inactivation of cardiac L-type Ca(2+) currents and promote proarrhythmic behavior in ventricular myocytes. *J Mol Cell Cardiol* 2014;**74**:115–124.
13. Gramlich M, Pane LS, Zhou Q, Chen Z, Murgia M, Schotterl S, Goedel A, Metzger K, Brade T, Parrotta E, Schaller M, Gerull B, Thierfelder L, Aartsma-Rus A, Labeit S, Atherton JJ, McGaughran J, Harvey RP, Sinnecker D, Mann M, Laugwitz KL, Gawaz MP, Moretti A. Antisense-mediated exon skipping: a therapeutic strategy for titin-based dilated cardiomyopathy. *EMBO Mol Med* 2015;**7**:562–576.
14. Erickson JR, Patel R, Ferguson A, Bossuyt J, Bers DM. Fluorescence resonance energy transfer-based sensor Camui provides new insight into mechanisms of calcium/calmodulin-dependent protein kinase II activation in intact cardiomyocytes. *Circ Res* 2011;**109**:729–738.
15. Liang P, Lan F, Lee AS, Gong T, Sanchez-Freire V, Wang Y, Diecke S, Sallam K, Knowles JW, Wang PJ, Nguyen PK, Bers DM, Robbins RC, Wu JC. Drug screening using a library of human induced pluripotent stem cell-derived cardiomyocytes reveals disease-specific patterns of cardiotoxicity. *Circulation* 2013;**127**:1677–1691.
16. Doss MX, Di Diego JM, Goodrow RJ, Wu Y, Cordeiro JM, Nesterenko VV, Barajas-Martinez H, Hu D, Urrutia J, Desai M, Treat JA, Sachinidis A, Antzelevitch C. Maximum diastolic potential of human induced pluripotent stem cell-derived cardiomyocytes depends critically on I(Kr). *PLoS One* 2012;**7**:e40288.
17. O'Hara T, Virag L, Varro A, Rudy Y. Simulation of the undiseased human cardiac ventricular action potential: model formulation and experimental validation. *PLoS Comput Biol* 2011;**7**:e1002061.
18. Meijer van Putten RM, Mengarelli I, Guan K, Zegers JG, Van Ginneken AC, Verkerk AO, Wilders R. Ion channelopathies in human induced pluripotent stem cell derived cardiomyocytes: a dynamic clamp study with virtual IK1. *Front Physiol* 2015;**6**:7.
19. Bartolucci C, Altomare C, Bennati M, Furini S, Zaza A, Severi S. Combined action potential- and dynamic-clamp for accurate computational modelling of the cardiac IKr current. *J Mol Cell Cardiol* 2015;**79**:187–194.
20. Rocchetti M, Alemanni M, Mostacciuolo G, Barassi P, Altomare C, Chisci R, Micheletti R, Ferrari P, Zaza A. Modulation of sarcoplasmic reticulum function by

PST2744 [istaroxime; (E,Z)-3-((2-aminoethoxy)imino) androstane-6,17-dione hydrochloride)] in a pressure-overload heart failure model. *J Pharmacol Exp Ther* 2008;**326**:957–965.

21. Paci M, Hyttinen J, Rodriguez B, Severi S. Human induced pluripotent stem cell-derived versus adult cardiomyocytes: an in silico electrophysiological study on effects of ionic current block. *Br J Pharmacol* 2015;**172**:5147–5160.
22. Guo J, Duff HJ. Calmodulin kinase II accelerates L-type Ca2+ current recovery from inactivation and compensates for the direct inhibitory effect of [Ca2+]i in rat ventricular myocytes. *J Physiol* 2006;**574**:509–518.
23. Maier LS, Bers DM. Role of Ca2+/calmodulin-dependent protein kinase (CaMK) in excitation-contraction coupling in the heart. *Cardiovasc Res* 2007;**73**:631–640.
24. Bers DM, Morotti S. Ca(2+) current facilitation is CaMKII-dependent and has arrhythmogenic consequences. *Front Pharmacol* 2014;**5**:144.
25. Schwartz PJ, Crotti L, Insolia R. Long-QT syndrome: from genetics to management. *Circ Arrhythm Electrophysiol* 2012;**5**:868–877.
26. Shamgar L, Ma L, Schmitt N, Haitin Y, Peretz A, Wiener R, Hirsch J, Pongs O, Attali B. Calmodulin is essential for cardiac IKS channel gating and assembly: impaired function in long-QT mutations. *Circ Res* 2006;**98**:1055–1063.
27. Wagner S, Dybkova N, Rasenack EC, Jacobshagen C, Fabritz L, Kirchhof P, Maier SK, Zhang T, Hasenfuss G, Brown JH, Bers DM, Maier LS. Ca^{2+}/calmodulin-dependent protein kinase II regulates cardiac Na^{+} channels. *J Clin Invest* 2006;**116**:3127–3138.
28. Rocchetti M, Sala L, Rizzetto R, Staszewsky LI, Alemanni M, Zambelli V, Russo I, Barile L, Cornaghi L, Altomare C, Ronchi C, Mostacciuolo G, Lucchetti J, Gobbi M, Latini R, Zaza A. Ranolazine prevents INaL enhancement and blunts myocardial remodelling in a model of pulmonary hypertension. *Cardiovasc Res* 2014;**104**:37–48.
29. Zaza A. Control of the cardiac action potential: the role of repolarization dynamics. *J Mol Cell Cardiol* 2010;**48**:106–111.
30. Zaza A, Rocchetti M. Calcium store stability as an antiarrhythmic endpoint. *Curr Pharm Des* 2015;**21**:1053–1061.
31. Jeppesen P, Bruun J, Nielsen-Kudsk F. Amlodipine dynamic effects and myocardial pharmacokinetics in the isolated and perfused guinea-pig heart. *Pharmacol Toxicol* 1998;**82**:250–256.
32. Erickson MG, Liang H, Mori MX, Yue DT. FRET two-hybrid mapping reveals function and location of L-type Ca^{2+} channel CaM preassociation. *Neuron* 2003; **39**:97–107.
33. Yamaguchi N, Xu L, Pasek DA, Evans KE, Meissner G. Molecular basis of calmodulin binding to cardiac muscle Ca(2+) release channel (ryanodine receptor). *J Biol Chem* 2003;**278**:23480–23486.
34. Sondergaard MT, Tian X, Liu Y, Wang R, Chazin WJ, Chen SR, Overgaard MT. Arrhythmogenic calmodulin mutations affect the activation and termination of cardiac ryanodine receptor-mediated Ca^{2+} release. *J Biol Chem* 2015;**290**:26151–26162.
35. Anderson ME. CaMKII and a failing strategy for growth in heart. *J Clin Invest* 2009;**119**:1082–1085.
36. Gherghiceanu M, Barad L, Novak A, Reiter I, Itskovitz-Eldor J, Binah O, Popescu LM. Cardiomyocytes derived from human embryonic and induced pluripotent stem cells: comparative ultrastructure. *J Cell Mol Med* 2011;**15**:2539–2551.
37. Trafford AW, Diaz ME, Eisner DA. Coordinated control of cell Ca(2+) loading and triggered release from the sarcoplasmic reticulum underlies the rapid inotropic response to increased L-type Ca(2+) current. *Circ Res* 2001;**88**:195–201.
38. Mangoni ME, Nargeot J. Genesis and regulation of the heart automaticity. *Physiol Rev* 2008;**88**:919–982.
39. Gilmour RF, Jr. A novel approach to identifying antiarrhythmic drug targets. *Drug Discov Today* 2003;**8**:162–167.

Basic Res Cardiol (2017) 112:12
DOI 10.1007/s00395-017-0602-9

ORIGINAL CONTRIBUTION

Late sodium current and intracellular ionic homeostasis in acute ischemia

Carlotta Ronchi[1] · **Eleonora Torre**[1] · **Riccardo Rizzetto**[1] · **Joyce Bernardi**[1] · **Marcella Rocchetti**[1] · **Antonio Zaza**[1]

Received: 5 July 2016 / Accepted: 3 January 2017 / Published online: 18 January 2017

Abstract Blockade of the late Na^+ current (I_{NaL}) protects from ischemia/reperfusion damage; nevertheless, information on changes in I_{NaL} during acute ischemia and their effect on intracellular milieu is missing. I_{NaL}, cytosolic Na^+ and Ca^{2+} activities (Na_{cyt}, Ca_{cyt}) were measured in isolated rat ventricular myocytes during 7 min of simulated ischemia (ISC); in all the conditions tested, effects consistently exerted by ranolazine (RAN) and tetrodotoxin (TTX) were interpreted as due to I_{NaL} blockade. The results indicate that I_{NaL} was enhanced during ISC in spite of changes in action potential (AP) contour; I_{NaL} significantly contributed to Na_{cyt} rise, but only marginally to Ca_{cyt} rise. The impact of I_{NaL} on Ca_{cyt} was markedly enhanced by blockade of the sarcolemmal(s) Na^+/Ca^{2+} exchanger (NCX) and was due to the presence of (Na^+-sensitive) Ca^{2+} efflux through mitochondrial NCX (mNCX). sNCX blockade increased Ca_{cyt} and decreased Na_{cyt}, thus indicating that, throughout ISC, sNCX operated in the forward mode, in spite of the substantial Na_{cyt} increment. Thus, a robust Ca^{2+} source, other than sNCX and including mitochondria, contributed to Ca_{cyt} during ISC. Most, but not all, of RAN effects were shared by TTX. (1) The paradigm that attributes Ca_{cyt} accumulation during acute ischemia to decrease/reversal of sNCX transport may not be of general applicability; (2) I_{NaL} is enhanced during ISC, when the effect of Na_{cyt} on mitochondrial Ca^{2+} transport may substantially contribute to I_{NaL} impact on Ca_{cyt}; (3) RAN may act mostly, but not exclusively, through I_{NaL} blockade during ISC.

Keywords Acute ischemia · Late sodium current · Ranolazine · Na^+ homeostasis · Ca^{2+} homeostasis · Mitochondria

Introduction

Acute myocardial ischemia results in a characteristic pattern of metabolic and intracellular ion changes, ultimately leading to cytosolic Ca^{2+} (Ca_{cyt}) accumulation [5] and the resulting functional and structural derangements. Enhanced Na^+ influx, exceeding the functional reserve of the Na^+/K^+ pump, is widely considered as the "primum movens" of this process, being coupled to Ca_{cyt} homeostasis through changes in the equilibrium potential of the sarcolemmal Na^+/Ca^{2+} exchanger (sNCX) (coupled exchanger theory) [9, 23, 28, 31].

Several mechanisms may account for enhanced a Na^+ influx during acute ischemia. While it is widely accepted that the Na^+/H^+ exchanger (NHE), driven by intracellular acidosis, may support large Na^+ influx upon reperfusion [19, 24, 47], there is disagreement about its role during ischemia [3, 32, 47]. Several studies show that blockade of a persistent component of Na^+ current (I_{NaL}), prevents Ca^{2+} overload and reduces injury following reperfusion [1, 7, 16, 45]. This suggests that I_{NaL} enhancement may contribute to increased Na^+ influx during the preceding ischemia. Exposure to ischemia components (i.e., H_2O_2, hypoxia and ischemic metabolites) has indeed been shown to enhance I_{NaL} in standard V-clamp experiments [26, 40, 43, 46]. On the other hand, membrane

---

Electronic supplementary material The online version of this article (doi:10.1007/s00395-017-0602-9) contains supplementary material, which is available to authorized users.

✉ Antonio Zaza
antonio.zaza@unimib.it

[1] Department of Biotechnologies and Biosciences, University Milano-Bicocca, Piazza della Scienza 2, 20126 Milan, Italy

depolarization and shortening of action potential duration (APD), both correlates of acute ischemia, may reduce overall Na^+ current availability and time for I_{NaL}-mediated Na^+ influx, respectively. Therefore, whether I_{NaL} is actually enhanced during acute ischemia and contributes to cytosolic Na^+/Ca^{2+} accumulation remains to be established. The present study aims to directly address these questions by measuring I_{NaL} and cytosolic ionic activities (Na_{cyt} and Ca_{cyt}) in isolated ventricular myocytes exposed to a simulated ischemia protocol.

The results obtained indicate that I_{NaL} was enhanced during simulated ischemia, in spite of the attending action potential (AP) changes, and significantly contributed to Na_{cyt} accumulation. However, the relationship between Na_{cyt} and Ca_{cyt} was more complex than predicted by the coupled exchanger theory, suggesting instead a role of ischemia-induced redistribution of Ca^{2+} between intracellular compartments, with mitochondria contributing as a Na_{cyt}-sensitive Ca^{2+} store.

Materials and methods

Cell isolation

Ventricular cardiomyocytes from male adult Sprague–Dawley rats (150–175 g) were isolated using a retrograde coronary perfusion method previously published with minor modifications [34]. Measurements were performed only in quiescent, rod-shaped, myocytes with clear striations. All experiment were approved and conducted accordingly to the guidelines stipulated by the Animal Care committee of University of Milano-Bicocca. The manuscript does not contain human data.

Simulated ischemia protocol

Cardiomyocytes were placed into a recording chamber and superfused at 36.5 °C with Tyrode's solution containing (mM): NaCl 154, KCl 4, $CaCl_2$ 2, $MgCl_2$ 1, HEPES 5, Glucose 5.5, adjusted to pH 7.3. Cells were paced at 1 Hz, either through the patch pipette or by field stimulation, throughout the protocol.

Ischemia was simulated by superfusing myocytes with a modified Tyrode's solution (ischemia mimic solution, ISC) containing (mM): NaCl 134, Na-lactate 20, KCl 8, $CaCl_2$ 2, $MgCl_2$ 1, HEPES 5, sucrose 37, adjusted to pH 6.8. Its composition reflects the major changes in the ischemic environment, as previously described by others [8, 10, 25, 30, 49].

ISC protocol has been performed here in normoxic condition, according to previous studies on ischemia [25] proving that the contribution of hypoxia to changes in cardiomyocyte contractility is negligible; nevertheless, its absence should be considered in the interpretation of results (see "Discussion").

The experimental protocol included pre-ISC stabilization in normal Tyrode's solution (about 2 min) followed by ISC superfusion for 7 min (Fig. S1). This ISC duration was selected in preliminary experiments as the maximal tolerated by the majority of cardiomyocytes; ISC wash-out (reperfusion) was almost invariably followed by contracture and death. In the following text, protocol phases are referred to as PRE (pre-ISC); 0.5ISC (0.5 min of ISC); 3ISC (3 min of ISC); 7ISC (7 min of ISC).

Cell shortening

Cardiomyocytes were field stimulated and the single-cell shortening was measured by video-edge detection system (Crescent electronics). The difference between maximal diastolic and systolic cell lengths was expressed as twitch amplitude, which was normalized within each cell to the value recorded in PRE conditions.

Electrophysiology

Myocytes were patch-clamped with borosilicate glass pipettes containing (mM): K^+-aspartate 110, KCl 23, $MgCl_2$ 3, HEPES KOH 5, EGTA KOH 0.5, GTP Na^+-salt 0.4, ATP Na^+-salt 5, creatine phosphate Na^+-salt 5, $CaCl_2$ 0.2 (calculated free-$Ca^{2+} = 10^{-7}$ M), adjusted to pH 7.2. Series resistance was <5 MΩ and was compensated to 80% of its value.

Action potentials (AP) were recorded (*I*-clamp with $I = 0$ pA) throughout the protocol. AP waveforms recorded in PRE condition and at 7ISC, respectively, were used as templates in AP-clamp experiments.

I_{NaL} was measured at PRE and 7ISC in AP-clamp mode as the current sensitive to 1 μM TTX [40]. To test whether ISC-induced changes in AP affected I_{NaL} magnitude during ISC, AP-clamp was applied with two modalities: (1) the AP templates recorded at PRE and 7ISC, which included ISC-induced changes, were applied during the corresponding phases of the protocol; (2) the AP template recorded at PRE, was applied at both PRE and 7ISC, thus disregarding ISC-induced changes. Differences between I_{NaL} recorded with the two AP-clamp modalities reflect the impact of ISC-induced membrane potential changes to I_{NaL}.

I_{NaL} magnitude during APs was quantified by integrating inward TTX-sensitive current from the beginning of repolarization to 90% of repolarization and dividing the result for the integration interval. This measurement, abbreviated in the following text and figures as "I_{NaL}", reflects mean Na^+ influx rate during repolarization.

Currents were normalized to cell capacitance and expressed as current density (pA/pF).

Measurement of intracellular ionic activities

Na_{cyt} and Ca_{cyt} were measured in intact, field-stimulated (1 Hz) cardiomyocytes, loaded with Asante Natrium Green-2 (ANG-2) for Na^+ and FLUO4-AM for Ca^{2+} measurements, respectively. Cardiomyocytes were incubated with the membrane-permeant form of the dyes for 30 min, and then washed for 15 min. ANG-2 and FLUO4-AM emissions were collected through a 535 nm band pass filter, converted to voltage, low-pass filtered (200 Hz) and digitized at 2 kHz after further low-pass digital filtering (FFT, 100 Hz) and subtraction of background luminescence [2].

For Na^+ measurement, fluorescence recorded during ISC (F) was normalized to that recorded during the PRE phase (F_0) and expressed as F/F_0. Considering that, Na_{cyt} changes were well within the range of linear dye response (Supplemental Figure S5), the uncalibrated Na^+ signal was considered adequate. Because dye response is slow relative to membrane potential changes, the Na^+ signal reflects an integrated value of Na_{cyt} during the whole electrical cycle.

Ca^{2+} fluorescence signal was calibrated by previously described methods [34], described in the Online Resource along with the potential bias introduced by intrinsic pH sensitivity of the dye. Since dye response is fast enough, the Ca^{2+} signal was evaluated as diastolic Ca^{2+} (Ca_D) and Ca^{2+} transient amplitude (Ca_T, i.e., difference between systolic Ca^{2+} and Ca_D). The sarcoplasmic reticulum (SR) Ca^{2+} content (Ca_{SR}) was estimated at 7ISC in separate subsets of cardiomyocytes, by applying an electronically timed 10 mM caffeine pulse. The caffeine solution was Ca^{2+} and Na^+ free, to prevent Ca^{2+} efflux through the sNCX. SR Ca^2 fractional release (Ca_{FR}) was obtained as the ratio between Ca_T at 7ISC and Ca_{SR}.

Pharmacological interventions

The contribution of different mechanisms to Na_{cyt} and Ca_{cyt} dynamics during ISC was evaluated by specific pharmacological interventions.

I_{NaL} contribution was tested by blocking the current with either ranolazine (RAN, 10 μM) or tetrodotoxin (TTX, 1 μM). Although at this concentration TTX can be safely considered to selectively block I_{NaL} [40], ancillary effects might be present for RAN. Therefore, whereas effects equally exerted by the two agents were considered to reflect I_{NaL} contribution, those peculiar of RAN may possibly result from ancillary effects of the drug. RAN and TTX were applied at the beginning of the PRE phase.

Contribution of sNCX and mNCX were tested by using the selective blockers SEA0400 (SEA, 1 μM) and CGP37157 (CGP, 1 μM), respectively. Cariporide (CAR, 1 μM) and ouabain (OUAB, 1 mM) were used to inhibit the NHE and the Na^+/K^+ pump, respectively. RU360 (RU, 10 μM) was used to block the mitochondrial Ca^{2+} uniporter (MCU) [29], the main path of Ca^{2+} entry into mitochondria [21]. These agents were also added to the ISC solution; DMSO concentration was balanced in all the solutions.

Statistical analysis

The time courses of Na_{cyt} and Ca_{cyt} (Ca_T and Ca_D) during the protocol, shown in figures, were obtained by averaging records from N cells and are presented as mean ± SE. Differences in twitch amplitude, Na_{cyt} and Ca_{cyt} were statistically evaluated at 0.5ISC, 3ISC, 7ISC (Supplemental figure S1). In the case of Na_{cyt}, peak value and the rate of rise (dNa^+/dt, by linear fitting of the rising phase) were also evaluated.

Differences between means were tested by paired T test or ANOVA as appropriate (Bonferroni's correction in post hoc comparisons). Statistical significance was defined as $p < 0.05$ (NS, not significant). Sample size is reported in each figure legend.

Results

Cell shortening and electrical activity

Twitch amplitude markedly decreased during early ISC (0.5ISC), to slowly recover to a stable level after 3 min (Fig. 1a). Twitch amplitude achieved a minimum at 0.5ISC ($-86.9 \pm 1.8\%$ of PRE; $p < 0.05$), recovered at 3ISC to $-12.4 \pm 18.5\%$ of PRE, without further changes at 7ISC ($-10.8 \pm 17.3\%$ of PRE) (Fig. 1b).

AP were elicited throughout ISC exposure (Fig. 1b), even when mechanical activity was almost absent. ISC partially depolarized diastolic potential (E_{diast}) and reduced dV/dt_{max} of phase 0 (Fig. 1c). APD at 90%, repolarization (APD90) prolonged up to 0.5ISC and then shortened (Fig. 1c). RAN treatment did not measurably affect AP response to ISC (Supplemental Figure S2).

Late Na^+ current

A small I_{NaL} was present during repolarization even in PRE conditions; this component was insensitive to blockade by RAN (Fig. 2). When the 7ISC AP template was applied at 7 min of ISC, I_{NaL} was increased by 77% ($p < 0.05$ vs PRE, Fig. 2b), a change completely prevented by RAN (Fig. 2b). When the PRE AP template was applied at 7ISC, I_{NaL} increment observed was, if anything, larger than seen

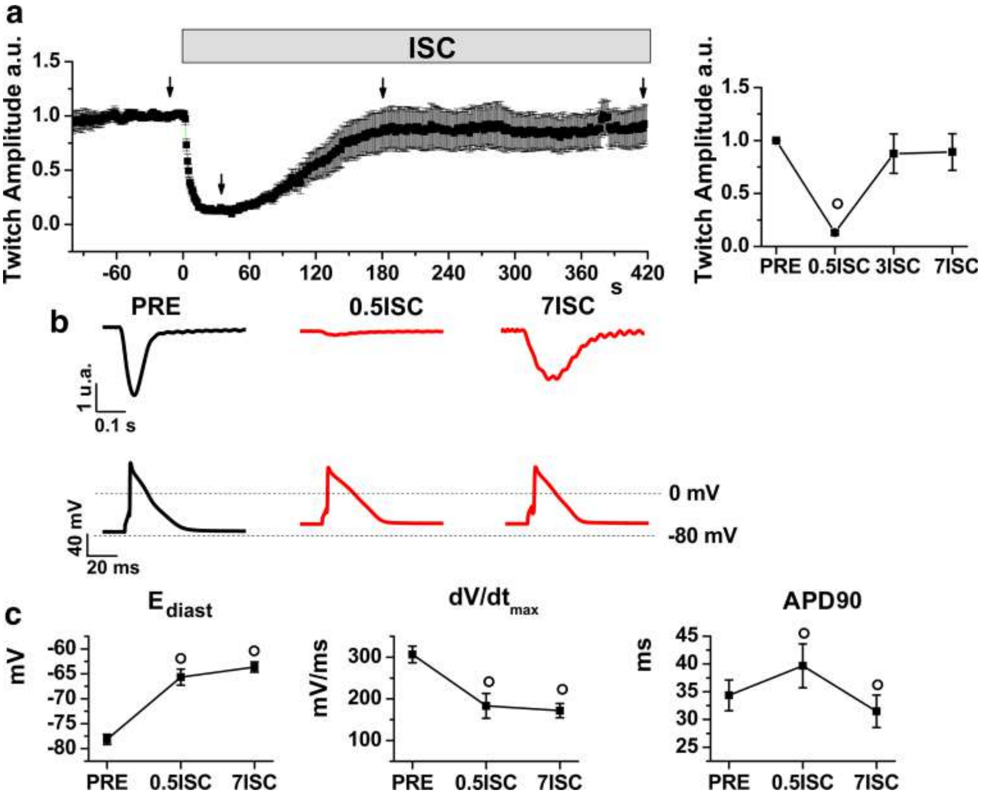

Fig. 1 Cell shortening and electrical activity during ISC. **a** Average traces ± SE of contraction amplitude (*left*) and statistics at discrete time points during the protocol (*arrows*). **b** Representative traces of contraction (*top*) and action potentials (*bottom*) at discrete time points (*arrows* in **a**). **c** Statistics for diastolic membrane potential (E_{diast}), maximum depolarization rate (dV/dt_{max}) and action potential duration at 90% repolarization (APD90). CTRL $N = 8$. °$p < 0.05$ vs PRE

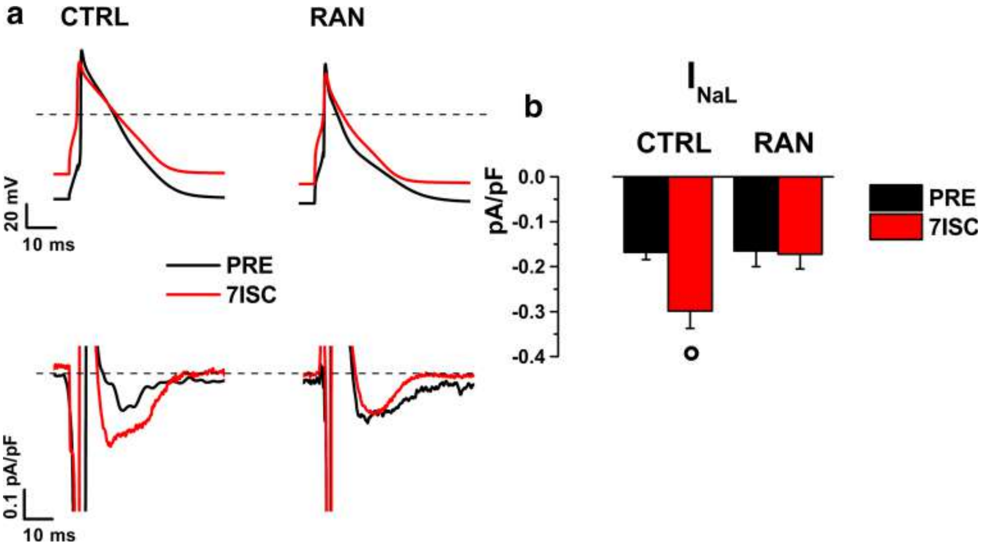

Fig. 2 Late Na^+ current (I_{NaL}) during ISC. **a** Representative action potentials templates (*top*) and the respective TTX-sensitive currents (*bottom*) at PRE (*black line*) and 7ISC (*red line*) time points in CTRL and RAN groups. **b** Statistics for I_{NaL} at PRE and 7ISC. $N > 6$ for both groups. °$p < 0.05$ vs PRE

with the previous protocol (88%, $p < 0.05$ vs PRE, Supplemental Figure S3). Thus, I_{NaL} may significantly increase during ISC in spite of the attending membrane potential changes, which, as expected, reduced overall I_{Na} availability (reduced dV/dt_{max}, see above).

Cytosolic Na^+

Changes in Na_{cyt} during ISC were assessed in intact, field-stimulated (1 Hz) cardiomyocytes in the absence (CTRL) and presence of I_{NaL} blockade by either RAN or TTX. After an initial dip, Na_{cyt} increased during ISC, reaching a peak at about 1–2 min, and then slowly declined (Fig. 3a). RAN and TTX significantly reduced peak Na_{cyt} (Fig. 3a) and the rate of Na_{cyt} increment (Fig. 3b); the effect was similar between the two agents. This suggests that I_{NaL} enhancement significantly contributed to, but was not the only factor, in Na_{cyt} accumulation during ISC. When both I_{NaL} and NHE were blocked simultaneously (CAR + TTX), ISC failed to induce Na_{cyt} accumulation

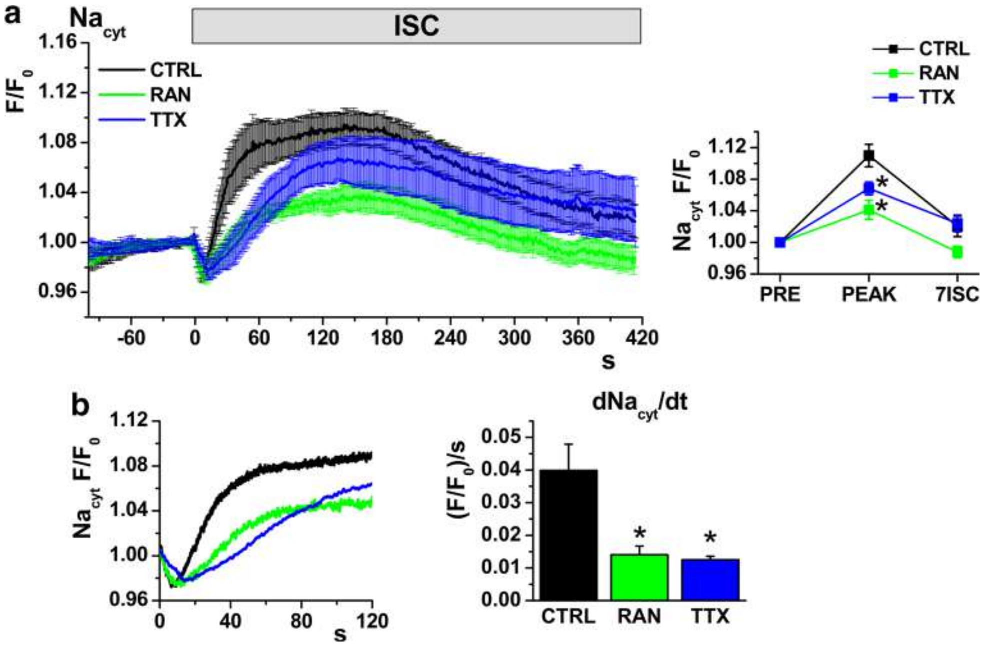

Fig. 3 Effect of I_{NaL} blockade (RAN, TTX) on cytosolic Na^+ (Na_{cyt}) during ISC. **a** Average traces ± SE of Na_{cyt} during the ISC protocol in CTRL, RAN and TTX treatment groups; statistics of Na_{cyt} changes (normalized to values at PRE) at peak Na_{cyt} and at 7ISC time points. **b** Average Na_{cyt} traces (as in a) during the early ISC phase to illustrate differences in Na_{cyt} accumulation rate; statistics for Na_{cyt} accumulation rate (dNa_{cyt}/dt). CTRL $N = 14$; RAN $N = 9$; TTX $N = 12$. $^*p < 0.05$ vs CTRL

(Supplemental Figure S4), thus pointing to NHE as the other Na^+ influx route [35].

To test whether the Na^+/K^+ pump remained functional during ISC and contributed to the late Na_{cyt} decline, cardiomyocytes were exposed to ISC in the presence of ouabain (OUAB). Under this condition, Na_{cyt} monotonically increased throughout ISC superfusion (Supplement Figure S5), indicating that in the present settings, the Na^+/K^+ pump was active and contributed to limit Na_{cyt} accumulation.

Cytosolic Ca^{2+}

Changes in Ca_{cyt} during ISC were assessed in intact, field-stimulated (1 Hz) cardiomyocytes (Fig. 4). Both Ca_D and Ca_T increased during ISC; at variance with Na_{cyt}, the increment was not preceded by a dip. Ca_D monotonically increased to achieve a more or less stable level at 3 min (Fig. 4a). Ca_T increment followed a sigmoidal time course, thus lagging behind Ca_D; it achieved a peak at about 3 min and then slowly declined (Fig. 4a). RAN slightly, but significantly, decreased Ca_D and visibly minimized its variability across cells, an effect not shared with TTX (Fig. 4a). The same was true for Ca_T even if, probably because of its larger variability, RAN effect on this parameter did not achieve significance (Fig. 4a). Both RAN and TTX tended to decrease Ca_{SR}, but when analyzed separately for each I_{NaL} blocker their effect did not achieve statistical significance (Fig. 4b). However, when the data from RAN and TTX groups were pooled, I_{NaL} blockade significantly reduced Ca_{SR} at 7ISC (80.7 ± 8.5 vs 60.8 ± 4.7 µM; $p < 0.05$, Fig. 4b). Ca_{FR} was not affected by I_{NaL} blockade (Fig. 4b).

These observations are consistent with the common notion that Ca_{cyt} increases during acute ischemia; however, neither its timing with respect to Na_{cyt}, nor its unexpected insensitivity to I_{NaL} blockade, were consistent with its dependency on enhanced Na^+ influx. The (small) effect of RAN on Ca_D, not shared by TTX, might reflect an agent-specific ancillary action.

The unexpected lack of Ca_{cyt} response to reduced Na^+ influx, led us to question sNCX role in mediating Ca_{cyt} accumulation during ISC. To address this point, Ca_{cyt} measurements were repeated in the presence of sNCX blockade.

Role of the sarcolemmal Na^+/Ca^{2+} exchanger

To assess the role of sNCX during ISC, its specific inhibitor SEA [42] was also added to the ISC solution (ISC + SEA, Fig. 5).

In the presence of SEA, ISC-induced Na_{cyt} accumulation was reduced and Ca_{cyt} accumulation (Ca_D, Ca_T, Ca_{SR}) was markedly enhanced (Supplemental Figure S6). The direction of the reciprocal changes in Na_{cyt} and Ca_{cyt} unequivocally indicates that, during ISC, sNCX still operated in its forward mode, thus supporting Ca^{2+} efflux, rather than influx. Notably, forward sNCX operation persisted in spite of the attending increase in Na_{cyt}; moreover, the Ca_{cyt} increment induced by ISC in the presence of sNCX blockade (SEA group) was twice as large as that observed during SEA alone (Supplemental Figure S7). These findings indicate that large, sNCX-independent, Ca^{2+} sources contribute to Ca_{cyt} build up during ISC.

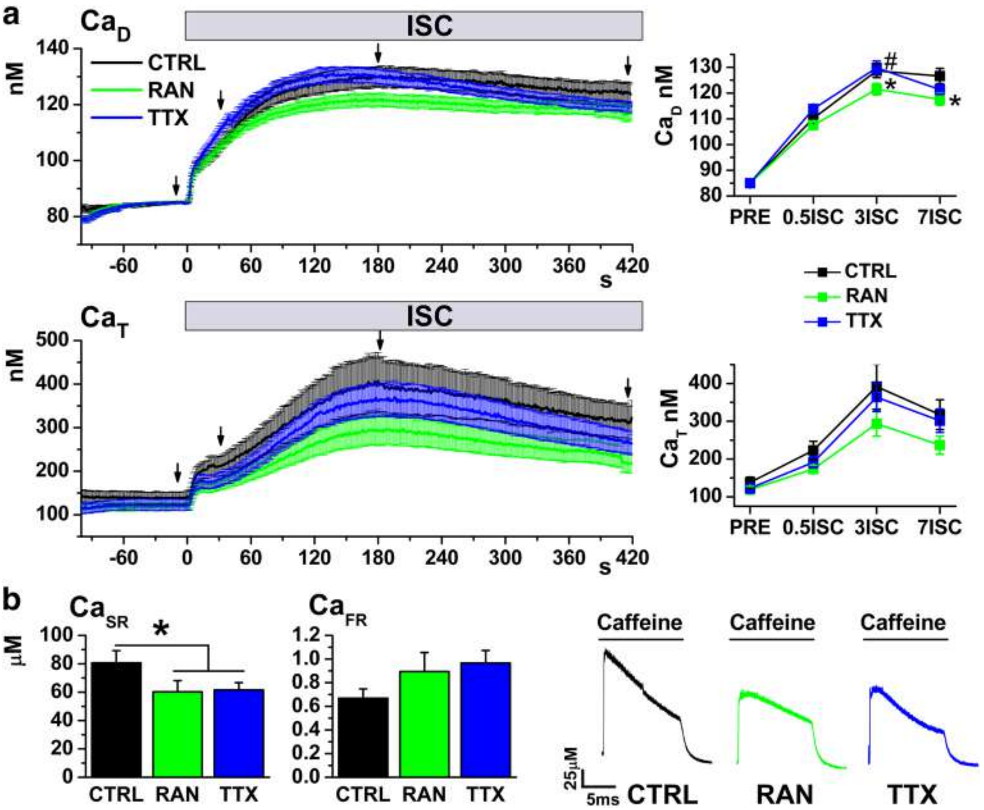

Fig. 4 Effect of I_{NaL} blockade (RAN, TTX) on cytosolic Ca^{2+} (Ca_{cyt}) during ISC. **a** Average traces ± SE of diastolic Ca^{2+} (Ca_D) and Ca^{2+} transient amplitude (Ca_T) during the ISC protocol in CTRL, RAN and TTX treatment groups; statistics of Ca_{cyt} at discrete time points (*arrows*) during the protocol (CTRL $N = 22$; RAN $N = 19$; TTX $N = 19$). **b** Statistics for SR Ca^{2+} content (Ca_{SR}) and SR Ca^{2+} fractional release (Ca_{FR}) at protocol end (CTRL $N = 19$; RAN $N = 13$; TTX $N = 10$); representative Ca^{2+} transient triggered by caffeine in each group. $*p < 0.05$ vs CTRL; $^{\#}p < 0.05$ vs RAN

Notably, during ISC + SEA, both RAN (+RAN) and TTX (+TTX) significantly reduced Ca_{cyt} accumulation (Fig. 5a), with their effect being substantially larger than during ISC alone (Fig. 4). This suggests the contribution to Ca_{cyt} accumulation of a Na^+-sensitive Ca^{2+} source, whose role was unveiled by sNCX blockade.

Consistent with the increase in overall cell Ca^{2+} content expected from sNCX blockade, Ca_{SR} at 7ISC was higher in ISC + SEA (SEA) than in ISC alone (CTRL) (116.7 ± 11.6 vs 80.7 ± 8.5 µM; $p < 0.05$; Supplemental Figure S6a). RAN slightly but significantly reduced Ca_{SR} even in the presence of SEA (Fig. 5b), thus suggesting its ability to modulate Ca_{cyt} independently of sNCX. This effect did not achieve significance with TTX, which, in this respect, was less efficient than RAN. Ca_{FR} was unchanged by either RAN or TTX (Fig. 5b) thus arguing against modulation of ryanodine receptors (RyRs) as a major player in the effects exerted by the two agents.

The significant effect of I_{NaL} blockade on Ca_{cyt} in Fig. 5 suggests that, at least under sNCX inhibition, a Na_{cyt}-sensitive intracellular compartment may contribute to its accumulation during ISC. Mitochondria are an intracellular Ca^{2+} compartment, potentially affected by ISC and endowed of Na_{cyt}-sensitive Ca^{2+} transport. The latter is represented by mNCX, which may either uptake or release Ca^{2+} from mitochondria depending on the electrochemical gradient for the transport. To test this hypothesis, the experiments were repeated in the presence of mNCX blockade.

Role of the mitochondrial Na^+/Ca^{2+} exchanger

mNCX was selectively blocked by CGP [12], which was added to the ISC solution either alone, or in the presence of SEA.

When applied alone (CGP group, Fig. 6 left), CGP did not measurably affect Ca_{cyt} accumulation during ISC (Fig. 6a); however, it significantly increased Ca_{SR} (Fig. 6b), thus suggesting a shift of Ca^{2+} from the mitochondrial to the SR compartment. On the other hand, when CGP was applied in the presence of SEA (+CGP group; Fig. 6 right), Ca_{cyt} accumulation and Ca_{SR} were significantly reduced. Thus, at least in the presence of the high Ca_{cyt} levels achieved under sNCX blockade, mitochondria provided a Ca^{2+} source, with mNCX supporting Ca^{2+} efflux to the cytosol [27]. Ca_{FR} was not affected by CGP

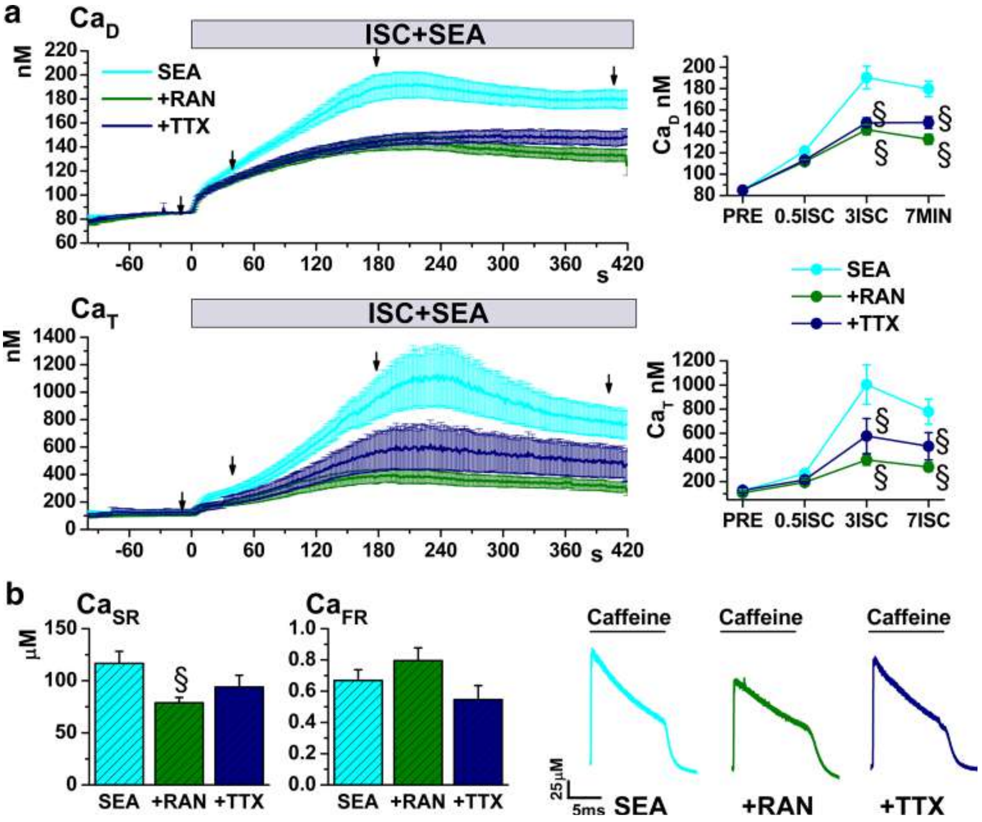

Fig. 5 Effect of I_{NaL} blockade (RAN, TTX) on cytosolic Ca^{2+} during ISC in the presence of sNCX blockade (SEA). **a** Average traces ± SE of diastolic Ca^{2+} (Ca_D) and Ca^{2+} transient amplitude (Ca_T) during the ISC protocol in CTRL, RAN and TTX treatment groups; statistics of Ca_{cyt} at discrete time points (*arrows*) during the protocol; statistics of Ca_{cyt} at discrete time points (*arrows*) during the protocol (SEA $N = 23$; SEA + RAN $N = 20$; SEA + TTX $N = 18$). **b** Statistics for SR Ca^{2+} content (Ca_{SR}) and SR Ca^{2+} fractional release (Ca_{FR}) at protocol end (SEA $N = 9$; SEA + RAN $N = 9$; SEA + TTX $N = 9$); representative Ca^{2+} transient triggered by caffeine superfusion in each group. $^{§}p < 0.05$ vs SEA

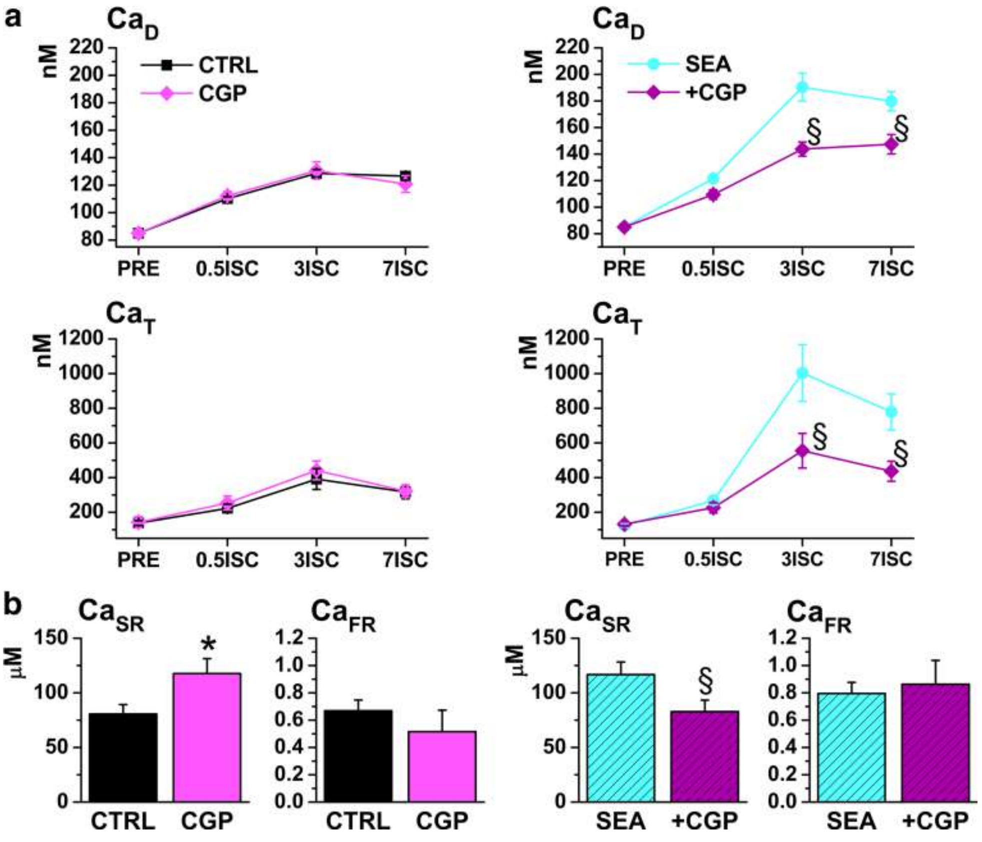

Fig. 6 Effect of mNCX blockade (CGP) on Ca_{cyt} and Ca_{SR} during ISC. *Left* effect of CGP alone; *right* effect of CGP in the presence of SEA. **a** Statistics for diastolic Ca^{2+} (Ca_D, *top*) and Ca^{2+} transient amplitude (Ca_T, *bottom*) at discrete protocol time points (CTRL $N = 22$; CGP $N = 8$; SEA $N = 23$; SEA + CGP $N = 16$); **b** statistics for SR Ca^{2+} content (Ca_{SR}) and SR fractional release (Ca_{FR}) at the end of protocol (CTRL $N = 19$; CGP $N = 8$; SEA $N = 10$; SEA + CGP $N = 14$). $*p < 0.05$ vs CTRL, $^{§}p < 0.05$ vs SEA

(Fig. 6b), again arguing against the involvement of RyRs modulation in the observed effects.

In the presence of sNCX blockade, the effects of CGP, RAN and TTX on Ca_{cyt} accumulation during ISC were strikingly similar (Supplemental Figure S8). This supports the view that I_{NaL} blockade may limit Ca_{cyt} accumulation by reducing Na_{cyt} availability to fuel mNCX-mediated Ca^{2+} efflux from mitochondria.

To further test the role of mitochondria as a Ca^{2+} source during ISC, MCU was selectively blocked by RU [29] in the presence of sNCX blockade (+RU). RU reduced Ca_{cyt} accumulation, achieving statistical significance for Ca_D (Fig. 7a). In the presence of SEA + RU, CGP failed to modify Ca_{cyt} (Supplement Figure S10). These observations confirm a role of mitochondria in Ca_{cyt} increment during ISC and support the view that the effect of CGP on Ca_{cyt} (Fig. 6 right) were due to inhibition of mitochondrial Ca^{2+} efflux. RU also increased Ca_{SR} (Fig. 7b) likely reflecting transfer of Ca^{2+} from the mitochondrial compartment to the SR one.

Discussion

The main findings of this study are that during ISC: (1) I_{NaL} was increased in spite of AP changes; (2) I_{NaL} blockade reduced Na_{cyt} accumulation, but failed to affect Ca_{cyt} accumulation unless sNCX was blocked; (3) sNCX contributed to Ca_{cyt} clearance (as opposed to accumulation) throughout ISC; (4) blockade of I_{NaL} and mNCX exerted similar effects on ISC-induced Ca_{cyt} accumulation, at least under conditions of substantial Ca^{2+} overload.

Relevance of ISC as a model of acute myocardial ischemia

Tissue response to acute ischemia is highly dynamic and closely dependent on a number of conditions; thus, any experimental model of acute ischemia is necessarily specific and unlikely to be of general applicability. Furthermore, an isolated myocyte, oxygenated through aqueous superfusion (low O_2 solubility) and contracting without external load, cannot be strictly compared to in vivo ischemia. Nevertheless, information of general relevance on the mechanisms that can contribute to ischemic damage, can still be acquired by observing the response to conditions known to occur during it. The ischemic condition adopted in this study (ISC), although encompassing the major factors present in tissue ischemia, differs from it for the absence of hypoxia. Although hypoxia was shown to have little role in the contractile pattern during ISC application [25], it might affect the mechanisms by which such a pattern is achieved in a given time-frame. For

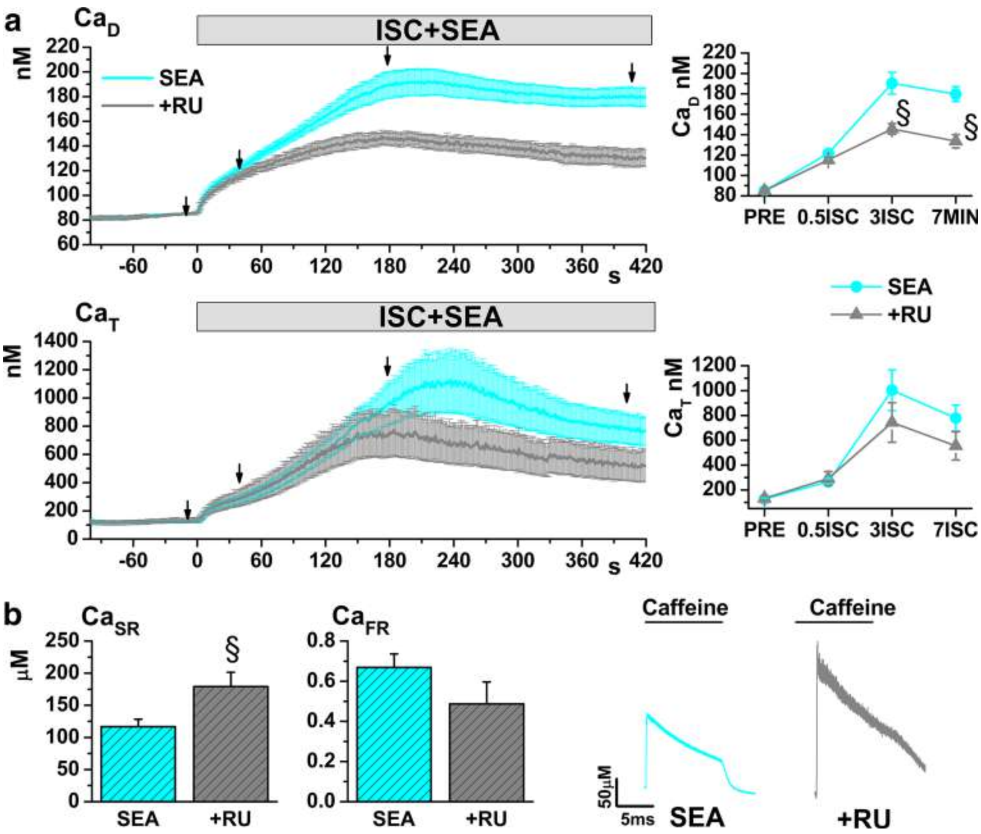

Fig. 7 Effect of MCU blockade (RU) on cytosolic Ca^{2+} during ISC (in the presence of sNCX blockade). **a** Average traces ± SE of diastolic Ca^{2+} (Ca_D) and Ca^{2+} transient amplitude (Ca_T) during ISC + SEA alone (SEA) and in the presence of MCU blockade (+RU); Ca_D and Ca_T statistics at discrete time points; **b** statistics for SR Ca^{2+} content (Ca_{SR}) and SR Ca^{2+} fractional release (Ca_{FR}) at protocol end; representative caffeine-induced Ca^{2+} transients. SEA $N = 9$; +RU $N = 10$. $^{\S}p < 0.05$ vs SEA

instance, hypoxia would likely accelerate ATP decay and reactive oxide species (ROS) production, both factors known to accelerate Na_{cyt} accumulation and facilitate reversal of sNCX transport. Therefore, failure of sNCX to switch to the reverse mode, and the modest effect of I_{NaL} blockade, might be model-specific. However, the contribution of sNCX-independent Ca^{2+} sources (including mitochondria) to Ca_{cyt} accumulation in the presence of factors certainly present during real ischemia, may have general relevance. A further factor to be considered is that, whereas generated within the myocyte under true ischemia, lactic acid was applied extracellularly. This might reduce NHE contribution to Na^+ loading, which was nonetheless substantial (Supplemental Figure S4).

To mimic what is reported to occur during ischemia, the ISC solution was slightly hyperosmolar [25]. The possibility that this accounted for the observed changes in the intracellular milieu was ruled out in preliminary experiments (Supplemental Figure S9).

Because of the above features, ISC reproduces conditions closer to those of a “border zone”, not directly ischemic (still energetically competent) but exposed to factors released by the neighboring ischemic area [11].

ISC-induced I_{NaL} enhancement

A link between I_{NaL} enhancement and ischemia/reperfusion injury has been firmly established by previous studies [1, 4, 7, 39, 50]. However, considering the opposing effect of ISC-induced membrane potential changes, I_{NaL} enhancement by ISC was far from predictable.

Contribution of I_{NaL} and Na^+/H^+ exchanger to cytosolic Na^+ accumulation

About 50% of ISC-induced Na_{cyt} accumulation was similarly prevented by RAN and TTX. Being shared by both agents, this effect is likely to result from I_{NaL} blockade. When NHE was also blocked (Supplemental Figure S4), ISC-induced Na_{cyt} accumulation was completely abolished; this suggests that Na^+ influx via NHE accounted for the remaining 50% (this quantitative estimate does not take into account potential interactions between the two transports). Although the presence in ISC of lactic acid likely afforded relatively fast H^+ equilibration across the membrane, acidosis was primarily extracellular in the present setting; this might explain the initial dip in Na_{cyt} time course (Fig. 3). The present findings suggest that, under the present experimental conditions, NHE was still active during ISC. The monotonic increase in Na_{cyt} during exposure to ouabain (Supplemental Figure S5) indicates that I_{NaL}- and NHE-mediated Na^+ influx were in balance with Na^+ extrusion through the Na^+/K^+ pump, which remained active throughout the ISC period and was responsible for the late decay in Na_{cyt}.

I_{NaL} contribution to cytosolic Ca^{2+} accumulation

In spite of its remarkable effect on Na_{cyt}, I_{NaL} blockade unexpectedly failed to affect ISC-induced Ca_{cyt} accumulation (Fig. 4). This might simply reflect inadequacy of the I_{NaL}-dependent Na_{cyt} perturbation in overriding Ca_{cyt} homeostatic control; indeed, I_{NaL} blockade tended to reduce Ca_{SR}, potentially revealing a role for SR in buffering I_{NaL}-induced perturbation. However, the observation that the effect of I_{NaL} blockade was unmasked by sNCX blockade implies that a Ca^{2+} source independent of sNCX, and at least partially sensitive to I_{NaL} blockade (or Na_{cyt}), must have contributed to ISC-induced Ca_{cyt} accumulation.

sNCX is often claimed to work in reverse mode during ischemia [43, 48], thereby providing a direct path for Ca^{2+} influx. This was clearly not the case in the present setting; however, sNCX mode may depend on the duration and extent of ischemia. Nevertheless, changes in Na_{cyt} compatible with forward sNCX operation have been reported after sNCX knock-out in intact murine hearts subjected to no-flow ischemia (Fig. 5 in Ref. [18]).

Mitochondrial contribution to cytosolic Ca^{2+} accumulation

Mitochondria represent a significant Ca^{2+} compartment, physiologically uptaking Ca^{2+} through MCU [21] and extruding it to cytosol through mNCX, a Na_{cyt}-sensitive transport [6, 27].

CGP effect in the absence of SEA suggests that, under basal conditions, mNCX blockade may promote a shift of Ca^{2+} from mitochondria to the SR. This implies that, during ISC, mitochondria contribute to buffer Ca_{cyt} through mNCX-mediated Ca^{2+} uptake. In the present setting, the impact of I_{NaL} blockade on mitochondrial buffering was probably small enough not to affect Ca_{cyt}.

On the other hand, when sNCX was blocked, CGP reduced ISC-induced Ca_{cyt} accumulation, thus supporting the view that sizable mNCX-mediated Ca^{2+} efflux from mitochondria may occur during ISC in the presence of substantial Ca^{2+} overload [6, 37, 44]. Because mNCX flux is Na_{cyt}-dependent, this might account for the I_{NaL}-sensitive component of Ca_{cyt} accumulation observed under sNCX blockade.

At the conditions used in the present experiments, RU is a selective blocker of MCU, without effect on I_{CaL} or SR Ca^{2+} uptake/release [29, 36]. Functional exclusion of the mitochondrial compartment by MCU blockade caused a shift of Ca^{2+} to the SR, reduced Ca_{cyt} accumulation and abolished the effect of mNCX blockade. Concomitance of reduced Ca_{cyt} with increased Ca_{SR} is consistent with microdomain communication between mitochondria and SR [22].

To summarize, sNCX blockade seemingly changed the role of mitochondria during ISC from Ca^{2+} sink to Ca^{2+} source; the simplest way to explain this effect is the rather dramatic increase in overall cell Ca^{2+} content present in this condition, possibly reducing mitochondrial and SR Ca^{2+} buffering reserves. We surmise that such a Ca^{2+} overload might be achieved, even in the absence of sNCX blockade, during in vivo cardiac ischemia. Therefore, the specific effect of mNCX inhibition might depend on the duration and extent of ischemia; nevertheless, the contribution of mitochondria as a further Na_{cyt}-sensitive compartment contributing to Ca_{cyt} changes may be regarded as an observation of general value.

Additional potential sources of cytosolic Ca^{2+} accumulation

As a Na_{cyt}-sensitive Ca^{2+} compartment, mitochondria are of particular relevance to changes caused by I_{NaL} enhancement. Nonetheless, they are unlikely to fully account for the large source of Ca_{cyt} required to support forward sNCX operation during ISC, in spite of the attending increase in Na_{cyt} and membrane depolarization (both favoring sNCX reversal).

Because voltage-gated Ca^{2+} channels are potently inhibited by acidosis [20, 38] I_{CaL} is unlikely to be enhanced during ISC; however, a H^+-gated background Ca^{2+} conductance (TRPA1) [17] is expressed in the heart and shown to contribute to ischemia/reperfusion damage [33].

Protons compete with Ca^{2+} for binding to intracellular buffers, troponin C in particular [15, 41]. In the present setting, this is suggested by the virtual absence of contraction during early ISC, occurring in spite of persisting Ca^{2+} transients. Therefore, acidosis might support substantial release of free Ca^{2+} to the cytosol through a mechanism independent of transmembrane fluxes. Because sarcolemmal Na^+ gradient is crucial for intracellular H^+ clearance through NHE, this Ca^{2+} source may also be modulated, albeit indirectly, by I_{NaL} blockade.

Discrepancy between TTX and RAN effects

RAN and TTX shared the majority of effects during ISC exposure, supporting their origin from I_{NaL} inhibition. However, unlike TTX, RAN reduced Ca_D during ISC under baseline condition and limited Ca_{SR} increment during SEA exposure. This points to modulation by RAN of a Ca^{2+} compartment insensitive to TTX. RAN has been shown to stabilize membrane potential of mitochondria during ischemia [1, 13, 14, 51], which would enhance their ability to retain Ca^{2+}. However, this has been attributed to limitation of Na_{cyt} accumulation, an effect that should be shared by TTX. The possibility that RAN may affect mitochondrial performance as a Ca^{2+} compartment also independently of I_{NaL} blockade may deserve further investigation.

Conclusions

Some of the observed effects of ISC may be model-specific (i.e., depend on the duration and extent of the ischemic condition) and, as such, of restricted applicability. These may include poor sensitivity of Ca_{cyt} to I_{NaL} blockade and persistence of forward sNCX operation. Nevertheless, other observations lead to conclusions likely of more general relevance: (1) I_{NaL} can be enhanced during acute ischemia, irrespective of membrane potential changes, and significantly contribute to Na_{cyt} accumulation; (2) Ca^{2+} sources other than sNCX substantially contribute to Ca_{cyt} increment and, at least in the early phase of acute ischemia, may oppose reversal of sNCX flux; (3) under conditions of Ca^{2+} overload, mitochondria may act as a Na_{cyt}-sensitive Ca_{cyt} source, thus providing a mechanism, beyond sNCX modulation, to account for I_{NaL}-induced perturbation of intracellular milieu. A further conclusion is that most, but not all, RAN effects on intracellular milieu may result from I_{NaL} blockade.

Acknowledgements This research was supported by grant from Gilead Inc. (Fremont, CA, US) and FAR 2015 to A. Zaza. We are grateful to Dr. Luiz Belardinelli for providing stimulating discussion throughout the execution of the study and Dr. Luca Sala for contributing to some experiments and providing insightful comments on the manuscript.

Compliance with ethical standards

All experiment were approved and conducted in accordance with guidelines issued by the Animal Care Committee of the University Milano-Bicocca, in compliance with the ethical standards laid down in the 1964 Declaration of Helsinki and its later amendments. The manuscript does not contain human data.

Conflict of interest The study has been partially funded by Gilead, Inc. (Fremont, CA), which is the patent holder for Ranolazine. The authors declare that they have no further conflict of interest.

References

1. Aldakkak M, Camara AK, Heisner JS, Yang M, Stowe DF (2011) Ranolazine reduces Ca2+ overload and oxidative stress and improves mitochondrial integrity to protect against ischemia

reperfusion injury in isolated hearts. Pharmacol Res 64:381–392. doi:10.1016/j.phrs.2011.06.018

2. Alemanni M, Rocchetti M, Re D, Zaza A (2011) Role and mechanism of subcellular Ca2+ distribution in the action of two inotropic agents with different toxicity. J Mol Cell Cardiol 50:910–918. doi:10.1016/j.yjmcc.2011.02.008
3. Allen DG, Xiao XH (2003) Role of the cardiac Na+/H+ exchanger during ischemia and reperfusion. Cardiovasc Res 57:934–941. doi:10.1016/s0008-6363(02)00836-2
4. Belardinelli L, Shryock JC, Fraser H (2006) Inhibition of the late sodium current as a potential cardioprotective principle: effects of the late sodium current inhibitor ranolazine. Heart 92(Suppl 4):iv6–iv14. doi:10.1136/hrt.2005.078790
5. Bernink FJ, Timmers L, Beek AM, Diamant M, Roos ST, van Rossum AC, Appelman Y (2014) Progression in attenuating myocardial reperfusion injury: an overview. Int J Cardiol 170:261–269. doi:10.1016/j.ijcard.2013.11.007
6. Boyman L, Williams GS, Khananshvili D, Sekler I, Lederer WJ (2013) NCLX: the mitochondrial sodium calcium exchanger. J Mol Cell Cardiol 59:205–213. doi:10.1016/j.yjmcc.2013.03.012
7. Calderon-Sanchez EM, Dominguez-Rodriguez A, Lopez-Haldon J, Jimenez-Navarro MF, Gomez AM, Smani T, Ordonez A (2016) Cardioprotective effect of ranolazine in the process of ischemia-reperfusion in adult rat cardiomyocytes. Rev Esp Cardiol (Engl Ed) 69:45–53. doi:10.1016/j.rec.2015.02.027
8. Caldwell JC, Burton FL, Cobbe SM, Smith GL (2012) Amplitude changes during ventricular fibrillation: a mechanistic insight. Front Physiol 3(147):1–8. doi:10.3389/fphys.2012.00147
9. Chen S, Li S (2012) The Na+/Ca(2)+ exchanger in cardiac ischemia/reperfusion injury. Med Sci Monit 18:RA161–RA165. doi:10.12659/MSM.883533
10. Cordeiro JM, Howlett SE, Ferrier GR (1994) Simulated ischaemia and reperfusion in isolated guinea pig ventricular myocytes. Cardiovasc Res 28:1794–1802. doi:10.1093/cvr/28.12.1794
11. Coronel R, Wilms-Schopman FJ, Fiolet JW, Opthof T, Janse MJ (1995) The relation between extracellular potassium concentration and pH in the border zone during regional ischemia in isolated porcine hearts. J Mol Cell Cardiol 27:2069–2073. doi:10.1016/0022-2828(95)90028-4
12. Cox DA, Conforti L, Sperelakis N, Matlib MA (1993) Selectivity of inhibition of Na(+)–Ca2+ exchange of heart mitochondria by benzothiazepine CGP-37157. J Cardiovasc Pharmacol 21:595–599. doi:10.1097/00005344-199304000-00013
13. Dehina L, Descotes J, Chevalier P, Bui-Xuan B, Romestaing C, Dizerens N, Mamou Z, Timour Q (2014) Protective effects of ranolazine and propranolol, alone or combined, on the structural and functional alterations of cardiomyocyte mitochondria in a pig model of ischemia/reperfusion. Fundam Clin Pharmacol 28:257–267. doi:10.1111/fcp.12033
14. Gadicherla AK, Stowe DF, Antholine WE, Yang M, Camara AK (2012) Damage to mitochondrial complex I during cardiac ischemia reperfusion injury is reduced indirectly by anti-anginal drug ranolazine. Biochim Biophys Acta 1817:419–429. doi:10.1016/j.bbabio.2011.11.021
15. Garciarena CD, Youm JB, Swietach P, Vaughan-Jones RD (2013) H(+)-activated Na(+) influx in the ventricular myocyte couples Ca(2)(+)-signalling to intracellular pH. J Mol Cell Cardiol 61:51–59. doi:10.1016/j.yjmcc.2013.04.008
16. Hale SL, Leeka JA, Kloner RA (2006) Improved left ventricular function and reduced necrosis after myocardial ischemia/reperfusion in rabbits treated with ranolazine, an inhibitor of the late sodium channel. J Pharmacol Exp Ther 318:418–423. doi:10.1124/jpet.106.103242
17. Hamilton NB, Kolodziejczyk K, Kougioumtzidou E, Attwell D (2016) Proton-gated Ca(2+)-permeable TRP channels damage myelin in conditions mimicking ischaemia. Nature 529:523–527. doi:10.1038/nature16519
18. Imahashi K, Pott C, Goldhaber JI, Steenbergen C, Philipson KD, Murphy E (2005) Cardiac-specific ablation of the Na+–Ca2+ exchanger confers protection against ischemia/reperfusion injury. Circ Res 97:916–921. doi:10.1161/01.RES.0000187456.06162.cb
19. Jung IS, Lee SH, Yang MK, Park JW, Yi KY, Yoo SE, Kwon SH, Chung HJ, Choi WS, Shin HS (2010) Cardioprotective effects of the novel Na+/H+ exchanger-1 inhibitor KR-32560 in a perfused rat heart model of global ischemia and reperfusion: involvement of the Akt-GSK-3beta cell survival pathway and antioxidant enzyme. Arch Pharm Res 33:1241–1251. doi:10.1007/s12272-010-0815-z
20. Kaibara M, Kameyama M (1988) Inhibition of the calcium channel by intracellular protons in single ventricular myocytes of the guinea-pig. J Physiol 403:621–640. doi:10.1113/jphysiol.1988.sp017268
21. Kirichok Y, Krapivinsky G, Clapham DE (2004) The mitochondrial calcium uniporter is a highly selective ion channel. Nature 427:360–364. doi:10.1038/nature02246
22. Kohlhaas M, Maack C (2013) Calcium release microdomains and mitochondria. Cardiovasc Res 98:259–268. doi:10.1093/cvr/cvt032
23. Lazdunski M, Frelin C, Vigne P (1985) The sodium/hydrogen exchange system in cardiac cells: its biochemical and pharmacological properties and its role in regulating internal concentrations of sodium and internal pH. J Mol Cell Cardiol 17:1029–1042. doi:10.1016/S0022-2828(85)80119-X
24. Linz WJ, Busch AE (2003) NHE-1 inhibition: from protection during acute ischaemia/reperfusion to prevention/reversal of myocardial remodelling. Naunyn Schmiedebergs Arch Pharmacol 368:239–246. doi:10.1007/s00210-003-0808-2
25. Lu J, Zang WJ, Yu XJ, Chen LN, Zhang CH, Jia B (2005) Effects of ischaemia-mimetic factors on isolated rat ventricular myocytes. Exp Physiol 90:497–505. doi:10.1113/expphysiol.2004.029421
26. Ma J, Song Y, Shryock JC, Hu L, Wang W, Yan X, Zhang P, Belardinelli L (2014) Ranolazine attenuates hypoxia- and hydrogen peroxide-induced increases in sodium channel late openings in ventricular myocytes. J Cardiovasc Pharmacol 64:60–68. doi:10.1097/FJC.0000000000000090
27. Maack C, Cortassa S, Aon MA, Ganesan AN, Liu T, O'Rourke B (2006) Elevated cytosolic Na+ decreases mitochondrial Ca2+ uptake during excitation-contraction coupling and impairs energetic adaptation in cardiac myocytes. Circ Res 99:172–182. doi:10.1161/01.RES.0000232546.92777.05
28. MacDonald AC, Howlett SE (2008) Differential effects of the sodium calcium exchange inhibitor, KB-R7943, on ischemia and reperfusion injury in isolated guinea pig ventricular myocytes. Eur J Pharmacol 580:214–223. doi:10.1016/j.ejphar.2007.10.055
29. Matlib MA, Zhou Z, Knight S, Ahmed S, Choi KM, Krause-Bauer J, Phillips R, Altschuld R, Katsube Y, Sperelakis N, Bers DM (1998) Oxygen-bridged dinuclear ruthenium amine complex specifically inhibits Ca2+ uptake into mitochondria in vitro and in situ in single cardiac myocytes. J Biol Chem 273:10223–10231. doi:10.1074/jbc.273.17.10223
30. Nakamura T, Hayashi H, Satoh H, Katoh H, Kaneko M, Terada H (1999) A single cell model of myocardial reperfusion injury: changes in intracellular Na+ and Ca2+ concentrations in guinea pig ventricular myocytes. Mol Cell Biochem 194:147–157. doi:10.1023/A:1006919929104
31. Namekata I, Shimada H, Kawanishi T, Tanaka H, Shigenobu K (2006) Reduction by SEA0400 of myocardial ischemia-induced cytoplasmic and mitochondrial Ca2+ overload. Eur J Pharmacol 543:108–115. doi:10.1016/j.ejphar.2006.06.012

32. Park CO, Xiao XH, Allen DG (1999) Changes in intracellular Na+ and pH in rat heart during ischemia: role of Na+/H+ exchanger. Am J Physiol 276:H1581–H1590
33. Robertson S, Thomson AL, Carter R, Stott HR, Shaw CA, Hadoke PW, Newby DE, Miller MR, Gray GA (2014) Pulmonary diesel particulate increases susceptibility to myocardial ischemia/reperfusion injury via activation of sensory TRPV1 and beta1 adrenoreceptors. Part Fibre Toxicol 11:12. doi:10.1186/1743-8977-11-12
34. Rocchetti M, Sala L, Rizzetto R, Staszewsky LI, Alemanni M, Zambelli V, Russo I, Barile L, Cornaghi L, Altomare C, Ronchi C, Mostacciuolo G, Lucchetti J, Gobbi M, Latini R, Zaza A (2014) Ranolazine prevents INaL enhancement and blunts myocardial remodelling in a model of pulmonary hypertension. Cardiovasc Res 104:37–48. doi:10.1093/cvr/cvu188
35. Salameh A, Dhein S, Beuckelmann DJ (2002) Role of the cardiac Na(+)/H(+)exchanger in [Ca(2+)](i)and [Na(+)](i)handling during intracellular acidosis. Effect of cariporide (Hoe 642). Pharmacol Res 45:35–41. doi:10.1006/phrs.2001.0908
36. Sanchez JA, Garcia MC, Sharma VK, Young KC, Matlib MA, Sheu SS (2001) Mitochondria regulate inactivation of L-type Ca2+ channels in rat heart. J Physiol 536:387–396. doi:10.1111/j.1469-7793.2001.0387c.xd
37. Saotome M, Katoh H, Satoh H, Nagasaka S, Yoshihara S, Terada H, Hayashi H (2005) Mitochondrial membrane potential modulates regulation of mitochondrial Ca2+ in rat ventricular myocytes. Am J Physiol Heart Circ Physiol 288:H1820–H1828. doi:10.1152/ajpheart.00589.2004
38. Sato R, Noma A, Kurachi Y, Irisawa H (1985) Effects of intracellular acidification on membrane currents in ventricular cells of the guinea pig. Circ Res 57:553–561. doi:10.1161/01.res.57.4.553
39. Soliman D, Wang L, Hamming KS, Yang W, Fatehi M, Carter CC, Clanachan AS, Light PE (2012) Late sodium current inhibition alone with ranolazine is sufficient to reduce ischemia- and cardiac glycoside-induced calcium overload and contractile dysfunction mediated by reverse-mode sodium/calcium exchange. J Pharmacol Exp Ther 343:325–332. doi:10.1124/jpet.112.196949
40. Song Y, Shryock JC, Wagner S, Maier LS, Belardinelli L (2006) Blocking late sodium current reduces hydrogen peroxide-induced arrhythmogenic activity and contractile dysfunction. J Pharmacol Exp Ther 318:214–222. doi:10.1124/jpet.106.101832
41. Swietach P, Youm JB, Saegusa N, Leem CH, Spitzer KW, Vaughan-Jones RD (2013) Coupled Ca2+/H+ transport by cytoplasmic buffers regulates local Ca2+ and H+ ion signaling. Proc Natl Acad Sci USA 110:E2064–E2073. doi:10.1073/pnas.1222433110
42. Tanaka H, Nishimaru K, Aikawa T, Hirayama W, Tanaka Y, Shigenobu K (2002) Effect of SEA0400, a novel inhibitor of sodium-calcium exchanger, on myocardial ionic currents. Br J Pharmacol 135:1096–1100. doi:10.1038/sj.bjp.0704574
43. Tang Q, Ma J, Zhang P, Wan W, Kong L, Wu L (2012) Persistent sodium current and Na+/H+ exchange contributes to the augmentation of the reverse Na+/Ca2+ exchange during hypoxia or acute ischemia in ventricular myocytes. Pflugers Arch 463:513–522. doi:10.1007/s00424-011-1070-y
44. Tanonaka K, Motegi K, Arino T, Marunouchi T, Takagi N, Takeo S (2012) Possible pathway of Na(+) flux into mitochondria in ischemic heart. Biol Pharm Bull 35:1661–1668. doi:10.1248/bpb.b12-00010
45. Undrovinas AI, Belardinelli L, Undrovinas NA, Sabbah HN (2006) Ranolazine improves abnormal repolarization and contraction in left ventricular myocytes of dogs with heart failure by inhibiting late sodium current. J Cardiovasc Electrophysiol 17(Suppl 1):S169–S177. doi:10.1111/j.1540-8167.2006.00401.x
46. Undrovinas AI, Fleidervish IA, Makielski JC (1992) Inward sodium current at resting potentials in single cardiac myocytes induced by the ischemic metabolite lysophosphatidylcholine. Circ Res 71:1231–1241. doi:10.1161/01.res.71.5.1231
47. van Borren MM, Baartscheer A, Wilders R, Ravesloot JH (2004) NHE-1 and NBC during pseudo-ischemia/reperfusion in rabbit ventricular myocytes. J Mol Cell Cardiol 37:567–577. doi:10.1016/j.yjmcc.2004.05.017
48. Wang XJ, Wang LL, Fu C, Zhang PH, Wu Y, Ma JH (2014) Ranolazine attenuates the enhanced reverse Na(+)-Ca(2)(+) exchange current via inhibiting hypoxia-increased late sodium current in ventricular myocytes. J Pharmacol Sci 124:365–373. doi:10.1254/jphs.13202FP
49. Wilde AA, Escande D, Schumacher CA, Thuringer D, Mestre M, Fiolet JW, Janse MJ (1990) Potassium accumulation in the globally ischemic mammalian heart. A role for the ATP-sensitive potassium channel. Circ Res 67:835–843. doi:10.1161/01.res.67.4.835
50. Williams IA, Xiao XH, Ju YK, Allen DG (2007) The rise of [Na(+)] (i) during ischemia and reperfusion in the rat heart-underlying mechanisms. Pflugers Arch 454:903–912. doi:10.1007/s00424-007-0241-3
51. Zaza A, Rocchetti M (2013) The late Na+ current—origin and pathophysiological relevance. Cardiovasc Drugs Ther 27:61–68. doi:10.1007/s10557-012-6430-0